Universidad de Alcalá
COMISIÓN DE ESTUDIOS OFICIALES
DE POSGRADO Y DOCTORADO

ACTA DE EVALUACIÓN DE LA TESIS DOCTORAL

(FOR EVALUATION OF THE ACT DOCTORAL THESIS)

Año académico (*academic year):* 2018/19

DOCTORANDO *(candidate PHD)*: **PINTO BENEL, FREDDY ALBERT**
D.N.I./PASAPORTE (*Id.Passport*): ******6641P**
PROGRAMA DE DOCTORADO *(Academic Committee of the Programme)*: **D445-TECNOLOGÍAS DE LA INFORMACIÓN Y LAS COMUNICACIONES**
DPTO. COORDINADOR DEL PROGRAMA *(Department)*: **TEORÍA DE LA SEÑAL Y COMUNICACIONES**
TITULACIÓN DE DOCTOR EN *(Phd title)*: **DOCTOR/A POR LA UNIVERSIDAD DE ALCALÁ**

En el día de hoy 05/02/19, reunido el tribunal de evaluación, constituido por los miembros que suscriben el presente Acta, el aspirante defendió su Tesis Doctoral **con Mención Internacional** (*In today assessment met the court, consisting of the members who signed this Act, the candidate defended his doctoral thesis with mention as International Doctorate)*, elaborada bajo la dirección de (*prepared under the direction of)* FERNANDO CRUZ ROLDÁN.

Sobre el siguiente tema *(Title of the doctoral thesis)*: *DESIGN AND EVALUATION OF TRANSCEIVERS FOR MULTICARRIER COMMUNICATIONS OVER THE POWER LINE NETWORK*

Finalizada la defensa y discusión de la tesis, el tribunal acordó otorgar la CALIFICACIÓN GLOBAL[1] de (**no apto, aprobado, notable** y **sobresaliente)** *(After the defense and defense of the thesis, the court agreed to grant the GLOBAL RATING (fail, pass, good and excellent)*: SOBRESALIENTE

Alcalá de Henares, a 5 de FEBRERO de 2019

Fdo. *(Signed)*: ROBERTO HOLGADO SÁNCHEZ

Fdo. *(Signed)*: MANUEL BLANCO

Fdo. *(Signed)*: LO VISTO

FIRMA DEL ALUMNO (candidate's signature),

Fdo. *(Signed)*: Freddy Albert Pinto Benel

Con fecha 25 de Febrero de 2019 la Comisión Delegada de la Comisión de Estudios Oficiales de Posgrado, a la vista de los votos emitidos de manera anónima por el tribunal que ha juzgado la tesis, resuelve:

☒ Conceder la Mención de "Cum Laude"
☐ No conceder la Mención de "Cum Laude"

La Secretaria de la Comisión Delegada

[1] La calificación podrá ser "**no apto**" "**aprobado**" "**notable**" y "**sobresaliente**". El tribunal podrá otorgar la mención de "cum laude" si la calificación global es de sobresaliente y se emite en tal sentido el voto secreto positivo por unanimidad. (*The grade may be "fail" "pass" "good" or "excellent". The panel may confer the distinction of "cum laude" if the overall grade is "Excellent" and has been awarded unanimously as such after secret voting.).*

INCIDENCIAS / OBSERVACIONES:
(Incidents / Comments)

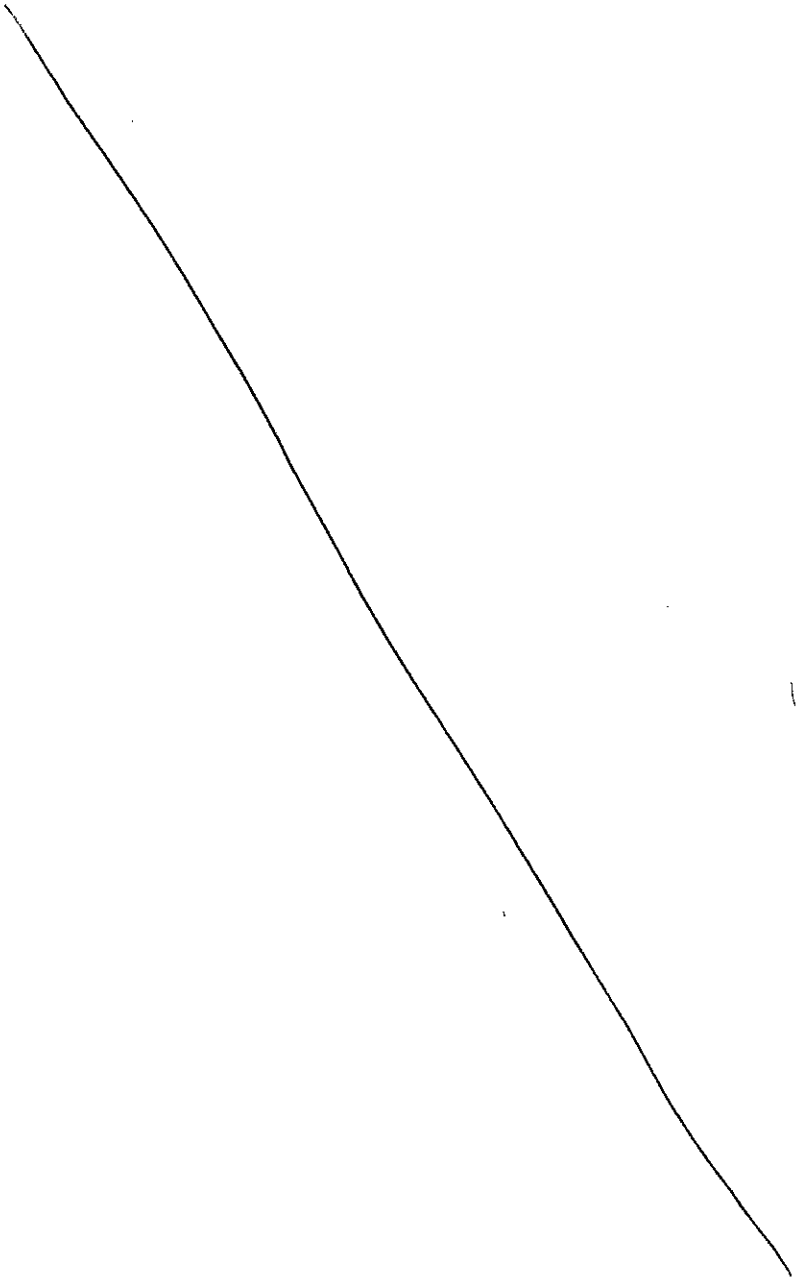

Universidad de Alcalá

COMISIÓN DE ESTUDIOS OFICIALES DE POSGRADO Y DOCTORADO

En aplicación del art. 14.7 del RD. 99/2011 y el art. 14 del Reglamento de Elaboración, Autorización y Defensa de la Tesis Doctoral, la Comisión Delegada de la Comisión de Estudios Oficiales de Posgrado y Doctorado, en sesión pública de fecha 25 de febrero, procedió al escrutinio de los votos emitidos por los miembros del tribunal de la tesis defendida por *PINTO BENEL, FREDDY ALBERT*, el día 5 de febrero de 2019, titulada *DESIGN AND EVALUATION OF TRANSCEIVERS FOR MULTICARRIER COMMUNICATIONS OVER THE POWER LINE NETWORK*, para determinar, si a la misma, se le concede la mención "cum laude", arrojando como resultado el voto favorable de todos los miembros del tribunal.

Por lo tanto, la Comisión de Estudios Oficiales de Posgrado **resuelve otorgar** a dicha tesis la

MENCIÓN "CUM LAUDE"

Alcalá de Henares, 25 de febrero de 2019

EL VICERRECTOR DE INVESTIGACIÓN Y TRANSFERENCIA

UNIVERSIDAD DE ALCALÁ · VICERRECTORADO DE INVESTIGACIÓN Y TRANSFERENCIA

D. Javier de la Mata de la Mata

Copia por e-mail a:
Doctorando: PINTO BENEL, FREDDY ALBERT
Secretario del Tribunal: MANUEL BLANCO VELASCO
Director de Tesis: FERNANDO CRUZ ROLDÁN

Universidad de Alcalá

ESCUELA DE DOCTORADO.
Servicio de Estudios Oficiales de Posgrado

DILIGENCIA DE DEPÓSITO DE TESIS.

Comprobado que el expediente académico de D./Dª FREDDY ALBERT PINTO BENEL reúne los requisitos exigidos para la presentación de la Tesis, de acuerdo a la normativa vigente, y habiendo presentado la misma en formato: ☒ soporte electrónico ☐ impreso en papel, para el depósito de la misma, en el Servicio de Estudios Oficiales de Posgrado, con el nº de páginas: 178 se procede, con fecha de hoy a registrar el depósito de la tesis.

Alcalá de Henares a 30 de NOVIEMBRE de 2018

UNIVERSIDAD DE ALCALÁ
SERVICIO DE ESTUDIOS OFICIALES DE POSGRADO

Aurora Juárez Abril

Fdo. El Funcionario

RESTAURAR IMPRIMIR

Universidad de Alcalá

Programa de Doctorado en Tecnologías de la Información y las Comunicaciones

Design and Evaluation of Transceivers for Multicarrier Communications over the Power Line Network

Freddy A. Pinto-Benel

2018

Universidad de Alcalá

Campus Universitario
Dpto. de Teoría de la Señal y Comunicaciones
Ctra. Madrid-Barcelona, Km. 36.6
28805 Alcalá de Henares (Madrid)
Telf: +34 91 885 88 99
Fax: +34 91 885 66 99

Dr. D. FERNANDO CRUZ ROLDÁN, Catedrático de Universidad del Área de Conocimiento de Teoría de la Señal y Comunicaciones de la Universidad de Alcalá,

HACE CONSTAR

Que la tesis "**Design and Evaluation of Transceivers for Multicarrier Communications over the Power Line Network**", presentada por D. Freddy Albert Pinto Benel, realizada en el Departamento de Teoría de la Señal y Comunicaciones bajo mi dirección, reúne méritos suficientes para optar al grado de Doctor, por lo que puede procederse a su depósito y lectura.

Alcalá de Henares, 5 de noviembre de 2018

Fdo.: Dr. D. Fernando Cruz Roldán

Universidad de Alcalá

Campus Universitario
Dpto. de Teoría de la Señal y Comunicaciones
Ctra. Madrid-Barcelona, Km. 36.6
28805 Alcalá de Henares (Madrid)
Telf: +34 91 885 88 99
Fax: +34 91 885 66 99

D. Freddy Albert Pinto Benel ha realizado en el Departamento de Teoría de la Señal y Comunicaciones y bajo la dirección del Dr. D. Fernando Cruz Roldán, la tesis doctoral titulada "**Design and Evaluation of Transceivers for Multicarrier Communications over the Power Line Network**", cumpliéndose todos los requisitos para la tramitación que conduce a su posterior lectura.

Alcalá de Henares, 5 de noviembre de 2018.

Coordinador del Programa de Doctorado

UNIVERSIDAD DE ALCALÁ * DPTO. DE TEORÍA DE LA SEÑAL Y COMUNICACIONES

Fdo: Dr. D. Sancho Salcedo Sanz.

Universidad de Alcalá

Programa de Doctorado en Tecnologías de la Información y las Comunicaciones

Design and Evaluation of Transceivers for Multicarrier Communications over the Power Line Network

Freddy A. Pinto-Benel

Supervisor:
Fernando Cruz-Roldán, Ph.D., Professor
Department of Signal Theory and Communications
University of Alcalá
Alcalá de Henares, Madrid, Spain

Alcalá de Henares, November 07, 2018

El esfuerzo de hoy es el descanso de mañana.

Fredy Pinto Amado.

Veni, vidi, vici.

Julio César.

Dedicado a mi familia, en especial a las dos grande figuras que me han servido de guía y ejemplo a lo largo de la vida, mis padres Mery Benel Mejía y Fredy Pinto Amado. Sin vuestro amor, dedicación, compresión, paciencia y consejos no habría sido capaz de llegar a donde estoy hoy. Gracias por animarme a seguir siempre para adelante.

A mis amigos, con los que he compartido penas y sobre todo alegrías, y que sin los cuales este periodo de mi vida hubiera sido sumamente aburrido. Gracias por estar siempre ahí.

A mi director, que ha sabido orientarme durante toda esta aventura que ha sido la tesis y motivarme cuando las cosas no salían como uno se esperaba y en lugar de avanzar parecía que se retrocedía. Gracias por todas las palabras de aliento.

Y finalmente, pero no por ello menos importante, a Diana Rincewind, que por muy oscuro que ha sido el camino, ella siempre lo ha iluminado con su sonrisa. Gracias por todo.

Acknowledgements

Me gustaría mostrar mi agradecimiento a los los profesores Francisco Javier Cañete Corripio, José Antonio Cortés Arrabal y Luis Díez del Río de la Universidad de Málaga, ya la profesora Virginie Degardin, de la University of Lille, por facilitar el modelo de ruido in-car y las medidas de los canales correspondientes a las aeronaves, respectivamente.

De manera especial me gustaría agradecer a los profesores Sergio Lima Neto, Paulo Diniz y Wallace Martins de la Universidad Federal de Río de Janeiro, y al profesor Moises Ribeiro de la Universidad Federal de Juiz de Fora, por compartir su sabiduría y amistad durante mi estancia en Brasil.

Finalmente, agradecer al Ministerio de Economía y Competitividad, ya que la investigación desarrollada durante esta tesis ha sido financiada en parte por los proyectos TEC2012-38058-C0 y TEC2015-64835-C3-1-R.

Abstract

Power line communications (PLC) is a technology that combines power and data transmission through the mains network. Although the concept of using the electrical wiring as communication channel dates back to the beginning of the 20th century, in recent years the interest in using PLC technology for in-home and out-door applications has grown considerably. This is because PLC is expected to play an important role in the development of smart grid and smart energy, as well as in the implementation of high-speed networks within the home (HAN networks) for the development of the Internet of Things (IoT). Nevertheless, PLC is not restricted to first-mile/last-mile applications, but today it is also an attractive solution for applications on transportation platforms (vehicles) because it simplifies the design, lowers the development cost and reduces weight.

However, the electrical network was not designed for communication purpose, and thus the channel frequency response of the power grid presents several and really deep frequency fades. Furthermore, the PLC noise is actually the combination of different types of noises. Therefore, systems with a very good performance are needed. In this sense, the standard: *"IEEE Standard for Broadband over Power Line Networks: Medium Access Control and Physical Layer Specifications"* (IEEE 1901) specifies two different modulation schemes. On the one hand, a windowed orthogonal frequency division multiplexing (windowed OFDM), which is a discrete Fourier transform (DFT)-based multicarrier modulation (MCM) system. On the other hand, an extended lapped transform (ELT)-based MCM, called by the standard as wavelet OFDM, which is a cosine modulated filter bank (CMFB). The main objective of this thesis is to develop an efficient ELT-based MCM transceiver, following the IEEE 1901 specifications, showing its performance and its feasibility for broadband PLC.

A review of the most important aspects of the modulation scheme to obtain the wavelet OFDM transmitter recommended is first given. In this way, one of the novel contributions of this thesis is the efficient implementation of the recommended transmitter and the proposal of a viable and compatible

receiver, with special emphasis on the fact that the time-domain waveform signal proposed by the standard is not the same that appears in the most of the available literature. Besides, the characteristics of the recommended prototype filters, such as the trade-off between the stopband attenuation and the transition bandwidth of the frequency responses and the perfect reconstruction property (PR) are studied. Likewise, the proposed prototype filters may not achieve the best performance, so alternative waveforms are studied and compared.

Given that the new communication systems are demanding higher data rate, the second main topic tackled in this thesis is related to the data rate. Since the filter bank multicarrier (FBMC) systems do not need any kind of redundancy (cyclic prefix or zero padding), it is supposed that they can achieve better performance in terms of transmission rate. However, the study of data rate in the wavelet OFDM systems remains an open topic, therefore, the theoretical expressions to obtain the achievable data rate of the baseband wavelet OFDM system are derived. The equations derived take into account that the noise presented in the power line network can not be modelled as additive white Gaussian noise (AWGN) and that an Adaptive Sine-modulated/Cosine-modulated filter bank Equalizer for Transmultiplexer (ASCET) has been employed as equalization technique.

Once the baseband ELT-MCM system is implemented, with the goal of extending its applications and achieving higher data rate, a passband version is studied and proposed. In the same way that for the baseband case, an efficient implementation is proposed and the computational cost associated to the fast implementation algorithm is obtained. Moreover, the theoretical expressions necessary to calculate the data rate of this new system are also derived.

Finally, the ELT-MCM system performance, in terms of bit-error-rate (BER) and achievable data rate, has been thoroughly studied and compared with windowed OFDM system performance. For that, different PLC channels, including in-home (low-voltage) and transportation platform (in-car and in-aircraft) scenarios, have been considered. Thus, in this thesis a summary of the different PLC channel and noise models has been performed.

Resumen

La comunicación a través de la red eléctrica (PLC) es una tecnología que combina la transmisión de energía y datos. Si bien el concepto de emplear el cableado eléctrico como canal de comunicación data de comienzos del sigo XX, en los últimos años el interés de emplear la tecnología PLC para aplicaciones dentro y fuera del hogar ha crecido notablemente. Esto se debe a que se espera que PLC juegue un papel importante en el desarrollo de los conceptos "ciudad inteligente" y "energía inteligente", así como en la implementación de redes de alta velocidad dentro del hogar (redes HAN) para el desarrollo del Internet de las cosas (IoT). No obstante, el uso de PLC no está restringido sólo a aplicaciones en el primer/último tramo del par de abonado, sino que hoy en día también es una solución atractiva para aplicaciones en plataformas de transporte (vehículos) debido a que simplifica el diseño, disminuye el coste de desarrollo y reduce peso.

Sin embargo, la red eléctrica no fue diseñada con la finalidad de enviar información a través de ella, por lo que el canal PLC presenta muchos y severos desvanecimientos en frecuencia. A esto hay que añadirle que el ruido presente en el canal es en realidad la combinación de diferentes tipos de ruido. Por todo ello, son necesarios sistemas que proporcionen un muy buen rendimiento. En este sentido, el estándar: *"IEEE Standard for Broadband over Power Line Networks: Medium Access Control and Physical Layer Specifications"* (IEEE 1901) especifica dos esquemas de modulación distintos. Por un lado, una multiplexación por división de frecuencia ortogonales enventanada (windowed OFDM), la cual es una modulación multiportadora basada en la transformada discreta de Fourier. Por el otro, una modulación multiportadora basada en la transformada extendida solapada (ELT-MCM), denominada por el estándar como wavelet OFDM, que se trata de un banco de filtros coseno modulado (CMFB). El objetivo principal de esta tesis es desarrollar un transceptor eficiente ELT-MCM, siguiendo las especificaciones del estándar IEEE 1901, demostrando su rendimiento y su viabilidad para comunicaciones PLC de banda ancha mediante la comparación con el esquema windowed OFDM.

En primer lugar, se presenta una revisión de los aspectos más importantes del esquema de modulación para obtener el transmisor ELT-MCM. De esta forma, una de las novedosas contribuciones de esta tesis es la implementación eficiente del transmisor recomendado y la propuesta de un receptor viable y compatible, haciendo especial énfasis en que la forma de onda propuesta por el estándar no es la misma que aparece en la mayoría de la bibliografía disponible. Además, se estudian las características de los filtros prototipos recomendados, tales como la relación de compromiso entre la atenuación de la banda eliminada y el ancho de la banda de transición, y la propiedad de reconstrucción perfecta (PR). Así mismo, es posible que los filtros prototipos propuestos no consigan el mejor rendimiento, por lo que otras formas de onda son estudiadas y comparadas.

El segundo tema principal abordado en esta tesis está relacionado con la velocidad de transmisión. Puesto que los sistemas de bancos de filtros multiportadora (FBMC) no emplean ningún tipo de redundancia (prefijo cíclico o rellenado de ceros) éstos pueden alcanzar un mejor rendimiento en términos de velocidad de transmisión. Sin embargo, el estudio del throughput en los sistemas wavelet OFDM sigue siendo un tema abierto, por lo tanto, en esta tesis se derivan las expresiones teóricas para obtener la capacidad y throughput de este tipo de sistemas. Las ecuaciones aquí presentadas tienen en cuenta que el ruido PLC no puede ser modelado por ruido blanco Gaussiano (AWGN) y asumen que se ha empleado la técnica de igualación Adaptive Sine-modulated/Cosine-modulated filter bank Equalizer for Transmultiplexer (ASCET).

Una vez que el sistema en banda base ELT-MCM es implementado, con el objetivo de extender su aplicación y alcanzar una mayor tasa de transmisión, se diseña una versión paso banda. Del mismo modo que para el caso banda base, se propone una implementación eficiente y se estudia el coste computacional asociado al algoritmo rápido de implementación. Así mismo, las expresiones teóricas necesarias para calcular la velocidad de transmisión de este nuevo sistema son derivadas.

Finalmente, el rendimiento del sistema ELT-MCM, en términos de tasa de error de bit (BER) y de velocidad de transmisión, ha sido detalladamente estudiado y comparado con el rendimiento obtenido por el sistema OFDM enventanado. Para ello, se han empleado diferentes escenarios PLC, incluyendo escenarios dentro del hogar (de baja tensión) y plataformas de transporte (en concreto automóviles y aeronaves). Por ello, en esta tesis se ha realizado un resumen de los diferentes modeles de canal y ruido PLC.

Table of contents

List of figures

List of tables

Glossary

Acronyms / Abbreviations

5G	Fifth generation of wireless networks
ARIB	Japanese Association of Radio Industries and Businesses
ASCET	Adaptive sine-modulated/cosine-modulated filter bank equalizer for transmultiplexer
AWGN	Additive white gaussian noise
BER	Bit error rate
CE	Convolutional encoder
CENELEC	Comité Européen de Normalisation Électrotechnique
CMFB	Cosine modulated filter bank
CM-PSE	Cosine-modulated per-subcarrier equalizer
CP	Cyclic prefix
CTP	Carrier transmission over powerlines
D8PSK	Differential eight phase-shift keying
DBPSK	Differential binary phase-shift keying
DFT	Discrete Fourier transform
DLL	Data link layer

DMT	Discrete multitone modulation
DQPSK	Differential quadrature phase-shift keying
ELT	Extended lapped transform
ELT-MCM	Extended lapped transform-based multicarrier modulation
FBMC	Filter bank multicarrier
FCC	Federal Communications Commission
FEC	Forward error correction
GBN	Generalized background noise
HAN	Home area network
IAT	Inter-arrival time
IBU	Illumination ballast unit
ICI	Inter-carrier interference
IED	Intelligent electronic device
IEEE 1901	IEEE Standard for Broadband over Power Line Networks: Medium Access Control and Physical Layer Specifications
IoT	Internet of things
ISI	Inter-symbol interference
LDPC-CC	Low-density parity-check convolutional code
LPTV	Linear periodically time-varying
LTI	Linear time invariant
MCM	Multicarrier modulation
MIMO	Multiple input and multiple output
OFDM/OQAM	OFDM offset quadrature amplitude modulation
OFDM	Orthogonal frequency division multiplexing
PSE	Per-subcarrier equalizer
PHY	Physical layer

PINA	Periodic impulsive noise asynchronous to the mains frequency
PINH	Periodic impulsive noises with high repetition rate
PINL	Periodic impulsive noises with low repetition rate
PINS	Periodic impulsive noise synchronous to the mains frequency
PLC	Power line communication
PR	Perfect reconstruction
PSD	Power spectral density
RCS	Ripple Carrier Signaling
ROBO	Robust modulation
RS	Reed-Solomon encoder
SISO	Single input single output
SMFB	Sine modulated filter bank
SM-PSE	Sosine-modulated per-subcarrier equalizer
SPDB	Secondary power distribution box
TMUX	Transmultiplexer
TWACS	Two-way automatic communications system
ZP	Zero padding

CHAPTER 1

Introduction

1.1 Motivation

Communications through the electrical power lines, also known as power line communications (PLC), will play an important and crucial role in the development of "Smart Energy", which is aimed at making electricity delivery more reliable, economical and sustainable. Besides, since PLC implements high-speed home area network (HAN) with reduced development cost, it could be a good choice for solving some problem associated to the "Internet of Things" (IoT). For instance, sensor, cameras, connectors, systems for pedestrian and traffic sign detection, autonomous driving, among other applications, are increasingly important components of the current vehicles in the automotive sector impacting on their cost, reliability and maintenance. Likewise, in the aeronautic domain there is a trend to replace the pneumatic and hydraulic energy sources with electrical ones, however, each electric system needs a power supply and a communication network [1]. Consequently, the use of PLC may also be extended to transportation platforms (vehicles) applications [2–4], due to the fact that it combines the power and data transmission, simplifying the design and reducing the development cost and the weight.

Different communication standards have been proposed with the aim of normalizing the data transmission through the electrical wiring. On the one hand, the physical layer specification for narrowband PLC can be found in PRIME [5], G3-PLC [6] or IEEE 1901.2 [7]. In this case, the former proposes orthogonal frequency division multiplexing (OFDM) meanwhile the other two recommend a windowed OFDM as modulation scheme. On the other hand, the standards ITU-T G.9960 [8], HomePlug AV [9] or IEEE 1901 [10] provide recommendations for broadband PLC. As can be appreciated in [8, Sec. 7.1.4.4] and in [9, pp. 3], respectively, the first two standards

promote windowed OFDM as the only medium access technique. Similarly, the standard IEEE 1901, which defines broadband over power line devices but including all classes of devices used for smart energy or in-vehicle applications, deploys both windowed OFDM (see [10, Sec. 13]) and a filter bank multicarrier (FMBC) (see [10, Sec. 14]) referred to as wavelet OFDM as modulation schemes. It must be highlighted that FBMC is also being considered for the fifth generation of wireless networks (5G) [11, 12].

As can be appreciated, multicarrier modulation (MCM) is not only most used medium access technique for current standards for broadband wireless and wired communications, but also it is the most used medium access technique for current standards for PLC. The principal idea behind it is to convert a broadband frequency channel into a set of overlapping and orthogonal or nearly orthogonal frequency-flat subchannels [13] aimed at sharing the media at the same time among all users. In this respect, Discrete multitone modulation (DMT) and OFDM, with or without windowing, are the most widely recommended systems for the current broadband communication standards. Both of them are discrete Fourier transform (DFT)-based MCM methods, need to employ redundancy (either cyclic prefix (CP) or zero padding (ZP)) to carry out the channel partition [14] and offer several advantages such as fast implementation, high system performance and spectrum efficiency, among others. However, they are sensitive to frequency synchronization, their performance decrease in noisy environments, and when a windowed technique is used, the protection against intersymbol interference (ISI) and intercarrier interference (ICI) is reduced in proportion to the roll-off interval length [15].

With the goal of solving some of the aforementioned problems, FBMC, also referred to as transmultiplexer (TMUX) [16, 17], has been proposed as an alternative to the DFT-based MCM. In [18, 19] a comparison between both of them in different applications is available. The main difference between FBMC and DFT-based MCM system is that in the former a pulse shaping is required to perform the channel partitioning and redundant samples are unnecessary [20]. The pulse shaped waveform is a key issue to get a perfect or nearly perfect reconstruction (PR or NPR) system. Besides, the FBMC presents appealing features such as greater spectral separation, reduced adjacent subchannel interference, higher robustness in noisy environments and since the redundancy is avoided, it can allow for higher data rate.

Different kinds of FBMC systems have been proposed in the literature such as overlapped discrete multitone [21], filter bank modulation [22], discrete subband multicarrier transceiver [23], filtered multitone [24], cosine-modulated multitone [25], among others. However, in this dissertation, special attention will be paid to a filter bank proposed by H. Malvar and referred to as extended lapped transform [26–30].

Recently, several works aimed at presenting a novel system which meets the need of current and next generation of PLC systems. In this respect, OFDM Offset QAM (OFDM/OQAM) has caught the researcher interest [15, 31–33]. In the same way, a special case of FBMC, based on the conventional modulation [34], has been studied in [35–37]. Nonetheless, none of these works are related to the wavelet OFDM system proposed by IEEE 1901.

The main motivation for conducting this research is the lack of works that focus on the transmitter deploys by the standard IEEE 1901 [10], in the study of compatible receivers, on their design, development, implementation, analysis of computational complexity and performance, in terms of bit-error-rate, capacity and data rate. With this work, we believe that this gap has been filled.

1.2 Hypothesis

The hypotheses of this thesis are formulated as follows:

- The whole wavelet OFDM system can be efficiently implemented. This efficient implementation can be performed by means of different structures, such as polyphase filter, lattice structures, among others.
- Each of the different wavelet OFDM implementations has different computational cost, however, just one should have the best trade-off between computational complexity and performance.
- The standard deploys the coefficient values of the prototype filters. There exists a simple expression that allows to obtain them in a simple way.
- Although the IEEE 1901 deploys a specific set of prototype filter, there could be a set or subset of waveforms that could be able to achieve higher yield.
- Considering a wavelet OFDM system, the different PLC channel distortions can be efficiently compensated for by means of the channel equalization technique Adaptive Sine-modulated/Cosine-modulated filter bank Equalizer for Transmultiplexer (ASCET).
- The transmission rate of the wavelet OFDM system, including the ASCET equalizer, can be theoretically calculated using a set of equations. In addition, these equations can be generalized for non-Gaussian noises (realistic PLC noises).
- Under the same simulations conditions, wavelet OFDM overcome the performance obtained by the windowed OFDM in the most hostile communication scenarios.
- Based on the baseband wavelet OFDM system, it is possible to develop a bandpass system that can increase the data rate of the former.
- The achievable data rate of the wavelet OFDM bandpass system can be also theoretically calculated using a set of equations. In the same way, it is expected that the ASCET equalizer, correctly adapted, will be able to compensate for the channel distortions.

1.3 Objectives

The main objectives pursued by this thesis are listed below

- The development of a wavelet OFDM, following the standard IEEE 1901 [10] specifications, for baseband broadband PLC. The computational complexity associated with this system must be within the limits that allow for their implementation in real time.
- Adaptive Sine-modulated/Cosine-modulated filter bank Equalizer for Transmultiplexer (ASCET) [38] is a frequency domain equalization technique for CMFB systems. One of the goals of this thesis is to corroborate that ASCET is a good choice for the power line environment. It should be kept in mind that a larger number of coefficients enables a better channel compensation, however, the computational complexity of the equalizer increase proportionally. Therefore, the trade-off between the number of coefficients, complexity and performance is analyzed.
- Evaluating the system performance in realistic conditions through PLC channel and noise models. This analysis takes into account low-voltage (in-home) and transportation platforms (in-vehicles) scenarios.
- With regard to the study of the achievable data rate of wavelet OFDM, it is derived the theoretical expression to obtain the powers of the inter-symbol interference (ISI) and the inter-carrier interference (ICI) associated with this kind of system. This study also takes into account that the noise in the power line channel is not necessarily AWGN, and that the ASCET has been used as channel equalization technique.
- Once the system is implemented and analyzed, a performance comparison is needed to test the validity of the proposed systems. To this end, a comparative analysis is carried out between windowed OFDM and wavelet OFDM, measuring different quality parameters.
- Extend the use of wavelet OFDM to different environments and applications through an alternative bandpass modulation scheme.

1.4 Methodology

Firstly, a thorough analysis of the wavelet OFDM physical layer specified by the standard IEEE 1901 [10, Section 14] for baseband broadband PLC is realized. This study is focused on the definition of time-domain waveform signal for the frame body [10, pp. 1194] as well as in the features and properties related to the prototype filter recommended in the standard [10, pp. 1205]. Besides, an extensive literature review relative to wavelet OFDM system is also presented.

Taking into account the information gathered in the previous works and with the perspective obtained after studying the standard, an efficient implementation of the wavelet OFDM transmitter is performed. Next, a compatible receiver, which provides perfect reconstruction under ideal conditions, is proposed. This receiver includes an efficient equalization process that compensates for the channel distortions [38]. Then, as a second step, the viability of ELT-MCM system is evaluated focusing

on broadband PLC. To this goal, an exhaustive bibliographical search of previous works related to in-home and in-vehicle PLC channel and noise models has been realized.

Once the PLC scenario is defined, the wavelet OFDM performance is measured and compared with a windowed OFDM system based on the specifications of the standard IEEE 1901. First, the wavelet OFDM system performance is evaluated in terms of bit-error-rate (BER), considering different levels of hostility (strong, medium and little signal attenuation). However, the BER as a figure of merit is insufficient for ensuring that wavelet OFDM can be considered as a good candidate for broadband communications. Given that new technologies are demanding higher data rate, the calculation of the achievable data rate is also needed. This study for wavelet OFDM is also conducted in this thesis.

Finally, in order to solve some problems presented in the transmission over the power line network, such as to increase the system data rate, a new bandpass system based on the ELT is proposed and evaluated under different PLC conditions.

1.5 Structure of the thesis

First of all, the basic and main ideas, which are the motivation of the different part that make up this doctoral thesis, as well as the desired aims and the methodology followed in this research are presented in this chapter.

In the second chapter, the state of the art related to communications over the electrical network is shown. This chapter gives an overview about the different advantages and applications that PLC provides, all of them grouped according to the operating voltage, i.e., high, medium and low voltage network. The last part of this chapter is focused on briefly summarizing some basic aspects related to the wavelet OFDM physical layer specification deployed by the standard IEEE 1901.

Before studying and comparing the ELT-MCM performance, it is necessary to establish the communication scenarios in which the analysis will be carried out. The third chapter details each and every PLC channel and noise models, including in-home and in-vehicle scenarios, used in this thesis.

In the fourth chapter, a large number of pages are aimed at the design and development of the wavelet OFDM system, including the issue related to the channel equalization, an in-depth analysis of the perfect reconstruction property of the proposed prototype filter, as well as a set of expressions to calculate their coefficients. An efficient implementation of the whole system based on different configuration is also realized and, in addition, the computational complexity associated with each implementation is presented. Furthermore, the theoretical expressions that allow the measurement of the system data rate are also derived. Finally, bit-error-rate and data rate have been obtained under both in-home and in-vehicle PLC conditions.

Chapter five describes the bandpass wavelet OFDM modulation scheme, also based on the extended lapped transform. It is also proposed an efficient implementation and the equations to calculate the system data rate are derived. The chapter also includes a performance analysis, which has been carried out under different PLC scenarios.

Finally, this work concludes with some final remarks and future research lines derived from this thesis. Moreover, the publications wholly or partially related to the different topic mentioned in this document are listed in a final Appendix section.

CHAPTER 2

An Overview of Power Line Communications

2.1 Introduction

The first idea of transmitting data through the electrical wiring was proposed in 1838 [39]. The goal was to remotely monitor the batteries' voltage level on the telegraph system between London and Liverpool. In 1897 J. Routin and C. E. L Brown patented the first power line signalling electricity meter. During the next years different progress, such as the automatic electromechanical meter repeaters (1913), thermionic valves (1927) and the transistor (1960), among others, were carried out. However, it was not until the late of 1980's and early 90's that the first PLC modem was implemented.

During the past century, different "power line carrier" systems, such as carrier transmission over powerlines (CTP) for high voltage network or ripple carrier signaling (RCS) for medium and low voltage network, were developed with the aim of protecting different sections of the power line network in case of faults and providing remote control, measuring and load management [40]. Despite these technological advances, since the mains network was not designed for communication purpose together with the fact that some cables were not unshielded (causing electromagnetic interference) and that the grid network does not provide a dedicated link between sources and sinks (since it is a shared medium), skepticism around PLC feasibility was generated. All of the above contributed considerably to the research on data transmission through the grid network was sidelined.

In recent years, new concepts such as "Smart City", "Smart Grid", "Smart Energy" and IoT have emerged. These ideas, especially Smart Grid and Smart Energy, seek to boost the energy generation and transmission efficiency, providing real-time monitoring and control as well as information about energy demand. In this respect, the urban IoT may provide a detailed view of the energy consumption within a city [41]. In the same way, by means of IoT, consumers can directly control and manage

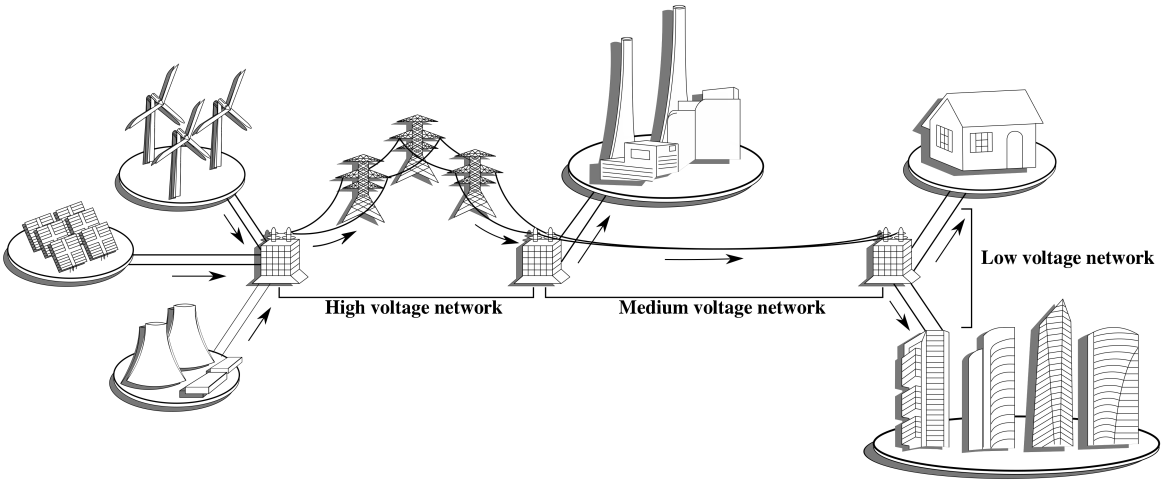

Fig. 2.1 Structure of the power supply network.

their power consumption to different energy prices throughout the day allowing them to save money. They can even produce their own energy and sell the excess to the grid. For this in-home IoT connection, the power line provides an attractive communication medium [42] and PLC has become a competitive candidate technology to provide high-speed coverage using existing infrastructure [43]. In addition, Smart Grid combines the weather forecasts and the information on energy flows for enhanced integration of distributed renewable energy sources, reducing the greenhouse gas emissions. For all these contributions, Smart Grid has attracted attention from the research community, the industry and the governments, e.g. in the last decade about 300 projects related to this topic have been financed by € 5.5 billion in Europe and it is still in the early stages of the deployment [44].

There is an open debate on which wireless and wired communication technologies will play a key role in the Smart Grid and IoT development. In this sense, PLC provides a natural upgrade from traditional electricity network to two-way electricity and data communications network [45]. Besides, it can be a good choice to solve the "last mile" and "last inch" problems, since it provides broadband communication to isolated places where other communication systems are not in place, and it implements high-speed HAN [46]. Nevertheless, it should be noted that there are other several applications where PLC offers a satisfactory solution, these can be easily summarized and grouped according to the operating voltage of the power supply network (see Fig. 2.1):

- High voltage network (110 - 380 kV), it consists of a set of long overhead supply cables which allows nationwide or international power exchange. Usually, high voltage lines have little or no branches presenting a propitious passband and time-invariant behaviour and making them a much better transmission medium in comparison with medium and low voltage lines. However, the high voltage power line noise, caused by the corona effect and discharge events, may fluctuate tens of dBs because of its climatic dependence [45].

The applications of PLC in high voltage network is two-fold. On the one hand, a communication system over long distance can be deployed, indeed, nowadays PLC allows a data rate higher than 300 kbps in 32 kHz band for a distance up to 100 km [47], further, for a 69 kV power line and 8 km a broadband connection at over 10 Mbps have been realized with just one repeater [48]. On the other hand, this technology can be also used for remote detection of failures in the transmission lines, such as short-circuits, surface calcification, cracks, shed damage, among others [49]. Besides, it is useful to implement real-time sag monitoring system for overhead transmission lines [50].

- Medium voltage network (10 - 30 kV), it is a set of overhead or underground lines and it is used for power transmission between cities, town or some big industrial costumers inside a country and it is connected to high voltage network by means of transformer unit (primary transformer).

  The intelligent electronic devices (IEDs) such as sectionalizers, capacitors banks, phasor measurement units and reclosers, are installed inside the substations within the medium voltage grid and they are used for power flow monitoring, metering and control. In case of fault, IEDs need to interchange information and this is where PLC can be a competitive technology since it provides a direct link between each other [45]. Furthermore, all these communications need a low data rate [47], so narrowband PLC offers an economical and practical solution. Additionally, PLC can be also used by monitoring systems (voltage measurement on the secondary winding of high voltage/medium voltage transformers, fault surveys, power quality measurement, among others) as well as for network management optimization and by security system [51].

  Another important issue in medium voltage grid is the islanding phenomenon. This phenomenon occurs when a distributed generator is cut off from the grid but it still supplying power. This phenomenon leads to phase failure, abnormal frequency behaviour among other problems [52] affecting the loads connected to grid and the grid itself. In this sense, PLC fulfills he protection requirements of distribution network [53] and it offers a superior islanding prevention that other technologies in grid connected photovoltaic systems [54].

- Low voltage network (110 - 400 V), connected to the medium voltage grid through secondary transformer unit, covers the last few hundred meters of power supply network until the end users. Usually, it is comprised of underground cables in urban areas, whereas, it is made up of overhead lines in rural areas. This grid topology can vary significantly from region to region, e.g., in Europe is quite common that just one secondary transformer supplies up to 100 households, whereas in the United States of America a small set of houses or even just one house get served from just one secondary transformer [45]. It should be kept in mind that a communication system between medium and low voltage network can be implemented, nevertheless, the secondary transformer units produce a really big signal attenuation (55 - 75 dB) [55].

Electrical installation inside households belong to this network but it owned by the user, so it is connected to the outdoor network by an electricity meter unit. Therefore, the two main applications of PLC over low voltage grid are, in first place, as access system providing broadband communication (out-door applications), and secondly, as communication system between any socket in the internal wiring (in-home applications). Nonetheless, PLC can also be used for many other purposes such as advanced metering infrastructure for automatic meter reading, allowing a remote interaction with the electricity meters units and improving customer awareness of electricity pricing on a real-time basis, as well as for demand side management, alleviating the peak demand and providing more information to the customers about their energy usage habits [56].

It must be highlighted that the communications over the electrical wiring are aim not only to implement communication systems over the different sectors of power distribution network, but also it can be employed to intelligent transportation applications, e.g. in [1, 4, 57] the PLC reliability inside an aircraft and spacecraft has been studied, [3, 27] shows that PLC is an attractive solution for the automotive sector, [58] presents a PLC system onboard trains whereas an analysis of PLC channels in a cruise ship has been performed in [59]. Another novel application is the communication between the vehicle and the grid (vehicle-to-grid communication), here an unambiguous physical association between a specific electric vehicle supply equipment and a specific vehicle can be established, offering several advantages in terms of authentication and security [47].

Furthermore, in recent years wearable computing has raised significant interests since it can be used by soldiers [60], fitness professional [61, 62] or even senior citizens [63] for physiological signals monitoring (heart rate, respiration, temperature, among others), referred to as wearable health monitoring. In this regard, the advantages of using direct current PLC are the reduction of the amount of cabling, the saving in installation time and maintenance, and it allows to distribute the system according to the body's load-carrying capabilities [64].

2.2 The status of the PLC standardizations

Over the last years, several and noninteroperable standards for communications over the power line network have been deployed by different industrial alliances and standards developing organizations. This section is aimed at summarizing most of them, distinguishing between them by frequency band employed. A special emphasis has been placed on the physical layer specifications of high data rate standards.

2.2.1 Ultra narrow band PLC

This PLC technology works either in the frequency band $[30-300]$ Hz or in $[0.3-3]$ kHz, it achieves a really low data rate (100 bps approx.) but covering a really huge distance (more than 150 km) [47]. In this category, some of the most widely used standardized communications systems are:

1. **Turtle system:** It is characterized by the extremely low data rate that it reaches, on the order of 1 bit per 10^3 seconds (it gets its name from this reason), and for its parallel communications (one logic channel for one remote device) [65]. This system is normally used for automated meter reading.

2. **Two-way automatic communications system (TWACS):** Proposed by Mak *et al* in 1982 [66, 67], this system can reach speeds of up to 1 bit per mains frequency cycle, in other words, 50 and 60 bps in Europe and US, respectively. TWACS is used for distribution automation as well as for automatic meter reading [65].

2.2.2 Narrowband PLC

Nowadays abovementioned proprietary technologies have left sideline in favor of the current narrowband PLC technology. Narrowband system operates in the frequency range from 3 kHz up to 500 kHz, following the specifications provided by the European Comité Européen de Normalisation Électrotechnique (CENELEC) which defines narrowband PLC for frequencies between 3 to 148.5 kHz, the US Federal Communications Commission (FCC) (10-490 kHz) and the Japanese Association of Radio Industries and Businesses (ARIB) (10-450 kHz). Using the same nomenclature that in [47], narrowband PLC system can be subdivided in terms of its data rate:

Low data rate

This kind of systems is able to achieve a throughput of a few kbps and typically is based on single carrier modulation. Some of the standards and recommendations regulating this technology are X-10, CE-Bus (CEA-600.31), LonWorks (ISO/IEC 14908-3) [68], home electronic system (HES) standard (ISO/IEC 14543-3-5) [69], distribution automation using distribution line carrier systems (IEC 61334-5-1, S-FSK) [70], among others [45, 47, 71].

High data rate

It is aimed at reaching higher data rate than the previous one, on the order of several hundred of kilobits per second. Some of the standards that can be found in this category are:

1. **PoweRline Intelligent Metering Evolution (PRIME):** It was developed by the PRIME Alliance Technical Working Group for the provision of all kinds of Smart Grid services over electricity distribution networks. PRIME physical layer (PHY) is defined to support communication in the band 3 kHz to 500 kHz, using OFDM as medium access technique. This range in divided into 8 subchannels, separated by guard interval of 7.3 kHz and with 97 equally spaced active subcarrier per subchannel. The first subchannel is between subcarrier 86 (41.992 kHz) and subcarrier 182 (88.867 kHz), the second one goes from 198 (96.679 kHz) to 94 (143.554 kHz), and so on. Furthermore, the physical layer specifies the IFFT size (2048 samples), the

frequency spacing between subcarriers ($\Delta_f = 488.28125$ Hz), the frequency sampling (1000 kHz) and the cyclic prefix length (192 samples).

The payload can be modulated by differential binary phase-shift keying (DBPSK), differential quadrature phase-shift keying (DQPSK) or differential eight phase-shift keying (D8PSK). A convolutional encoder (CE) in combination with repetition block are proposed as forward error correction (FEC) blocks. The convolutional encoding is applied to the input data of the scrambler block, them if the repetition block is activated the scrambler output is repeated by a factor of four, and finally the scrambler output (or the repetition block output) is interleaved. The pseudo-random noise sequence of the scrambler is obtained by generator polynomial $x^7 + x^4 + 1$ and the coding rate of the CE is $1/2$, with constraint length 7, and generators 171 and 133 (octal). It is worth noting that the CE is optional. For more details of the specifications deployed by this standard, we refer the reader to [5].

2. **G3-PLC:** The system deployed by this standard must support the frequency band between 35.9 to 90.6 kHz, i.e., within the CENELEC A band. In order to reduce the out of band emission and the spectral side lobe, a windowed OFDM modulation scheme with a raised cosine shaping, as windowing process, is proposed. The recommended primary mappings are DBPSK and DQPSK. Furthermore, the frequency sampling is fixed to 0.4 MHz, the IFFT size is 256, the number of usable subcarriers is 36 (the first one located at 35.938 kHz and the last one at 90.625 kHz), and the frequency spacing is equal to 1.5625 kHz. Besides, the number of samples in the cyclic prefix and the number of samples overlapped at each side of one symbol are 30 and 8, respectively.

   Like the above standard, the pseudo-random noise sequence of the scrambler is generated by the polynomial $x^7 + x^4 + 1$, and its output is encoded by the forward error correction block. FEC block is composed by a Reed-Solomon (RS) encoder followed by a CE. For RS, the code generator ($g_{RS}(x)$) and the field generator ($p_{RS}(x)$) polynomials are defined as

$$g_{RS}(x) = \prod_{i=1}^{2t_{RS}} \left(x - \alpha^i\right),$$

$$p_{RS}(x) = x^8 + x^4 + x^3 + x^2 + 1 (435 \text{ octal}).$$

   Moreover, the maximum code length (n_{RS}) is 255 whereas the number of correctable symbol errors (t_{RS}) can be either 4 or 8, thus, using Galois Field $\mathrm{GF}\left(2^8\right)$ the maximum number of bits (k_{RS}) is 247 or 239 ($k_{RS} = n_{RS} - 2 * t_{RS}$). For CE, its features are the same than the depicted by the PRIME standard (coding rate $1/2$, constraint length 7, generators 171 and 133). Finally, the output of the CE is interleaved in order to provide protection against burst error and frequency deep fade.

Table 2.1 OFDM specifications by IEEE 1901.2

	CENELEC A	**CENELEC B**	**ARIB 1**	**ARIB 2**	**FCC-Low**	**FCC above CENELEC**
Actives subcarrier	36	16	18	54	18	72
First active subcarrier (kHz)	35.9375	98.4375	37.5	154.6875	37.5	154.6875
Last active subcarrier (kHz)	90.625	121.875	117.1875	403.125	117.1875	487.5
Δ_f **(kHz)**	1.5625	1.5625	4.6875	4.6875	4.6875	4.6875
Frequency sampling (MHz)	0.4	0.4	1.2	1.2	1.2	1.2
IFFT size	256	256	256	256	256	256
Overlapped samples	8	8	8	8	8	8
Cyclic prefix samples	30	30	30	30	30	30
Long cyclic prefix samples	- -	- -	52	52	52	52

Optionally, by means of a repetition code block each bit can be repeated four or even six times. This block would be implemented between the CE and the interleaver. For more details, we refer the reader to [6].

3. **IEEE 1901.2:** It defines the PHY and medium access control layer (MAC) for narrowband PLC for frequencies between 10 kHz and 490 kHz, being thus supported the CENELEC, FCC and ARIB bands. The system deployed by this standard is based on windowed OFDM. However, some of its parameters change depending on the frequency band that has been used. Table 2.1 summarizes the OFDM parameters.

   Two modulations modes must be supported. A mandatory differential mode (DBPSK, DQPSK and D8PSK) and an optional coherent mode (BPSK, QPSK, 8PSK and 16QAM). A scrambler block is proposed to give the data a random distribution and it is based on the same polynomial that has been used by aforementioned standards. The FEC encoder is composed of an RS followed by a CE, and if a robust OFDM is needed, a repetition block can be applied after the CE in order to repeat the bits four or six times. Both RS and CC deployed by this standard follow the same guidelines that have been recommended in G3-PLC.

   Interleaving is carried out in two steps after the convolutional encoding, or repetition process. First, each column is circularly shifted a different number of times in order to spread a possible corrupted OFDM symbol over different symbols. Second, each row is circularly shifted a different number of times to mitigate a deep frequency fade. The number of shifts is defined by n_i, n_j, m_i, m_j which are selected based on two parameters: the number of active carriers and the parameter n

$$n = ceil\left(\frac{N_{bits}}{m \cdot k}\right) k$$

Table 2.2 OFDM parameters by ITU-T G.9902

Parameters	Value
Number of subcarriers (M)	128 or 256
Δf (kHz)	3.125 or 1.5625
Cyclic prefix samples	$^{12}/_{128} \cdot M$ or $^{24}/_{128} \cdot M$
Overlapped samples	Any even integer between 0 and $^{M}/_{16}$

where $ceil\,(\cdot)$ denotes the ceiling operator, N_{bits} is the total number of bits, m is the number of active subcarriers and k is the modulation size (1 for BPSK, 2 for QPSK, 3 for 8PSK, and 4 for 16QAM). Additional information about the interleaver is available in [7, Sec. 6.14].

The OFDM symbol is generated by a 256-point IFFT with the data on each carrier index placed on the corresponding input of the IFFT with all other inputs set to zero. Then, the real part of the output is taken, and the final 30 samples are used as cyclic prefix. Optionally, if the system is using the FCC or the ARIB specifications, a long cyclic prefix of 50 samples can be applied. Regarding the windowing process, the window function is left to the implementers and the only parameter provided is the number of overlapped samples, which is fixed to 8.

For further information about the frame control header, the tone mask, the transmit power control, the pilot tones, and other parameters of the PHY and MAC, see [10].

4. **ITU-T standards:** Originally, the PHY and data link layer (DLL) specifications to develop windowed OFDM-based transceiver for narrowband PLC have been detailed in ITU-T G.9955 and ITU-T G.9956, respectively. However, nowadays the contents of these recommendations are reorganized into recommendations ITU-T G.9901 [72], ITU-T G.9902 [73], ITU-T G.9903 [74] and ITU-T G.9904 [75], which are technically equivalent. As it can be appreciated, G3-PLC as well as PRIME have been approved as ITU recommendation since both of them have been proposed in [74] and [75], respectively. Nonetheless, it should be emphasized that ITU-T G.9904 presents some changes compared to PRIME, such as the baseband clock (it changes from 1 MHz to 250 kHz) and the IFFT size (from 2048 to 512) [72, Table C.1].

   ITU-T G.hem [73] recommends its own narrowband PLC system over frequencies below 500 kHz, based on windowing OFDM and using BPSK, QPSK and 16QAM as primary mapping. As in IEEE 1901.2, this standard does not describe any kind of window delegating responsibility to the developer, but it specifies the OFDM parameter listed in Table 2.2.

   In addition, a concatenated FEC scheme with Reed-Solomon and convolutional coding has been proposed, and a repetition rate of 1, 2, 4, 6 or 12 can be applied. More details about the PHY and DLL layer can be found in each ITU-T recommendations, and it is referred to [72] for power spectral density specifications.

2.2.3 Broadband PLC

Broadband communications over the electrical wiring have been developed with to goal of providing high-speed system addressing both access and in-home applications. These systems operate at frequencies below 100 MHz, achieving data rates of hundred of Mbps [76]. At the beginning of the 21st century, several industrial standards were established, highlighting among them the HomePlug Powerline Alliance (HomePlug) proposal and the High-Definition Power Line Communication (HD-PLC) alliance specifications. Nonetheless, during the last decade the standards developing organizations, such as ITU and IEEE, have developed their own recommendations. This subclause is aimed at giving an overview of some of these proposals.

HomePlug

During the last two decades, this alliance publish several recommendations from HomePlug 1.0 [77], which has been adopted by the Telecommunications Industry Association (TIA) as international standard TIA-1113, through HomePlug AV 1.1 [78] to HomePlug AV 2.0 [79] which adds new features to increase the data rate, including a specific standard focuses on Smart Grid applications (HomePlug Green [80]). Here, a brief review about the PHY specifications of the most relevant and newest recommendations is presented. For more details, we refer the reader to [8, 10, 45, 47, 71, 76–81].

1. **HomePlug AV 1.1:** Simply referred to as HomePlug AV, it deployed a windowed OFDM-based system in the frequency band of [1.8 - 30] MHz with modulation BPSK, QPSK, 8QAM, 16QAM, 64QAM, 256QAM or 1024QAM.

   The OFDM time-domain signal is generated using a 3072-point IFFT with a 75 MHz sampling clock and 917 usable subcarriers, the roll-off interval (number of sample overlapped) is fixed to 372 and the number of samples taken from the end of the OFDM symbol and inserted as cyclic prefix is variable (417, 567, or 3534). A higher cyclic prefix length provides a more robust system but decreases the data rate, the choice being determined by the hostility of the channel.

   Firstly, the information bits are passed through a scrambler, then they are encoded by the turbo convolutional code (TCC) encoder and the output is subsequently interleaved by the channel interleaver. The repeating pseudo noise sequence is defined by the generator polynomial $x^{10} + x^3 + 1$. The TCC is based on two rates $2/3$, 8-states recursive systematic convolutional constituent codes and one turbo interleaver, and then the encoded output is punctured to a code rate of either $1/2$ or $16/21$. The channel interleaver basically divides its input into four blocks and sets each block into each column of a $4 \times {}^{\text{Total\_length}}/_{4}$ matrix. Next, starting from row 0, groups of 4 bits of the same row are read out and the row pointer is increased by 4 or 16. When the end of the matrix has been reached, the process is repeated but the row pointer is initialized to 1. Additionally, an optional repetition block with a repetition rate of 2, 4 or 5 can be applied.

2. **HomePlug AV 2.0:** Better known as HomePlug AV2, this standard changes some features from the previous standard HomePlug AV, such as the sampling clock from 75 MHz to 200

MHz, and adds new ones. These new features include multiple input multiple output (MIMO) technique, wider frequency band, efficient notching, among others. As a result, the data rate is increased from 200 Mbps (achieved by HomePlug AV) to 1.5 Gbps.

In general, electrical wiring is composed of three individual wires: Phase (or line), neutral and ground, and in general the PLC system uses the line-neutral pair for communication. MIMO technique uses either the phase-ground or the neutral-ground pair as the second communication channel to transmit a second independent signal, depending on the proper choice on the power line channel features. In those places where the third wire is not present, such as buildings with older electrical installation or countries like Peru, the MIMO system automatically switch to single input single output (SISO) configuration. Therefore, a configuration of 2 transmitters and N_R receivers ($2 \times N_R$) is specified, where the number of receivers can be 2, 3, 4.

The frequency band is extended up to 86.13 MHz, however, the transmit power spectral density above 30 MHz must be lower than -80 dBm/Hz. Besides, HomePlug AV2 removes the requirement to notch using a windowing technique, and thus an alternative implementation such as FIR or IIR filters or a combination of both windowing and filters are allowed. For that, a new smaller transition interval has been added and, in contrast to the roll-off interval of HomePlug AV, it might be reduced to zero.

3. **HomePlug Green:** It is designed to support Smart Grid applications, and it includes new features to reduce the power consumption and development cost, and to increase the robust and reliable communication.

   The PHY deployed by this standard follows the same PHY protocol recommended by HomePlug AV, but with the caveat that the payload transmission is restricted to standard robust modulation (ROBO), High-Speed ROBO (HS-ROBO) or mini ROBO (MINI-ROBO) modes. In addition, QPSK and $1/2$ turbo convolutional coding are the only modulation and FEC block required, respectively.

   HomePlug Green includes the power save mode, which allows the reduction of the average power consumption by means of periodically transitioning between “awake” and “sleep” states. In the former, the system can transmit and receive information through the electrical wiring, whereas, in the latter, the system temporarily suspends transmission and reception of data, reducing the average power consumption [80, Sec. 5.9].

IEEE 1901

This standard is intended to develop high-speed communication devices over the power line network using frequencies below 100 MHz. All classes of broadband power line devices are considered for the use of this standard, including devices for first-mile and last-mile connections as well as for Smart Energy and transportation platform applications. The PHY procedures specify either a windowed

OFDM or wavelet OFDM. Since the latter is the main topic of this thesis, just the PHY specifications of the former are here summarized.

The windowed OFDM system deployed by the standard uses 917 are active subcarriers in the frequency range from 1.8 MHz to 30 MHz, but they can be increased up to 1974 if the range is increased up to 50 MHz. Nonetheless, support for carriers above 30 MHz is optional. The frequency sampling is fixed to 100 MHz, the IFFT size equals 4096, the subcarrier spacing is approximately 24.414 kHz, the system must support a payload symbol guard interval of 556, 756 or 4712 samples and a roll-off interval of 496 samples. Optionally, a frequency sampling of 50 MHz and 25 MHz can be supported but just for access services, they are not supported by in-home applications. The payload data are mapped into a quadrature amplitude modulation (BPSK, QPSK, 8QAM, 16QAM, 64QAM, 256QAM, 1024QAM, or optional 4096-QAM) and they must be scaled to produce a unity average power symbol [10, Table 13-26].

The FEC encoder is based on a scrambler, a turbo convolutional encoder, and a channel interleaver. The scrambler, the TCC and the channel interleaver, are based on the same specifications that have been provided by HomePlug AV, but an extra code rate of $16/18$ is included. Nonetheless, operation with code rate $16/18$ is optional. In the same way, if a more robust mode is needed, an optional repetition block with a repetition rate of 2, 4 or 5 can be applied, but the code rate must be fixed to $1/2$.

Regarding the power spectral density, it is limited to -55 dBm/Hz and to -85 dBm/Hz for the active subcarriers bellow and above 30 MHz, respectively. The spectral mask is detailed in [10, Table 13-29]. For further information, see [10, Sec 13].

ITU-T G.9960

This recommendation defines the physical layer specifications not only for PLC transceivers, but for all types of HAN transceiver over premises' wiring, including coaxial cable, telephone wiring, plastic optical fibers, and any combination of these.

The payload shall be scrambled with a pseudo random sequence generated by the polynomial $x^{23}+x^{18}+1$. Then, the data are encoded by the FEC block and, optionally, a repetition encoding with a rate of 2, 3, 4, 6, 8 can be applied. The FEC block consists of an LDPC-BC encoder followed by a puncturing block and their parameters are detailed in [8, Table 7-56].

Table 2.3 Main PHY specifications deployed by the different narrowband PLC standards

Narrowband PLC standards			
	Prime	**G3-PLC**	**IEEE 1901.2**
Frequency range	[3-500] kHz	[35.9-90.6] kHz	[10-490] kHz
IFFT size	2048	256	256
Active subcarriers	97	36	16, 18, 36, 54, 72
Guard interval (GI) [samples]	192	30	30, 52
Roll-off interval (RI) [samples]	- -	8	8
Frequency sampling [MHz]	1	0.4	0.4, 1.2
Frequency spacing (Δf)[kHz]	0.4883	1.5625	1.5625, 4.6875
Modulation	DBPSK, DQPSK, D8PSK	DBPSK, DQPSK, D8PSK	DBPSK, DQPSK, D8PSK Op. BPSK, QPSK, 8PSK, 16-QAM
FEC	CE	RS+CE	RS+CE
Repetition rate	4	4, 6	4, 6

Table 2.4 Main PHY specifications deployed by the different broadband PLC standards

Broadband PLC standards				
	HomePug AV	**HomePug AV2**	**IEEE 1901**	**ITU G.9960**
Frequency range	[1.8-30] MHz	[1.8-86.13] MHz	[1.8-100] MHz	[1.8-100] MHz
IFFT size	3072	8192	4096	$M = 1024, 2048, 4096$
Active subcarriers	917	3455	917	developer's responsibility
Guard interval (GI) [samples]	417, 567, 3534	developer's responsibility	556, 756, 4712	$\frac{M}{32}k; k = 1,2,\ldots 8$
Roll-off interval (RI) [samples]	375	developer's responsibility	496	$\frac{M}{8}$
Frequency sampling [MHz]	75	200	100	25, 50, 100
Frequency spacing (Δf)[kHz]	24.414	24.414	24.414	24.414
Modulation	BPSK, QPSK 8-, 1024-QAM	BPSK, QPSK 8-, 4096-QAM	BPSK, QPSK 8-, 4096-QAM	b-order modulation $b = 1, 2, 3, \ldots 12$
FEC	TCC	TCC	TCC	LDPC-BC
Repetition rate	2, 4, 5	2, 4, 5	2, 4, 5	2, 3, 4, 6, 8

Concerning to modulation scheme, a windowed OFDM-based system with b-order modulation is recommended. Since this standard is intended to any HAN system, different configurations must be supported, i.e., different number of subcarrier ($M = 256, 512, 1024, 2048, 4096$), subcarrier spacing ($\Delta_f = 24.4140625 \times k$; $k = 1, 2, 4, 8, 16, 32, 64$), roll-off interval (any even integer $\in [0, M/4]$), guard interval, which by default is fixed to $M/4$ (but $k \times M/32$; $k = 1, 2, 3, \ldots 8$, must also be supported), and modulations ($b = 1\,2, 3, \ldots 12$). Nonetheless, following the specifications provided by [81], the windowed OFDM modulation scheme specific to PLC transceivers uses 1024, 2048 or 4096-point IFFT in the range of [0-25] MHz, [0-50] MHz, [0-100] MHz, respectively. It also employs a roll-off interval equals $M/8$ and $\Delta_f = 24.414$ kHz. On the other hand, constellation mappings for even and odd values shall be derived following the steps deployed by the standard in [8, Sec. 7.1.4.3.1.1] and [8, Sec. 7.1.4.3.1.2], respectively.

The maximum power spectral density can be found in [81, Table 6-5] and it is -55 dBm/Hz and -85 dBm/Hz below and above 30 MHz, respectively. Unlike the standards described above, this recommendation does not specify the number of active subcarrier, delegating this responsibility to the developer.

Finally, to easily show the difference and similarities among the different standards that have been briefly described throughout this subsection, the main PHY specifications for narrowband and broadband PLC have been summarized in Table 2.3 and in Table 2.4, respectively.

2.3 Wavelet OFDM Physical Layer

As mentioned above, PHY procedures deployed by IEEE 1901 specify either a windowed OFDM or a wavelet OFDM as MCM schemes. Table 2.5 presents the main parameters of both methods. Although the latter scheme is referred to as wavelet OFDM, this denomination is a misnomer [35] because, as we will show later, the recommended wavelet OFDM is a class of FBMC based on the Extended Lapped Transform (ELT) [26, 28], and there exists another class of multicarrier systems that are based on true wavelets (e.g., [82]). For this reason, hereinafter we will refer to wavelet OFDM also as ELT-MCM.

It is well known that one important drawback of OFDM is the use of redundant data, which reduces the achievable data rate. As an alternative, FBMC is a viable and attractive solution for communications over the mains, because it does not require any kind of redundancy, it has higher robustness in noisy environments, greater spectral separation, and reduced adjacent subchannel interference, among others.

Since OFDM with and without windowing has been recommended in other standards, e.g., HomePlug AV [9], it has received widespread attention by researchers, unlike Wavelet OFDM. Therefore, the main purpose of this subsection is to introduce some basic aspects of the wavelet OFDM physical layer. In successive chapters, further study will be made of baseband and passband communications systems over power line networks. For that, a briefly description about DFT-based

Table 2.5 Widowed OFDM and Wavelet OFDM PHYs Major Specifications

	Wavelet OFDM	**Windowed OFDM**
Forward Error Correction (FEC)	Reed-Solomon + Convolutional encoder LDPC-CC (optional)	TCC encoder
Primary Modulation	2-PAM to 16-PAM, 32-PAM (optional)	BPSK, QPSK, 8-QAM to 1024-QAM, 4096-QAM (optional)
Number of subcarriers	$M = 512$	$M = 4096$
Prototype Filter Length (2mM)	$m = 2, 3$	–
Frequency band	1.8 MHz- 28 MHz	1.8MHz - 50 MHz
Symbol length (μs)	8.192 16.384 (optional) 32.768 (optional)	40.96
Sampling frequency (MHz)	62.5	100
Frequency spacing (kHz)	61.035	24.414

system and conventional CMFB is introduced. Likewise, some key features, as FEC blocks are clarified.

2.3.1 Block-based transform MCM

Fig. 2.2 depicts the general block diagram of a multicarrier modulation system [83]. As it can be appreciated, at the transmitter side a M-points inverse transform T_a^{-1} is applied to the input symbols ($s_{k,m}$), where M is the number of subcarriers. On the other hand, at the receiver side a direct transform T_b^{-1} is applied tp the received symbols $y_{k,m}$. The equalization process is performed on the frequency domain by a set of coefficients e_i, which are obtained from the channel impulse response by means of third transform T_c (not represented in the Fig. 2.2).

DFT-based system

This kind of systems perform the transformation blocks T_a and T_b by means of the DFT. OFDM and DMT, with or without windowing, are the most DFT-based system recommended for broadband communications due to its several advantages, such as fast implementation. Besides, it uses cyclic prefix (or zeros) as redundant samples to carry out the channel partition [14], thus, the channel matrix $\mathbf{H}$ can be modelled as a right-circulant matrix, which can be expressed as [13, 83]

$$\mathbf{H} = \mathbf{W}^{-1} \cdot \mathbf{D} \cdot \mathbf{W} \tag{2.1}$$

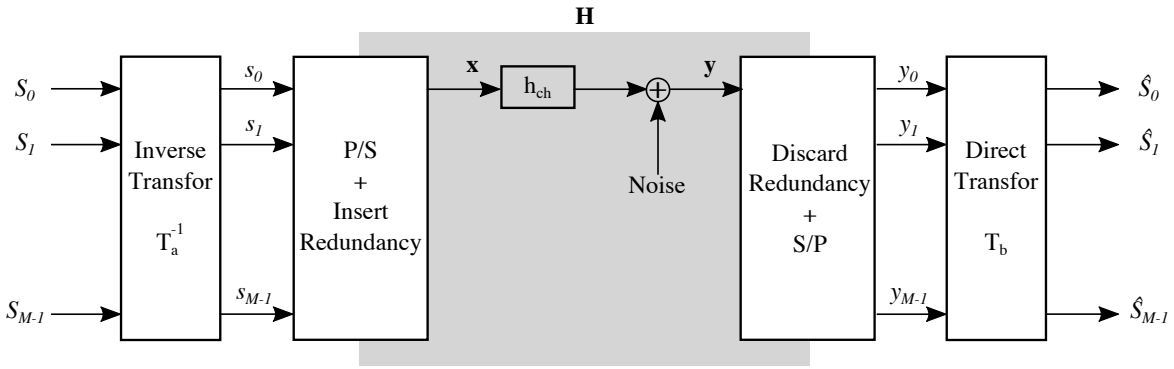

Fig. 2.2 General block diagram of block-based transform MCM system over a channel with additive noise.

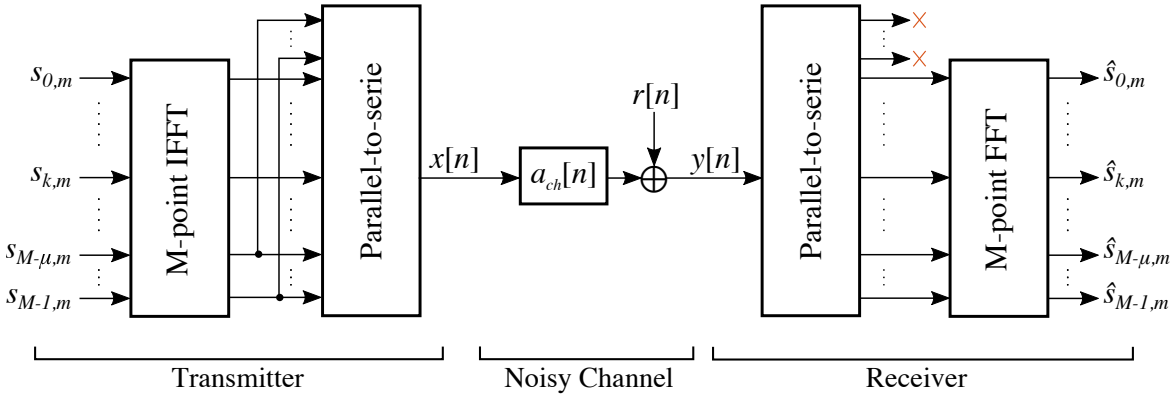

Fig. 2.3 Efficient implementation of OFDM.

where $\mathbf{W}^{-1}$ and $\mathbf{W}$ are, respectively, the DFT and the IDFT matrices, and $\mathbf{D}$ is a diagonal matrix, in which the diagonal elements d_i, $0 \leq i \leq M-1$ are obtained as the M-points DFT of the channel impulse response. Therefore, the frequency domain equalizer can be implemented with the zero-forcing criterion, i.e., $e_i = 1/d_i$, correcting the different channel effects. The OFDM modulation scheme is depicted in Fig. 2.3.

Windowed OFDM

If a window with smoothened edges is used instead of a rectangular one, we get a windowed OFDM system, also referred to as pulse shaped-OFDM (PS-OFDM). Raised cosine window is the most widely used for different communications systems. However, the following window has also been deployed by IEEE 1901[10] and HomePlug [80] for broadband PLC:

$$w_{rise}[n] = \begin{cases} \frac{0.2}{52}n, & 0 \leq n \leq 51, \\ 0.2 + \frac{0.6}{267}(n-52), & 52 \leq n \leq 319, \\ 0.8 + \frac{0.2}{52}(n-319), & 320 \leq n \leq RI-1, \end{cases}$$

$$w_{fall}[n] = 1 - w_{rise}[n], \qquad 0 \leq n \leq RI - 1,$$

and

$$w[n] = \begin{cases} w_{rise}[n], & 0 \leq n \leq RI - 1, \\ 1, & RI \leq n \leq T + GI - 1, \\ w_{fall}[n - (T + GI)], & T + GI \leq n \leq T + GI + RI - 1, \end{cases}$$

where RI depicts the roll-off interval, T is IFFT interval and GI is the guard interval, and $\mu = GI + RI$. Windowed OFDM can be efficiently implemented by the system shown in Fig. 2.3, but including the windowing and overlap and add processes at the transmitter side and the opposite processes at the receiver side.

OFDM (with or without windowing) is the most widely recommended technique for both narrowband and broadband PLC standards. This is because of its several advantages such as its inherent adaptability in the presence of frequency selective channels, its resilience to narrowband interference, and its robustness to impulsive noise. However, it is well known that one important drawback of OFDM is its insertion of redundancy, which reduces the throughput. Furthermore, when a windowed technique is used, the protection against intersymbol interference (ISI) and intercarrier interference (ICI) is reduced in proportion to the roll-off interval length [15].

2.3.2 Filter bank multicarrier system

In MCM system, a modulated signal (e.g., PAM signal or QAM signal) is split into M parallel signal $s_k[n]$, $k = 0, \ldots M-1$. Then, $s_k[n]$ are interpolated by a factor of M_1 and passed through the transmitting filter $f_k[n]$. The transmitted signal can be expressed as follows

$$x[n] = \sum_{k=0}^{M-1} \sum_{m=-\infty}^{\infty} s_{k,m} f_k[n - mM_1]. \tag{2.2}$$

On the other hand, the receiver is defined as analysis filter bank with receiving filter $h_k[n]$. The kth subchannel signal is given by

$$\begin{aligned} y_k[n] &= \sum_{\tau} h_k[\tau] y[nM_1 - \tau] \\ &= \sum_{\tau} h_k[\tau] \sum_{l} a_l x[nM_1 - \tau] + r[nM_1 - \tau], \end{aligned} \tag{2.3}$$

where a_l is the coefficient of the discrete channel impulse response and $r[n]$ denotes the additive noise. Fig. 2.4 shows a general block diagram of multicarrier modulation system by a filter bank approach.

It should be noted that, the filter bank system is referred to as critically sampled, or minimal transmultiplexer, if $M_1 = M$, while non-critically sampled, or redundant transmultiplexer, if $M_1 > M$.

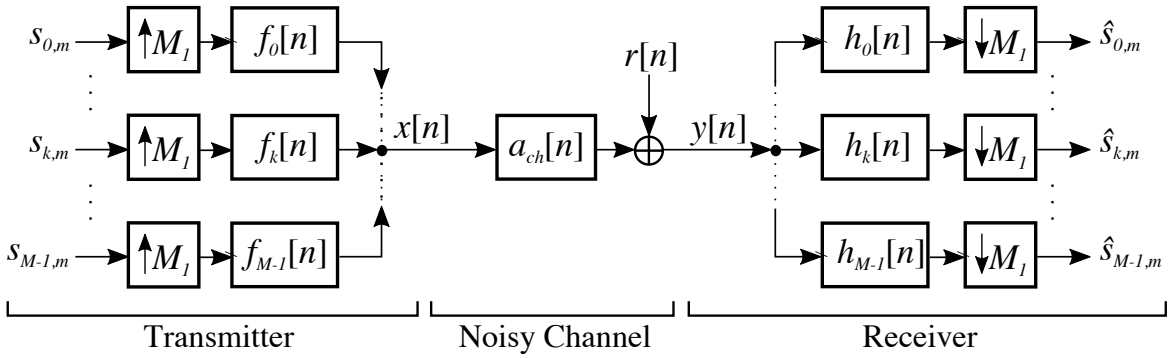

Fig. 2.4 General block diagram of a filter bank in a transmultiplexer configuration.

Conventional cosine modulated filter bank

From both the design and implementation points of view, CMFBs are attractive since all the analysis and synthesis filter are generated by using a single prototype filter, and the system can be efficiently implemented using fast algorithms of the discrete cosine transform[84].

In the conventional scheme of modulation, the kth cosine modulated synthesis and analysis filter are defined as follows [64]

$$f_k[n] = p[n]\cos\left(\frac{\pi}{M}\left(k+\frac{1}{2}\right)\left(n-\frac{N-1}{2}\right)-\underbrace{(-1)^k\frac{\pi}{4}}_{\phi_k}\right), \tag{2.4}$$

$$h_k[n] = p[n]\cos\left(\frac{\pi}{M}\left(k+\frac{1}{2}\right)\left(n-\frac{N-1}{2}\right)+\underbrace{(-1)^k\frac{\pi}{4}}_{\phi_k}\right), \tag{2.5}$$

where $0 \leq n \leq N-1$, $N = 2\kappa M$ and κ is the overlapping factor. The choice of the angle ϕ_k is important since it has influence on several distortion and errors present in the system [26].

It should be emphasized that this filter bank is referred to as quadrature mirror filters (QMF) and belong to the set odd-stacked filter banks. As it was shown in [85], the odd-stacked filter bank corresponds to a lapped transforms and for that they are also called modulated lapped transform [26] or extended lapped transform [64]. Perhaps, this could be the main reason why this system has been confused with the wavelet OFDM system deployed by the IEEE P1901 Working Group. While it is true that the main differences between both systems are the scaling factor and the phase, each of them provides a different modulation scheme.

2.3.3 Forward error correction processing

Two kind of FEC have been deployed. On the one hand, Reed-Solomon encoding is applied to the input data of the scrambler block, and then convolutional encoding is applied to the output of the

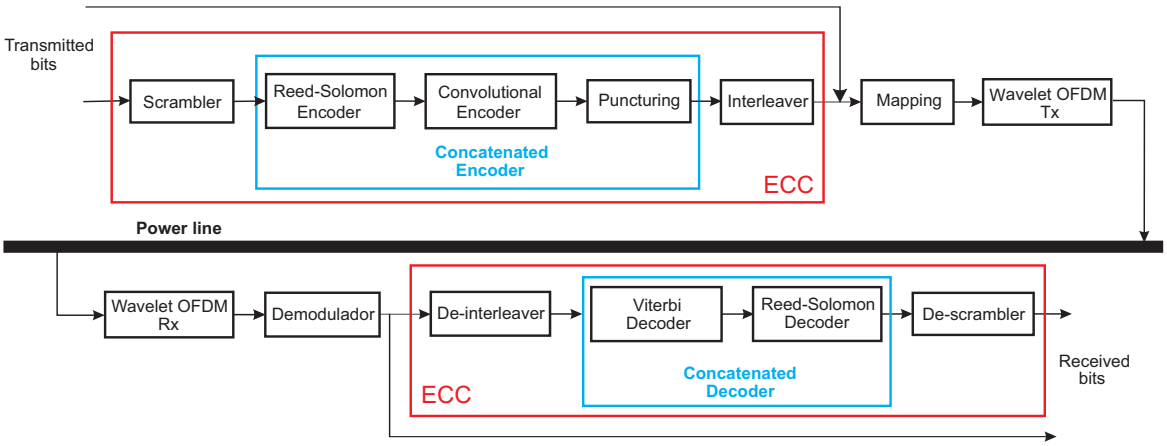

Fig. 2.5 Broadband ELT-MCM transceiver.

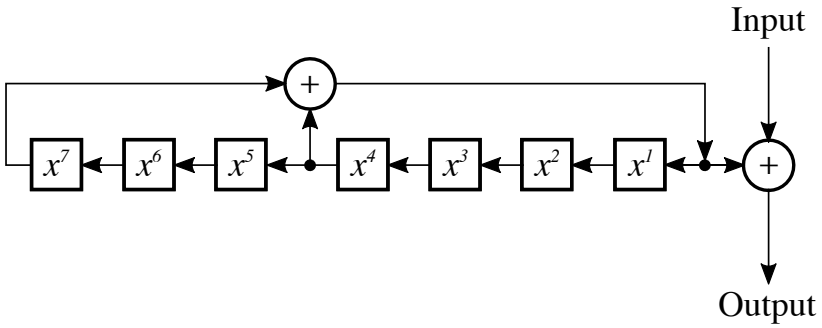

Fig. 2.6 Scrambler.

Reed-Solomon encoder, referred this configuration to as concatenated encoder. On the other hand, a convolutional codes defined by low-density parity-check polynomials (LDPC-CC) is proposed. Nonetheless, support for LDPC-CC is optional, and thus its study is not included in this thesis. Fig. 2.5 depicts each of the ELT-MCM system sections.

Scrambler

It is defined in [10, pp. 1171]. The data in the frame body shall be scrambled using the generator polynomial: $x^7 + x^4 + 1$. At the beginning of each frame, the bits in the scrambler shall be initialized to all ones, and for each symbol the first bit becomes the most significant bit (MSB) of that symbol. Fig 2.6 depicts the scrambler blocks.

Reed-Solomon

For the RS (n,k) encoder the field generator polynomial ($p_{RS}(x)$) and the code generator polynomial ($g_{RS}(x)$) are defined as follows [10, pp. 1172]:

$$p_{RS}(x) = x^8 + x^4 + x^3 + x^2 + 1,$$

Table 2.6 Puncturing.

Coding Rate	Puncture Pattern (Y(1))	Puncture Pattern (Y(2))
2/3	10	11
3/4	101	110
4/5	1000	1111
5/6	10101	11010
6/7	100101	111010
7/8	1000101	1111010

$$g_{RS}(x) = \{x - \alpha r\}\{x - \alpha(r+1)\}\{x - \alpha(r+2)\}\ldots\{x - \alpha(2t+r-1)\},$$

where the field is equal to GF(2^m) with $m = 8$, $t = 8$ and $r = 0$. The maximum code length (n) is fixed to 255 whereas the maximum number of bits (k) equals 239.

Convolutional encoder and puncturing

Fig. 2.7 shows the CC and its features are the following [10, pp. 1173]:

- Coding rate of the encoder: $1/2$.
- Constraint length: 7.
- Generator polynomials (in octal): 171 and 133.
- The convolutional encoder is reset to zero state at the beginning of each symbol.
- The output of the $1/2$ encoder can be punctured according to a puncture pattern represented in Table 2.6.

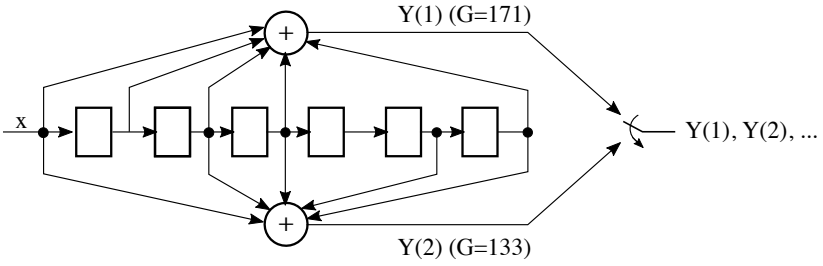

Fig. 2.7 Convolutional encoder.

Interleaver

The interleaver for one wavelet OFDM symbol [10, pp. 1180] presents an $(S \times D)$-memory with $S = \lceil N/D \rceil$, N and D denote the number of bits per symbol and interleave depth, respectively. For the frame body, D must be equal to 16. Basically, the bit interleaver input data are written in input

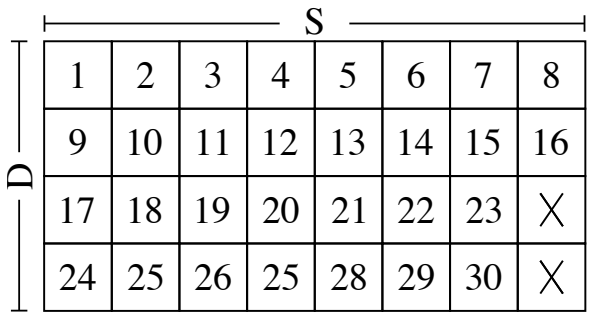

(a) Bit interleaver input

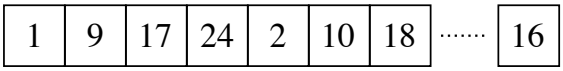

(b) Bit interleaver output

Fig. 2.8 Simple example of the interleaving process for $N = 30$ and $D = 4$.

order in the horizontal direction in memory, and after writing all $N-$bit data, they are read by column direction starting with the first column. Fig 2.8 clarifies the interleaving process. Optionally, an interleaver for multiple wavelet OFDM symbols (see [10, pp. 1181]) can be implemented instead of the preceding one.

CHAPTER 3

PLC channel and noise modelling

Power line is one of the most hostile channel since it is frequency-selective and time-varying channel. Furthermore, it presents different kind of noises such as colored background noise, impulsive noises and narrowband interferences [86]. For all these reasons, the PLC channel and noise modelling is a really hard task, nevertheless, several approaches for in-home scenarios [10, 87–91] and in-vehicle scenarios [4, 58, 92–96] have been presented.

This chapter is aimed at describing the different PLC channel and noise model used in this thesis. On the one hand, an overview about in-home PLC scenarios is given. Firstly, the model proposed by Zimmermann and Dostert [87], which is considered as the fundamental PLC channel model, is presented. This model will not be used in this thesis, but we think that an overview about it is necessary to understand the rest of PLC models that will be employed, such as the statistical model introduced by Tonello in [88]. As third in-home PLC channel model, a channel model based on the physical structure of the electrical networks [91] is described, referred to as Cañete's model. Furthermore, two PLC noise models, based on [97] and [98], are introduced. On the other hand, we focus on in-vehicle PLC scenario. Specifically, the in-car and in-aircraft PLC channel models described in [93] and [4] are outlined, respectively. Likewise, the PLC noise model for each of theses two cases are presented.

3.1 In-home PLC scenario

3.1.1 Channel models

The different in-home PLC channel models here described are for broadband communications over low voltage network.

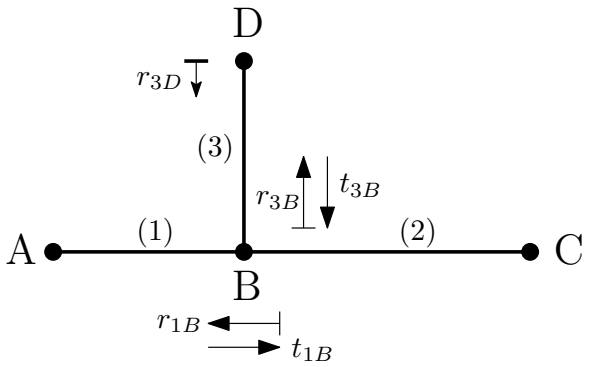

Fig. 3.1 Example of multipath signal propagation through a single tap cable [87].

Zimmermann's Model

Unfortunately the electrical wiring is not point-to-point connection. In general, the link between the power substation an the customers is a shared medium which consists of a series connection of distributor cables and branching house connection cables. Similarly, the indoor wiring is interconnected in a tree-like manner spread out from the electrical meter unit to the electrical sockets. All these connections, each of them with its own impedance, cause multiples reflections that must be considered in the signal propagation.

Zimmermann's model studies the multipath signal propagation inside the electrical wiring. Let us use the example depicted in Fig. 3.1 [87, Fig. 1] to better explained of this concept. The cable has just one branch and is composed of 3 segments whose lengths and characteristic impedances are denoted by l_1, l_2, l_3 and Z_1, Z_2, Z_3, respectively.

With the objective of simplifying the considerations, A and C are assumed to be matched, i.e. $Z_A = Z_1$ and $Z_C = Z_2$, therefore, there is not reflections in that points. The reflection and transmission factors of the points B and C are denoted by r_{1B}, r_{3B}, r_{1D} and t_{1B}, t_{3B}, respectively. Based upon these assumptions, an infinite number of propagation paths is possible in principle due to multiple reflections (for instance: $A \to B \to C$, or $A \to B \to D \to B \to C$, or $A \to B \to D \to B \to D \to B \to C$ and so on). Each path i has its corresponding weighting factor (g_i) which represents the product of the reflection and transmission factors along the path. Besides, all reflection and transmission are basically less or equal to one, therefore $|g_i| \leq 1$.

The ith path delay can be obtained as

$$\tau_i = \frac{d_i\sqrt{\varepsilon_r}}{c} = \frac{d_i}{v_p}, \tag{3.1}$$

where ε_r is the dielectric constant, c is the the speed of light and d_i denotes the length of the ith cable.

The losses of cables cause an attenuation ($A(f,g)$) that increases with length and frequency, therefore, longer paths exhibit higher attenuation. Besides, the more transitions/reflections along a path, the smaller the weighting factor will be. Thus, the infinite number of paths can already

Table 3.1 Parameters of the 4-path PLC channel model

Parameters	**Value**
k	1
a_0	0
a_1 (s/m)	$7.8 \cdot 10^{-10}$
g_i	$[0.64, 0.38, -0.15, 0.05]$
d_i (m)	$[200, 222.4, 244.8, 267.5]$

be approximated by the N dominant paths and it can be as small as possible. Taking all these considerations into account, the channel frequency response can be expressed as follows:

$$H(f) = \sum_{i=1}^{N} g_i \cdot A(f, d_i) \cdot e^{-j2\pi \cdot f \cdot \tau_i}, \tag{3.2}$$

with

$$A(f, d) = e^{-(a_0 + a_1 f^k)d}, \tag{3.3}$$

where a_0 and a_1 are the attenuation parameters and k is the exponent of the attenuation factor (typical values are between 0.5 and 1). In general, a_0, a_1 and k are derived from measured transfer functions and they must be properly chosen to simulate PLC channel correctly.

Finally, combining the multipath effect (3.2) and the attenuation (3.3), the PLC channel frequency response model yields

$$H(f) = \sum_{i=1}^{N} |g_i(f)| \, e^{\phi_{g_i(f)}} \cdot e^{-(a_0 + a_1 f^k)d_i} \cdot e^{-j2\pi \cdot f \cdot \tau_i}, \tag{3.4}$$

where complex frequency-dependent g_i has been assumed. However, assuming that g_i are only real-valued, the channel frequency response can be simplified as follows:

$$H(f) = \sum_{i=1}^{N} g_i \cdot e^{-(a_0 + a_1 f^k)d_i} \cdot e^{-j2\pi \cdot f \cdot \tau_i}. \tag{3.5}$$

Figs. 3.2 and 3.3 depict the channel impulse response and the frequency response of a 4-path PLC channel model and a 15-path PLC channel model, respectively. The parameters have been obtained from [87] and are summarized in Table 3.1 and 3.2.

Top-Down Model in [88, 90]

The deterministic Zimmermann's model is a really simple way to approach the PLC channel behaviour, nonetheless, it could not be the best option for the design and testing of transmission systems. In this regard, the model proposed by Tonello [88, 90], which is a top-down approach to the statistical modelling for the PLC channel transfer function, may be more beneficial. Based on (3.5), Tonello

Table 3.2 Parameters of the 15-path PLC channel model

Parameters	**Value**
k	1
a_0	0
a_1 (s/m)	$7.8 \cdot 10^{-10}$
g_i	$[0.029, 0.043, 0.103, -0.058, -0.045, -0.040, 0.038, -0.038, 0.071, -0.035, 0.065, -0.055, 0.042, -0.059, 0.049]$
d_i (m)	$[90, 102, 113, 143, 148, 200, 260, 322, 411$ $490, 567, 740, 960, 1130, 1250]$

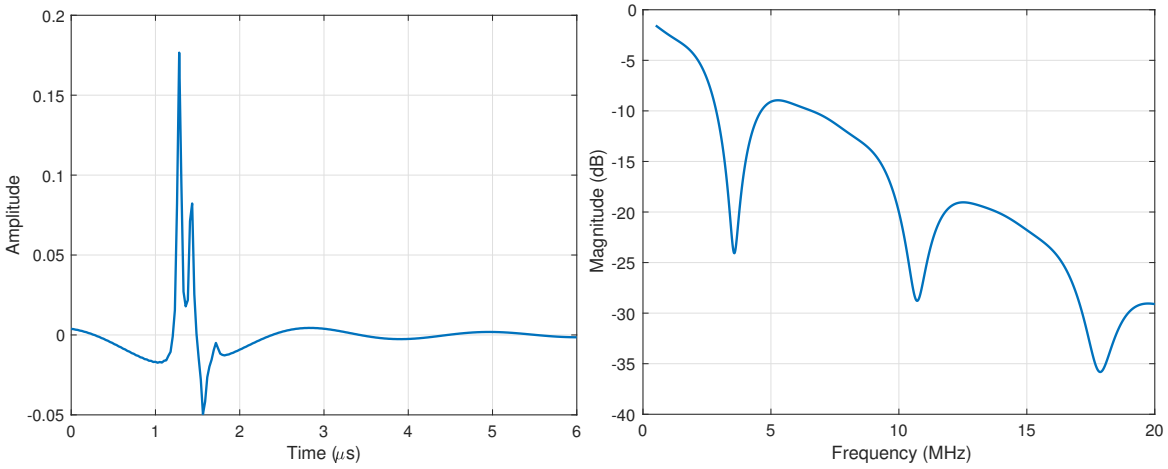

(a) (b)

Fig. 3.2 (a) Channel impulse response and (b) magnitude response of a 4-path PLC channel model.

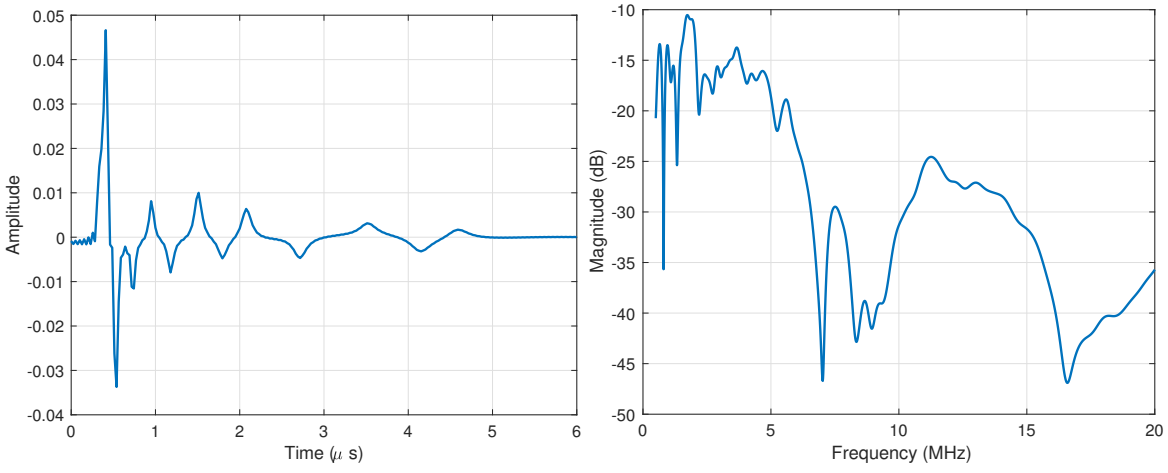

(a) (b)

Fig. 3.3 (a) Channel impulse response and (b magnitude response of a 15-path PLC channel model.

proposes the following expression

$$H(f) = A\sum_{i=1}^{N} g_i \cdot e^{-(a_0+a_1 f^k)d_i} \cdot e^{-j2\pi \cdot f \cdot \tau_i},\ 0 \le B_1 \le f \le B_2, \tag{3.6}$$

where A allows adding an attenuation to the frequency response. In order to obtain the statistical model, the idea is to assume the reflectors are placed over a finite distance interval and are located according to a Poisson arrival process with intensity $\Lambda[\mathrm{m}^{-1}]$ and the maximum network length is denoted by L_{max}. The number of paths (N) has a Poisson distribution with mean $L_{max}\Lambda$, whereas the inter-arrival path distances are independent and exponentially distributed with mean $1/\Lambda$.

Since g_i is in general complex, they can be modelled as independent complex random variables with log-normally distributed amplitude and with uniform phase in $[0, 2\pi]$. Another possible model considers the weighting factors follows a real uniform distribution $[-1, 1]$.

It is important to note that when $k = 1$, the channel impulse response can be expressed in closed form as follows

$$g_{ch}^{+}(t) = A\sum_{p=1}^{N_p}\left[\left(g_p e^{-a_0 d_p}\frac{a_1 d_p + j2\pi\left(t-\frac{d_p}{v}\right)}{(a_1 d_p)^2 + 4\pi^2\left(t-\frac{d_p}{v}\right)^2}\right)\left(e^{j2\pi B_1\left(t-\frac{d_p}{v}\right)-a_1 B_1 d_p} - e^{e^{j2\pi B_2\left(t-\frac{d_p}{v}\right)-a_1 B_2 d_p}}\right)\right]. \tag{3.7}$$

Nonetheless, in this model k could be either larger or smaller than one. The rest of parameters (a_0, a_1) are assumed to be constant but must be chosen properly. In particular, the channel can be normalized such that the average path loss at zero frequency is equal to one. Therefore, the parameter a_0 can be chosen to satisfy the following expression

$$\sqrt{\frac{\Lambda}{3}\frac{1-e^{-\Lambda L_{max}}}{2a_0}\left(1-e^{-2L_{max}a_0}\right)} = 1, \tag{3.8}$$

and the desired average path loss at zero frequency can be obtained by the factor A [89].

A source code to generate a statistical PLC channel assuming the parameters provided in [90, pp. 55] (see Table 3.3), can be found in [90, pp. 61]. The channel impulse response and the magnitude response of 4 realizations are shown in Fig 3.4a and 3.4b, respectively. As it can be seen, the generated PLC channels present a random behaviour.

In this thesis, one hundred impulse response realizations representative of Classes 1 (strong signal attenuation), Class 5 (medium attenuation) and Class 9 (little attenuation) will be used[1]. The statistically representative channel frequency responses have been computed using the script available on-line in [100]. Specifically, it has been employed the release 2.0, since it allows for the generation of channels according to the model parameters given in [101, Table I] for the different classes described in [89, 90]. The channel frequency response of the first 10 realizations of the Class 9, 5 and 1 have been represented in 3.5a, 3.5b and 3.5c, respectively.

[1] Classification based on [89] and [99]

Table 3.3 Parameters of the Tonello's model [90, pp. 55]

Parameters	Value
ε_r	1.5
k	1
a_0	$0.3 \cdot 10^{-2}$
a_1 (s/m)	$4 \cdot 10^{-10}$
L_{max} (m)	800
Λ (m^{-1})	0.2
B_1 (MHz)	0
B_2 (MHz)	100
Truncation (μs)	5.56

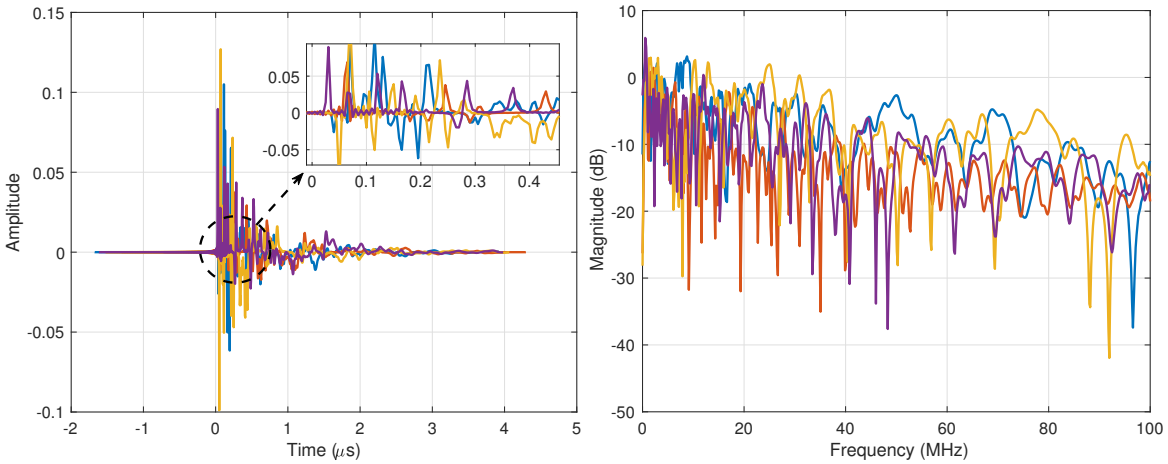

(a) (b)

Fig. 3.4 (a) Impulse response and (b) magnitude response of 4 Tonello's model realization, based on [90, pp. 61]

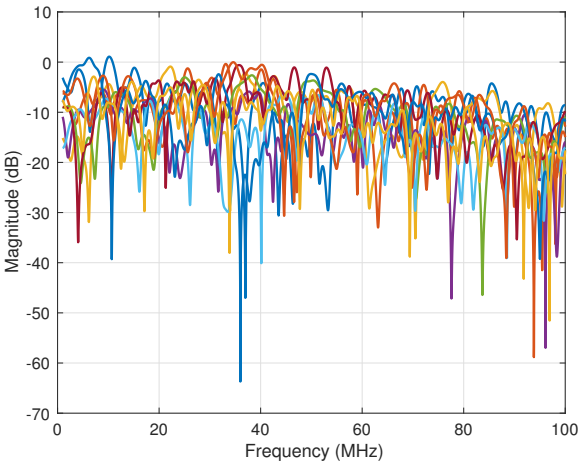

(a) Class 9

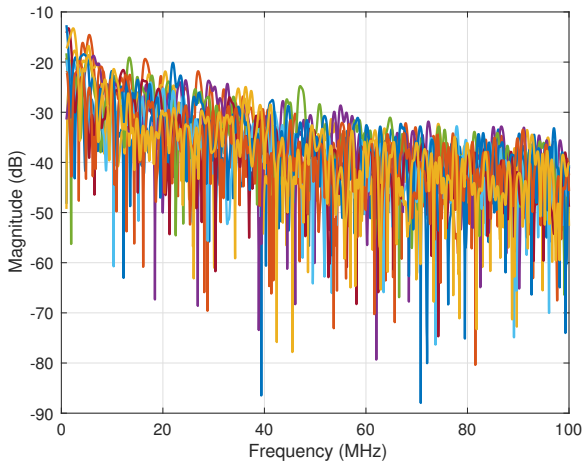

(b) Class 5

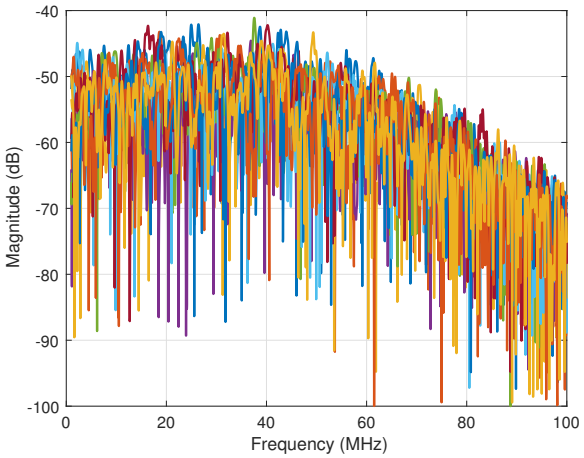

(c) Class 1

Fig. 3.5 Magnitude responses of ten different realization of the Tonello's model, based on [100] .

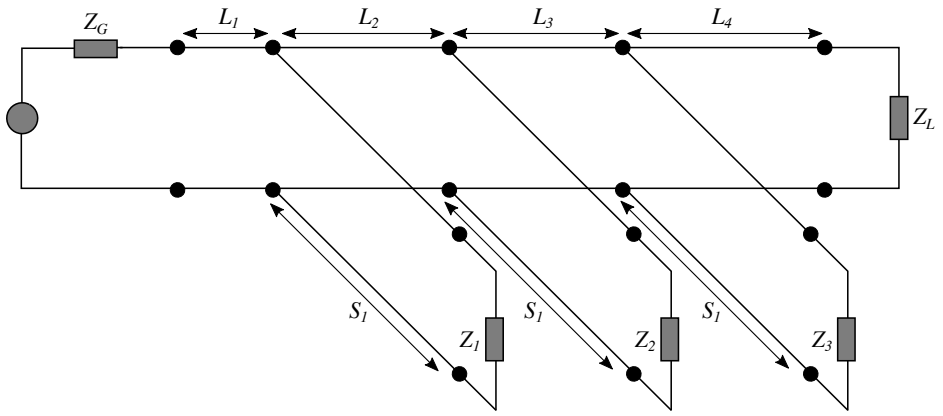

Fig. 3.6 Topology for the in-home PLC channel model [91].

Bottom-up Model in [91]

Finally, the last in-home PLC channel model that will be used in this thesis was proposed by Cañete *et al* [91]. This approach provides realistic channel realizations by using structural parameters instead of behavioral parameters based on statistics, as Tonello's model. Thus, the channel response is obtained in a deterministic way from a simplified topology and load models (see Fig. 3.6).

Three load models are described: constant impedances, time-invariant but frequency-selective impedances and time-varying and frequency-selective impedances. For the first one, the values of $\{5, 50, 150, 1000, \infty\}$ are reasonable. For the frequency selective impedances, the load model is implemented by a parallel RLC resonant circuit, whose impedance can be obtained as follows:

$$Z(\omega) = \frac{R}{1 + jQ\left(\frac{\omega}{\omega_0} - \frac{\omega_0}{\omega}\right)}. \tag{3.9}$$

where R, Q and ω_0 denote the resistance at resonance, the quality factor and the resonance angular frequency, respectively.

On the other hand, the time-varying impedances can be classified in two groups as well. In the former, the impedances have a commuted behavior, between Z_A and Z_B, synchronous with the mains voltage period T_0. Two parameters describe this case: the state duration (T) and the delay with respect to the mains voltage zero-crossing (D), further, the transition between Z_A and Z_B can be considered ideal. In the latter, the impedances has a more "harmonic" variation along the mains period that can be expressed as

$$Z(\omega,t) = Z_A(\omega) + Z_B(\omega)\left|\sin\left(\frac{2\pi}{T_0}t + \phi\right)\right| \tag{3.10}$$

where $0 \leq t \leq T_0$, Z_A is the the offset impedance, Z_B is the amplitude of the variation, and ϕ is the phase term which serves to reference the variation with respect to the mains voltage zero-crossing. The diagram of these time-varying impedance models can be found in [91, Fig. 2b].

Table 3.4 Indoor electrical wiring features [91, Table 1]

Cable type	**0**	**1**	**2**	**3**	**4**
Section (mm^2)	1.5	2.5	4	6	10
ε_{eq}	1.45	1.52	1.56	1.73	2
$Z_0\ (\Omega)$	270	234	209	178	143
$C\ (^{pF}/_{M})$	15	17.5	20	25	33
$L\ (^{\mu H}/_{M})$	1.08	0.96	0.87	0.78	0.68
R_0	12	9.34	7.55	6.25	4.98
G_0	30.9	34.7	38.4	42.5	49.3

This model allows generating both linear time invariant (LTI) and linear periodically time-varying (LPTV) channel impulse responses. LTI channels are calculated by manipulating matrices with the parameter ABCD of each section, whereas, LPTV channels are represented by the responses of a periodical series of LTI systems. The following parameters are suggested for LTI channel generation in the frequency band up to 30 MHz:

- The number of points in the positive axis and the resolution are fixed to 2048 and 14 kHz, respectively.
- The transmitter impedance (Z_G) and receiver impedance (Z_L) are assumed constant and equal to $50\,\Omega$.
- The cable type is randomly chosen, with uniform distribution, from Table 3.4. $R = R_0 \cdot 10^{-5}\sqrt{f}$ $(^{\Omega}/_{m})$ and $G = G_0 \cdot \ell \cdot 10^{-14} \cdot 2\pi f$ $(^{S}/_{m})$, where ℓ is a correction factor used to achieve a better match between the modelled and measured curves.
- Line section lengths L_i, $i \in 1, 2, \ldots, 5$ and S_j, $j = 1, 2, 3$ follow a uniform distribution between 0.5 and 50 m $(L_i, S_j \sim U(0.5, 50)[m])$.
- Z_1, Z_2 and Z_3 are modelled as frequency selective function impedances with the following parameters:
  - $R \sim (200, 1800)[\Omega]$.
  - $\omega_0/2\pi \sim U(2, 28)[MHz]$.
  - $Q \sim U(5, 25)$.

Fig. 3.7 illustrates some frequency-selective impedance obtained by means of the parameters described above. Here, R, w_0 and Q have been randomly chosen and they are equal to $\{1.7315, 0.9766, 1.4804\}$ (kHz), $\{5.689, 12.9658, 25.8091\}$ (MHz) and $\{20.8441, 24.1898, 18.1148\}$, respectively.

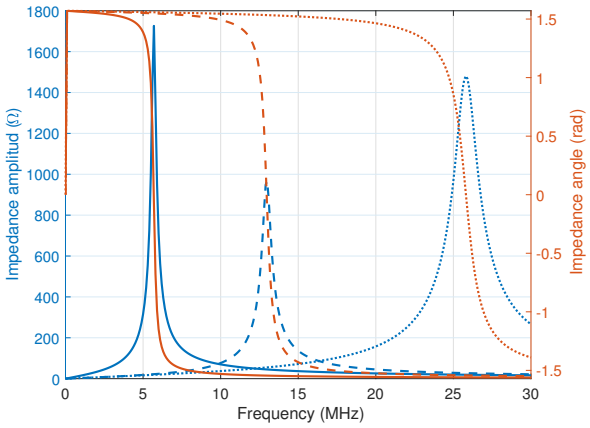

Fig. 3.7 Frequency selective impedance model [91].

For LPTV channel generation, for simplicity, just one of the three loads (Z_1, Z_2, Z_3) is considered time-varying. Thus, the resulting channel response will exhibit a commuted or harmonic time variation, depending on the choice. The proposed set of parameters are describe next:

- 50 invariance intervals (M) in a mains cycle for a resolution of 400 ms have been chosen.
- Given Z_1, Z_2 and Z_3, two of them are designed as frequency selective function impedances (as described above), while the other one is designed as a time-varying impedance. In case that a commuted variation is desired, the following parameters must be applied:
  - Z_B is also a frequency selective impedance with parameters R, ω_0 and Q randomly chosen.
  - $Z_A = 0.5 \cdot Z_B$.
  - $T \sim U(1, M/4)$.
  - $D \sim U(1, M/2 - T)$.
- If the harmonic variation is desired, the parameters would be selected as follows:
  - Z_B is defined exactly as in commuted variation case.
  - $Z_A = 50\,\Omega$.
  - $\phi \sim U(0, \pi)[rad]$.

In this thesis, just the LTI case has been considered. The channel impulse response have been obtained from the software tool software package PLC channel generator 2, available online in [102]. Specifically, the "best-case channel" (which present an average attenuation of 20 dB, an effective length of 0.3 μs and a coherence bandwidth of 628 kHz), "medium-case channel" (average attenuation of 33.6 dB, effective length of 0.9 μs and coherence bandwidth of 219 kHz) and the "worst-case channel" (average attenuation of 46 dB, effective length of 1.6 μs and coherence bandwidth of 102 kHz) have been used. Fig. 3.8 shows the channel impulse response and the magnitude responses obtained with this model.

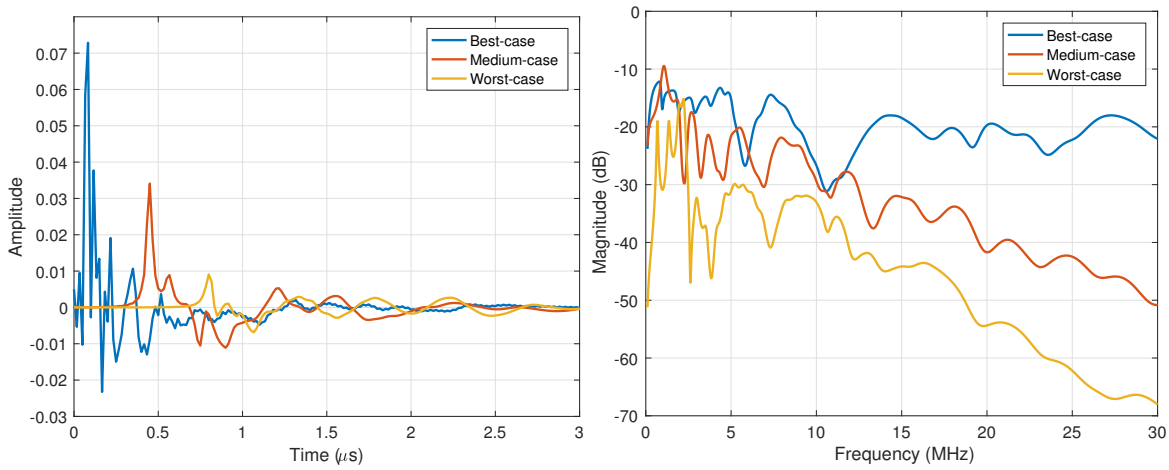

(a) (b)

Fig. 3.8 (a) Impulse response and (b) magnitude response based on [102].

3.1.2 Noise models

As in the case of in-home PLC channel models, the different PLC noise models detailed in this subsection are for broadband communications over low voltage network. The in-home PLC channel noise can be divided into five general classes of noises [86]:

- **Colored background noise:** It is mainly caused by the contribution of several noise sources with low power. It has a relatively low frequency-varying power spectral density (PSD).
- **Periodic impulsive noise synchronous to the mains frequency (PINS):** It is caused by switching of rectifier diodes in power supplies, which occurs synchronously with the mains cycle. The impulses have a duration of some microseconds and have a PSD decreasing with frequency. This noise has a repetition rate of 50/100 Hz in Europe.
- **Periodic impulsive noise asynchronous to the mains frequency (PINA):** This kind of noise is mostly caused by switched power supplies and has a repetition rate between 50 and 200 kHz.
- **Asynchronous impulsive noise (AIN):** It is caused by switching transients in the network (connection and disconnection of electrical devices). This noise presents a duration from some microseconds to few milliseconds with random occurrence. Besides, its PSD can achieve values of more than 50 dB above the background noise.
- **Narrowband noise or narrowband interference:** It is mostly sinusoidal signals with modulated amplitudes caused by different sources such as broadcast stations, spurious disturbances caused by electrical devices with a transmitter/receiver [97], among others. Its intensity is generally varying with daytime.

Several PLC noise models have been performed. Zimmermann and Klaus Dostert present a statistical model of the time behavior of random impulsive noise based on a partitioned Markov chain

[86]. H. Meng *et al* propose a background noise model based on the Nakagami-m distribution in [103]. In this thesis, the model proposed by J. A.Cortés in [97], referred to as Cortés' model, and by L. Lampe in [98], referred to as Lampe's model, have been chosen. These two model are briefly described below.

Model in [97]

This model is derived from a measurement campaign realized in three different scenarios: in laboratories and offices of a university building, in an apartment of about 80 m^2, and in a detached house of about 300 m^2. The mathematical formulation of the different types of noise is described below

1. **Background noise model:** This model ensures that the probability density function of the background noise match with the Gaussian curve (see [97, Fig. 15]), therefore, it can be concluded that the background noise presents a Gaussian behaviour. As it is done in [104], the background noise is obtained by filtering white Gaussian noise with a filter that is characterized by the magnitude response

$$|G(f)|^2 = S_{BGN}(f), \tag{3.11}$$

   where $S_{BGN}(f)$ is the PSD of background noise.

   Fig 3.9 shows 15 equally spaced snapshots of the instantaneous PSD of the background noise registered in a university laboratory (heavily disturbed scenario), in a detached house (medium disturbed scenario) and in a apartment (weakly disturbed scenario), which are available online in [102]. All these PSD have been obtained at a sampling frequency 50 Msamples/s [97]. The time-domain waveform of some background noise generated with these PSD model have been represented in Fig. 3.10. It is important to note that the generated time-domain waveform for all the noises described in this subsection must be re-sampled according to the sampling frequency defined by [10] for ELT-MCM system (62.5 MHz).

2. **PINS model:** This noise appears in a twofold manner: as a series of isolated impulses with a considerable amplitude and duration (Type I), or as impulse trains in which the number of impulses and separation between them varies from cycle to cycle (Type II). Besides, impulses within a given train are not equally spaced. The common characteristic to both components is that they appear always in the same instant of the mains cycle and, in Europe, they present a repetition rate of 50/100 Hz. Fig. 3.11 shows the Type I periodic synchronous pulse waveform, that that will be used in this thesis (available online in [102]). The main parameters of this noise component has been summarized in Table 3.5.

3. **PINA model:** It has been found that it presents a repetition rates ranging from 12 up to 217 kHz, despite it is claimed in [86] that this noise has a repetition rate between 50 and 200 kHz. Furthermore, it can be considered cyclostationary since this noise also exhibits an underlying period equal to the mains one. This kind of noise appears at the same instant of the mains cycle

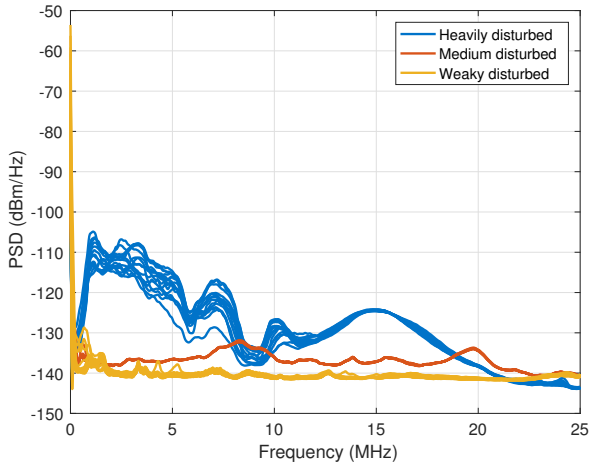

Fig. 3.9 Power spectral density of the background noise [102].

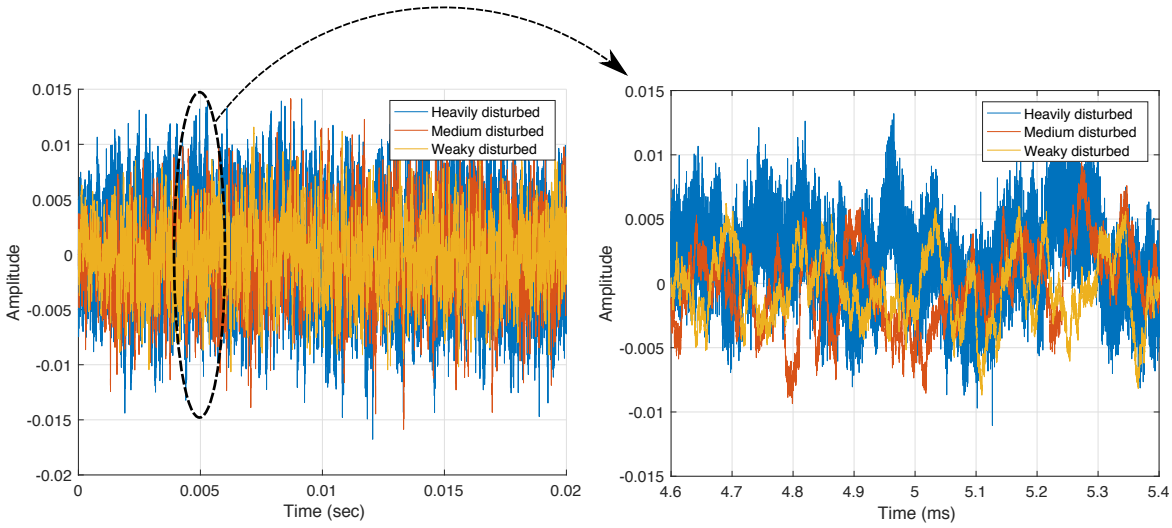

Fig. 3.10 Time-domain waveform of the background noise generated.

Table 3.5 Type I PINS characteristic [97, Table I]

Parameter	**Value**
Impulses within a mains cycle	≤ 10
Duration (μs)	$[2-300]$
Amplitude (V)	$[5\cdot 10^{-3}-1.5]$
Central Frequency	Typically less than 500 kHz, occasionally up to 3 MHz
Bandwidth	Typically less than 250 kHz, occasionally up to 2 MHz

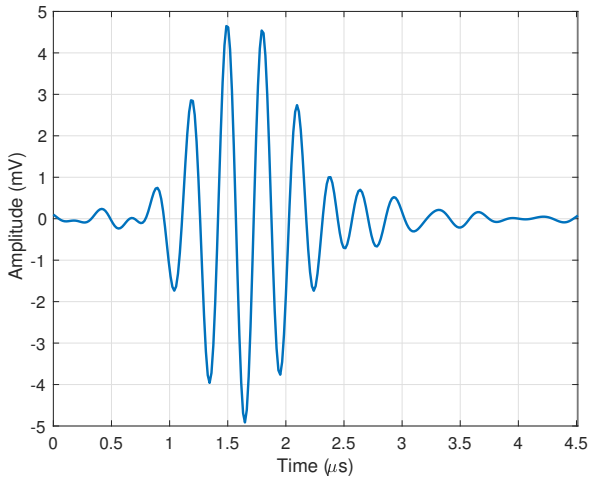

Fig. 3.11 Time-domain waveform of PINS [102].

Table 3.6 PINA characteristic [97, Table II]

Parameter	**Value**
Impulses within a mains cycle	1 or 3 in weakly disturbed scenarios, more than 3 in highly disturbed ones
Duration	Typically less than 1.5 μs , occasionally up to 10 μs
Amplitude	Typically less than 4 mV, occasionally up to 40 mV
Repetition rates (kHz)	12.6; 15.6; 26.4; 48.9; 56.5; 59.1; 70; 90.1; 217.2
Central Frequency (MHz)	$[2-13]$
Bandwidth (MHz)	$[2-13]$

as the Type 2 periodic synchronous impulsive noise (above described), but the difference is that the impulses within a given train of the Type 2 periodic synchronous noise are not equally spaced. Table 3.6 presents the main features of PINA model.

In this thesis, we use two PINA with a repetition rate of 26.3 and 48.93 kHz, respectively. Fig. 3.12 shows both periodic asynchronous pulse waveforms (available online in [102]).

4. **AIN model:** This is the most unpredictable impulsive noise and there two type of components. The first one is based on isolated impulses with considerable amplitudes and widths (Type I), whereas, the second one takes the form of impulse trains with arbitrary separation between the constituent pulses (Type II). The latter have lower amplitude and smaller duration than the former. The main characteristics of both type of components have been listed in [97, Table III].

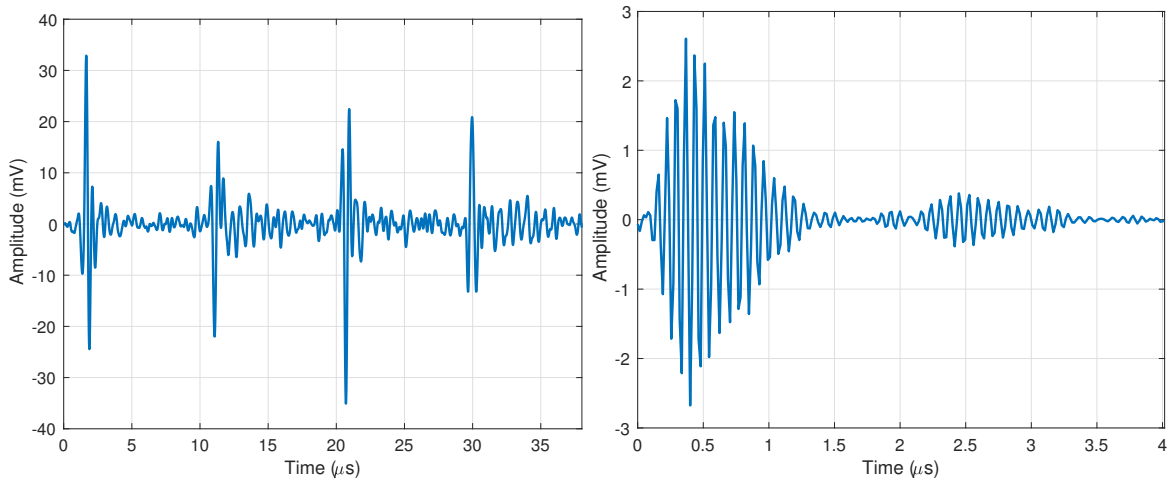

(a) (b)

Fig. 3.12 Time-domain waveform of PINA components with repetition rate of (a) 26.3 kHz and (b) 48.93 kHz [102].

However, since there is not an available online waveforms of this noise, this kind of noise has not been included.

5. **Narrowband noise model:** The narrowband interferences are classified, according to the shape of their PSD, as follows:

   (a) Interference with multiple discrete frequency components: The PSD of this kind of noise consists of several equally spaced narrowband components but they are not harmonically related. They can be found above 4 MHz with a frequency spacing up to 50 kHz.

   (b) Interference with one frequency component: Its PSD consists of a single-narrowband term with a bandwidth below 20 kHz and it can reach values more than 30 dB over the background noise. This kind of interference are usually located below 2 MHz and above 20 MHz.

   In this thesis the interference with one frequency component model has been selected. Fig. 3.13 depicts the time-domain waveform and the PSD of two realizations (located at 1 and 25 MHz, respectively) based on this model.

Model in [105]

As it can be appreciated, the model in [97] provides in some cases a deterministic way to simulate the in-home PLC noises (e.g. PINS and PINA). However, given the hostility of PLC channel, a single representation could not be enough to model the in-home PLC noise scenario. For that, the statistical model provided by Lutz Lampe *et al* in [105], according to the model presented in [98], could be a better option. In this respect, the different kinds of noise can be modelled as follows:

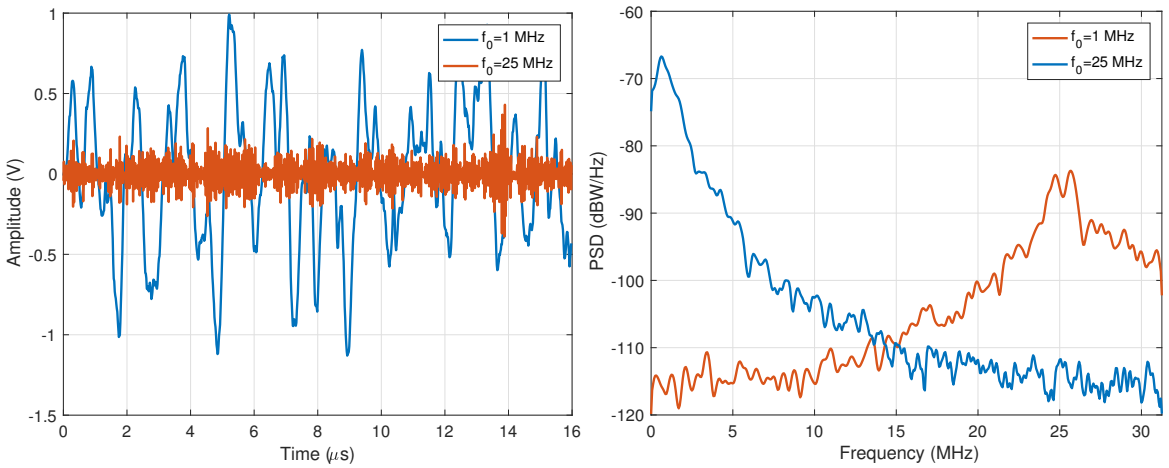

(a) Time-domain waveform (b) PSD

Fig. 3.13 Narrowband noises with one frequency component at 1 and 25 MHz.

Table 3.7 Value of the BGN model parameters for the best and the worst cases [106, Table 1]

	a	b	c
Best case	-140	38.75	-0.72
Worst case	-145	53.23	-0.337

1. **Background noise model:** The PSD of the background noise can be modelled by the expression given in [106]

$$S_{BGN}(f) = a + b|f|^{-c}, \text{ (dBmW/Hz)} \tag{3.12}$$

where parameters a, b, and c are constants and f denotes frequency in MHz. The parameter values for the best and worst case are provided in Table 3.7 ([106, Table 1]). With the aim at providing different background noise levels, the Lampe's model generates the parameters a, b and c uniformly distributed between the best and worst cases. The PSD of a background noise randomly generated ($a = -144.402$, $b = 42.8304$, $c = -0.4554$), as well as the PSD of the background noise associated to the best and the worst case, are depicted in Fig. 3.14a. It is important to note that this expression is also recommended by the standard IEEE 1901 [10, eq. F-4] to simulate this type of noise.

Finally, the background noise is obtained filtering white Gaussian noise with a filter characterized by the PSD generated by the model. Fig. 3.14b shows the time-domain waveforms obtained for each case.

2. **PINS model:** This kind of noise can be modelled, in time-domain, as a sum of damped sinusoids

$$n_{PINS}(t) = \sum_{k=0}^{N_{imp}} P_k(t - kT_d), \tag{3.13}$$

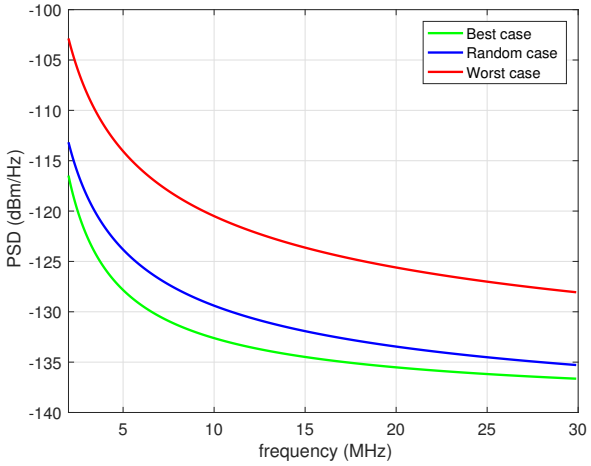

(a) PSD for different levels of the background noise.

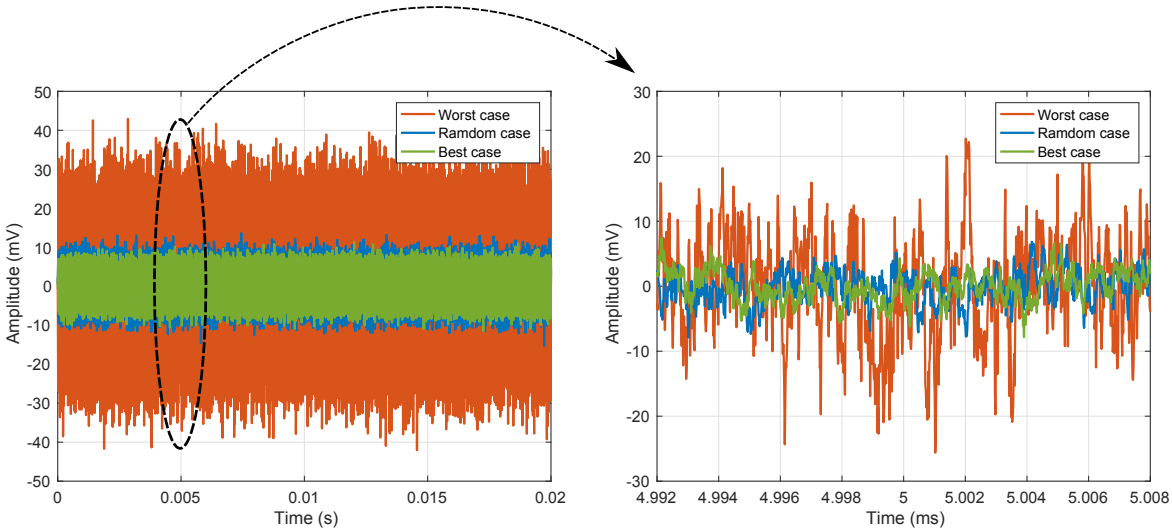

(b) Waveform of the BGN generated by Lampe's model.

Fig. 3.14 BGN generated with the model in [105].

Table 3.8 Parameters of the Lampe's PINS model

	T_d	N_{imp}	A_i
Best case	2 μs	1	5 mV
Worst case	300 μs	10	1.5 V
Otherwise	$U \sim (2\,\mu s, 300\,\mu s)$	$U \sim (1, 10)$	$U \sim (5\,\text{mV}, 1.5\,\text{V})$

where, N_{imp} is the number of impulses in one main cycle, T_d denotes the impulse duration and P_k are independent realizations of a sum of damped sinusoids [10, eq. F-7] given by

$$P_k(t) = \sum_{i=0}^{N_1-1} A_i e^{\alpha_i |t|} e^{j2\pi f_i t}, \tag{3.14}$$

where N_1 is the number of damped sinusoids in an impulse, and A_i, α_i and f_i denote the impulse amplitude, the damping factor and the pseudo frequency of the ith sinusoid, respectively.

The parameters of this model are defined as follows. Based on Cortés' model [97, Table 1], the pseudo frequency and the inter-arrival time (IAT) are uniformly distributed, the former between 250 kHz and 500 kHz ($f \sim U(250\text{ kHz}, 500\text{ kHz})$) and the latter between 200000 and 10000 samples $U(10000, 200000)$. On the other hand, according to [107] the number of damped sinusoids (N_1) is fixed to 3. The value of the impulse duration, the number of impulses in one main cycle and the amplitude of the impulse are listed in Table 3.8. Finally, the damping factor is equal to $0.005 \cdot fs$, where fs denotes the sampling frequency which is fixed to 62.5 MHz by [10] for wavelet OFDM.

Fig. 3.15a and 3.15b show the waveform and the PSD of three realization (best, worst and random case), within one mains cycle, obtained with this model, respectively.

3. **PINA and AIN model:** These two components have been modelled by the same expressions used for PINS ((3.13), (3.14)). The parameters of both kinds of noise are summarized in Table 3.9. Fig. 3.16 and 3.17 depict the time-domain waveform and PSD of different realization generated by the PINA and the AIN models. It should be pointed out that the PINA best case has not been represent since, under this conditions, there is not any pulse.

4. **Narrowband noise model:** The power spectral density of the narrowband interferences can be modelled as a parametric Gaussian function [104]:

$$S_{NBI}(f) = \sum_{k=0}^{N_2-1} C_k e^{-\frac{(f-f_{0,k})^2}{2B_k^2}} \tag{3.15}$$

where N_2 is the number of narrowband interferences, C_k, $f_{0,k}$ and B_k denote he amplitude, center frequency and bandwidth of the kth narrowband signal. $S_{NBI}(f)$ is individually generated in

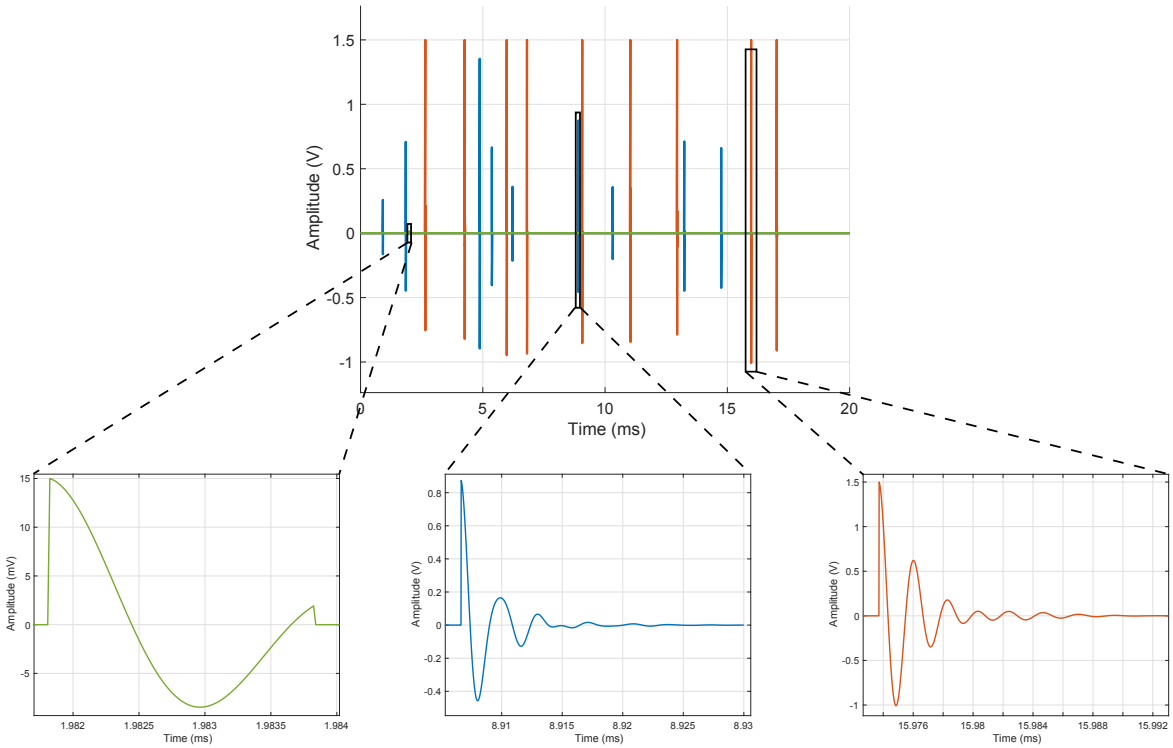

(a) Time-domain waveform

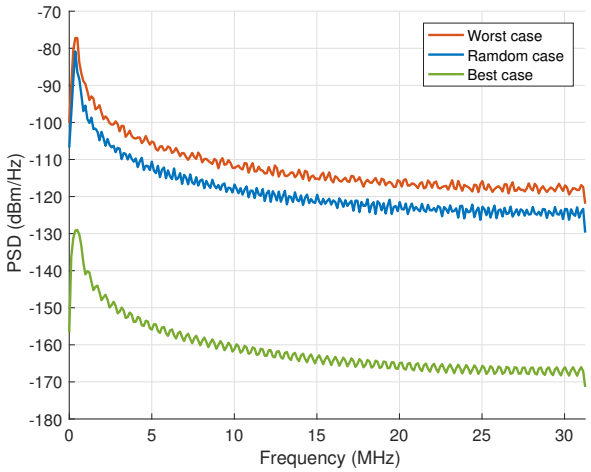

(b) PSD

Fig. 3.15 PINS within one mains cycle, based on [105].

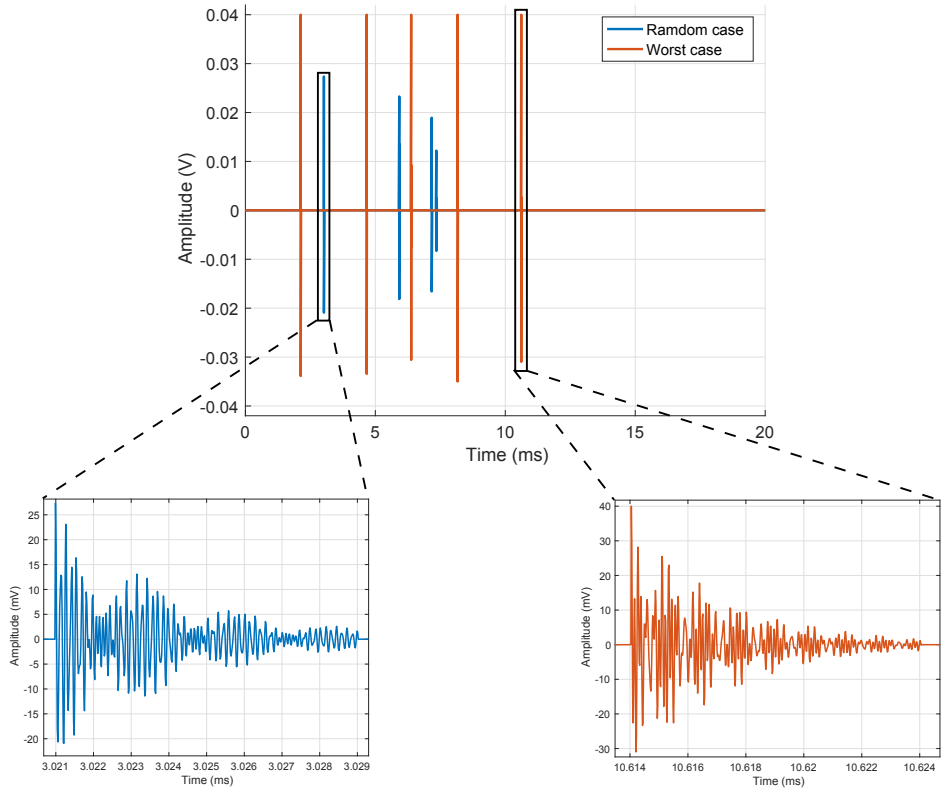

(a) Time-domain waveform

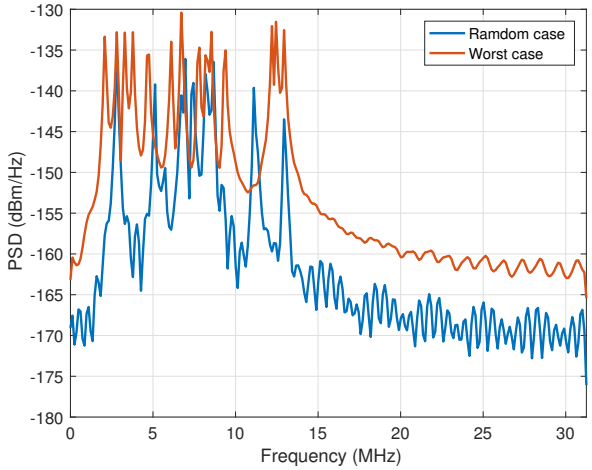

(b) PSD

Fig. 3.16 PINA within one mains cycle, based on [105].

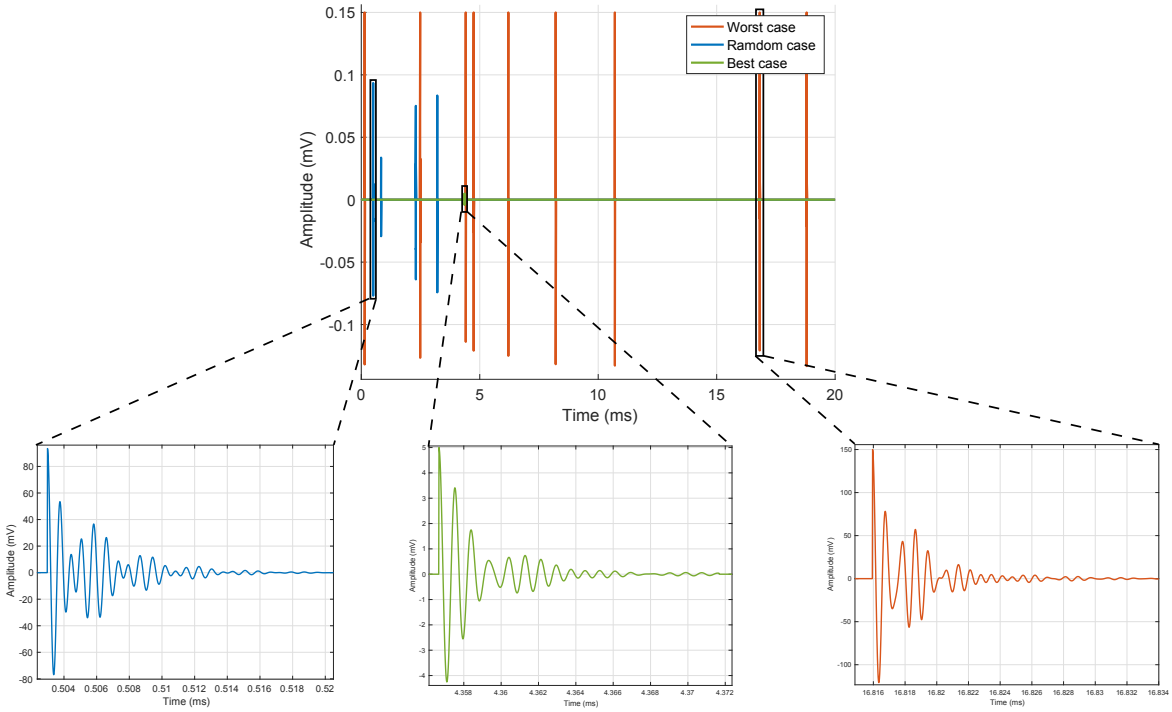

(a) Time-domain waveform

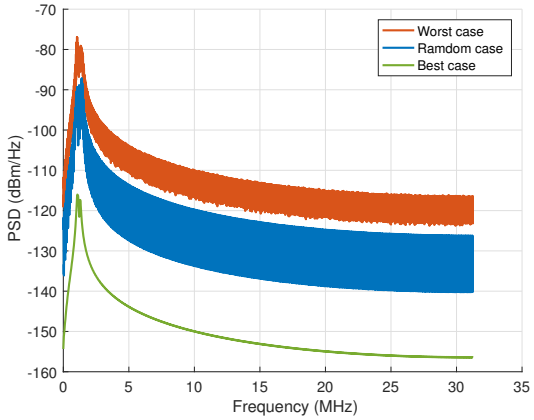

(b) PSD

Fig. 3.17 AIN within one mains cycle, based on [105].

Table 3.9 Parameters of the PINA and the AIN models following [105]

	Periodic impulse noise asynchronous with the mains cycle	**Asynchronous impulse noise**
α_i	$0.005 \cdot f_s$	$0.005 \cdot f_s$
N_d[a]	3	3
N_{imp}[b]	0 (Best case) 5 (Worst case) $\sim U(0,5)$ (Otherwise)	1 (Best case) 10 (Worst case) $\sim U(1,10)$ (Otherwise)
T_d[b]	1.5 μs (Best case) 10μs (Worst case) $\sim U(1.5\,\mu s, 10\,\mu s)$ (Otherwise)	15 μs (Best case) 150μs (Worst case) $\sim U15\,\mu s, 150\,\mu s)$ (Otherwise)
f[b]	$\sim U(2$ MHz$, 13$ MHz$)$	$\sim U(500$ kHz$, 1$ MHz$)$
A_i[b]	$\sim U(4$ mV$, 40$ mV$)$	$\sim U(20$ mV$, 150$ mV$)$
Inter-arrival time	$\sim U(10000, 200000)$	$\sim exp(100$ ms$)$[a]

[a] Based on [107].
[b] Based on [97].

three frequency bands: $[0-10]$ MHz, $[10-20]$ MHz and $[20-30]$ MHz. All of them are concatenated to form the overall narrowband noise.

The parameters take different values depending on the frequency range and the type of building (residential or office) [107]. Nonetheless, in any case, N_2 follows a normal distribution with a mean μ_{N_2} and standard derivation σ_{N_2} ($N_2 \sim N(\mu_{N_2}, \sigma_{N_2})$), $B_k \sim exp(\lambda_B)$ with a minimum bandwidth equal to 0.23 Mhz (0.19 MHZ) for residential building (office building). In addition, A_k is normally ($A_k \sim N(\mu_A, \sigma_A)$), log-normally ($A_k \sim LN(\mu_{L_A}, \sigma_{L_A})$) or even uniformly distributed ($A_k \sim U(\mu_A, \sigma_A)$). The characteristic values of the probability densities of the parameters of the narrowband noise are detailed in [104, Table 2].

The time-domain waveform is obtained by passing a white Gaussian noise through a filter, in the same way as in the background noise model (see Fig. 3.18). Thus, the PSD of generalized background noise (GBN) ($S(f)$) is defined as the the sum of the background noise and the narrowband noise [104]

$$S(f) = S_{BGN}(f) + S_{NBI}(f) = a + b|f|^{-c} + \sum_{k=0}^{N_2-1} C_k e^{-\frac{(f-f_{0,k})^2}{2B_k^2}}, \tag{3.16}$$

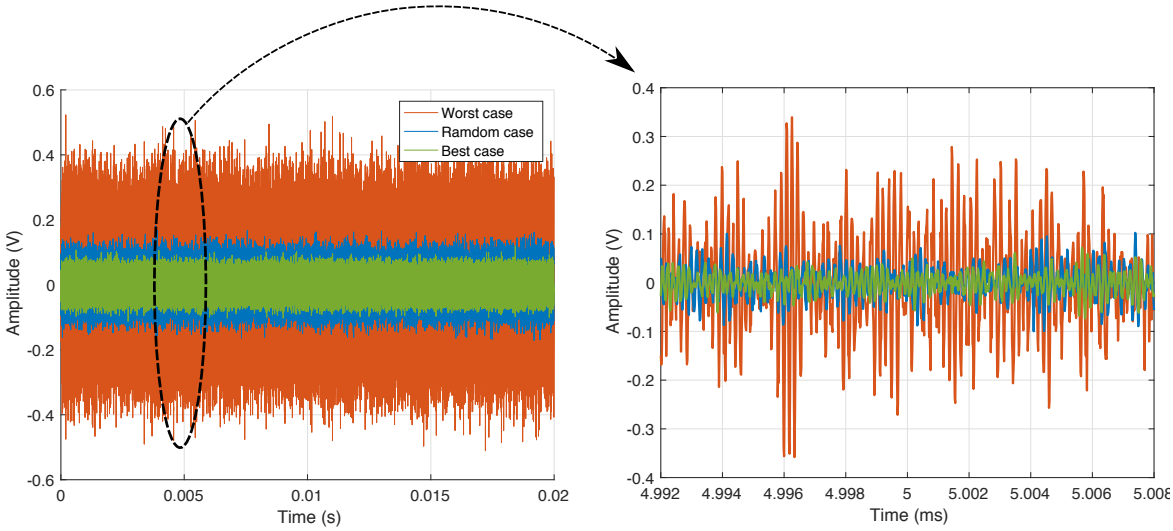

Fig. 3.18 Waveform of the GBN model based on [105]

3.2 In-vehicle PLC scenario

3.2.1 In-car PLC channel model

Several measurement campaigns have been carried out inside different cars, e.g. [92, 95, 108, 109]. But in this thesis we focus our attention on the model proposed by Lutz Lampe, which is obtained from the measurement campaign performed and described in [94], since it is available online [93].

In these campaigns, different parts of the vehicle has been analyzed as possible communication points. Particularly, the body control module (BCM), the cigarette lighter (CIG), the outside view mirror controller, the heating ventilating air conditioning fan button, the left and right front lights (LFL and RFL, respectively) as well as the left and right rear lights (LRL and RRL, respectively). Furthermore, this database holds measurements taken from different automobiles, such as 2006 Pontiac Solstice, 2008 Lexus RX 305, 2009 FVT EVaro, among others.

Since the 2006 Pontiac Solstice was the vehicle under study in [94], the two-port frequency domain scattering measurements obtained from it will be used in this thesis. In this respect, there are available 166 measurements of power line channels, recorded during different possible operating states of the car (e.g. engine turned on/off, idle, running), in the frequency band from 30 kHz to 100 MHz. Fig. 3.23 depicts the scattering parameter S_{21} associated with all the channels. In particular, the blue and red curves are the parameter S_{21} related to the links RFL-BCM and RRL-BCM, respectively, at two different states (solid and dotted lines).

The channel transfer function can be calculated as follows [94]:

$$H(\omega) = \frac{S_{21}(1+\Gamma_L)(1-\Gamma_S)}{2(1-S_{22}\Gamma_L)(1-\Gamma_{in}\Gamma_S)}, \tag{3.17}$$

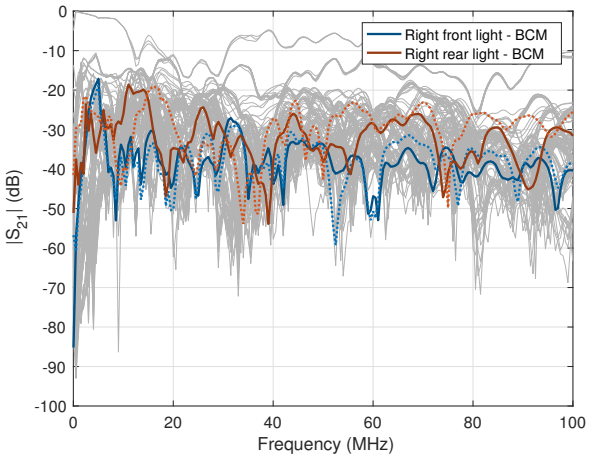

Fig. 3.19 Magnitude response of the parameter S_{21} associated with all the channels obtained from a 2006 Pontiac Solstice.

where

$$\Gamma_L = \frac{Z_L - Z_0}{Z_L + Z_0}, \tag{3.18a}$$

$$\Gamma_S = \frac{Z_S - Z_0}{Z_S + Z_0}, \tag{3.18b}$$

$$\Gamma_{in} = S_{11} + \frac{S_{12}S_{21}\Gamma_L}{1 - S_{22}\Gamma_L}, \tag{3.18c}$$

and assuming that $Z_L = Z_S = Z_0$, the expression (3.17) yields

$$H(\omega) = \frac{S_{21}}{2}. \tag{3.19}$$

Finally, the channel impulse response can be obtained by the inverse Fourier transform of (3.19). It must be emphasized that the channels obtained by this model must be filtered to adapt them to the frequency range fixed by the IEEE 1901 standard.

3.2.2 In-car PLC noise model

Over the past two decades, several researchers have focused their attention on this matter. Possibly, the study by A. Schiffer [110] pioneered the research on this issue. In this paper, the in-car PLC noise is divided into two classes: background noise and the impulsive noise component. On the one hand, the background noise can be modelled sufficiently accurate as Gaussian noise ($\sim N(\mu, \sigma)$) and its parameters depend on the location inside the vehicle, e.g., next to the battery $\mu = -0.0087$ and $\sigma^2 = 3.16 \cdot 10^{-6}$ whereas at 8 meter to the battery $\mu = -0.0013$ and $\sigma^2 = 3.15 \cdot 10^{-5}$ [110, Table I]. On the other hand, exponential and triangular oscillations can be used to model the impulsive noise and their parameters have been summarized in [110, Table II].

In [111] the background noise is also modelled by a Gaussian noise with a PSD of -130 dBm/Hz, which is consistent with the PSD reported in [94] (between -140 dBm/Hz and -120 dBm/Hz) and in [95] (between -115 dBm/kHz and -120 dBm/kHz). The impulsive noise has been characterized as a single (single transient) or as series of successive damped sinusoids (burst); in addition, different vehicle states (cruising and accelerating/braking phase) have been taking into account in this model. Thus, the main pulse characteristics of this kind of noise are modelled by a Gaussian, gamma or Weibull distribution (see [111, Table II]).

Granado *et al* [112] propose two impulsive noise models for gasoline and diesel vehicle, respectively. For the gasoline case, this kind of noise has been classified in pseudo synchronous noise and asynchronous noise. For the former, the maximum amplitude is modelled as Weibull distribution (MaxAmp $\sim W(a = 2.43, b = 56.76)$), the impulsive width (ImpWidth) is fixed to 3.1 μs and the IAT is equal to $30/RPM$, where RPM is the number of revolutions per minute of the engine. For the latter, the maximum amplitude is modelled by two Weibull distribution ($W(0.43, 41.42)$ or $W(0.64, 72.14)$), the impulse width is equiprobable between 5 μs or 30 μs and the inter-arrival time is fixed to 27 ms. However, there is only asynchronous noise components in the diesel case, and its parameters are modelled as follows: MaxAmp $\sim N(\mu = 0.19, \sigma = 0.061)$, ImpWidth $\sim GEV(K = 0.60, \sigma = 15.87, \mu = 51.13)$ and IAT $\sim U(0.1ms, 1.4ms)$, where GEV stands for Generalized Extreme Value distribution.

Having thus briefly summarized the state of the art related to this topic, the background noise will be modelled as has been described in [94], but nonetheless, two different models will be used to model the impulsive noise. On the one hand, the periodic impulsive noises with high repetition rate (PINH) and with low repetition rate (PINL) described in [113] are used, therefore, this model will be referred to as Cortes' model. The main features of each of these noises are detailed in Table 3.10 and 3.11, respectively. The time-domain waveform and PSD of both kinds of noises have been depicted in Fig. 3.20 and Fig. 3.21. On the other hand, the impulsive noise is modelled as a sum of damped sinusoids, and its parameters are based on the statistical analysis realized in [114], therefore, it will be referred to as Degardin's model. The impulsive noise is calculated as a sum of damped sinusoids, the number of damped sinusoids are equal to 4 or 5 (randomly chosen), the damping factor is fixed to $0.005 \cdot f_s$, where f_s is the sampling frequency, and the impulse amplitude, pseudo frequency, IAT, pulse duration are listed in Table 3.12. Fig. 3.22 shows the time-domain waveform of 100 realizations and three of them have been highlighted (blue, red and green curves).

3.2.3 In-aircraft PLC channel model

For this case, the channel frequency responses obtained from the measurement campaigns [1, 4] have been chosen. These measurements were carried out between the secondary power distribution box (SPDB) and the illumination ballast units (IBU) within the cabin of an aircraft. The communications are carried out between SPDB and 14 IBUs [4, Fig. 2], and two kinds of transmission over the electrical wiring have been considered: either between a wire and a ground plane (common-mode, CM), or between two wires (differential-mode, DM).

Table 3.10 Features of periodic PINH [113, Table II].

Parameter	Value
Number of component	From 1 up to 5, depending on the activated functions
Duration	Less than $2\,\mu s$, occasionally up to $4\,\mu s$
Amplitude	Less than $2\,mV$, occasionally up to $20\,mV$
Repetition rates	15.68 kHz, 42.72 kHz, 63.93 kHz, 64.75 kHz, 83.33Hz, 124.21 kHz, 128.8 kHz, 129.52 kHz
Central frequency	From 11 MHz up to 19 MHz
Bandwidth	From 1 MHz up to 22 MHz

Table 3.11 Features of periodic PINL [113, Table III].

Parameter	Value
Number of component	From 1 up to 4, depending on the activated functions
Duration	Less than $4\,\mu s$, occasionally up to $240\,\mu s$
Amplitude	Less than $6\,mV$, occasionally up to $500\,mV$
Repetition rates	26 Hz, 44.6 Hz, 50 Hz, 60 Hz, 79.5 Hz, 100 Hz, 146Hz, 172.1 Hz, 250.12 Hz, 400 Hz, 1.05 kHz, 3.5 kHz, 3.86 kHz
Central frequency	From 250 kHz up to 19.5 MHz
Bandwidth	From 500 kHz up to 12 MHz

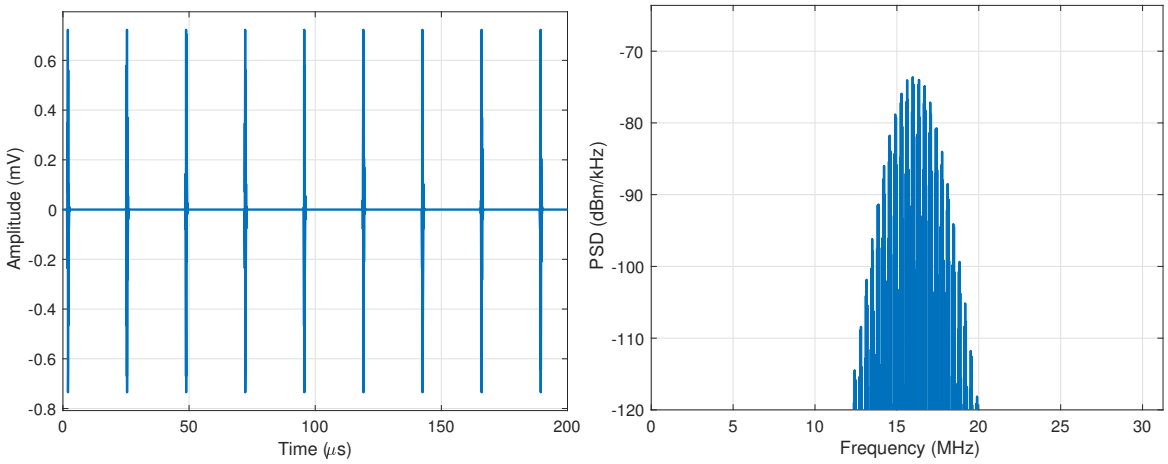

(a) Time-domain waveform.

(b) PSD.

Fig. 3.20 Periodic impulsive noises with high repetition rate, based on [113].

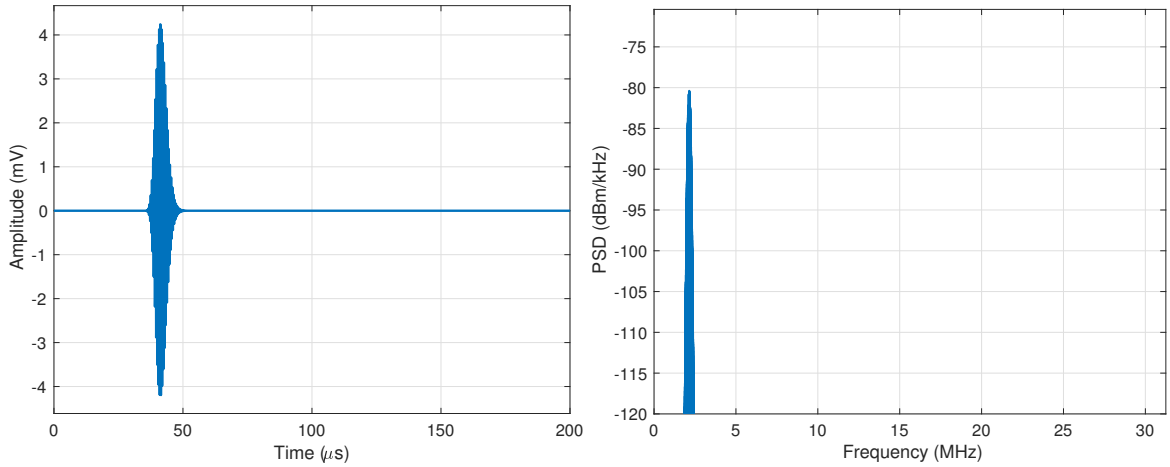

(a) Time-domain waveform. (b) PSD.

Fig. 3.21 Periodic impulsive noises with low repetition rate, based on [113].

Table 3.12 Parameters of the Degardin's model [114].

Parameter	**Interval**	**Probability** $(\mathbf{P}(\mathbf{A}))$	**Distribution**
Amplitude	$A < 0.31$ V	0.48	$Gamma(9.58, 0.02)$
	0.31 V $< A < 0.67$ V	0.38	$Gamma(29.52, 0.01)$
	$A > 0.67$ V	0.14	$Gamma(7.01, 0.14)$
Pseudofrequency	$f_0 < 1.2$ MHz	0.25	$Gamma(6.03, 0.12)$
	1.2 MHz $< f_0 < 6.5$ MHz	0.3	$Gamma(10.79, 0.43)$
	$f_0 > 6.5$ MHz	0.45	$Gamma(79.22, 0.13)$
Pulse duration	$D < 4.88\,\mu s$	0.72	$Gamma(3.67, 0.53)$
	$D > 4.88\,\mu s$	0.28	$Gamma(4.91, 1.76)$
IAT	$\log(IAT) < 2.32$	0.27	$Gamma(12.43, 0.12)$
	$2.32 < \log(IAT) < 3.29$	0.13	$Gamma(165.92, 0.01)$
	$3.29 < \log(IAT) < 5.18$	0.45	$Gamma(93.55, 004)$
	$\log(IAT) > 5.18$	0.15	$Gamma(179.11, 0.03)$

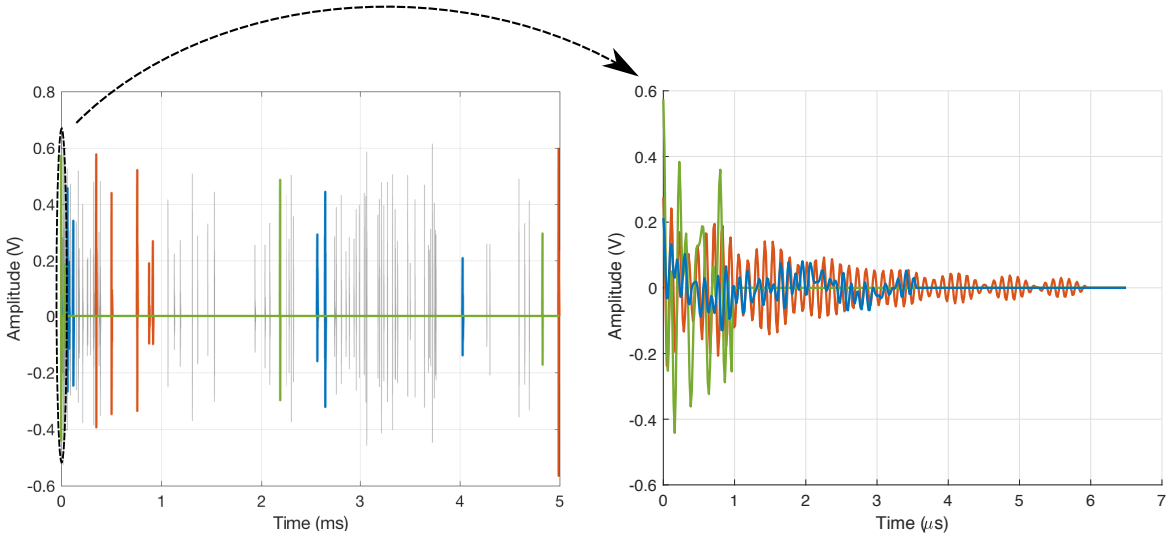

Fig. 3.22 In-car impulse noise waveform generated by Degardin's model [114].

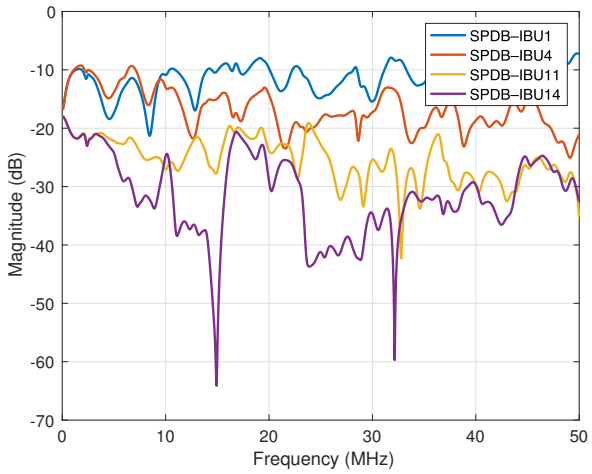

Fig. 3.23 Magnitude response of in-aircraft PLC channels obtained from [4] .

In this thesis, 4 in-aircraft PLC channels in differential-mode will be used: two short lines of 11.6m (SPDB-IBU1) and 17.9m (SPDB-IBU4), and two long lines of 34.9m (SPDB-IBU11) and 42.7m (SPDB-IBU11), respectively. In must be highlighted that the successive multiplying connectors, referred to as virtual termination (VT), have also been taking into account in the modelled architecture. Thus, there is one VT in the SPDB-IBU1 link, 2 VTs in the IBU4 and the IBU 11 connections, and 3 VTs in the SPDB-IBU14 link. Fig. 3.23 depicts the channel magnitude response of these 4 channels.

3.2.4 In-aircraft PLC noise model

Finally, based on [1] and subsequently in [4], the in-aircraft PLC noise is assumed as white Gaussian noise with a current density equals to -8 dBμA/kHz. Furthermore, since the maximum DM current

can reach 45 dBμA/kHz [4], it means that the maximum transmitted signal power must not exceed -58 dBm/Hz (for a load of 50 Ω).

CHAPTER 4

ELT-MCM for baseband PLC

The main characteristics of the ELT-MCM physical layer for baseband communication, as well as the recommended waveforms, FEC blocks and the correct definition provided by the standard were described in Ch. 2. Nevertheless, its implementation and performance has not been analyzed yet.

In this chapter, some key features, as the kind of FBMC proposed as transmitter, or the waveforms recommended as prototype filters to obtain the transmitting filters, are studied. Furthermore, efficient implementations for both transmitter and receiver, based on polyphase filters [115] and butterfly structures with symmetric matrices [26], are presented. The coefficients of the polyphase filters are obtained from the prototype filter, and each pair of filters can be implemented using a direct or a transpose form, or lattice structures, singly or in pairs. The computational complexities of the proposed fast algorithms of implementation, for each different structure, are also derived. Besides, the performance of an easy frequency-domain equalizer, which can help to correct the distortion of the power line channel, is proposed and investigated.

On the other hand, OFDM with and without windowing has received widespread attention by researchers. In this respect, there have been previous studies that derive the achievable data rate of OFDM-based systems. For instance, in [31] the discrete multi-tone (DMT) capacity was analyzed. The performance of windowed OFDM systems was studied in [15, 116]. Recent literature has proposed contributions with specific emphasis on OFDM/OQAM (FBMC/OQAM) [15, 31–33]. A special case of FBMC, based on the conventional modulation [34], has been studied in [36, 37, 117]. However, to the best of the author's knowledge, the study of the data rate for the system based on the ELT-MCM deployed by IEEE 1901, is still an open problem and it will be tackled in this chapter.

4.1 Baseband Transmitter

The standard considers three different number of subchannels: $M = 512, 1024, 2048$, and the following prototype filter lengths: $N = 2\kappa M$, where κ denotes the overlapping factor and it equals 2, 3. On the other hand, the corresponding frame may be transmitted either baseband or by modulation to a bandpass carrier. We focus for the rest of this section on $M = 512$ subchannels and baseband, mandatory for in-home and access applications.

In this case, the equation to obtain the time-domain waveform signal for the frame body is stated as follows [10, p. 1194]:

$$\frac{1}{16}\left[\sum_{c=0}^{3}\sum_{k\in\mathbb{K}_{on}} PAM_{k,c}\cdot p[n+512c]\cdot\cos\left(\frac{\pi}{512}\left((n+512c)+\frac{512+1}{2}\right)\left(k+\frac{1}{2}\right)+\theta_k\right)\right] \tag{4.1}$$

where an overlapping factor of 2 is assumed, $0 \leq n < 512$, $\mathbb{K}_{on} \subseteq \{0,\cdots,511\}$ is the set of active subchannels defined by the tone mask [10], $PAM_{k,c}$ is the PAM symbol in the subcarrier-time position (k, c), $p[n]$ is the prototype filter, and θ_k is a phase vector for peak power reduction. The values of θ_k for $M = 512$ are defined in [10, Table 14-10], and they are equal to 0 or π. When the total number of used carriers exceeds 512, the phase vector is constituted by repeating the phase group from carrier number 1 to 512.

It is important to note that the scale factor $\frac{1}{16}$ matches with $\sqrt{\frac{2}{M}}$, and that the phase vector θ_k only affects the sign of the time-domain waveform, since it equals 0 or π. Accordingly, the impulse-response coefficients of the M-channel transmitting filters are given by

$$f_k[n] = \sqrt{\frac{2}{M}}\cdot p[n]\cdot\cos\left[\left(k+\frac{1}{2}\right)\frac{\pi}{M}\left(n+\frac{M+1}{2}\right)\right]\cdot\cos(\theta_k), \tag{4.2}$$

where $k \in \mathbb{K}_{on}$. This expression, excluding the term $\cos(\theta_k)$, is nothing but the synthesis filters of an ELT introduced by H. Malvar [26].

The transmitter given by (4.2) leads us to propose a receiver based on the scheme of modulation recommended by H. Malvar for the analysis bank or direct ELT [26]. In addition, the phase factors θ_k of (4.2) must be included to guarantee perfect symbol recovery in absence of a transmission channel and noise. Fig. 4.1 shows the block diagram of the ELT-MCM transceiver, in which the receiving filters are given by

$$h_k[n] = \sqrt{\frac{2}{M}}\cdot p[n]\cdot\cos\left[\frac{\pi}{M}\left(k+\frac{1}{2}\right)\left(N-1-n+\frac{M+1}{2}\right)\right]\cdot\cos(\theta_k). \tag{4.3}$$

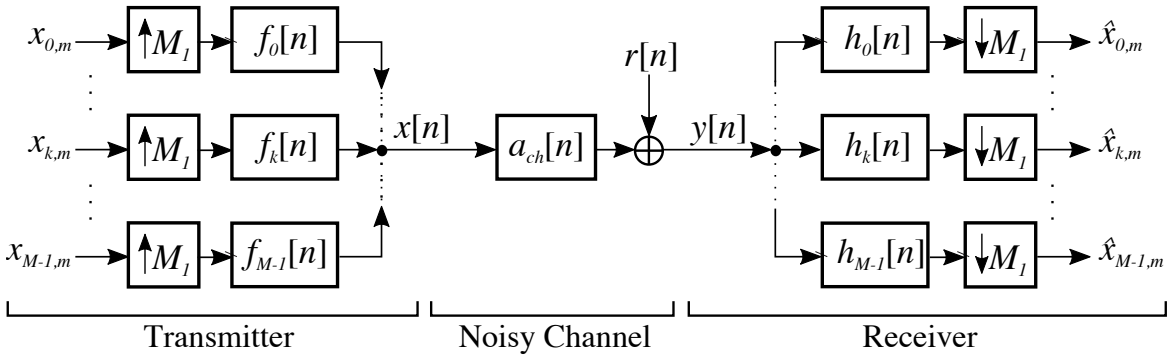

Fig. 4.1 General block diagram of a baseband ELT-MCM system.

4.2 Prototype Filter

Different prototype filters are proposed in the standard for the cases of $M = 512$, 1024 and 2048 subchannels, and for overlapping factors κ equals 2 or 3. For the case of $\kappa = 2$, the prototype filter coefficients $p[n]$ can be obtained from a "mother filter" $p_0[n]$, given in [10, p. 1205], as follows:

- $M = 512$ subchannels:

$$p[n] = \frac{1}{2}\{p_0[4n+1] + p_0[4n+2]\} \quad 0 \leq n < 2M. \tag{4.4}$$

- $M = 1024$ subchannels:

$$p[n] = \frac{1}{2}\{p_0[2n] + p_0[2n+1]\} \quad 0 \leq n < 2M. \tag{4.5}$$

- $M = 2048$ subchannels:

$$p[n] = p_0[n] \quad 0 \leq n < 2M. \tag{4.6}$$

- For $M = 512, 1024, 2048$ subchannels:

$$p[n] = p[4M-1-n] \quad 2M \leq n < 4M. \tag{4.7}$$

As it can be seen that the resulting prototype filter presents an even symmetry ($p[N-1-n] = p[n]$). Unfortunately, the standard does not provide expressions that allow designers to quickly obtain the corresponding coefficients. However, it can be proved by computer simulations that the prototype filters belong to a parametrized family of windows proposed by H. Malvar [26] whose coefficients

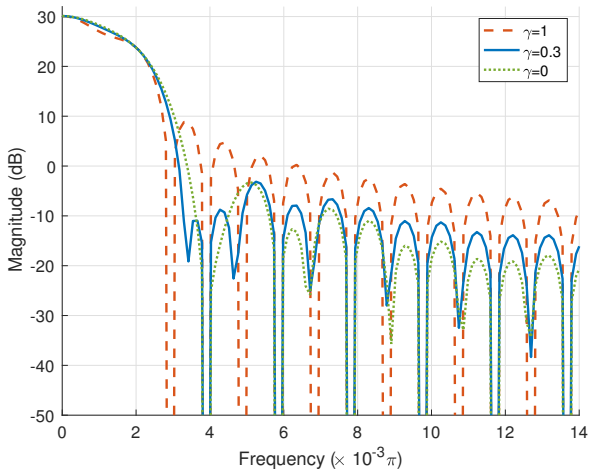

Fig. 4.2 Comparison between the first subband filter for $M = 512$, $\gamma = 1$, $\gamma = 0.3$ (IEEE 1901 prototype filter) and $\gamma = 0$.

can be generated by [118]:

$$p[n] = \cos(\theta_{n0}) \cdot \cos(\theta_{n1}), \tag{4.8a}$$

$$p[M-1-n] = \sin(\theta_{n0}) \cdot \cos(\theta_{n1}), \tag{4.8b}$$

$$p[M+n] = \cos(\theta_{n0}) \cdot \sin(\theta_{n1}), \tag{4.8c}$$

$$p[2M-1-n] = -\sin(\theta_{n0}) \cdot \sin(\theta_{n1}), \tag{4.8d}$$

for $n = 0, 1, ..., \frac{M}{2} - 1$, where

$$\theta_{n0} = -\frac{\pi}{2} + \mu_{n+\frac{M}{2}}, \tag{4.9a}$$

$$\theta_{n1} = -\frac{\pi}{2} + \mu_{\frac{M}{2}-1-n}, \tag{4.9b}$$

and

$$\mu_q = \left[\left(\frac{1-\gamma}{2M}\right)(2q+1) + \gamma\right]\frac{(2q+1)\pi}{8M}. \tag{4.10}$$

Following the above expressions (4.8)-(4.10), it can be proved that the prototype filters recommended by [10] are identical to the Malvar's prototype filters with the parameter $\gamma = 0.3$, for $M = 512$, 1024, and 2048. Notice that γ, which typically varies in range $[0, 1]$, controls the trade-off between stopband attenuation and transition band width of the filter frequency responses. The higher γ value, the greater stopband power, and the lower transition width. Figs. 4.2 and 4.3 show a comparison to check the aforementioned properties. Besides, Fig. 4.5 depicts the ambiguity functions for different γ values.

On the other hand, for the case of $\kappa = 3$, the standard specifies in three different tables the coefficients of each prototype filter ([10, pp. 120, 1288 y 1292]). Unlike the previous case, the design

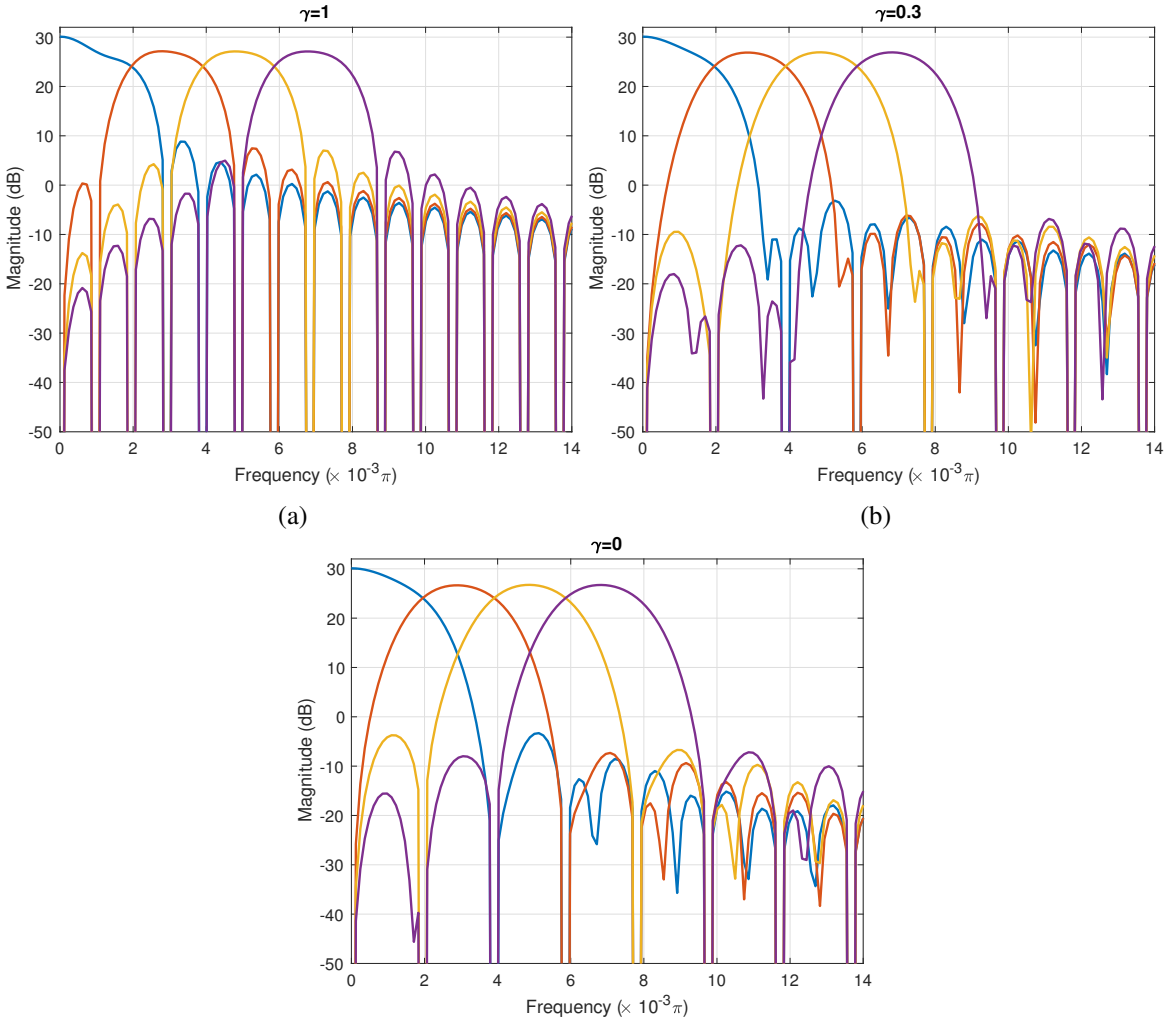

Fig. 4.3 Magnitude responses of the first four subband filters for $M = 512$ and (a) $\gamma = 0$, (b) $\gamma = 0.5$ and (c) $\gamma = 1$.

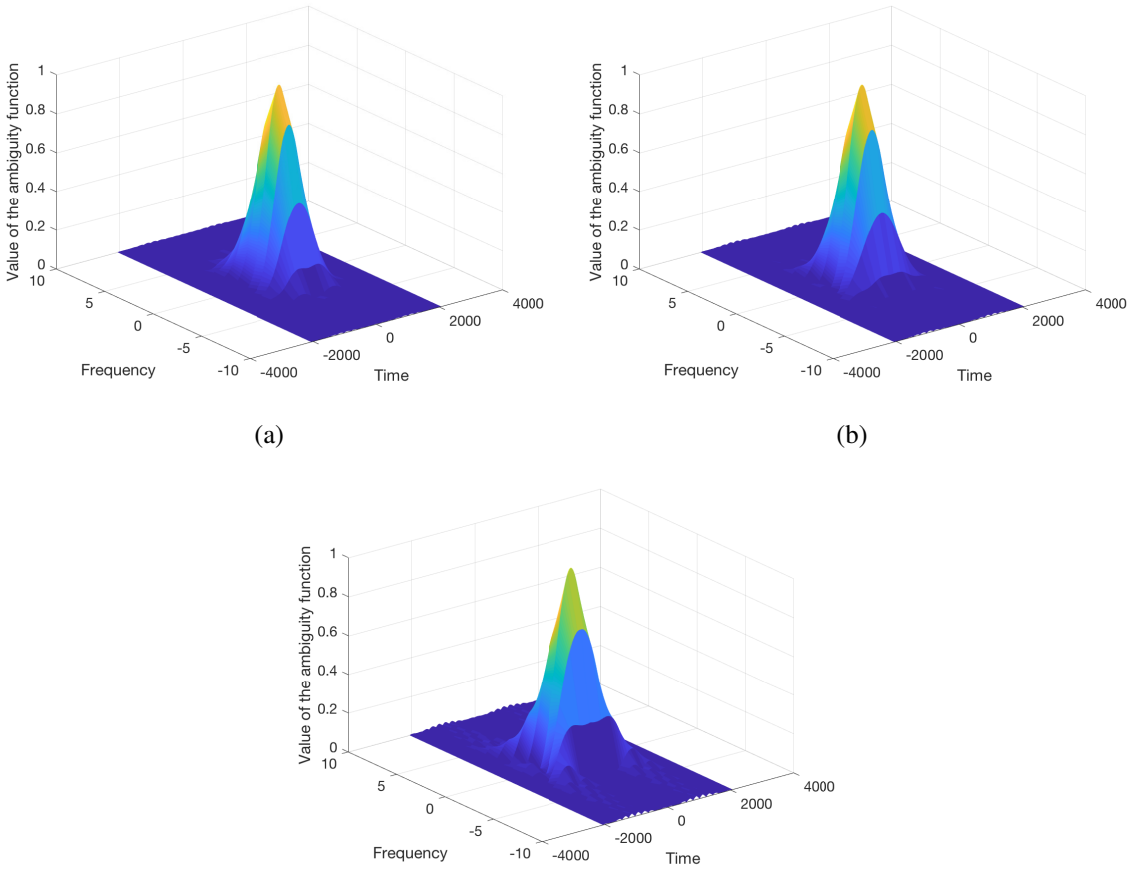

(a)

(b)

(c)

Fig. 4.4 The ambiguity function for (a) $\gamma = 0$, (b) $\gamma = 0.5$ and (c) $\gamma = 1$ assuming $M = 512$.

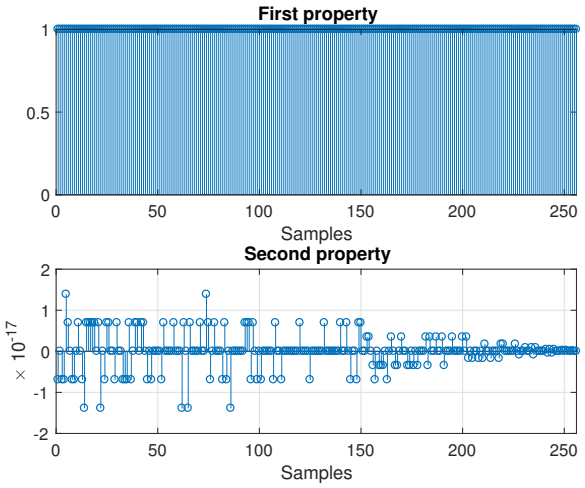

(a) Equation (4.12a) and (4.12b)

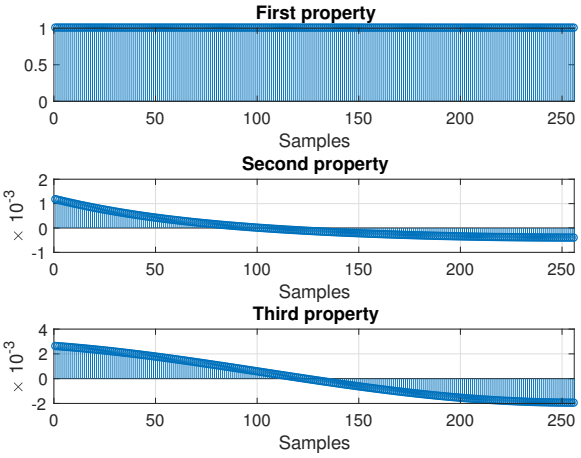

(b) Equation (4.13a), (4.13b) and (4.13c)

Fig. 4.5 PR conditions of the recommended prototype filter for $M = 512$. a) $N = 2048$ and b) $N = 3072$.

of the ELT window for $\kappa > 2$ is based on optimization techniques [26]. It is important to note that these prototype filters can be also employed in the case of bandpass communication system.

4.2.1 Perfect reconstruction property

In order to obtain the perfect reconstruction (PR) property in ELT-based systems, it is necessary to choose a window that presents even symmetry and satisfies the following condition:

$$\sum_{i=0}^{2\kappa-2s-1} g[n+iM]g[n+iM+2sM] = \delta[s], \tag{4.11}$$

where $n = 0, 1, \ldots, \frac{M}{2} - 1$ and $s = 0, 1, \ldots, \kappa - 1$. Replacing $\kappa = 2$ in the above equation, it yields:

$$g^2[n] + g^2[n+M] + g^2[n+2M] + g^2[n+3M] = 1, \tag{4.12a}$$

$$g[n]g[n+2M] + g[n+M]g[n+3M] = 0. \tag{4.12b}$$

Fig. 4.5a shows, by computer simulations, that the recommended prototype filter for $\kappa = 2$ fulfills the PR conditions.

Likewise, if $\kappa = 3$ the PR conditions are given by:

$$g^2[m] + g^2[m+M] + g^2[m+2M] + g^2[m+3M] + g^2[m+4M] + g^2[m+5M] = 1, \tag{4.13a}$$

$$g[m]g[m+2M] + g[m+M]g[m+3M] + g[m+2M]g[m+4M] + g[m+3M]g[m+5M] = 0, \tag{4.13b}$$

$$g[m]g[m+4M] + g[m+M]g[m+5M] = 0. \tag{4.13c}$$

The above equations have been tested by computer simulations and the results obtained are depicted in Fig. 4.5b, assuming $M = 512$ and $N = 3072$. It can be easily noticed that this prototype filter does not fulfill the PR conditions (in like manner for $M = 1024$ and $M = 2048$). In a nutshell, the IEEE P1901 working group deploys a PR window for $\kappa = 2$ and NPR window for $\kappa = 3$.

4.3 Efficient implementation

4.3.1 Transceiver based on polyphase filters

Transmitting bank

The aim of this subsection is to present an implementation of the wavelet transceiver using polyphase filters at the transmitting filter bank. To this goal, let us formulate (4.2) in the z-domain using matrices. Let $P(z) = \sum_{n=0}^{N-1} p[n] \cdot z^{-n}$ be the $(N-1)$th-order prototype filter transfer function, which can be expressed by means of the $2M$ type-I polyphase decomposition [115]:

$$P(z) = \sum_{\ell=0}^{2M-1} z^{-\ell} G_\ell\left(z^{2M}\right), \tag{4.14}$$

where $G_\ell\left(z^{2M}\right)$ is the z-transform of $g_\ell[n] = p[2nM+\ell]$, $\ell = 0, \cdots, (2M-1)$ and M denotes the number of subchannels.

From the above equation, the transmitting filters $F_k(z)$ can be expressed in the following way:

$$F_k(z) = \sum_{n=0}^{N-1} f_k[n] z^{-n} = \sum_{\ell=0}^{2M-1} c_{\ell,k}^f \cdot \cos\theta_k \cdot z^{-\ell} \cdot G_\ell\left(-z^{2M}\right), \tag{4.15}$$

where

$$c_{\ell,k}^f = \sqrt{\frac{2}{M}} \cdot \cos\left[\frac{\pi}{M}\left(k+\frac{1}{2}\right)\left(\ell+\frac{M+1}{2}\right)\right], \tag{4.16}$$

for $0 \leq k \leq (M-1)$. The above relation is the result of the periodicity of the cosine function which satisfies [119]:

$$c_{\ell+2mM,k}^f = (-1)^m c_{\ell,k}^f.$$

The transmitting filters of (4.15) are written in a matrix form as:

$$\mathbf{f}^T(z) = \left[\begin{array}{cccc} F_0(z) & F_1(z) & \cdots & F_{M-1}(z) \end{array}\right] = \mathbf{t}^T(z) \cdot \left[\begin{array}{cc} \mathbf{g}_0\left(z^{2M}\right) & z^{-M}\mathbf{g}_1\left(z^{2M}\right) \end{array}\right] \cdot \hat{\mathbf{C}}_{Tx}, \tag{4.17}$$

where

$$\left[\hat{\mathbf{C}}_{Tx}\right]_{\ell,k} = c_{\ell,k}^f \cdot \cos\theta_k, \tag{4.18}$$

$$\mathbf{t}(z) = \left[\begin{array}{cccc} 1 & z^{-1} & \cdots & z^{-(M-1)} \end{array}\right]^T, \tag{4.19}$$

and $\mathbf{g}_0$ and $\mathbf{g}_1$ are $M \times M$ diagonal matrices with elements

$$[\mathbf{g}_0(z)]_{k,k} = G_k(-z), \qquad [\mathbf{g}_1(z)]_{k,k} = G_{k+M}(-z). \tag{4.20}$$

Let us partition $\hat{\mathbf{C}}_{Tx}$ as

$$\hat{\mathbf{C}}_{Tx} = \begin{bmatrix} \mathbf{B}_0 \\ \mathbf{B}_1 \end{bmatrix} \cdot \mathbf{\Theta}, \tag{4.21}$$

where $\mathbf{\Theta}$ is an $M \times M$ diagonal matrix with elements $[\mathbf{\Theta}]_{k,k} = \cos(\theta_k)$, $\mathbf{B}_0$ and $\mathbf{B}_1$ are also $M \times M$ matrices, being the elements of the first one given by

$$[\mathbf{B}_0]_{\ell,k} = c^{4e}_{\ell,k} \cdot \cos(\lambda_{k0}) + s^{4e}_{\ell,k} \cdot \sin(\lambda_{k0}), \tag{4.22}$$

with

$$[\mathbf{C}_{4e}]_{\ell,k} = c^{4e}_{\ell,k} = \sqrt{\frac{2}{M}} \cos\left(\left(k+\frac{1}{2}\right)\frac{\pi}{M} \cdot \left(\ell+\frac{1}{2}\right)\right), \tag{4.23}$$

$$[\mathbf{S}_{4e}]_{\ell,k} = s^{4e}_{\ell,k} = \sqrt{\frac{2}{M}} \sin\left(\left(k+\frac{1}{2}\right)\frac{\pi}{M} \cdot \left(\ell+\frac{1}{2}\right)\right), \tag{4.24}$$

$$[\mathbf{\Lambda}_{C0}]_{k,k} = \cos(\lambda_{k0}) = \cos\left(\left(k+\frac{1}{2}\right)\frac{\pi}{2}\right), \tag{4.25}$$

$$[\mathbf{\Lambda}_{S0}]_{k,k} = \sin(\lambda_{k0}) = \sin\left(\left(k+\frac{1}{2}\right)\frac{\pi}{2}\right). \tag{4.26}$$

Notice that $\mathbf{C}_{4e}$ and $\mathbf{S}_{4e}$ are, respectively, the type-IV even discrete cosine transform (DCT4e) and the type-IV even discrete sine transform (DST4e) matrices [120, 121].
Regarding the second matrix $\mathbf{B}_1$, each of its elements can be expressed as

$$[\mathbf{B}_1]_{\ell,k} = c^{4e}_{\ell,k} \cdot \cos(\lambda_{k1}) + s^{4e}_{\ell,k} \cdot \sin(\lambda_{k1}), \tag{4.27}$$

where

$$[\mathbf{\Lambda}_{C1}]_{k,k} = \cos(\lambda_{k1}) = \cos\left(\left(k+\frac{1}{2}\right)\frac{3\pi}{2}\right), \tag{4.28}$$

$$[\mathbf{\Lambda}_{S1}]_{k,k} = \sin(\lambda_{k1}) = \sin\left(\left(k+\frac{1}{2}\right)\frac{3\pi}{2}\right). \tag{4.29}$$

Thus, matrices $\mathbf{B}_0$ and $\mathbf{B}_1$ can be written as given below:

$$\mathbf{B}_0 = \mathbf{C}_{4e} \cdot \mathbf{\Lambda}_{C0} - \mathbf{S}_{4e} \cdot \mathbf{\Lambda}_{S0}, \tag{4.30a}$$

$$\mathbf{B}_1 = \mathbf{C}_{4e} \cdot \mathbf{\Lambda}_{C1} - \mathbf{S}_{4e} \cdot \mathbf{\Lambda}_{S1}. \tag{4.30b}$$

Important properties are $\mathbf{\Lambda}_{S0} = \mathbf{\Gamma} \cdot \mathbf{\Lambda}_{C0}$, $\mathbf{\Lambda}_{C1} = -\mathbf{\Lambda}_{C0}$, $\mathbf{\Lambda}_{S1} = \mathbf{\Gamma} \cdot \mathbf{\Lambda}_{C0}$, and $\mathbf{S}_{4e} \cdot \mathbf{\Gamma} = \mathbf{J} \cdot \mathbf{C}_{4e}$, where $\mathbf{\Gamma}$ is an $M \times M$ diagonal matrix with elements $[\mathbf{\Gamma}]_{k,k} = (-1)^k$, for $0 \leq k \leq (M-1)$, and $\mathbf{J}$ denotes the counter-identity matrix.
Using the above properties, we have

$$\mathbf{B}_0 = (\mathbf{I} - \mathbf{J}) \cdot \mathbf{C}_{4e} \cdot \mathbf{\Lambda}_{C0}, \tag{4.31a}$$

$$\mathbf{B}_1 = (-\mathbf{I} - \mathbf{J}) \cdot \mathbf{C}_{4e} \cdot \mathbf{\Lambda}_{C0}. \tag{4.31b}$$

where matrix $\mathbf{I}$ denotes the identity matrix. As a result, the transmitting filters can be expressed as follows:

$$\mathbf{f}^T(z) = \mathbf{t}^T(z) \cdot \begin{bmatrix} \mathbf{g}_0\left(z^{2M}\right) & z^{-M}\mathbf{g}_1\left(z^{2M}\right) \end{bmatrix} \cdot \begin{bmatrix} (\mathbf{I} - \mathbf{J}) \\ (-\mathbf{I} - \mathbf{J}) \end{bmatrix} \cdot \mathbf{C}_{4e} \cdot \mathbf{\Lambda}_{C0} \cdot \mathbf{\Theta}. \tag{4.32}$$

Receiving bank

Taking the z transform in (4.3), we obtain the system function for the receiving filters $H_k(z)$:

$$H_k(z) = \sum_{n=0}^{N-1} h_k[n] z^{-n} = \sum_{\ell=0}^{2M-1} c_{k,\ell}^h \cdot \cos\theta_k \cdot z^{-\ell} \cdot G_\ell\left(-z^{2M}\right), \tag{4.33}$$

where

$$c_{k,\ell}^h = \sqrt{\frac{2}{M}} \cdot \cos\left[\frac{\pi}{M}\left(k + \frac{1}{2}\right)\left(N - 1 - \ell + \frac{M+1}{2}\right)\right].$$

Using matrices, the transmitting filters can be expressed as

$$\mathbf{h}(z) = \begin{bmatrix} H_0(z) \\ H_1(z) \\ \vdots \\ H_{M-1}(z) \end{bmatrix} = \hat{\mathbf{C}}_{Rx} \cdot \begin{bmatrix} \mathbf{g}_0\left(z^{2M}\right) \\ z^{-M}\mathbf{g}_1\left(z^{2M}\right) \end{bmatrix} \cdot \mathbf{t}(z), \tag{4.34}$$

with

$$\left[\hat{\mathbf{C}}_{Rx}\right]_{k,\ell} = c_{k,\ell}^h \cdot \cos\theta_k. \tag{4.35}$$

Notice that now the fast implementation of the receiving system depends on the value of κ ($N = 2\kappa M$). As it has been mentioned above, the standard recommends two different overlapping factors: $\kappa = 2$ and $\kappa = 3$. Operating as in the previous subsection, the following result is obtained:

$$\hat{\mathbf{C}}_{Rx} = \mathbf{\Theta} \cdot \mathbf{\Lambda}_{C0} \cdot \mathbf{C}_{4e} \cdot \begin{bmatrix} \zeta(\mathbf{I} + \mathbf{J}) & \zeta(\mathbf{I} - \mathbf{J}) \end{bmatrix}, \tag{4.36}$$

where $\zeta = 1$ for $\kappa = 2$, and $\zeta = -1$ for $\kappa = 3$. Therefore, the final expression that characterizes the proposed receiver is the following:

$$\mathbf{h}(z) = \mathbf{\Theta} \cdot \mathbf{\Lambda}_{C0} \cdot \mathbf{C}_{4e} \cdot \begin{bmatrix} \zeta(\mathbf{I}+\mathbf{J}) & \zeta(\mathbf{I}-\mathbf{J}) \end{bmatrix} \cdot \begin{bmatrix} \mathbf{g}_0\left(z^{2M}\right) \\ z^{-M}\mathbf{g}_1\left(z^{2M}\right) \end{bmatrix} \mathbf{t}(z). \tag{4.37}$$

The implementation of the whole transceiver is shown in Fig. 4.6. In this figure, the matrix $\mathbf{\Lambda}_{cn} = \sqrt{2} \cdot \mathbf{\Theta} \cdot \mathbf{\Lambda}_{C0}$, where

$$[\mathbf{\Lambda}_{C0}]_{k,k} = \cos(\lambda_{k0}) = \cos\left(\left(k+\frac{1}{2}\right)\frac{\pi}{2}\right). \tag{4.38}$$

This leads to $[\mathbf{\Lambda}_{cn}]_{k,k} = \pm 1$. To compensate for the constant $\sqrt{2}$, its inverse value is multiplying both the transmitting and the receiving signals. As it can be appreciated in Fig. 4.6, the output signals of the corresponding transmitting polyphase filters are added, whereas on the receiving side, each pair of polyphase filters are fed with the same input signal.

4.3.2 Transceiver based on lattice structures

The prototypes proposed in the standard are linear-phase filters, and the same prototypes can be employed for both the transmitting and the receiving sides. Let us assume the case of $N = 2\kappa M$ for $M = 512$ and $\kappa = 2$. In this case, the Type-I polyphase components of each filter recommended in [10] satisfy the following condition:

$$\tilde{G}_i(z) \cdot G_i(z) + \tilde{G}_{i+M}(z) \cdot G_{i+M}(z) = 1, \tag{4.39}$$

where $\tilde{G}(z) = G^*\left(z^{-1}\right)$, which means that the filter bank is paraunitary[1]. This leads to a joint implementation of pairs of filters, i.e., each pair of polyphase filters can be implemented at the same time using a single lattice structure [122].

Each polyphase filter of Fig. 4.7a has a length equals $2\kappa - 1 = 3$, and the intermediate coefficient is zero. Therefore, the ith and $i+M$th polyphase filters can be expressed respectively as

$$G_i(-z^2) = a + bz^{-2}, \quad G_{i+M}(-z^2) = c + dz^{-2}. \tag{4.40}$$

The lattice coefficients of the structure of Fig. 4.7b are obtained as [122]

$$v_{2n} = \frac{-d}{\sqrt{b^2+d^2}}, \qquad \hat{v}_{2n} = \frac{b}{\sqrt{b^2+d^2}}, \tag{4.41}$$

$$r_{0n} = \frac{-ad+bc}{\sqrt{b^2+d^2}}, \qquad s_{0n} = -\sqrt{b^2+d^2}. \tag{4.42}$$

Each normalized lattice structure of Fig. 4.7b has six multipliers. As alternative, two equivalent denormalized lattices, which require four multipliers, can be obtained [122]. In the first denormalized

[1] This only holds for PR system

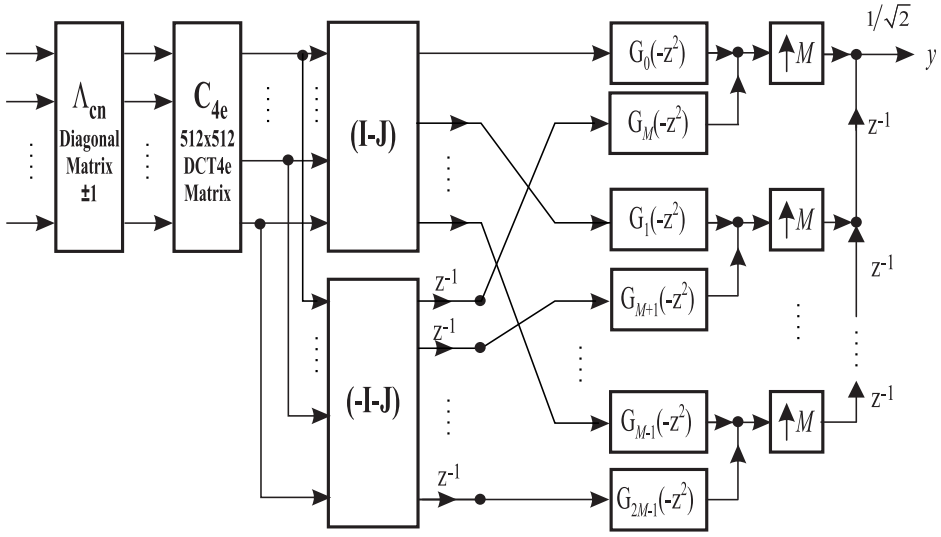

(a) Tansmitter

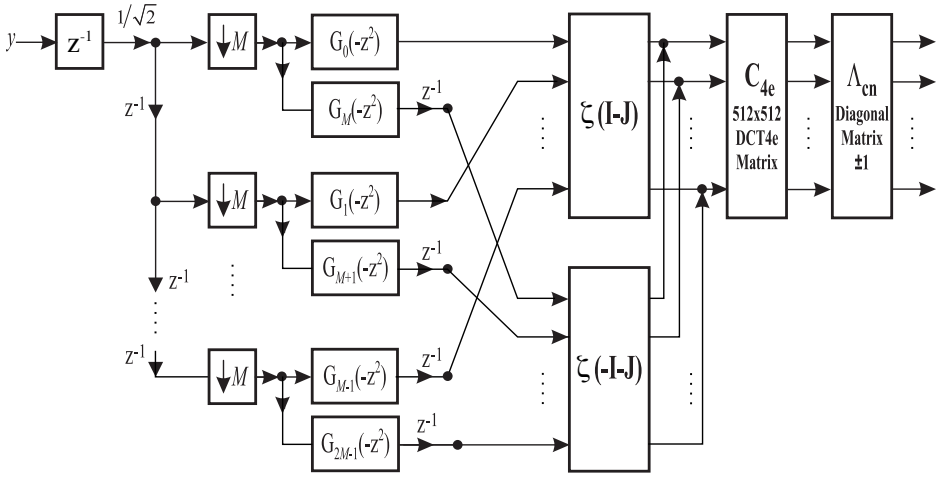

(b) Receiver

Fig. 4.6 Block diagram of the baseband Wavelet OFDM transceiver implemented with polyphase filters ($M = 512$).

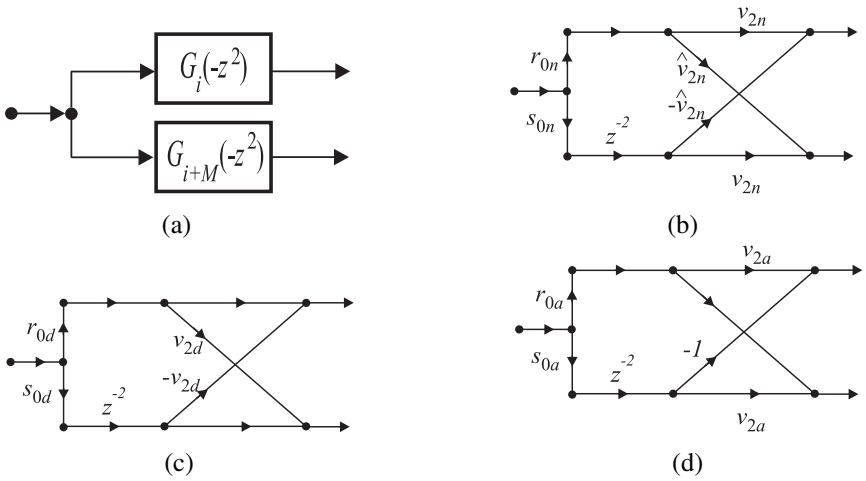

Fig. 4.7 (a) Pair of polyphase filters. (b) Implementation using normalized lattice structure. (c) Implementation using denormalized lattice structure requiring four multipliers. (d) Alternative implementation using denormalized lattice structure also requiring four multipliers.

structure depicted in Fig. 4.7c, the coefficients are calculated as:

$$v_{2d} = \frac{\hat{v}_{2n}}{v_{2n}}, \qquad r_{0d} = r_{0n} \cdot v_{2n}, \qquad s_{0d} = s_{0n} \cdot v_{2n}. \tag{4.43}$$

Similarly, the coefficients of the second denormalized structure (Fig. 4.7d) are given by

$$v_{2a} = \frac{v_{2n}}{\hat{v}_{2n}}, \qquad r_{0a} = r_{0n} \cdot \hat{v}_{2n}, \qquad s_{0a} = s_{0n} \cdot \hat{v}_{2n}. \tag{4.44}$$

4.3.3 Transceiver based on butterfly structures

Due to wavelet OFDM is based on ELT, the whole system can be efficiently implemented by means of butterfly structures with symmetric matrices, which have the form [26, 123]

$$\mathbf{D}_k = \begin{bmatrix} -\mathbf{C}_k & \mathbf{S}_k\mathbf{J} \\ \mathbf{J}\mathbf{S}_k & \mathbf{J}\mathbf{C}_k\mathbf{J} \end{bmatrix}, \tag{4.45}$$

where the submatrices $\mathbf{C}_k$ and $\mathbf{S}_k$ are diagonals with elements

$$[\mathbf{C}_k]_{\ell,\ell} = \cos(\vartheta_{\ell,k}), \qquad [\mathbf{S}_k]_{\ell,\ell} = \sin(\vartheta_{\ell,k}), \tag{4.46}$$

for $0 \leq \ell \leq \left(M/2 - 1\right)$. The values of each $\theta_{\ell,k}$ term are obtained from the prototype filter coefficients, as has been shown (4.9). These butterfly matrices have nonzero values only on their diagonals and antidiagonals, and they are identical for both the inverse and the direct ELT structures. Furthermore, using the property of the butterfly structures shown in [123], the number of operations are reduced if

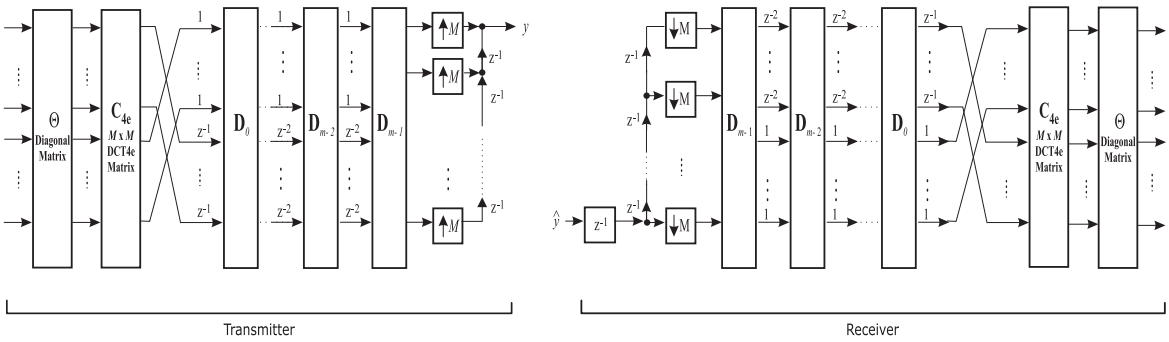

Fig. 4.8 Block diagram of the ELT-MCM transceiver implemented with butterfly structures.

all the coeficients in $\mathbf{D}_k$, $k > 0$, are scaled. In this case, the new matrices $\bar{\mathbf{D}}_k$ are defined as:

$$\bar{\mathbf{D}}_k \equiv diag\left\{\mathbf{C}_k^{-1},\, \mathbf{J}\mathbf{C}_k^{-1}\mathbf{J}\right\}\mathbf{D}_k, \tag{4.47}$$

for $1 \leq k \leq m-1$, and

$$\bar{\mathbf{D}}_0 \equiv diag\left\{\prod_{k=1}^{m-1}\mathbf{C}_k,\, \mathbf{J}\prod_{k=1}^{m-1}\mathbf{C}_k^{-1}\mathbf{J}\right\}\mathbf{D}_0. \tag{4.48}$$

Fig. 4.8 shows the efficient implementation using cascaded orthogonal butterflies and pure delays. In this figure, $\mathbf{C}_{4e}$ is a type-IV even discrete cosine transform (DCT4e) matrix and $\boldsymbol{\Theta}$ is an $M \times M$ diagonal matrix with elements

$$[\boldsymbol{\Theta}]_{k,k} = \cos(\theta_k). \tag{4.49}$$

4.4 Channel equalization

One of the main drawbacks of the FBMC systems is the channel equalization process, which is not as understandable and efficient as for the standardized DFT-based MCM. In [38], one of the simplest equalizer to correct the channel effects for CMFB systems is proposed and referred to as ASCET.This equalization technique compensates for the channel distortion using an analysis sine modulated filter bank (SMFB) system connected in parallel to the analysis CMFB. Besides, per-subcarrier equalizer (PSE) is included at each receiving cosine and sine modulated filter banks. The use of ASCET for PLC is proposed in [37], but not for the ELT-MCM system deployed by the wavelet OFDM physical layer of [10]. In this section, an appropriate scheme for this system is derived.

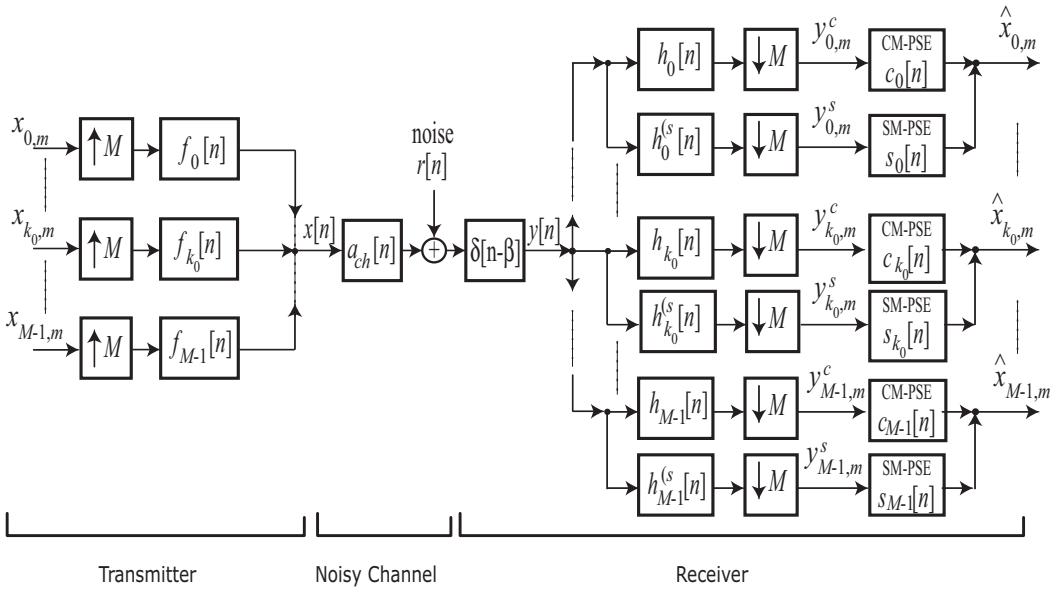

Fig. 4.9 General block diagram of a baseband ELT-MCM with ASCET.

4.4.1 Efficient implementation

Polyphase filters

Fig. 4.9 shows the general block diagram of the ELT-MCM transceiver. In this system, the impulse response of the filters of the analysis SMFB is given by

$$h_k^s[n] = \sqrt{\frac{2}{M}} \cdot p[n] \cdot \sin\left[\frac{\pi}{M}\left(k+\frac{1}{2}\right)\left(N-1-n+\frac{M+1}{2}\right)\right] \cdot \cos(\theta_k). \tag{4.50}$$

With the aim of deriving a matrix formulation for the above filter bank with polyphase filters, the system function $H_k^s(z)$ of each filter of (4.50) is considered:

$$H_k^s(z) = \sum_{n=0}^{N-1} h_k^s[n] z^{-n} = \sum_{\ell=0}^{2M-1} s_{k,\ell}^h \cdot \cos\theta_k \cdot z^{-\ell} \cdot G_\ell\left(-z^{2M}\right), \tag{4.51}$$

for $0 \leq k \leq (M-1)$, and

$$s_{k,\ell}^h = \sqrt{\frac{2}{M}} \cdot \sin\left[\frac{\pi}{M}\left(k+\frac{1}{2}\right) \cdot \left(N-1-\ell+\frac{M+1}{2}\right)\right]. \tag{4.52}$$

Operating as previously, a compact expression for the analysis SMFB is derived:

$$\mathbf{h}^s(z) = \boldsymbol{\Theta} \cdot \boldsymbol{\Lambda}_{C0} \cdot \mathbf{S}_{4e} \cdot \begin{bmatrix} \boldsymbol{\zeta}(\mathbf{I}-\mathbf{J}) & \boldsymbol{\zeta}(\mathbf{I}+\mathbf{J}) \end{bmatrix} \begin{bmatrix} \mathbf{g}_0\left(z^{2M}\right) \\ z^{-M}\mathbf{g}_1\left(z^{2M}\right) \end{bmatrix} \mathbf{t}(z). \tag{4.53}$$

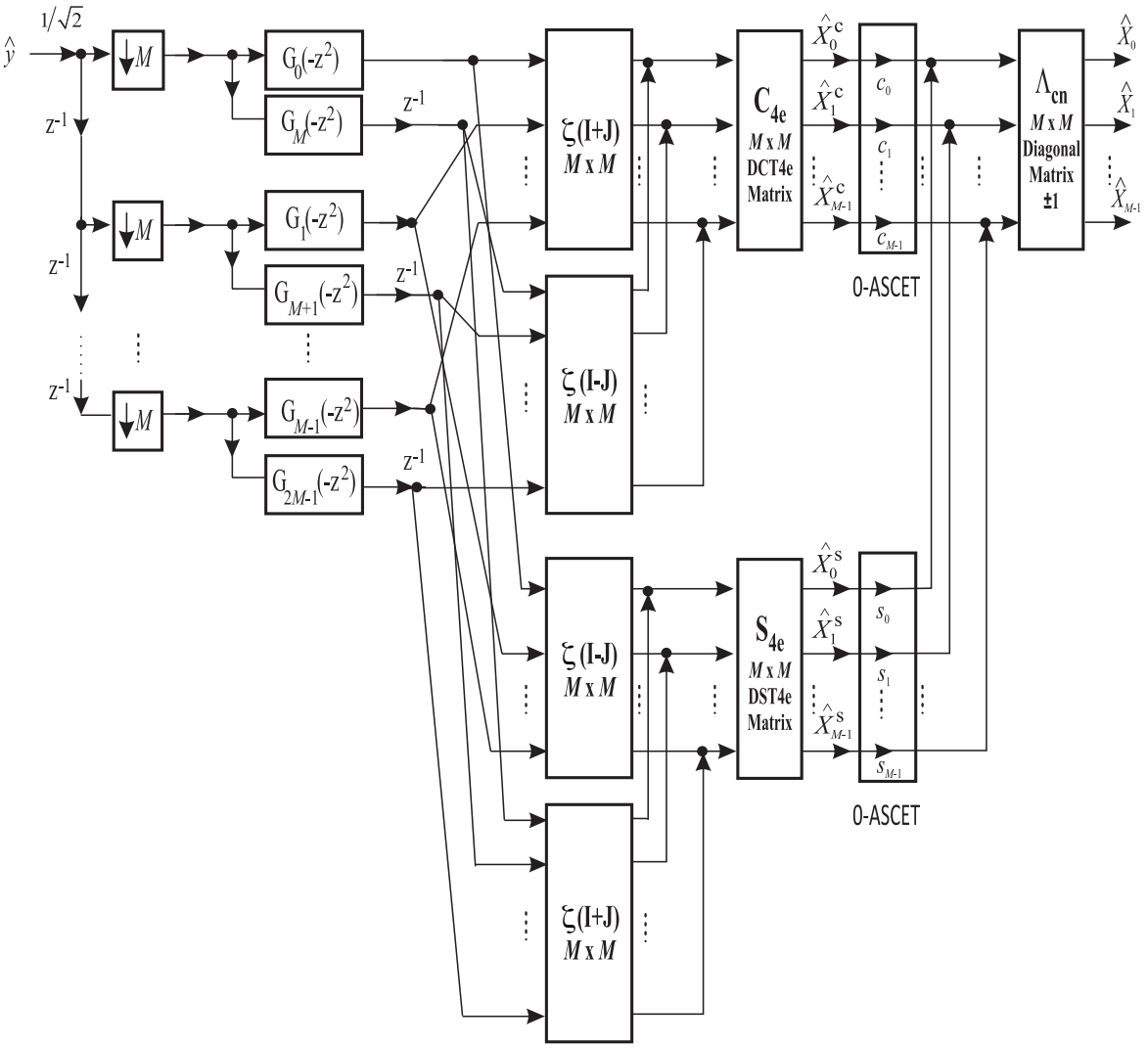

Fig. 4.10 Fast implementation of the baseband ELT-MCM receiver including a 0–ASCET with polyphase filters.

Fig. 4.10 depicts the whole receiver implemented with polyphase filters. It should be noted that there are some common terms in these expressions that can be grouped in order to implement them simultaneously and, therefore, to reduce the number of operations. In addition, since the prototype filter used for both analysis CMFB and SMFB is the same, the lattice structures derived above can be directly applied from the former to the latter.

Butterfly structures

The implementation using butterfly structures for the ELT-based SMFB can be found in [124]. Considering the proposed SMFB of the receiver and based on the facts that $h_k^s[n] = (-1)^{k+m} f_k[n]/\cos(\theta_k)$

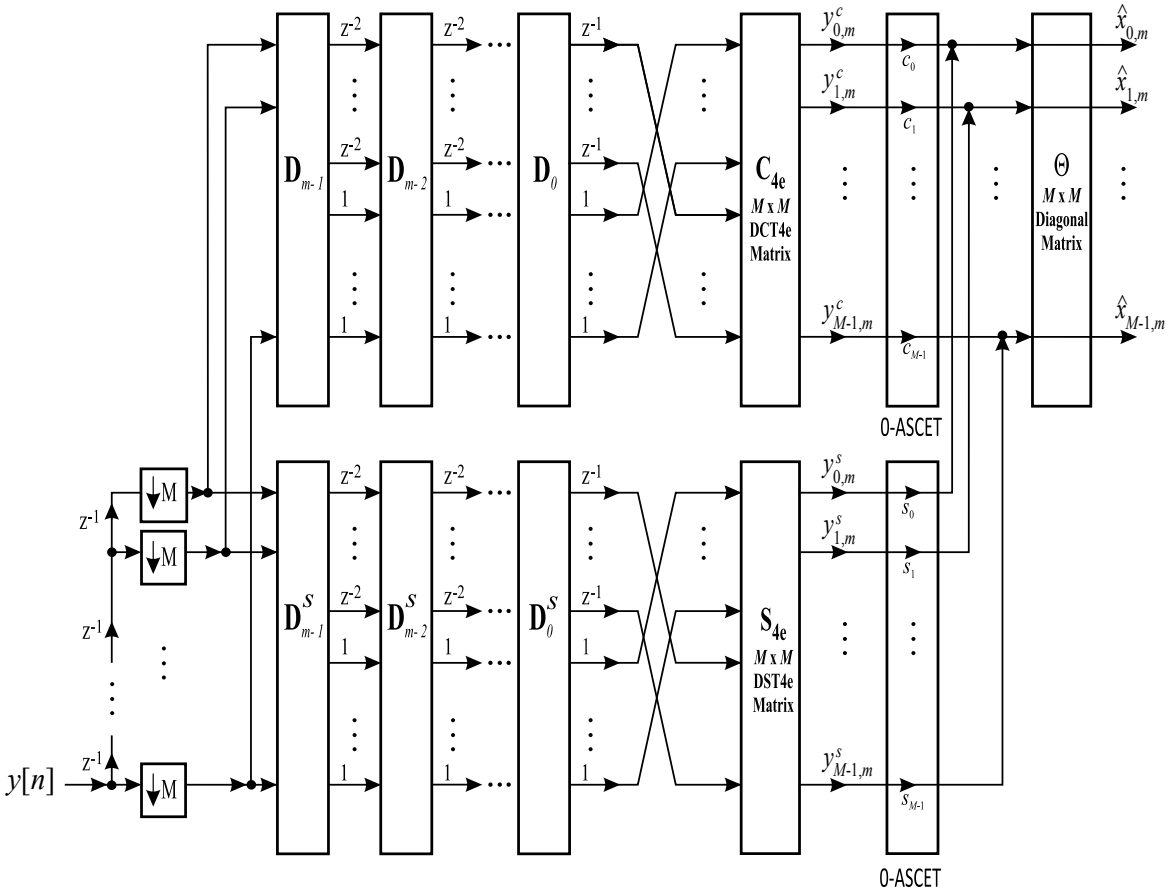

Fig. 4.11 Fast implementation of the baseband ELT-MCM receiver including a 0–ASCET with butterfly structures.

and that $f_k^s[n] = (-1)^{k+m} h_k^c[n]/\cos(\theta_k)$, it can be derived the following butterfly matrices:

$$\mathbf{D}_k^s = \begin{bmatrix} -\mathbf{C}_k & -\mathbf{S}_k\mathbf{J} \\ -\mathbf{J}\mathbf{S}_k & \mathbf{J}\mathbf{C}_k\mathbf{J} \end{bmatrix}, \tag{4.54}$$

which can be used to implement this part of the receiver [124]. The ELT structure with the SMFB employs a Type-IV even discrete sine transform (DST4e) instead of the DCT4e. Moreover, it is shown in [124, subsect 3.2] an alternative approach for obtaining the SMFB using the original butterfly structure of the ELT. The whole receiver is represented in Fig. 4.11.

4.4.2 Per-subcarrier equalizer

Once the SMFB is defined, we focus now on the equalizer block $E(z)$, which is included at each output of both the analysis/receiving CMFB and SMFB. These equalization blocks are referred to as cosine-modulated per-subcarrier equalizer (CM-PSE) and sine-modulated per-subcarrier equalizer (CM-PSE), respectively.

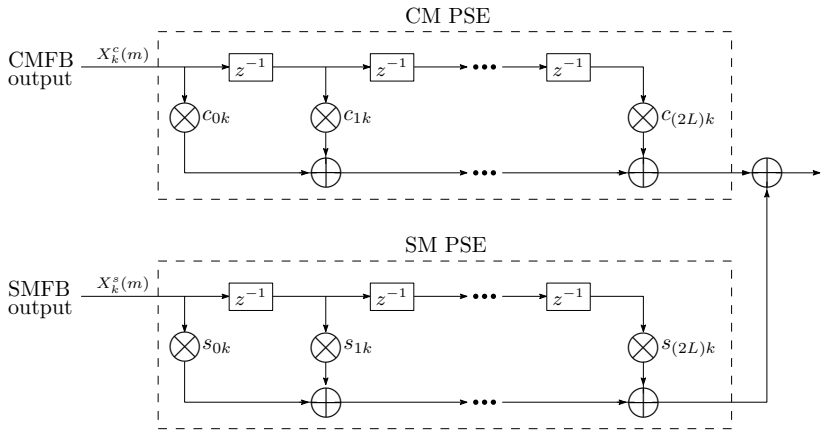

Fig. 4.12 General block diagram of each per-subcarrier equalizing structure of the L-ASCET.

Following the minimum mean square error (MMSE) criterion and assuming AWGN [37], the kth subchannel equalizer block is defined as follows:

$$E_k(\omega) = \frac{H_{ch}^*(\omega)}{|H_{ch}(\omega)|^2 + \frac{1}{\text{SNR}}}, \tag{4.55}$$

where $H_{ch}(\omega)$ is the channel frequency response and SNR is the signal-to-noise ratio.

0-ASCET

The complex function $E_k(\omega)$ can be expressed as

$$E_k(\omega)|_{\omega=(2k+1)\frac{2\pi}{4M}} = c_k - j \cdot s_k,$$

for $0 \leq k < M$, where c_k and s_k are the real and the imaginary part of E_k, respectively. The simplest way to implement this kind of equalizer is only with one coefficient per-subcarrier, in other words, the transmission channel effects are compensated for by multiplying each output of the CM and SM receiving filter bank by the constant numbers c_k and s_k, respectively (see Figs. 4.10 and 4.11). This equalizer is referred to as zero-order ASCET (0-ASCET).

1-ASCET

As it is claimed in [38], the 0-ASCET is adequate for channels with no fast variations within the subchannel bandwidth. Unfortunately, this is not the case of the PLC channel and, therefore, it could be necessary to increase the order of the equalizer to improve the system performance. These equalizers are called L_A-order ASCET (L_A-ASCET). In this case, the multiplications employed in 0-ASCET must be changed by FIR filters, as shown in Fig. 4.12.

Following the development presented in [125], a 3-tap FIR filter can be defined as:

$$E_k(e^{j\omega}) = \varepsilon_{0k}e^{j\omega} + \varepsilon_{1k} + \varepsilon_{2k}e^{-j\omega}, \tag{4.56}$$

which corresponds to a non causal form; nonetheless, in practice, a causal version is employed for each equalizing structure[2]. In order to obtain the the value of the coefficients of each FIR filter, some frequency points are selected at each k subchannel. Following the steps of [37, 125, 126], the frequency points $\omega = 0$, $\frac{\pi}{2}$, π, for even subbands, and $\omega = -\pi$, $-\frac{\pi}{2}$, 0, for odd subbands, are chosen. As a result, the following equations are derived:

- Even subbands

$$E_k\left(e^{j\omega}\right) = \begin{cases} \varepsilon_{0k} + \varepsilon_{1k} + \varepsilon_{2k} = \eta_{0k}, & \omega = 0, \\ j\varepsilon_{0k} + \varepsilon_{1k} - j\varepsilon_{2k} = \eta_{1k}, & \omega = \frac{\pi}{2}, \\ -\varepsilon_{0k} + \varepsilon_{1k} - \varepsilon_{2k} = \eta_{2k}, & \omega = \pi. \end{cases} \tag{4.57}$$

- Odd subbands

$$E_k\left(e^{j\omega}\right) = \begin{cases} -\varepsilon_{0k} + \varepsilon_{1k} - \varepsilon_{2k} = \eta_{0k}, & \omega = -\pi, \\ -j\varepsilon_{0k} + \varepsilon_{1k} + j\varepsilon_{2k} = \eta_{1k}, & \omega = -\frac{\pi}{2}, \\ \varepsilon_{0k} + \varepsilon_{1k} + \varepsilon_{2k} = \eta_{2k}, & \omega = 0. \end{cases} \tag{4.58}$$

In these previous equations, k denotes the subchannel under consideration, and

$$\eta_{ik} = \frac{H_{ch}^{*}\left(e^{j\frac{\pi}{4M}(2k+i)}\right)}{\left|H_{ch}\left(e^{j\frac{\pi}{4M}(2k+i)}\right)\right|^2 + \frac{1}{\mathrm{SNR}}}, \tag{4.59}$$

for $i = 0, 1, 2$. Then, the 1-ASCET coefficients can be obtained as follows

$$\varepsilon_{0k} = \pm\frac{1}{2}\left(\frac{\eta_{0k} - \eta_{2k}}{2} - j\left(\eta_{1k} - \frac{\eta_{0k} + \eta_{2k}}{2}\right)\right), \tag{4.60a}$$

$$\varepsilon_{1k} = \frac{\eta_{0k} + \eta_{2k}}{2}, \tag{4.60b}$$

$$\varepsilon_{2k} = \pm\frac{1}{2}\left(\frac{\eta_{0k} - \eta_{2k}}{2} + j\left(\eta_{1k} - \frac{\eta_{0k} + \eta_{2k}}{2}\right)\right), \tag{4.60c}$$

where the positive signs stand for even subbands and the negative ones for odd subbands. Since ε_{0k}, ε_{1k} and ε_{2k} are complex numbers, we have:

$$\varepsilon_{ik} = c_{ik} - js_{ik}, \tag{4.61}$$

where the real c_{ik} and the imaginary s_{ik} parts are the kth CM-PSE and SM-PSE, respectively.

[2] $e^{-j\omega}E(e^{j\omega})$.

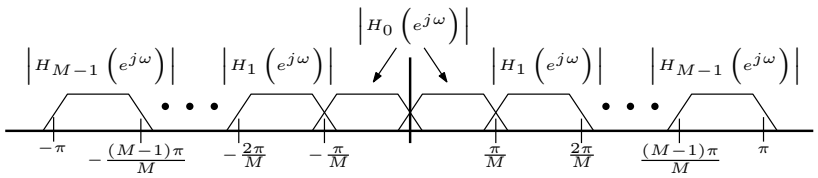

(a) Transmitter

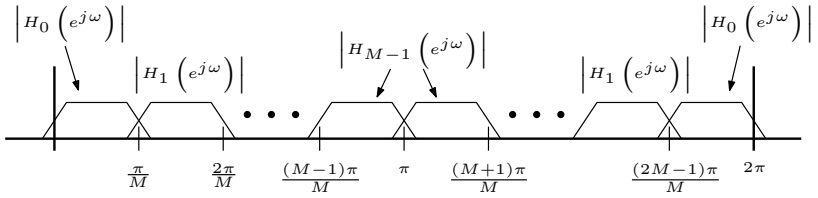

(b) Receiver

Fig. 4.13 (a) Magnitude responses for the receiving filters, (b) equivalent magnitude responses.

2-ASCET

As can be inferred from the previous clause, the higher order of the equalizer, the higher performance; however, the computational complexity of the receiver also increases. Therefore, with the aim at analyzing the trade-off between equalizer complexity and system performance, the expressions to obtain the 2-ASCET coefficients are developed.

Following a similar reasoning to that described above, the 2-ASCET can be expressed as a 5-tap FIR filter[3]

$$E(e^{j\omega}) = \varepsilon_0 e^{j2\omega} + \varepsilon_1 e^{j\omega} + \varepsilon_2 + \varepsilon_3 e^{-j\omega} + \varepsilon_4 e^{-2j\omega}. \tag{4.62}$$

It is well known that the analysis stage of the CMFB consists of a set of M filters (H_i, $i = 0, 1, \ldots, M-1$), which are obtained from the prototype filter. Fig. 4.13 shows the position of each subband along the frequency axis (right-shifted version, the amount of right-shift being $\pi/2M$). As it can bee seen, the bandwidth of each subbband is equal to $\frac{\pi}{M}$ and they are symmetric about π. As in the previous case, some frequency points are needed to calculated the filter coefficients. Focusing on even subbands, the frequency points are located at normalized pulses $\omega = \left\{0, \frac{\pi}{4}, \frac{\pi}{2}, \frac{3\pi}{4}, \pi\right\}$, while the frequencies are located at $\omega = \left\{-\pi, -\frac{3\pi}{4}, -\frac{\pi}{2}, -\frac{\pi}{4}, 0\right\}$ for odd subbands. The process has been depicted in Fig. 4.14.

Finally, the system of equations for the kth subband is the following:

- Even subbands

[3] In practice, the causal form is employed: $e^{-2j\omega}E(e^{j\omega})$.

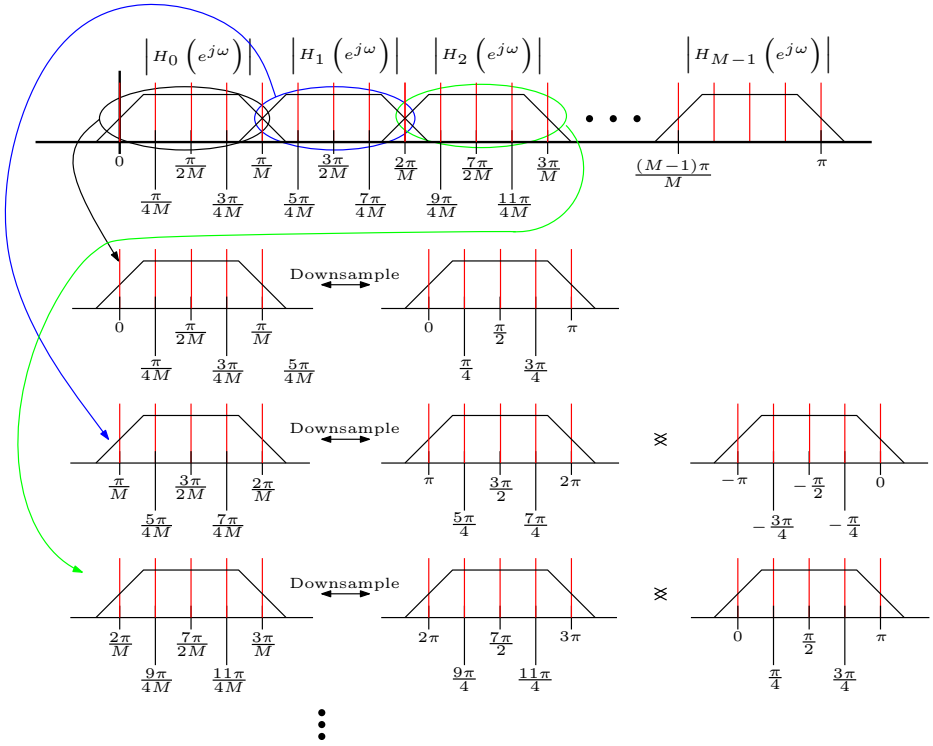

Fig. 4.14 Frequency points chosen for 2-ASCET.

$$E_k\left(e^{j\omega}\right) = \begin{cases} \varepsilon_{0k} + \varepsilon_{1k} + \varepsilon_{2k} + \varepsilon_{3k} + \varepsilon_{4k} = \eta_{0k}, & \omega = 0, \\ j\varepsilon_{ok} + \alpha\varepsilon_{1k} + \varepsilon_{2k} + \beta\varepsilon_{3k} - j\varepsilon_{4k} = \eta_{1k}, & \omega = \frac{\pi}{4}, \\ -\varepsilon_{0k} + j\varepsilon_{1k} + \varepsilon_{2k} - j\varepsilon_{3k} - \varepsilon_{4k} = \eta_{2k}, & \omega = \frac{\pi}{2}, \\ -j\varepsilon_{0k} - \beta\varepsilon_{1k} + \varepsilon_{2k} - \alpha\varepsilon_{3k} + j\varepsilon_{4k} = \eta_{3k}, & \omega = \frac{3\pi}{4}, \\ \varepsilon_{0k} - \varepsilon_{1k} + \varepsilon_{2k} - \varepsilon_{3k} + \varepsilon_{4k} = \eta_{4k}, & \omega = \pi. \end{cases} \tag{4.63}$$

- Odd subbands

$$E_k\left(e^{j\omega}\right) = \begin{cases} \varepsilon_{0k} - \varepsilon_{1k} + \varepsilon_{2k} - \varepsilon_{3k} + \varepsilon_{4k} = \eta_{0k}, & \omega = -\pi, \\ j\varepsilon_{ok} - \alpha\varepsilon_{1k} + \varepsilon_{2k} - \beta\varepsilon_{3k} - j\varepsilon_{4k} = \eta_{1k}, & \omega = -\frac{3\pi}{4}, \\ -\varepsilon_{0k} - j\varepsilon_{1k} + \varepsilon_{2k} + j\varepsilon_{3k} - \varepsilon_{4k} = \eta_{2k}, & \omega = -\frac{\pi}{2}, \\ -j\varepsilon_{0k} + \beta\varepsilon_{1k} + \varepsilon_{2k} + \alpha\varepsilon_{3k} + j\varepsilon_{4k} = \eta_{3k}, & \omega = -\frac{\pi}{4}, \\ \varepsilon_{0k} + \varepsilon_{1k} + \varepsilon_{2k} + \varepsilon_{3k} + \varepsilon_{4k} = \eta_{4k}, & \omega = 0, \end{cases} \tag{4.64}$$

with

$$\eta_{ik} = \frac{H_{ch}^{*}\left(e^{j\frac{\pi}{4M}(4k+i)}\right)}{\left|H_{ch}\left(e^{j\frac{\pi}{4M}(4k+i)}\right)\right|^2 + \frac{1}{\mathrm{SNR}}}, \quad i = 0,1,2,3,4, \tag{4.65}$$

and

$$\alpha = \frac{\sqrt{2}}{2}(1+j), \tag{4.66}$$

$$\beta = \frac{\sqrt{2}}{2}(1-j). \tag{4.67}$$

Solving equations (4.63) and (4.64), we obtain the coefficients of $E_k(z)$

$$\begin{aligned}\varepsilon_{0k} =& \frac{1}{4}\Bigg[(\eta_{1k} - 2\eta_{2k} + \eta_{3k}) + \frac{\sqrt{2}}{2}(-\eta_{0k} + 2\eta_{1k} - 2\eta_{2k} + 2\eta_{3k} - \eta_{4k}) \\ & + j\left(-\eta_{1k} + \eta_{3k} + \frac{\sqrt{2}}{2}(\eta_{ok} - \eta_{4k})\right)\Bigg],\end{aligned} \tag{4.68}$$

$$\varepsilon_{1k} = \pm\frac{1}{4}\left[\eta_{0k} - \eta_{4k} - j\left((\eta_{0k} - 2\eta_{1k} + 2\eta_{2k} - 2\eta_{3k\cdot} + \eta_{4k}) \cdot \left(1+\sqrt{2}\right)\right)\right], \tag{4.69}$$

$$\varepsilon_{2k} = \frac{1}{2}\left[(\eta_{0k} - \eta_{1k} + 2\eta_{2k} - \eta_{3k} + \eta_{4k}) + \frac{\sqrt{2}}{2}(\eta_{0k} - 2\eta_{1k} + 2\eta_{2k} - 2\eta_{3k} + \eta_{4k})\right], \tag{4.70}$$

$$\varepsilon_{3k} = \pm\frac{1}{4}\left[\eta_{0k} - \eta_{4k} + j\left((\eta_{0k} - 2\eta_{1k} + 2\eta_{2k} - 2\eta_{3k} + \eta_{4k}) \cdot \left(1+\sqrt{2}\right)\right)\right], \tag{4.71}$$

$$\begin{aligned}\varepsilon_{4k} =& \frac{1}{4}\Bigg[(\eta_{1k} - 2\eta_{2k} + \eta_{3k}) + \frac{\sqrt{2}}{2}(-\eta_{0k} + 2\eta_{1k} - 2\eta_{2k} + 2\eta_{3k} - \eta_{4k}) \\ & - j\left(-\eta_{1k} + \eta_{3k} + \frac{\sqrt{2}}{2}(\eta_{0k} - \eta_{4k})\right)\Bigg],\end{aligned} \tag{4.72}$$

where, positive or negative sign is for even or odd subbands, respectively. It should be highlighted that the order of the ASCET can be increased still further, but increasing the order of the equalizer directly leads to an increase in the computational complexity for the receiver. For this reason, 2-ASCET seems to be a good choice.

4.5 Computational complexity

In this section, the computational complexity, in terms of multiplications and additions for input sample blocks of length M, of each algorithm proposed to implement the ELT-MCM system, is analyzed. Central to the operation of this system is the DCT4e as the basic transform block at both

Table 4.1 Number of Multiplications for Input Sample Blocks of Length M of Various Efficient Algorithms of Implementation of DCT4e.

Algorithm	**Multiplications (MUL)**
Ref. [127]	$\frac{M}{2}\left(\log_2 M+2\right)$
Ref. [128]	$M\log_2 M+\frac{2}{3}M-\frac{2}{3}\left(-1\right)^{\log_2 M}$
Ref. [129]	$MUL_{best}=\frac{5M}{9}\log_2 M+\frac{2}{9}\left(-1\right)^{\log_2 M}\log_2 M+\frac{10}{27}M-\frac{10}{27}\left(-1\right)^{\log_2 M}$

Table 4.2 Number of Additions for Input Sample Blocks of Length M of Various Efficient Algorithm of Implementation of DCT4e .

Algorithm	**Additions (ADD)**
Ref. [127]	$\frac{3M}{2}\log_2 M$
Ref. [128]	$\frac{4M}{3}\log_2 M-\frac{2}{9}M+\frac{2}{9}\left(-1\right)^{\log_2 M}$
Ref. [129]	$ADD_{best}=\frac{4M}{3}\log_2 M+\frac{7}{9}M+\frac{2}{9}\left(-1\right)^{\log_2 M}$

the receiver and the transmitter sides. This transform has played a key role in numerous applications, such as audio signals compression, and thus many fast computational structures can be found (see, e.g., [127–129]). Tables 4.1 and 4.2 include the computational cost of some efficient algorithms to implement the DCT4e, and as it can be seen, the algorithm proposed in [129] provides the lower flop count and the lower number of multiplications. Notice that exactly the same flop count is obtained for the DST4e, since it is related to DCT4e by means of sign changes and reversals of the input and output sequences [129].

Regarding the whole receiver, Table 4.3 includes the computational complexity considering the lattice and butterfly implementations and assuming the 0-ASCET as equalization technique. This computational complexity has been counted for length-M blocks, sign changes have not been computed as multiplications, and DCT4e is implemented with the procedure presented in [129]. Moreover, MUL_{best} and ADD_{best} denote, respectively, the number of multiplications and additions necessary to carry out the algorithm in [129].

For the lattice structures case, the remaining multiplications are contributed by the first constant term (M), the polyphase filtering ($4M$ direct or transpose form, $6M$ normalized and $4M$ denormalized lattices), and the 0-ASCET equalizers ($2M$). The additions are contributed by the polyphase filtering ($2M$), the operations with matrices $\mathbf{I}$ and $\mathbf{J}$ ($4M$), their outputs ($2M$) and the 0-ASCETs outputs (M). Although the computational complexity is almost the same for the three lattice structures, the most suitable fast algorithms are based on direct/transpose filters or denormalized lattices. On the other hand, for the butterfly structures case the number of multiplications and additions required for the analysis/receiving CMFB is equal to $\kappa M+M/2$ and $\kappa M+M/2$, respectively [26, Sec. 4.4.4]. Therefore assuming $\kappa=2$, the multiplications of the whole receiver are contributed by the analysis CMFB

Table 4.3 Computational complexity of the efficient ELT-MCM receivers ($\kappa = 2$).

	MPIS	APIS
Butterfly Structure	$7M + 2 \cdot MUL_{best}$	$6M + 2 \cdot ADD_{best}$
Direct or Transpose	$7M + 2 \cdot MUL_{best}$	$9M + 2 \cdot ADD_{best}$
Normalized Lattices	$9M + 2 \cdot MUL_{best}$	$9M + 2 \cdot ADD_{best}$
Denormalized Lattices	$7M + 2 \cdot MUL_{best}$	$9M + 2 \cdot ADD_{best}$

Table 4.4 Example of computational complexity of ELT-MCM receivers for $M = 512$, $\kappa = 2$, and $N = 2048$.

	MPIS	APIS
Butterfly Structure	9080	16156
Direct or Transpose	9080	17692
Normalized Lattices	10104	17692
Denormalized Lattices	9080	17692

($2M + M/2$), the analysis SMFB ($2M + M/2$) and the 0-ASCET equalizers ($2M$). The additions are contributed by the CMFB ($2M + M/2$), the SMFB ($2M + M/2$) and the 0-ASCET equalizers (M). Table 4.4 presents an example for $M = 512$, $\kappa = 2$ and $N = 2048$.

4.6 Data rate analysis

This section discusses the expressions to determinate the theoretical throughput of a baseband ELT-MCM system. This derivation is based on each transfer function that relates any input of the transmitter side to any output at the receiver side. In addition, a constellation of infinity granularity has been assumed which means that each subcarrier can transport a fractional and unlimited number of bits.

With the aim at extending the study here presented, the general block diagram of the ELT-MCM transceiver, depicted in Fig. 4.9, has been considered. The discrete-time transmitted signal is defined as

$$x[n] = \sum_{k \in \mathbb{K}_{on}} \sum_{m \in \mathbb{Z}} x_{k,m} \cdot f_k [n - mM], \tag{4.73}$$

where $\mathbb{K}_{on} \subseteq \{0, \cdots, M-1\}$ is the set of active subchannels defined by the tone mask [10], and $x_{k,m}$ are the symbols in the subcarrier-time position (k,m), assumed to be zero-mean wide-sense stationary (WSS) processes. In particular, the variance σ_x^2 is assumed to be identical for all $x_{k,m}$, which are independent and identically distributed for every k in $\mathbb{K}_{on}$. We assume that the PLC channel can be

modeled as a time-invariant frequency selective channel:

$$a_{ch}[n] = \sum_{l=0}^{L-1} a_l \cdot \delta[n-l], \tag{4.74}$$

where L is the length of the channel. We also assume that there is no significant variation during a frame transmission. The received signal is given by

$$y[n] = \sum_{l=0}^{L-1} a_l \cdot x[n-l-\beta] + r[n-\beta], \tag{4.75}$$

where $r[n]$ is additive noise and β is a delay included to obtain proper system operation. In this clause, we assume the noise to be additive white Gaussian noise with zero mean and variance σ_r^2. Lastly, the signal at the k_0-subcarrier output can be written as

$$y^c_{k_0,n} = \sum_{\tau=0}^{N} h_{k_0}[\tau] \cdot y[nM-\tau] = \sum_{\tau=0}^{N} h_{k_0}[\tau] \sum_{l=0}^{L-1} a_l \sum_{k\in\mathbb{K}_{on}} \sum_{m\in\mathbb{Z}} x_{k,m} \cdot f_k[nM-\tau-l-\beta-mM] + \sum_{\tau=0}^{N} h_{k_0}[t] \cdot r[nM-\beta-\tau]. \tag{4.76}$$

In the following subsections, we will obtain the signal-to-interference-plus-noise ratio (SINR) under the reasonable assumption that the number of subcarriers used is quite large, so that the interference on a given subcarrier is normally distributed [116].

4.6.1 Transmitting over a channel without noise

Noise apart, the output symbol at the position (k_0, m_0) can be written as

$$y^c_{k_0,m_0} = \sum_{k\in\mathbb{K}_{on}} \sum_{m\in\mathbb{Z}} x_{k,m} \sum_{l=0}^{L-1} a_l \cdot G^c_{k_0,m_0}(k,m,l), \tag{4.77}$$

where

$$G^c_{k_0,m_0}(k,m,l) = \sum_{\tau=0}^{N} f_k[m_0M-\tau-l-\beta-mM] \cdot h_{k_0}[\tau]. \tag{4.78}$$

The expression (4.77) can be separated into the signal, $(k,m) = (k_0,m_0)$, and interference, $(k,m) \neq (k_0,m_0)$. The first part gives rise to the signal of interest

$$\Psi^c_{k_0,m_0} = x_{k_0,m_0} \sum_{l=0}^{L-1} a_l \cdot G^c_{k_0,m_0}(k_0,m_0,l) = x_{k_0,m_0} \cdot Q^c_{k_0,m_0}(k_0,m_0), \tag{4.79}$$

the second one to the ISI

$$I^c_{k_0,m_0} = \sum_{\substack{m\in\mathbb{Z}\\ m\neq m_0}} x_{k_0,m} \sum_{l=0}^{L-1} a_l \cdot G^c_{k_0,m_0}(k_0,m,l) = \sum_{\substack{m\in\mathbb{Z}\\ m\neq m_0}} x_{k_0,m} \cdot Q^c_{k_0,m_0}(k_0,m), \tag{4.80}$$

and, finally, the ICI

$$J^c_{k_0,m_0} = \sum_{\substack{k\in\mathbb{K}_{on}\\ k\neq k_0}} \sum_{m\in\mathbb{Z}} x_{k,m} \cdot \sum_{l=0}^{L-1} a_l \cdot G^c_{k_0,m_0}(k,m,l) = \sum_{\substack{\mathbb{K}_{on}\\ k\neq k_0}} \sum_{m\in\mathbb{Z}} x_{k,m} \cdot Q^c_{k_0,m_0}(k,m), \tag{4.81}$$

with

$$Q^c_{k_0,m_0}(k,m) = \sum_{l=0}^{L-1} a_l \cdot G^c_{k_0,m_0}(k,m,l). \tag{4.82}$$

Therefore, the CMFB output symbol can be expressed as

$$y^c_{k_0,m_0} = \Psi^c_{k_0,m} + I^c_{k_0,m_0} + J^c_{k_0,m_0}. \tag{4.83}$$

Following the same reasoning, the SMFB output symbol at the position (k_0,m_0) is

$$y^s_{k_0,m_0} = \Psi^s_{k_0,m} + I^s_{k_0,m_0} + J^s_{k_0,m_0}, \tag{4.84}$$

where the expressions of the signal of interest, ISI and ICI are similar to (4.79)-(4.81), but $G^c_{k_0,m_0}(k,m,l)$ must be replaced by

$$G^s_{k_0,m_0}(k,m,l) = \sum_{\tau=0}^{N} f_k[m_0M - \tau - l - \beta - mM] \cdot h^s_{k_0}[\tau], \tag{4.85}$$

and

$$Q^s_{k_0,m_0}(k_0,m_0) = \sum_{l=0}^{L-1} a_l \cdot G^s_{k_0,m_0}(k_0,m_0,l). \tag{4.86}$$

4.6.2 Noise Effects

Taking the noise into consideration, (4.83) and (4.84) can be rewritten as

$$y^c_{k_0,m_0} = \Psi^c_{k_0,m_0} + I^c_{k_0,m_0} + J^c_{k_0,m_0} + r^c_{k_0,m_0}, \tag{4.87}$$

$$y^s_{k_0,m_0} = \Psi^s_{k_0,m_0} + I^s_{k_0,m_0} + J^s_{k_0,m_0} + r^s_{k_0,m_0}, \tag{4.88}$$

where

$$r^c_{k_0,m_0} = \sum_{\tau=0}^{N} h_{k_0}[\tau] \cdot r[m_0M - \beta - \tau], \tag{4.89}$$

$$r^s_{k_0,m_0} = \sum_{\tau=0}^{N} h^s_{k_0}[\tau] \cdot r[m_0 M - \beta - \tau]. \tag{4.90}$$

4.6.3 The SINR of the system considering 0-ASCET

As stated above in subsection 4.4.2, the CM-PSE and SM-PSE are constants in the 0-ASCET:

$$c_k[n] = c_k, \qquad s_k[n] = s_k. \tag{4.91}$$

Thus, the demodulated (k_0, m_0)th symbol in the absence of noise can be written as

$$\begin{aligned} \hat{x}_{k_0,m_0} &= y^c_{k_0,m_0} \cdot c_{k_0} + y^s_{k_0,m_0} \cdot s_{k_0} \\ &= \underbrace{\Psi^c_{k_0,m_0} \cdot c_{k_0} + \Psi^s_{k_0,m_0} \cdot s_{k_0}}_{\Psi^T_{k_0,m_0}} + \underbrace{I^c_{k_0,m_0} \cdot c_{k_0} + I^s_{k_0,m_0} \cdot s_{k_0}}_{I^T_{k_0,m_0}} + \underbrace{J^c_{k_0,m_0} \cdot c_{k_0} + J^s_{k_0,m_0} \cdot s_{k_0}}_{J^T_{k_0,m_0}}, \end{aligned} \tag{4.92}$$

where $\Psi^T_{k_0,m_0}$, $I^T_{k_0,m_0}$ and $J^T_{k_0,m_0}$ are the signal and the total interference parts at the (k_0, m_0)th symbol.

The signal power can then be calculated as the second central moment:

$$\begin{aligned} P_\Psi(k_0) &= E\left[\left|\Psi^T_{k_0,m_0}\right|^2\right] \\ &= \sigma_x^2 \left|Q^c_{k_0,m_0}(k_0,m_0) \cdot c_{k_0} + Q^s_{k_0,m_0}(k_0,m_0) \cdot s_{k_0}\right|^2, \end{aligned} \tag{4.93}$$

where $E[\cdot]$ is the expected value. Next, the intersymbol interference power is obtained as

$$\begin{aligned} P_{\mathrm{ISI}}(k_0) &= E\left[\left|I^T_{k_0,m_0}\right|^2\right] \\ &= \sigma_x^2 \sum_{\substack{m\in\mathbb{Z} \\ m\neq m_0}} \left|Q^c_{k_0,m_0}(k_0,m) \cdot c_{k_0} + Q^s_{k_0,m_0}(k_0,m) \cdot s_{k_0}\right|^2. \end{aligned} \tag{4.94}$$

On the other hand, the total intercarrier interference power can be obtained as

$$\begin{aligned} P_{\mathrm{ICI}}(k_0) &= E\left[\left|J^T_{k_0,m_0}\right|^2\right] \\ &= \sigma_x^2 \sum_{\substack{\mathbb{K}_{on} \\ k\neq k_0}} \sum_{m\in\mathbb{Z}_0} \left|Q^c_{k_0,m_0}(k,m) \cdot c_{k_0} + Q^s_{k_0,m_0}(k,m) \cdot s_{k_0}\right|^2. \end{aligned} \tag{4.95}$$

The noise at the demodulated (k_0, m_0)th symbol can be expressed as

$$P_r(k_0) = E\left[\left|r^c_{k_0,m_0} \cdot c_{k_0} + r^s_{k_0,m_0} \cdot s_{k_0}\right|^2\right] = \sigma_r^2 \sum_{\tau=0}^{N} \left|c_{k_0} \cdot h_{k_0}[\tau] + s_{k_0} \cdot h^s_{k_0}[\tau]\right|^2. \tag{4.96}$$

Considering (4.93), (4.94), (4.95), and (4.131), the SINR at the k_0th subcarrier is obtained as

$$\mathrm{SINR}(k_0) = \frac{P_\Psi(k_0)}{P_{\mathrm{ISI}}(k_0) + P_{\mathrm{ICI}}(k_0) + P_r(k_0)}. \tag{4.97}$$

4.6.4 The SINR of the system considering L_A-ASCET

In the L_A-ASCET, the constant coefficients employed in 0-ASCET are replaced by FIR filter (see subsection 4.4.2), i.e., we have

$$c_k[n] = \sum_{\mu=-L_A}^{L_A} c_{k,\mu} \cdot \delta[n-\mu], \tag{4.98}$$

$$s_k[n] = \sum_{\mu=-L_A}^{L_A} s_{k,\mu} \cdot \delta[n-\mu]. \tag{4.99}$$

In this case and in the absence of noise, the demodulated (k_0, m_0)th symbol is given by

$$\hat{x}_{k_0,m_0} = \sum_{\mu=-L_A}^{L_A} \sum_{k\in\mathbb{K}_{on}} \sum_{m\in\mathbb{Z}} x_{k,m} \cdot \left(Q^c_{k_0,m_0-\mu}(k,m) \cdot c_{k_0,\mu} Q^s_{k_0,m_0-\mu}(k,m) \cdot s_{k_0,\mu} \right). \tag{4.100}$$

As in the previous case, the equations can be split into two groups: the signal, $(k,m) = (k_0,m_0)$, and the interferences, $(k,m) \neq (k_0,m_0)$. For the first group, the following term

$$\Psi^T_{k_0,m_0} = \sum_{\mu=-L_A}^{L_A} x_{k_0,m_0} \cdot \left(Q^c_{k_0,m_0-\mu}(k_0,m_0) \cdot c_{k_0,\mu} + Q^s_{k_0,m_0-\mu}(k_0,m_0) \cdot s_{k_0,\mu} \right), \tag{4.101}$$

includes the desired symbol. Otherwise, the interference part can be defined as

$$I^T_{k_0,m_0} = \sum_{\mu=-L_A}^{L_A} \sum_{\substack{m\in\mathbb{Z} \\ m\neq m_0}} x_{k_0,m} \cdot \left(Q^c_{k_0,m_0-\mu}(k_0,m) \cdot c_{k_0,\mu} + Q^s_{k_0,m_0-\mu}(k_0,m) \cdot s_{k_0,\mu} \right), \tag{4.102}$$

and

$$J_{k_0,m_0} = \sum_{\mu=-L_A}^{L_A} \sum_{\substack{k\in\mathbb{K}_{on} \\ k\neq k_0}} \sum_{m\in\mathbb{Z}} x_{k,m} \left(Q^c_{k_0,m_0-\mu}(k,m) \cdot c_{k_0,\mu} + Q^s_{k_0,m_0-\mu}(k,m) \cdot s_{k_0,\mu} \right). \tag{4.103}$$

The desired signal power can be expressed as

$$P_\Psi(k_0) = \sigma_x^2 \sum_{\mu=-L_A}^{L_A} \left| Q^c_{k_0,m_0-\mu}(k_0,m_0) \cdot c_{k_0,\mu} . Q^s_{k_0,m_0-\mu}(k_0,m_0) \cdot s_{k_0,\mu} \right|^2. \tag{4.104}$$

On the other hand, the interference power can be obtained as

$$P_{\mathrm{ISI}}(k_0) = \sigma_x^2 \sum_{\mu=-L_A}^{L_A} \sum_{\substack{m\in\mathbb{Z} \\ m\neq m_0}} \left| Q^c_{k_0,m_0-\mu}(k_0,m) \cdot c_{k_0,\mu} Q^s_{k_0,m_0-\mu}(k_0,m) \cdot s_{k_0,\mu} \right|^2, \tag{4.105}$$

and

$$P_{\mathrm{ICI}}(k_0) = \sigma_x^2 \sum_{\mu=-L_A}^{L_A} \sum_{\substack{k\in\mathbb{K}_{on} \\ k\neq k_0}} \sum_{m\in\mathbb{Z}} \left| Q^c_{k_0,m_0-\mu}(k,m)\cdot c_{k_0,\mu} + Q^s_{k_0,m_0-\mu}(k,m)\cdot s_{k_0,\mu} \right|^2. \tag{4.106}$$

The noise power can be calculated as

$$P_r(k_0) = \sigma_r^2 \sum_{\tau=0}^{N+2L_A} \left| h_{k_0,\mu}[\tau] + h^s_{k_0,\mu}[\tau] \right|^2, \tag{4.107}$$

where

$$h_{k_0,\mu}[n] = h_{k_0}[n] * c_k[n], \qquad h^s_{k_0,\mu}[n] = h^s_{k_0}[n] * s_k[n]. \tag{4.108}$$

Finally, (4.104), (4.105), (4.106) and (4.107) allow obtaining the SINR at the k_0th subcarrier:

$$\mathrm{SINR}(k_0) = \frac{P_\Psi(k_0)}{P_{\mathrm{ISI}}(k_0) + P_{\mathrm{ICI}}(k_0) + P_r(k_0)}. \tag{4.109}$$

4.6.5 Generalized and simplified data rate expressions

A novel and more efficient way to obtain the theoretical expressions that calculate the data rate of an ELT-MCM system, when the channel noise is not AWGN, is here presented. As in the previous subsection, a constellation of infinity granularity has been assumed, thus each subcarrier can transport a fractional and unlimited number of bits.

The discrete-time transmitted signal can be expressed in the z-domain as follows

$$X(z) = \sum_{k=0}^{M-1} F_k(z)\cdot X_k\left(z^M\right), \tag{4.110}$$

where $F_k(z)$ is the system function of each filter given in (4.2). Let us consider the channel impulse response and the channel noise in the z-domain, respectively expressed as $H_{ch}(z)$ and $R(z)$. The first block in the receiver side introduces a delay of β samples, so the received signal can be written as

$$Y(z) = X(z)\cdot H_{ch}(z)\cdot z^{-\beta} + R(z)\cdot z^{-\beta}. \tag{4.111}$$

The i-th output of the synthesis CMFB in the absence of noise can be expressed in the z-domain as

$$\begin{aligned} Y_i^c(z) =& \frac{1}{M}\sum_{l=0}^{M-1} H_i^c\left(z^{\frac{1}{M}}W^l\right) Y\left(z^{\frac{1}{M}}W^l\right) \\ =& \frac{1}{M}\sum_{l=0}^{M-1} H_i^c\left(z^{\frac{1}{M}}W^l\right) X\left(z^{\frac{1}{M}}W^l\right) H_{ch}\left(z^{\frac{1}{M}}W^l\right)\left(z^{\frac{1}{M}}W^l\right)^{-\beta} \\ =& \frac{1}{M}\sum_{l=0}^{M-1} H_i^c\left(z^{\frac{1}{M}}W^l\right)\left[\sum_{k=0}^{M-1} F_k\left(z^{\frac{1}{M}}W^l\right)\cdot X_k\left(\left(z^{\frac{1}{M}}W^l\right)^M\right)\right] H_{ch}\left(z^{\frac{1}{M}}W^l\right) z^{-\frac{\beta}{M}} W^{-l\beta}, \end{aligned} \tag{4.112}$$

where $W = \exp^{-j\frac{2\pi}{M}}$. Rearranging terms, we obtain

$$\begin{aligned} Y_i^c(z) =& \frac{1}{M}\sum_{l=0}^{M-1} H_i^c\left(z^{\frac{1}{M}}W^l\right)\left[\sum_{k=0}^{M-1} F_k\left(z^{\frac{1}{M}}W^l\right)\cdot X_k(z)\right] H_{ch}\left(z^{\frac{1}{M}}W^l\right) z^{-\frac{\beta}{M}} W^{-l\beta} \\ =& \frac{1}{M}\sum_{k=0}^{M-1} X_k(z)\sum_{l=0}^{M-1} H_i^c\left(z^{\frac{1}{M}}W^l\right) F_k\left(z^{\frac{1}{M}}W^l\right) H_{ch}\left(z^{\frac{1}{M}}W^l\right) z^{-\frac{\beta}{M}} W^{-l\beta}, \end{aligned} \tag{4.113}$$

where $H_i^c(z)$ and $H_i^s(z)$ are the z-transform or the filters given in (4.3) and (4.50), respectively.Then, defining $T_{i,k}^c(z) = H_i^c(z)F_k(z)H_{ch}(z)$, we get

$$Y_i^c(z) = \frac{1}{M}\sum_{k=0}^{M-1} X_k(z)\sum_{l=0}^{M-1} T_{i,k}^c\left(z^{-\frac{1}{M}}W^l\right) z^{-\frac{\beta}{M}} W^{-l\beta} = \sum_{k=0}^{M-1} X_k(z)U_{i,k}^c(z), \tag{4.114}$$

where the relation in the time-domain between $U_{i,k}^c(z)$ and $T_{i,k}^c(z)$ is given by $u_{i,k}^c[n] = t_{i,k}^c[nM-\beta]$, i.e., $u_{i,k}^c[n]$ is a delayed and decimated version of $t_{i,k}^c[n]$. Following the same reasoning, the ith output of the synthesis SMFB is given by

$$Y_i^s(z) = \frac{1}{M}\sum_{k=0}^{M-1} X_k(z)\sum_{l=0}^{M-1} T_{i,k}^s\left(z^{-\frac{1}{M}}W^l\right) z^{-\frac{\beta}{M}} W^{-l\beta} = \sum_{k=0}^{M-1} X_k(z)U_{i,k}^s(z), \tag{4.115}$$

where $T_{i,k}^s(z) = H_i^s(z)F_k(z)H_{ch}(z)$ and $u_{i,k}^s[n] = t_{i,k}^s[nM-\beta]$.

It is important to highlight that when the subchannel filters show high selectivity and discrimination between subcarriers, the functions $t_{i,k}^c[nM-\beta]$ and $t_{i,k}^s[nM-\beta]$ are nearly zero when $k \neq i-1, i$, and $i+1$.

Next, assuming that an L_A-ASCET is chosen as channel equalization technique, the ith demodulated symbol can be written as

$$\begin{aligned} \hat{X}_i(z) =& Y_i^c(z)\cdot C_i(z) + Y_i^s(z)\cdot S_i(z) \\ =& \sum_{k=0}^{M-1} X_k(z)\left(U_{i,k}^c(z)\cdot C_i(z) + U_{i,k}^s(z)\cdot S_i(z)\right) \\ =& \sum_{k=0}^{M-1} X_k(z)V_{i.k}(z), \end{aligned} \tag{4.116}$$

where $C_i(z)$ and $S_i(z)$ are, respectively, the z-transform of

$$c_i[n] = \sum_{\mu=-L_A}^{L_A} c_{i,\mu}\cdot\delta[n-\mu], \tag{4.117}$$

$$s_i[n] = \sum_{\mu=-L_A}^{L_A} s_{i,\mu}\cdot\delta[n-\mu], \tag{4.118}$$

with $c_i[n]$ and $s_i[n]$ being the impulse response of the subcarrier filters that carry out the frequency domain equalization. These filters are included at each output of both the CMFB and the SMFB receiving system [38, 28] (see 4.4). Then, the reconstructed symbol can be rewritten as follows

$$\hat{X}_i(z) = X_i(z)V_{i,i}(z) + \sum_{\substack{k=0 \\ k\neq i}}^{M-1} X_k(z)V_{i,k}(z), \tag{4.119}$$

and expressed in time-domain as

$$\begin{aligned}\hat{x}_i[n] =& \sum_{\ell} v_{i,i}[\ell]\cdot x_i[n-\ell] + \sum_{\substack{k=0 \\ k\neq i}}^{M-1}\sum_{\ell} v_{i,k}[\ell]\cdot x_i[n-\ell] \\ =& v_{i,i}[0]\cdot x_i[n] + \underbrace{\sum_{\substack{\ell \\ \ell\neq 0}} v_{i,i}[\ell]\cdot x_i[n-\ell]}_{\text{ISI}} + \underbrace{\sum_{\substack{k=0 \\ k\neq i}}^{M-1}\sum_{\ell} v_{i,k}[\ell]\cdot x_i[n-\ell]}_{\text{ICI}},\end{aligned} \tag{4.120}$$

where ISI and ICI denote, respectively, the intersymbol and the intercarrier interference.
The power of the *i*th subcarrier signal can be calculated as

$$P_\gamma(i) = \sigma_x^2 \left|v_{i,i}[0]\right|^2. \tag{4.121}$$

Similarly, the power corresponding to the intersymbol and intercarrier interference of the *i*th subcarrier ($P_{ISI}(i)$ and $P_{ICI}(i)$) can be obtained as

$$P_{INT}(i) = P_{ISI}(i) + P_{ICI}(i) = \sigma_x^2 \left(\sum_{\substack{\ell \\ \ell\neq 0}} |v_{i,i}[\ell]|^2 + \sum_{\substack{k=0 \\ k\neq i}}^{M-1}\sum_{\ell} |v_{i,k}[\ell]\cdot|^2 \right).$$

With regard to the noise at the *i*th output of the synthesis CMFB/SMFB, it can be calculated as

$$\begin{aligned}\Upsilon_i^c(z) =& \frac{1}{M}\sum_{l=0}^{M-1} H_i^c\left(z^{\frac{1}{M}}W^l\right) R\left(z^{\frac{1}{M}}W^l\right)\left(z^{\frac{1}{M}}W^l\right)^{-\beta} \\ =& \frac{1}{M}\sum_{l=0}^{M-1} \Gamma_{i,k}^c\left(z^{-\frac{1}{M}}W^l\right) z^{-\frac{\beta}{M}} W^{-l\beta},\end{aligned} \tag{4.122}$$

and

$$\begin{aligned}\Upsilon_i^s(z) =& \frac{1}{M}\sum_{l=0}^{M-1} H_i^s\left(z^{\frac{1}{M}}W^l\right) R\left(z^{\frac{1}{M}}W^l\right)\left(z^{\frac{1}{M}}W^l\right)^{-\beta} \\ =& \frac{1}{M}\sum_{l=0}^{M-1} \Gamma_{i,k}^s\left(z^{-\frac{1}{M}}W^l\right) z^{-\frac{\beta}{M}} W^{-l\beta},\end{aligned} \tag{4.123}$$

respectively, where $\Gamma_i^c(z) = H_i^c(z)R(z)$ and $\Gamma_i^s(z) = H_i^s(z)R(z)$. In the time-domain, (4.122) and (4.123) can be expressed as

$$r_i^c[n] = \sum_t h_i^c[t] \cdot r[nM - t - \beta], \tag{4.124}$$

$$r_i^s[n] = \sum_t h_i^s[t] \cdot r[nM - t - \beta]. \tag{4.125}$$

Therefore, the noise at the ith demodulated symbol is

$$\sum_{\mu=-L_A}^{L_A} r_i^c[n-\mu] \cdot c_{i,\mu} + r_i^s[n-\mu] \cdot s_{i,\mu}. \tag{4.126}$$

Since, the noise power is equal to the second central moment of (4.126), it yields

$$\begin{aligned}
P_r(i) =& E\left[\left|\sum_{\mu=-L_A}^{L_A} r_i^c[n-\mu] \cdot c_{i,\mu} + r_i^s[n-\mu] \cdot s_{i,\mu}\right|^2\right] \\
=& E\left[\left(\sum_{\mu_1=-L_A}^{L_A} r_i^c[n-\mu_1] \cdot c_{i,\mu_1} + r_i^s[n-\mu_1] \cdot s_{i,\mu_1}\right)\right. \\
& \left.\left(\sum_{\mu_2=-L_A}^{L_A} r_i^c[n-\mu_2] \cdot c_{i,\mu_2} + r_i^s[n-\mu_2] \cdot s_{i,\mu_2}\right)^*\right] \\
=& \sum_{\mu_1=-L_A}^{L_A}\sum_{\mu_2=-L_A}^{L_A} c_{i,\mu_1} c_{i,\mu_2} E\left[r_i^c[n-\mu_1]\left(r_i^c[n-\mu_2]\right)^*\right] \\
& + 2\sum_{\mu_1=-L_A}^{L_A}\sum_{\mu_2=-L_A}^{L_A} c_{i,\mu_1} s_{i,\mu_2} E\left[r_i^c[n-\mu_1]\left(r_i^s[n-\mu_2]\right)^*\right] \\
& + \sum_{\mu_1=-L_A}^{L_A}\sum_{\mu_2=-L_A}^{L_A} s_{i,\mu_1} s_{i,\mu_2} E\left[r_i^s[n-\mu_1]\left(r_i^s[n-\mu_2]\right)^*\right],
\end{aligned} \tag{4.127}$$

with

$$\begin{aligned}
E\left[r_i^c[n-\mu_1](r_i^c[n-\mu_2])^*\right] =& E\left[\sum_{t_1} h_i^c[t_1] r\left[(n-\mu_1)M - t_1 - \beta\right] \sum_{t_2} h_i^c[t_2] r^*\left[(n-\mu_2)M - t_2 - \beta\right]\right] \\
=& \sum_{t_1}\sum_{t_2} h_i^c[t_1] h_i^c[t_2] E\left[r\left[(n-\mu_1)M - t_1 - \beta\right] r^*\left[(n-\mu_2)M - t_2 - \beta\right]\right] \\
=& \sum_{t_1}\sum_{t_2} h_i^c[t_1] h_i^c[t_2] E\left[r\left[nM - \beta - (t_1 + \mu_1 M)\right] r^*\left[nM - \beta - (t_2 + \mu_2 M)\right]\right] \\
=& \sum_{t_1}\sum_{t_2} h_i^c[t_1] h_i^c[t_2] R_r(t_1 + \mu_1 M, t_2 + \mu_2 M),
\end{aligned} \tag{4.128}$$

where $R_r(t_1, t_2)$ is the noise autocorrelation between times t_1 and t_2. The other terms of (4.127) are

$$E\left[r_i^c[n-\mu_1](r_i^s[n-\mu_2])^*\right] = \sum_{t_1}\sum_{t_2} h_i^c[t_1] h_i^s[t_2] R_r(t_1 + \mu_1 M, t_2 + \mu_2 M), \tag{4.129}$$

and

$$E\left[r_i^s[n-\mu_1](r_i^s[n-\mu_2])^*\right] = \sum_{t_1}\sum_{t_2} h_i^s[t_1]h_i^s[t_2]R_r\left(t_1+\mu_1 M, t_2+\mu_2 M\right). \tag{4.130}$$

Therefore, the noise power yields

$$P_r(i) = \sum_{\mu_1=-L_A}^{L_A}\sum_{\mu_2=-L_A}^{L_A}\left[\sum_{t_1}\sum_{t_2} R_r\left(t_1+\mu_1 M, t_2+\mu_2 M\right) \times \left(c_{i,\mu_1}c_{i,\mu_2}h_i^c[t_1]h_i^c[t_2] + s_{i,\mu_1}s_{i,\mu_2}h_i^s[t_1]h_i^s[t_2] + 2c_{i,\mu_1}s_{i,\mu_2}h_i^c[t_1]h_i^s[t_2]\right)\right]. \tag{4.131}$$

Assuming that the PLC noise is a stationary stochastic processes, the equation (4.131) can rewritten as

$$P_r(i) = \sum_{\mu_1=-L_A}^{L_A}\sum_{\mu_2=-L_A}^{L_A}\left[\sum_{t_1}\sum_{t_2} R_r(\tau)\left(c_{i,\mu_1}c_{i,\mu_2}h_i^c[t_1]h_i^c[t_2] + s_{i,\mu_1}s_{i,\mu_2}h_i^s[t_1]h_i^s[t_2] + 2c_{i,\mu_1}s_{i,\mu_2}h_i^c[t_1]h_i^s[t_2]\right)\right], \tag{4.132}$$

where $\tau = (t_2 - t_1) + M(\mu_2 - \mu_1)$. It is important to note that if the PLC noise is AWGN, (4.131) can be simplified to expression (4.107).

4.7 Achievable Data Rate Analysis

The theoretical data rate can be calculated by the following expression:

$$R = \Delta_f \sum_{k\in\mathbb{K}_{on}} C(k), \tag{4.133}$$

where Δ_f is the subcarrier spacing, $\mathbb{K}_{on}$ is the set of active subcarriers and $C(k)$ is the maximal data rate for the kth subchannel, which can be calculated by means of the following expression:

$$C(k) = \log_2\left(1 + \frac{\mathrm{SINR}(k)}{\chi}\right). \tag{4.134}$$

where the SINR is given by (4.97) or (4.109), and Γ is the SINR gap. Since IEEE 1901 [10] proposes the PAM as the primary mapping for the ELT-MCM PHY, and assuming that an M-QAM is like 2 M-PAM independent modulations [13, 20], χ is defined by

$$\chi \approx \frac{1}{3}\left[Q^{-1}\left(\frac{\mathrm{SER}}{2}\right)\right]^2. \tag{4.135}$$

where SER stands for the symbol error rate and $Q^{-1}(\cdot)$ is the inverse tail probability of the standard normal distribution [13, 20]. For $\chi = 1$, $C(k)$ is the capacity of the kth subchannel.

4.8 Simulation results

In this section, the performance of a baseband system through several computer simulations is investigated. The ELT-MCM system performance is analyzed in terms BER and data rate. The general block of the transceiver has been depicted in Fig. 2.5.

Let us assume some specifications deployed by IEEE 1901 for the baseband ELT-MCM system that employs the prototype filter recommended for $M = 512$ and $\kappa = 2$. In this scheme, there are 360 active subcarriers (used for data modulation) in the frequency range from 1.8 MHz to 30 MHz, and the frequency spacing (δ_f) is fixed to 61.035 kHz. Furthermore, an error-correcting-code system (see 2.3.3), with a codification rate of $1/2$, has been used to calculate the BER. Meanwhile, a non ECC system has been employed to obtain the data rate.

4.8.1 Main results

In-home PLC scenarios

The first set of simulations consist in averaging the outcome of 100 transmissions through different impulse response realizations representative of classes 1 (strong signal attenuation), 5 (medium attenuation) and 9 (little attenuation), all of then generated by Tonello's model (see 3.1.1). Besides, the PLC background noise (BGN) and the periodic impulsive noise synchronous (PINS) and asynchronous (PINA), based on Corte's model (see 3.1.2), have also been included. It is important to note that the SNR is obtained from the receiver side. For each SNR, more than one million binary data were generated and converted into parallel data to be transmitted over the active 360 subcarriers described in [10]. Before proceeding with the multicarrier modulation, the data at each subcarrier are mapped by 2-PAM (a.k.a. BPSK). We assume that the channel remains constant during each multicarrier symbol, though it changes independently among different symbols. Furthermore, we also assume both perfect synchronization and channel estimation. Finally, 0- and 1-ASCET have been chosen as equalizers.

Fig. 4.15 shows the average BER of the transceiver system under the above conditions, and as it can be seen, the first remark that can be made on the results is that 1-ASCET always outperforms 0-ASCET. Nevertheless, and as it was expected, we can notice that the gains in the BER results for good channels (class 9) are lower than the ones observed for the simulations of classes 5 and 1. For instance, considering class 9 channels, the 1-ASCET system shows gains of only 0.3 dB for BER $= 10^{-4}$, whereas for class 5 is around 1 dB. Finally, the 1-ASCET for class 1 exhibits BER values below 10^{-2} for SNR $\geq$ 11.9 dB, whereas more than 25 dB are needed to obtain a similar BER value with the 0-ASCET system.

As a second scenario, a narrowband interference (NBI) with one frequency component located at 200 kHz, simulating an interference form comercial AM radio station, is also considered in classes 9 and 1. As it can be seen in Fig. 4.16, the 1-ASCET shows a gain of around 16 dB for a BER value of 10^{-3} for class 9. It even yields a better performance in class 1: the BER value is below 10^{-4} for SNR $\geq$ 19.1 dB. Conversely, the systems reach error floors around 40 dB for 0-ASCET. In conclusion,

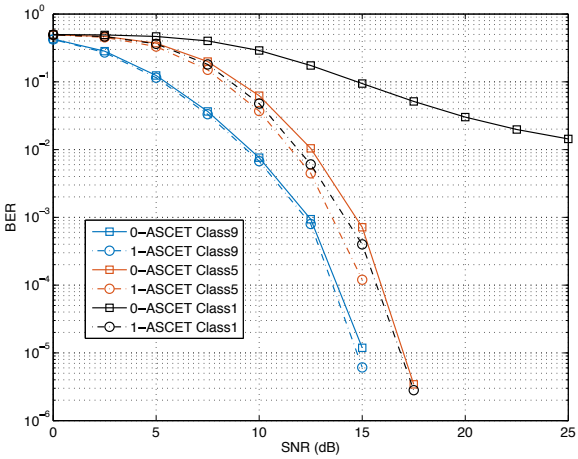

Fig. 4.15 BER performance comparison in 2-PAM under colored background, impulsive, synchronous and asynchronous noises.

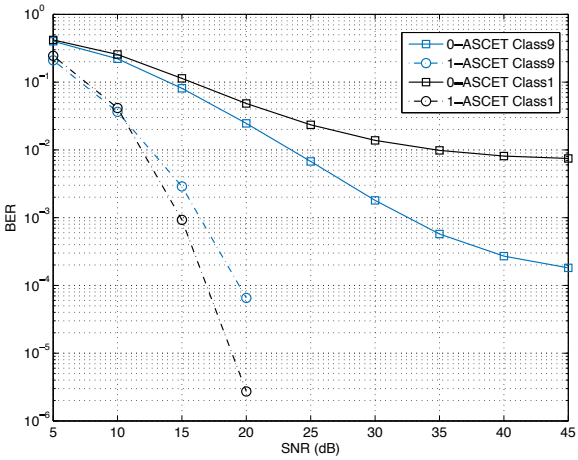

Fig. 4.16 BER performance comparison in 2-PAM under all different PLC noises.

the 1-ASCET outperforms the 0-ASCET scheme, but with different strength depending on the class of channels. The former really takes advantage over the latter for the most disturbed channels and under the presence of different types of noise.

In the last experiment, the BER performance of the baseband ELT-MCM transceiver is analyzed assuming the same kind of noise described in the second scenario. However, in this experiment, the LTI best-case and worst-case channels, based on Cañete's model (see 3.1.1), has been employed. Besides, a coding rate equal to $2/3$ has been also considered to calculate its impact on the system perfromance. As seen from Fig. 4.17, 1-ASCET does not achieve improvement performance compared to 0-ASCET. Furthermore and as expected, the best-case channel exhibits the best performance. Finally, increasing the value of the coding rate creates a separation in BER performance of around 6.5 dB (best-case) and 5 dB (worst-case) for BER $= 5 \cdot 10-3$.

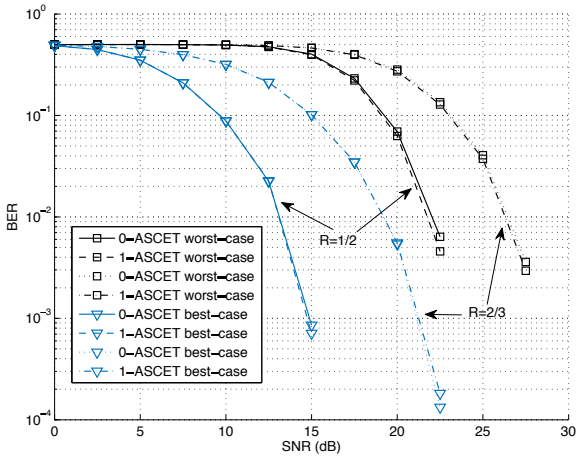

Fig. 4.17 BER performance comparison in 2-PAM under all different PLC noises and different coding rates.

Hereafter the baseband ELT-MCM system performance in terms of data rate, considering a constellation of infinity granularity, is presented. Furthermore, it is compared with the windowed OFDM system performance. The specifications of the windowed OFDM system are also based on [10]. This system uses 4096 subcarriers with up to 917 usable subcarriers in the range of $[1.8-30]$ MHz and the subcarrier spacing (Δ_f') is approximately 24.414 kHz. In addition, the standard fixes a mandatory payload symbol guard interval (GI) equals 556, 756 or 4712 samples, thus, the GI is chosen to be 756 to provide good system performance and to not penalize this transceiver. The theoretical data rate can be calculated using (4.133), but, since this technique needs a guard interval, the data rate formula yields [15]

$$R' = \Delta_f' \sum_{k \in \mathbb{K}_{on}'} \frac{M}{M+\mathrm{GI}} \log_2 \left(1 + \frac{\mathrm{SINR}'(k)}{\chi'}\right), \tag{4.136}$$

where $\mathbb{K}_{on}'$ is the set of active subcarriers, SINR' can be calculated as follows [15]

$$\mathrm{SINR}'(k_0) = \frac{\sigma_x^2(k_0)|H_{k_0}|^2}{\sigma_n^2(k_0) + P_{ICI+ISI}^{Wofdm}(k_0)}, \tag{4.137}$$

where H_{k_0} denotes the frequency channel coefficient on the kth subcarrier, and χ' is defined by

$$\chi' \approx \frac{1}{3}\left[Q^{-1}\left(\frac{\mathrm{SER}}{4}\right)\right]^2 \tag{4.138}$$

for 2^{2K}-QAM constellations. In (4.135) and (4.138), the SER has been fixed to 10^{-3} for both wavelet OFDM and windowed OFDM systems. Besides, following the same process as in [15, 31], the ELT-MCM system is evaluated with 0-ASCET (1-tap), 1-ASCET (3-tap), and 2-ASCET (5-tap), while a zero-forcing equalizer is used in windowed OFDM system.

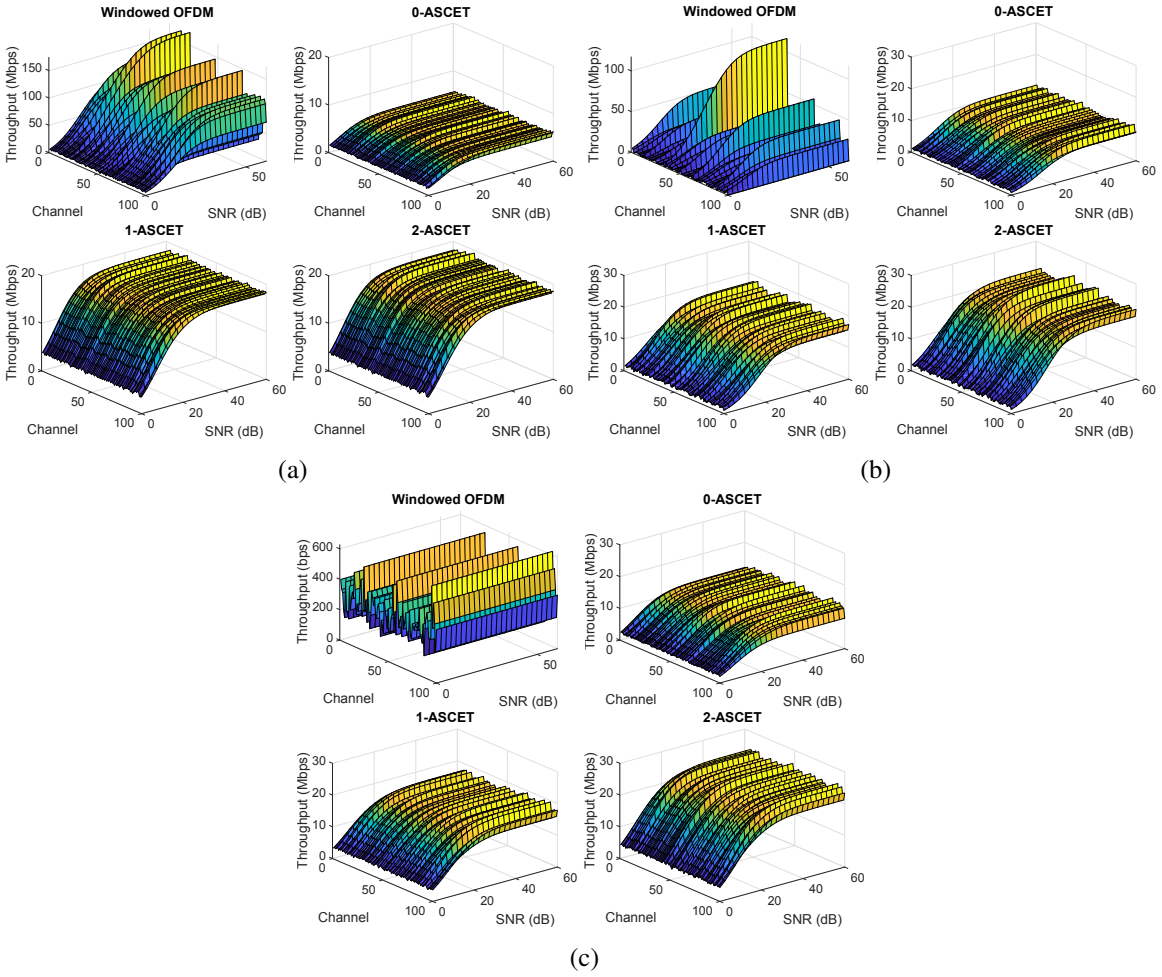

Fig. 4.18 Comparison of windowed OFDM and ELT-MCM (with 0-, 1-, 2-ASCET) for channels of a) class 9, b) class 5 and c) class 1 and AWGN.

In the fourth simulation, the windowed OFDM data rate is compared with that of the wavelet OFDM, over class 9 in-home PLC channels and assuming AWGN as PLC noise. Fig. 4.18a depicts the theoretical data rate obtained under these conditions. As can be appreciated, a significant difference can be seen: Windowed OFDM outperforms ELT-MCM, almost tripling the data rate at high SNR values. Moreover, since the PLC channel is one of the most hostile channels, the 0-ASCET is not enough to compensate for the channel distortion.

In the next comparison, we investigate the performance of both multicarrier schemes under the same conditions as the previous one, but in the presence of PLC channels of class 5. Fig. 4.18b shows the resulting data rate, and as it can be seen, the highest values are achieved by the ELT-MCM system with 2-ASCET. These results are obtained when 1-ASCET or 2-ASCET are employed. Actually, the ELT-MCM data rate associated with 2-ASCET is 179.5% higher for SNR=20 dB.

As sixth scenario, both multicarrier schemes have been analyzed in the same conditions than in the fourth one but with class 1 PLC channels. As shown in Fig. 4.18c, the data rate of windowed

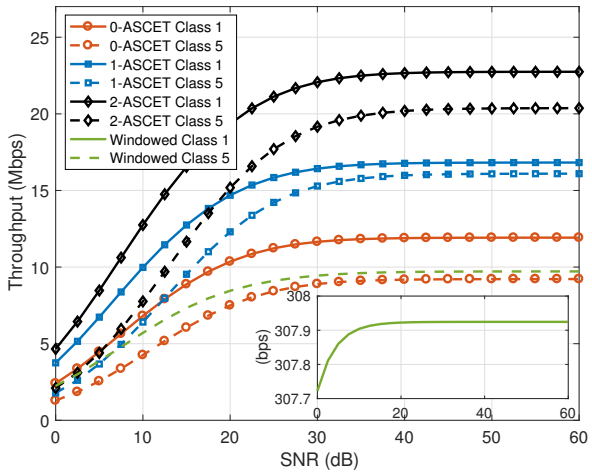

Fig. 4.19 Mean value of data rate in presence of class 1 and class 5 channels, assuming AWGN as channel noise.

OFDM system is considerably reduced and it is outperformed by the ELT-MCM, which shows better results than those shown in the first simulation. Finally, to easily prove the gain related to ELT-MCM over windowed OFDM, the mean value of the data rate related to the second and third simulations is shown in Fig. 4.19.

In the following set of experiments, the AWGN has been replaced by in-home PLC background noise, which is associated with a heavily disturbed channel and it is based on Corte's model (see 3.1.2). In this example, the resulting data rate is obtained once again over class 9 in-home PLC channels for both windowed OFDM and ELT-MCM. Fig. 4.22a depicts the theoretical data rate obtained under these conditions: windowed OFDM outperforms ELT-MCM in the same way as it did with AWGN, tripling the data rate.

We investigate now the performance of both multicarrier schemes over PLC channels of class 5 under strong BGN. The resulting data rate are shown in Fig. 4.22b, and as can be seen, the highest values are achieved by the ELT-MCM system with 2-ASCET. Actually, the ELT-MCM data rate associated with 2-ASCET is 156% higher for SNR=20 dB.

Finally, both multicarrier schemes have been compared over class 1 PLC channels. As shown in Fig. 4.20c, the data rate of windowed OFDM system is considerably reduced and it is outperformed by the ELT-MCM. To easily prove the gain associated to the ELT-MCM system in the above set of simulations, the mean value of the data rate in the presence of class 5 and class 1 channels is depicted in Fig. 4.21.

Based on the experiments, it can be appreciated that the ELT-MCM performs better than windowed OFDM when the signal attenuation increases (more hostile channels). This phenomenon can be explained analyzing the interference power ($P_{ISI} + P_{ICI}$) of both multicarrier schemes. Fig. 4.22 represents the interference power of windowed OFDM and ELT-MCM assuming a maximum allowed power spectral density of -55 dBm/Hz (defined by the standard) and the first channel realization. It

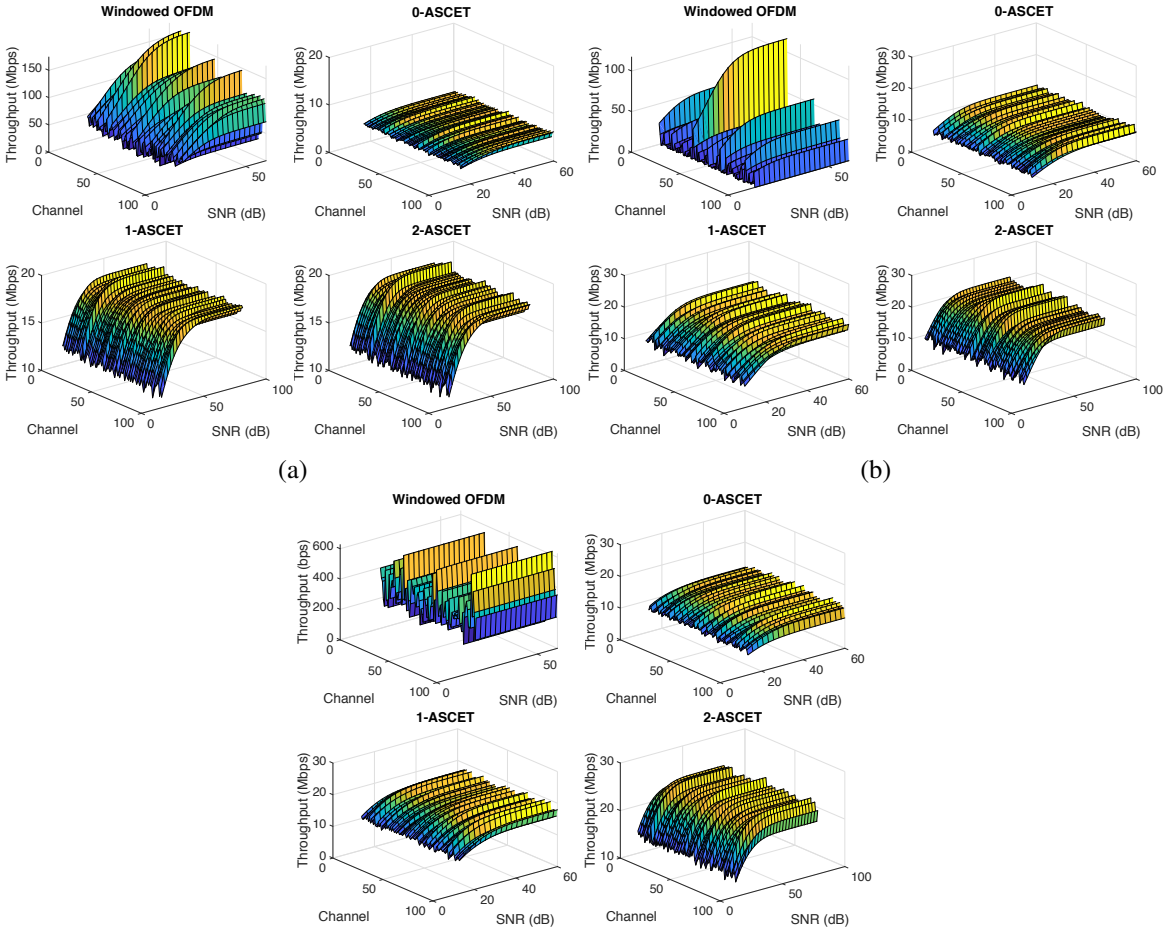

Fig. 4.20 Comparison of windowed OFDM and ELT-MCM (with 0-, 1-, 2-ASCET) for channels of a) class 9, b) class 5 and c) class 1 and strong BGN.

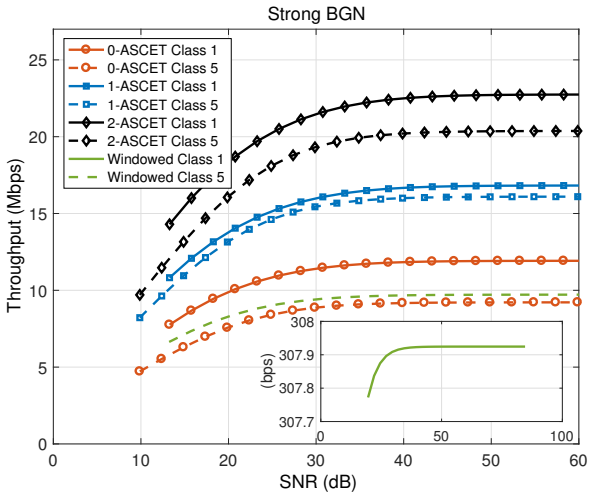

Fig. 4.21 Mean value of the obtained data rate for class 1 and class 5 channels, assuming BGN as channel noise.

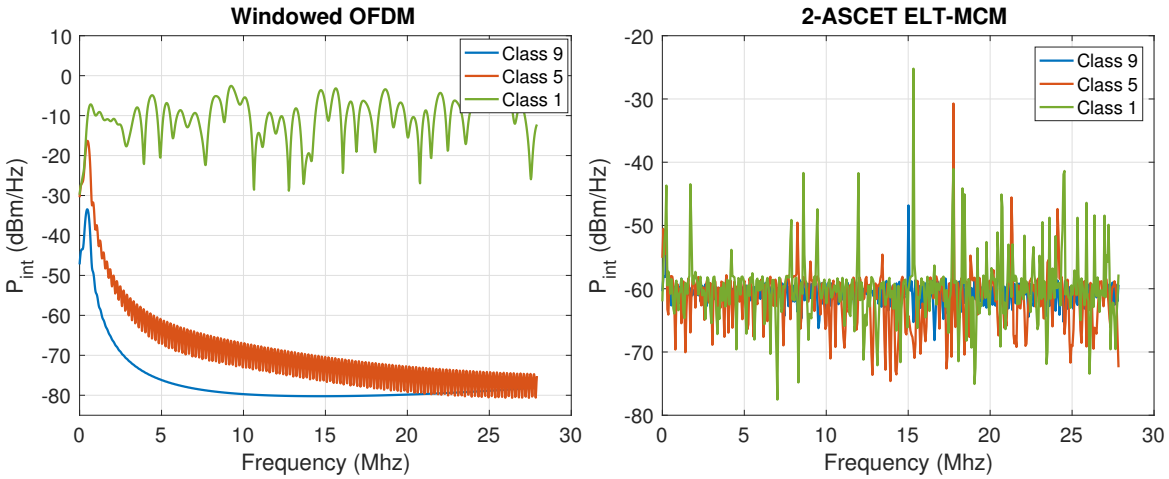

(a) (b)

Fig. 4.22 (a) FFT OFDM PHY and (b) ELT-MCM interference power in each PLC channel.

can be seen how the windowed OFDM interference power rises when the channel hostility rises too, reaching an average of -10 dBm/Hz for the PLC channel class 1 (66 dB higher than the interference power obtained for the class 9). On the other hand, the ELT-MCM interference power remains more uniform for little, middle and strong signal attenuation, proving that wavelet OFDM is more robust to hostile channel than windowed OFDM. Furthermore, the data rate of windowed OFDM varies considerably among the channel tested, e.g., from 64 Mbps to 125 Kbps as shown in Fig. 4.18b. Meanwhile, the performance of ELT-MCM is more homogeneous, achieving data rate between 19 Mbps and 11 Mbps under the same conditions.

In-vehicle PLC scenarios

As mentioned above, the ELT-MCM transmitting and receiving filters are obtained from a prototype filter which, for $\kappa = 2$, belongs o a family of windows proposed in [26] which fulfills the PR property. Nevertheless, based on (4.10), the question that arises is: Does the γ factor affect the ELT-MCM system performance?

The results here presented seek to clarify the ELT-MCM system performance with different γ factor. As the standard IEEE 1901 specifies that the deployed system can also be used on platforms, in-car and in-aircraft scenarios are assumed. For this purpose, the BER and the data rate are obtained for the following γ values: 0, 0.3 (recommended in [10]), 0.5, 0.75 and 1. For all of the simulations, the system uses 512 subcarriers, which just 360 active subcarriers, as it is recommended in [2, 28] MHz; the frequency spacing ($\triangle f = 61.035$ KHz) defined in [10] has been used. Besides, ASCET with 1 (0-ASCET), 3 (1-ASCET) and 5 (2-ASCET) [27] coefficients have been chosen as equalization technique [37, 38]. A concatenated encoder, with a codification rate of 1/2, has been used as FEC block to calculate the BER. However, a non FEC system has been employed to obtain the data rate.

1. **In-car PLC channel scenario:**

   The BER has been obtained considering the in-car PLC noise environment described in Sec. 3.2.1, in addition, it is assumed a 2-PAM modulation and a code rate equals $1/2$. As can be appreciated in Fig. 4.23, there is no single solution for all the cases, indeed, the best system performance is achieved in each case for a different γ value. For instance, when in-car PLC noise is modelled only as BGN, the best system performance is obtained for $\gamma = 0$ ($\gamma = 1$, $\gamma = 0$) when 0-ASCET (1-ASCET, 2-ASCET) has been employed as equalization technique. However, due to the ECC blocks, the difference between the best and the worst performance is not significant.

   On the other hand, the resulting achievable data rate, considering a constellation of infinity granularity, is shown in Fig. 4.24. In the light of the results of theses simulations, it can be seen that $\gamma = 1$ achieve the highest throughput in almost all cases. In fact, the data rate got by $\gamma = 1$ is 11.95%, 11.62% and 9.41% higher than that obtained with the IEEE 1901 prototype filter in each case, for the different PLC noise cases and assuming a 2-ASCET equalizer (left column).

   Furthermore and in view of the results, one may conclude that the periodic impulse noise (with high or low repetition rate) has a small impact in the system performance.

2. **In-aircraft PLC channel simulation:**

   Fig. 4.25 shows the BER obtained under the conditions described previously. As in the former simulation there is no single solution, for each particular case, there is a different γ value for which the best performance is obtained. But again, due to the FEC blocks, the variation between the worst and the best result is minimum.

   Fig. 4.26 depicts the resulting system data rate. As can be appreciated, the best performance is achieved for $\gamma = 1$ in all the cases. In fact, for the case of SPBD-IBU14 PLC channel and 0-ASCET equalizer, the system performance achieved for $\gamma = 0$ is 27.76% higher than that obtained with the recommended prototype filter ($\gamma = 0.3$). Likewise, for the same γ factor and PLC channel but with higher order ASCET (1- and 2-ASCET), the system achieves a data rate 4.77% and 11.47% higher than those obtained with $\gamma = 0.3$.

   We can conclude from these results that the system performance is most affected by the number of VTs than by the distance. For instance, the BER and the data rate obtained in the links SPDB-IBU 4 and SPDB-IBU 11 are approximately the same, even when the path length in the latter is almost twice than in the former.

4.8.2 Other results

After studying the trade-off between stopband attenuation and transition band and how it influences in the ELT-MCM system performance, another question arises: Is the recommended prototype filter (referred to as Malvar window) the best choice for PLC? With the goal of solving this question,

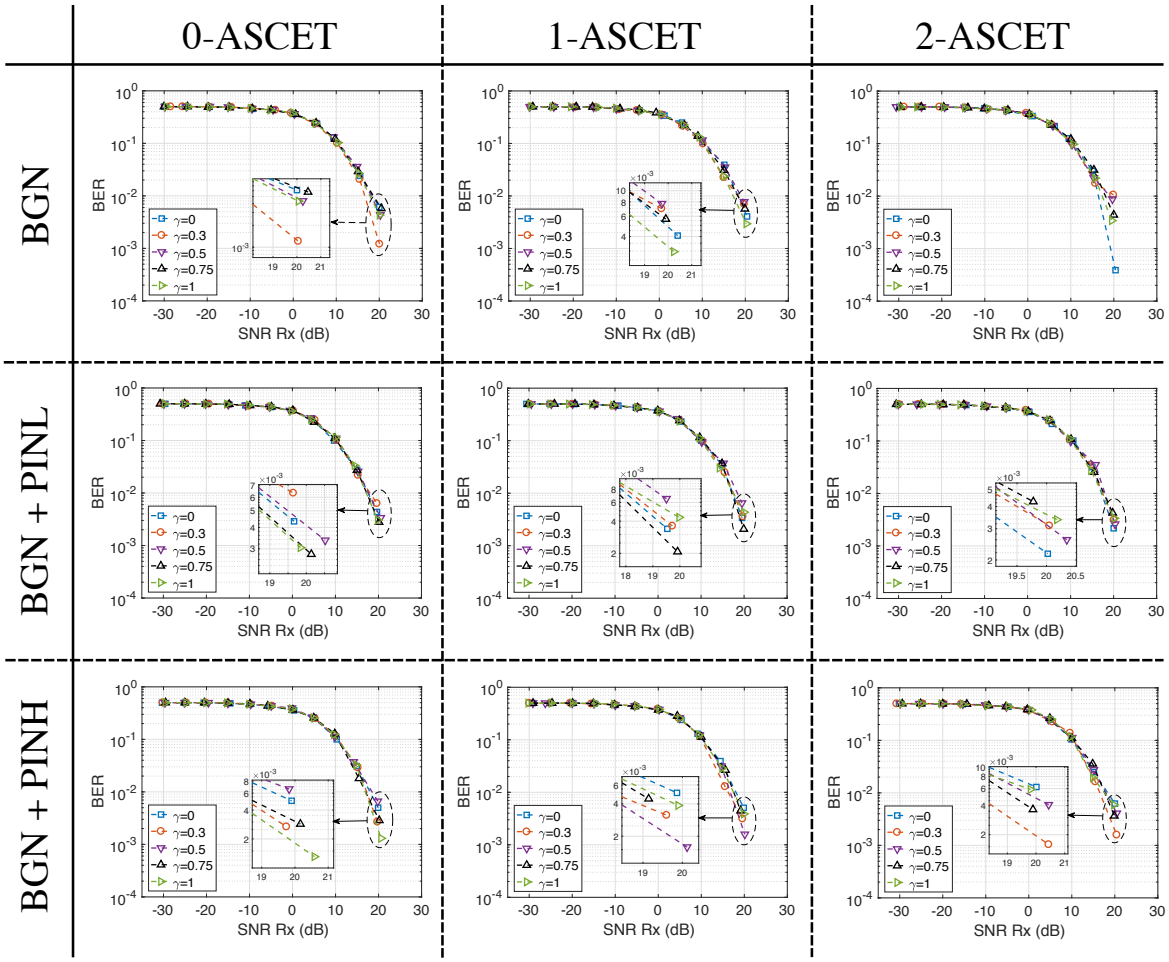

Fig. 4.23 BER for different in-car PLC channel, noises and equalizers.

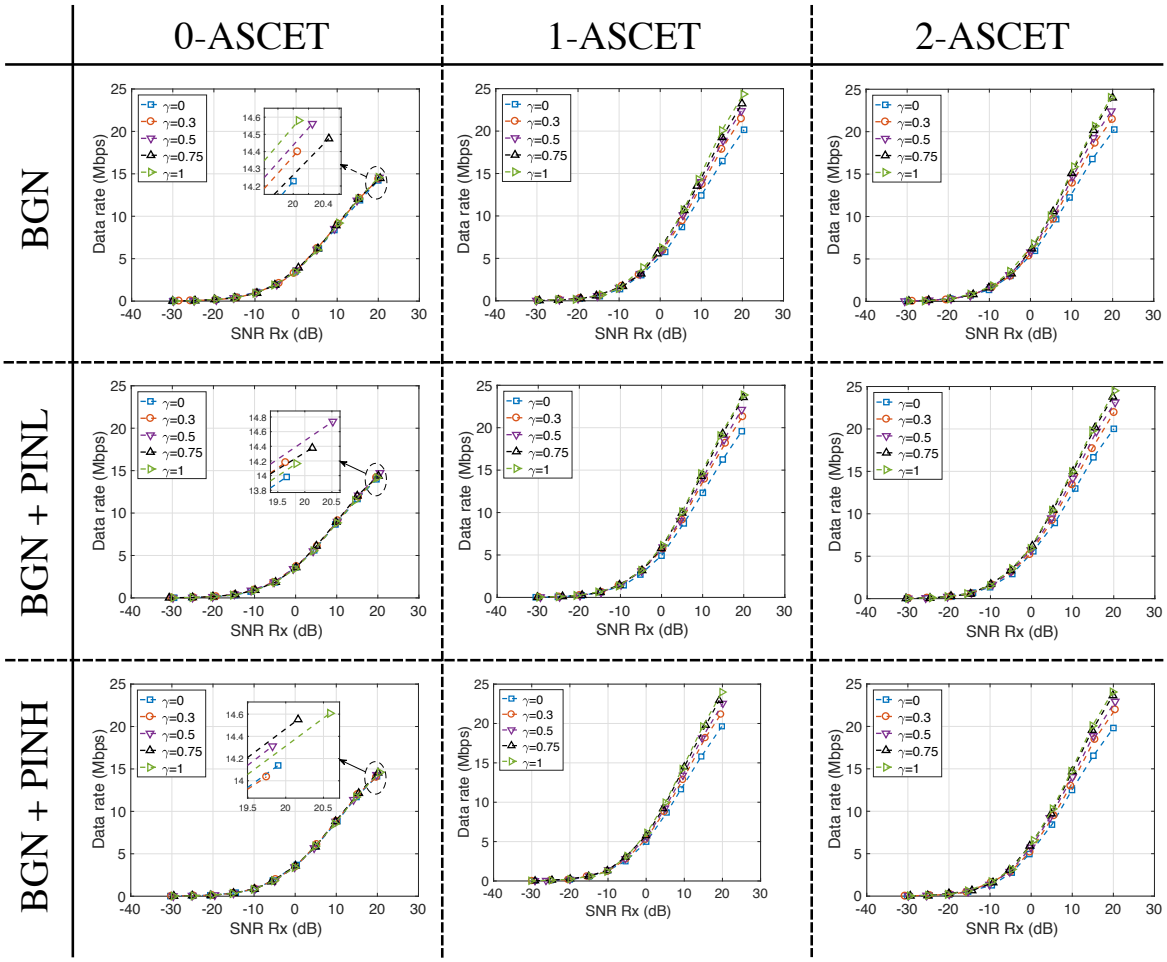

Fig. 4.24 Achievable data rate for different in-car PLC channel, noises and equalizers.

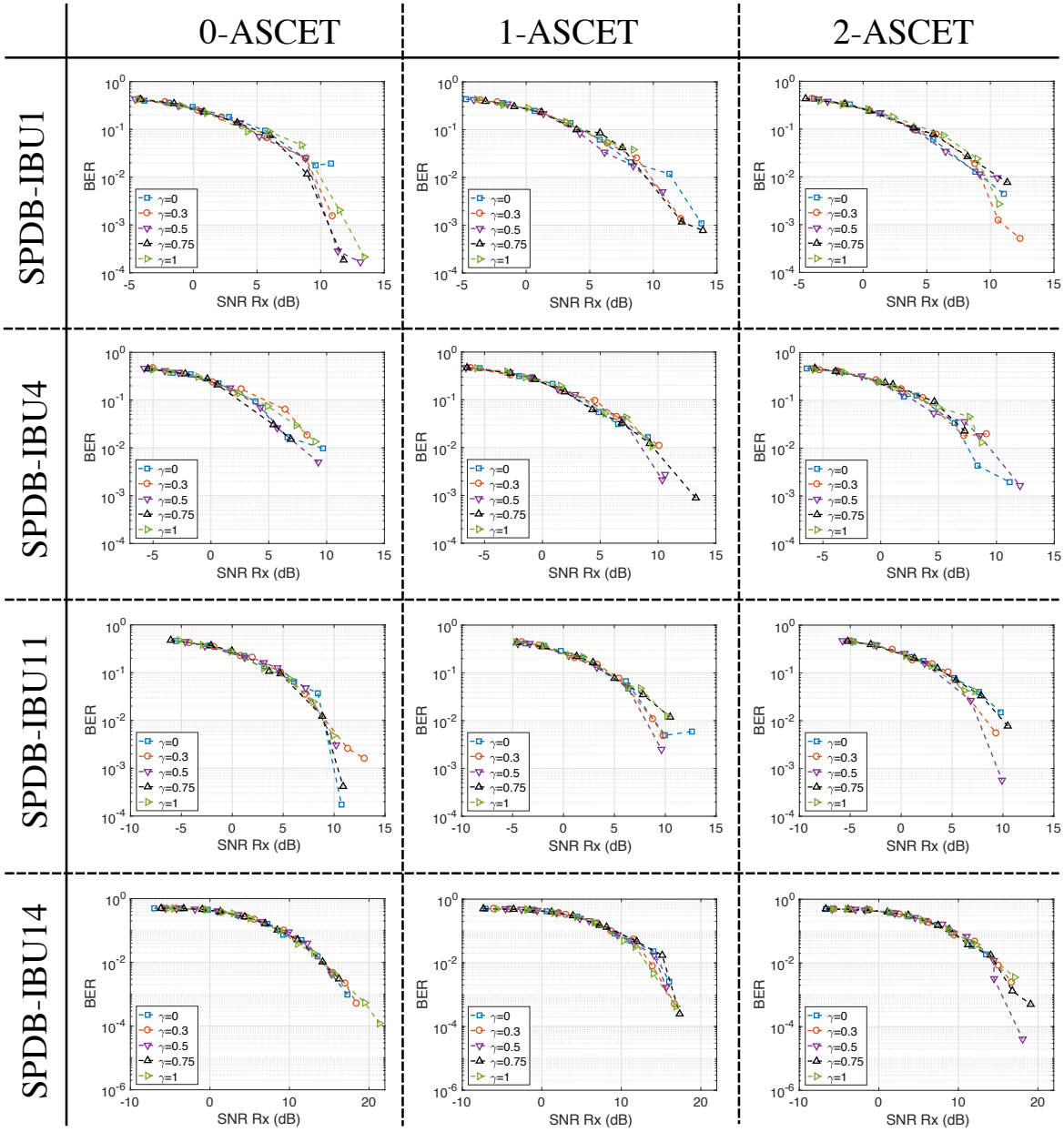

Fig. 4.25 BER for different in-aircraft PLC channel, noises and equalizers.

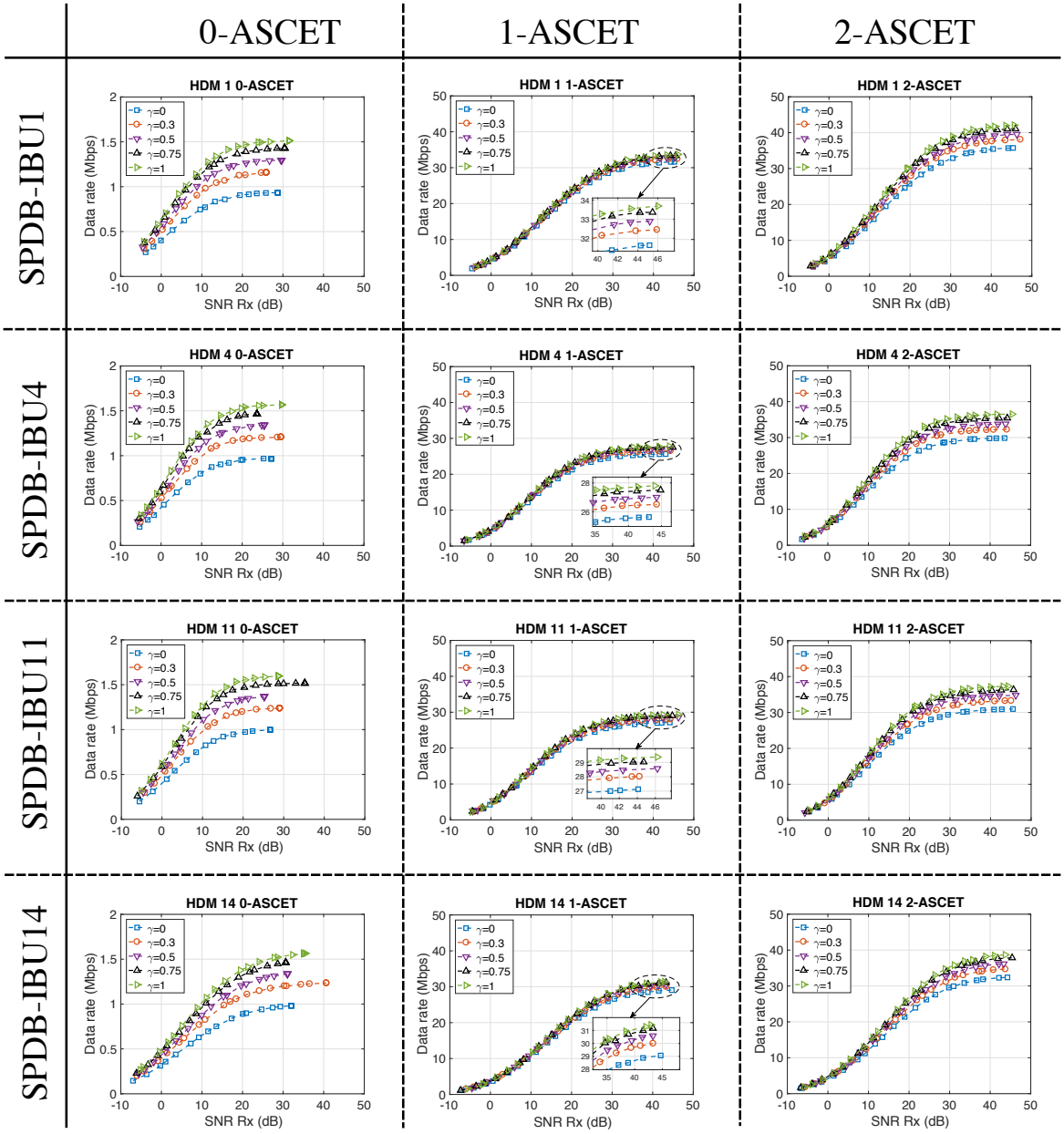

Fig. 4.26 Achievable data rate for different in-aircraft PLC channel, noises and equalizers.

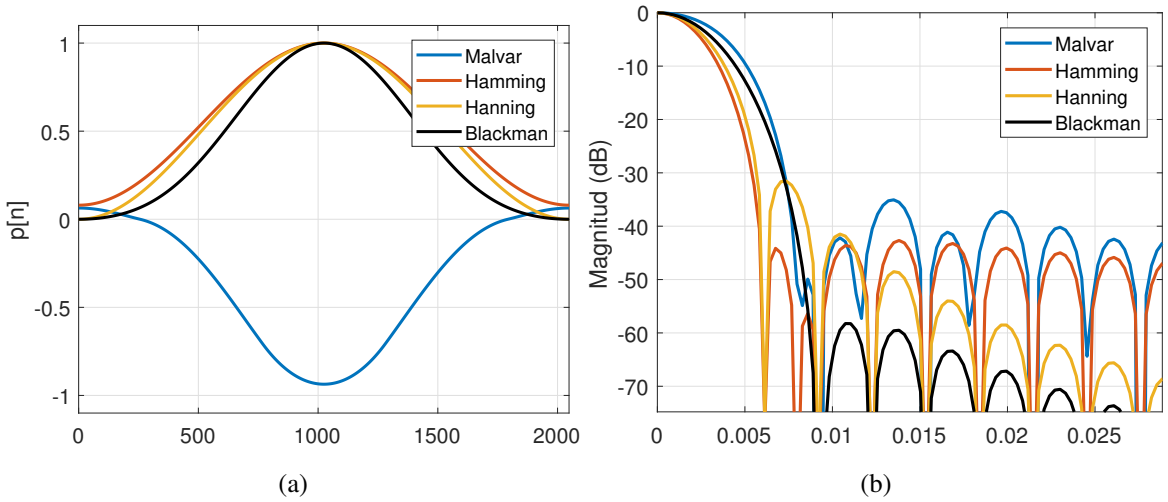

Fig. 4.27 a) Time-domain waveform and b) magnitude of the different windows under analysis.

the system performance obtained with different windows will be compared with other windows, specifically, Malvar (with $\kappa = 2$), Hanning, Hamming and Blackman window. Fig. 4.27a and 4.27b show, respectively, the time-domain waveform and the magnitude of the different windows under analysis. The system follows the specifications described at the beginning of this section (see 4.8), nonetheless, just 0- and 1-ASCET have been considered. Class 9, class 5 and AWGN have been chosen as in-home PLC channels and noise, respectively.

As can be appreciated in Fig. 4.28, the lowest BER is achieved by the system when the Malvar or the Blackman window is implemented, with just a minimum difference between both. However, when the data rate is analyzed the difference increases, in this case, the Blackman window performance is 20% higher than the Malvar window at 5 dB.

The second comparison is performed under the same conditions than in the previous one, but 0-ASCET equalizer has been replaced by 1-ASCET. The results have been shown in Fig. 4.29. Predictably, the Malvar window efficiency increases, nevertheless, it remains lower than the performance obtained with the Blackman window for both BER and data rate.

Finally, Fig. 4.30 depicts the third comparison but considering a class 5 channel. Surprisingly, under these conditions, Malvar windows provides the worst performance, while the best one is achieved by the Hamming window for both BER and data rate. Indeed, the latter achieves a BER 7 times lower and a data rate 197% higher than the former at 15 dB. However, if the equalizer complexity is increased (see Fig. 4.31), the Blackman windows outperforms the rest of windows.

In the light of these results, it is concluded that there are another waveforms that could provide a better system performance than that obtained with the recommended prototype filter (with $\kappa = 2$), at least for baseband broadband communications over the electrical wiring.

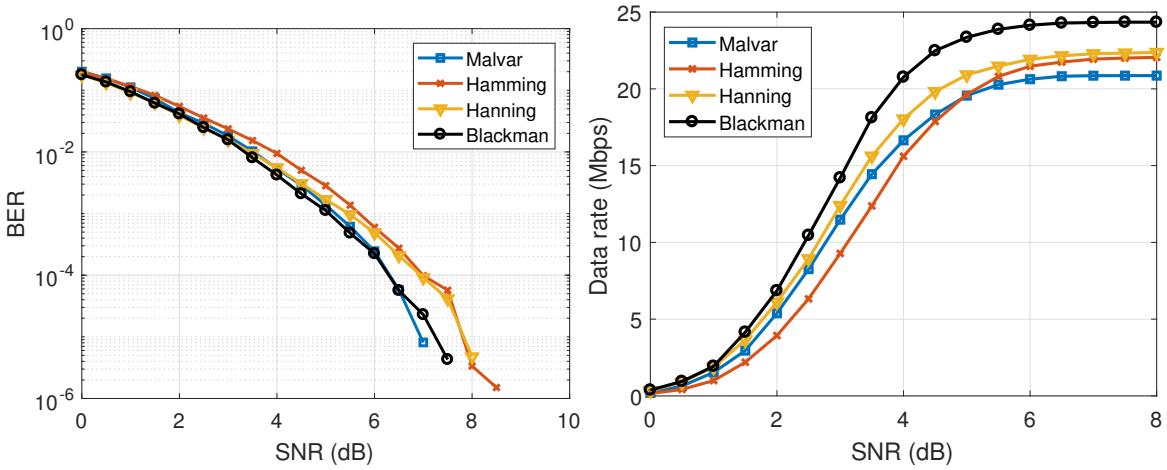

(a) BER (b) Data rate

Fig. 4.28 System performance comparison between different windows assuming class 9 and 0-ASCET.

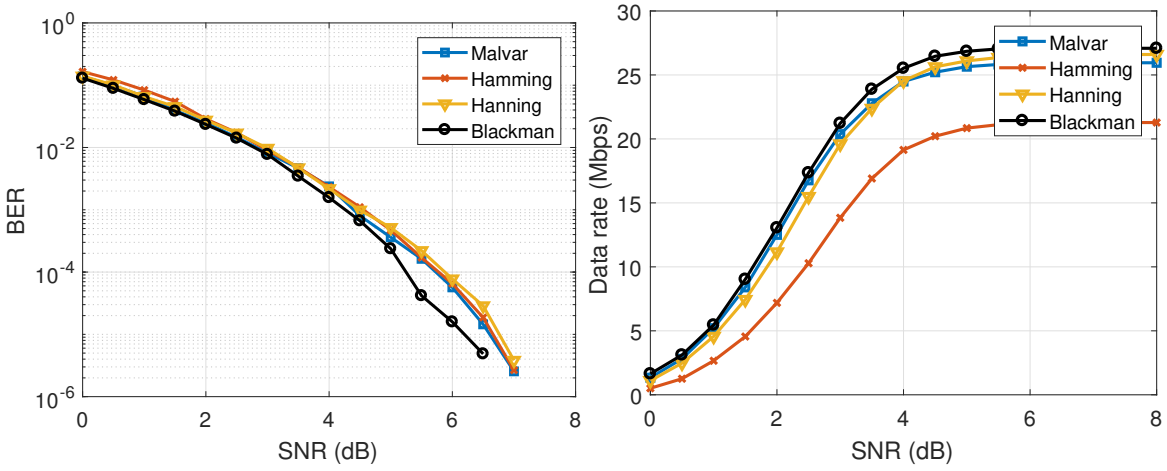

(a) BER (b) Data rate

Fig. 4.29 System performance comparison between different windows assuming class 9 and 1-ASCET.

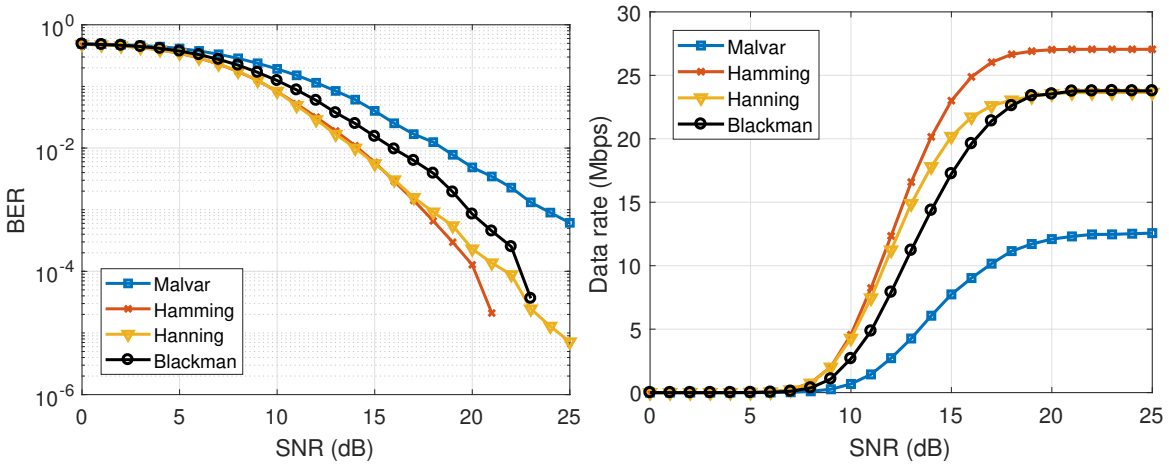

(a) BER (b) Data rate

Fig. 4.30 System performance comparison between different windows assuming class 5 and 0-ASCET.

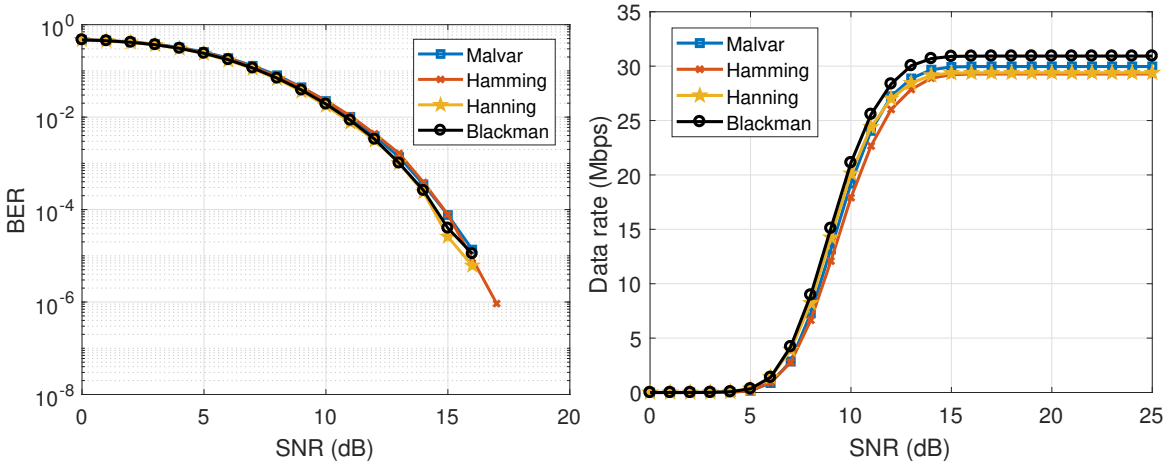

(a) BER (b) Data rate

Fig. 4.31 System performance comparison between different windows assuming class 5 and 1-ASCET.

CHAPTER 5

ELT-MCM for bandpass PLC

In the previous chapter, the baseband ELT-MCM system for broadband PLC, based on the IEEE 1901 specifications, has been developed. Nonetheless, the standard also deploys a bandpass wavelet OFDM transmitter with the goal of keeping spectral efficiency for bandpass communications [10, pp. 1196].

This chapter is intended to study the bandpass transmitter deployed by the standard and to propose a compatible receiver to demodulate the transmitted data. As in the previous chapter, an ASCET has been selected as equalization technique. Thus, an efficient implementation of the whole system based on butterfly structures, including an analysis of its computational complexity, is carried out. Likewise, the theoretical expressions to calculate the ISI, ICI, the power of the noise and the data rate are derived. Finally, the system performance is analyzed under different PLC scenarios.

5.1 Bandpass system

5.1.1 Transmitting Filter Bank

Just as with the baseband system, the standard [10] deploys for bandpass communications prototype filters $p[n]$ that can have different lengths: $N = 2\kappa M$, with $\kappa = 2$, 3, and different number of subcarriers ($M = 512, 1024, 2048$).

Assuming an overlapping factor $\kappa = 2$, the in-phase $S^I[n]$ and quadrature $S^Q[n]$ time-domain waveform signals for the frame body are stated as follows [10, pp. 1200]:

$$S^I[n] = \frac{1}{16}\left[\sum_{m=0}^{3}\sum_{k\in K_{on}} x^+_{m,k}\cdot p\,[n+Mm]\cos\left(\frac{\pi}{M}\left((n+Mm)+\frac{M+1}{2}\right)\left(k+\frac{1}{2}\right)+\theta_k\right)\right] - \frac{1}{16}\left[\sum_{m=0}^{3}\sum_{k\in K_{on}} x^-_{m,k}\cdot p\,[n+Mm]\sin\left(\frac{\pi}{M}\left((n+Mm)+\frac{M+1}{2}\right)\left(k+\frac{1}{2}\right)+\theta_k\right)\right], \quad (5.1a)$$

$$S^Q[n] = \frac{1}{16}\left[\sum_{m=0}^{3}\sum_{k\in K_{on}} x^+_{m,k}\cdot p\,[n+Mm]\cos\left(\frac{\pi}{M}\left((n+Mm)+\frac{M+1}{2}\right)\left(k+\frac{1}{2}\right)+\theta_k\right)\right] + \frac{1}{16}\left[\sum_{m=0}^{3}\sum_{k\in K_{on}} x^-_{m,k}\cdot p\,[n+Mm]\sin\left(\frac{\pi}{M}\left((n+Mm)+\frac{M+1}{2}\right)\left(k+\frac{1}{2}\right)+\theta_k\right)\right], \quad (5.1b)$$

where $0 \le n < M$, M denotes the number of subcarriers, $\mathbb{K}_{on} \subseteq \{0,\ldots,M\}$ is the set of active subchannels[1] defined by the tone mask [10], and θ_k is the phase constant for peak power reduction. Carrier data on positive and negative frequencies relative to the bandpass carrier are denoted by positive x^+ and negative x^- superscripts. Then, (5.1a) and (5.1b) can be rewritten as:

$$S^I[n] = \sum_{m\in\mathbb{Z}}\sum_{k\in\mathbb{K}_{on}}\left(x^+_{m,k}\cdot f^c_k[n-mM] - x^-_{m,k}\cdot f^s_k[n-mM]\right), \quad (5.2a)$$

$$S^Q[n] = \sum_{m\in\mathbb{Z}}\sum_{k\in\mathbb{K}_{on}}\left(x^+_{m,k}\cdot f^c_k[n-mM] + x^-_{m,k}\cdot f^s_k[n-mM]\right), \quad (5.2b)$$

where

$$f^c_k[n] = \sqrt{\frac{2}{M}}p[n]\cos\left[\left(\frac{\pi}{M}\left(k+\frac{1}{2}\right)\left(n+\frac{M+1}{2}\right)\right)\right]\cos(\theta_k), \quad (5.3a)$$

$$f^s_k[n] = \sqrt{\frac{2}{M}}p[n]\sin\left[\left(\frac{\pi}{M}\left(k+\frac{1}{2}\right)\left(n+\frac{M+1}{2}\right)\right)\right]\cos(\theta_k), \quad (5.3b)$$

Notice that, as for baseband ELT-MCM, θ_k only affects the sign of the time-domain waveform and the scale factor $\frac{1}{16}$ matches with $\sqrt{\frac{2}{M}}$ for $M = 512$. Finally, $f^c_k[n]$ and $f^s_k[n]$ are, respectively, the synthesis filters of a CMFB and a SMFB of an ELT. The set of both systems constitutes the synthesis filters of an exponentially ELT-MCM, where the transmitting filters can be written as [84]

$$f_k[n] = f^c_k[n] + j\cdot f^s_k[n] = \sqrt{\frac{2}{M}}p[n]e^{j\cdot\left(\frac{\pi}{M}\left(k+\frac{1}{2}\right)\left(n+\frac{M+1}{2}\right)\right)}\cdot\cos(\theta_k). \quad (5.4)$$

The recommended transmitter scheme is depicted in Fig. 5.1 [10, Figure 14-26], whereas the general block diagram is plotted in Fig. 5.2. Taking into account the studies performed in

[1] The index k is defined into the range of $[0, M-1]$ for the positive or negative subbands.

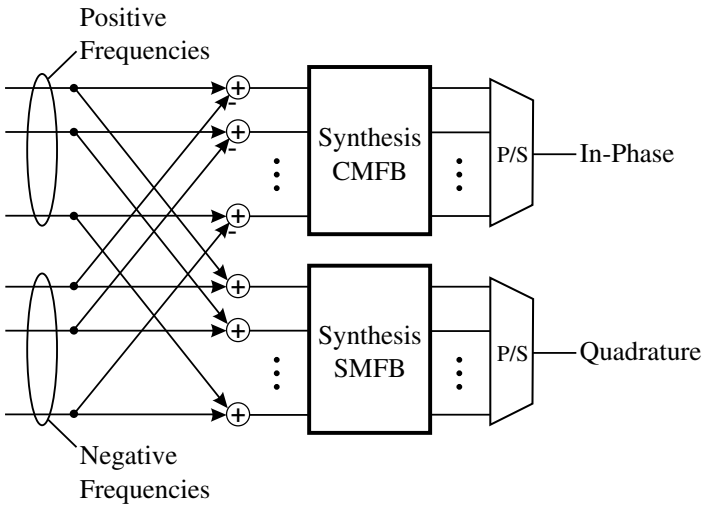

Fig. 5.1 Block diagram of the passband transmitter deployed by the standard.

[130, 124, 126], the kth complex synthesis filter can be expressed as

$$f_k^{\pm}[n] = \pm f_k^c[n] + j \cdot f_k^s[n], \tag{5.5}$$

where the positive signs stand for positive bandpass frequencies and the negative signs stand for negative frequencies. The complex bandpass Wavelet OFDM system is based on an ELT-MCM and on its sine modulated counterpart, which can be efficiently implemented by means of butterfly structures [123, 124]. Fig. 5.3 depicts an example of the proposed transmitter employing cascaded orthogonal butterflies and pure delays. Here, $\mathbf{C}_{4e}$ is a type-IV even discrete cosine transform (DCT4e) matrix, $\mathbf{S}_{4e}$ is a type-IV even discrete sine transform (DST4e) matrix, $\mathbf{\Theta}$ is an $M \times M$ diagonal matrix with elements $[\mathbf{\Theta}]_{k,k} = \cos(\theta_k)$, and $\mathbf{D}_i$ and $\mathbf{D}_i^s$ are defined as follows

$$\mathbf{D}_k = \begin{bmatrix} -\mathbf{C}_k & \mathbf{S}_k\mathbf{J} \\ \mathbf{J}\mathbf{S}_k & \mathbf{J}\mathbf{C}_k\mathbf{J} \end{bmatrix}, \tag{5.6}$$

$$\mathbf{D}_k^s = \begin{bmatrix} -\mathbf{C}_k & -\mathbf{S}_k\mathbf{J} \\ -\mathbf{J}\mathbf{S}_k & \mathbf{J}\mathbf{C}_k\mathbf{J} \end{bmatrix}. \tag{5.7}$$

where the submatrices $\mathbf{C}_k$ and $\mathbf{S}_k$ are diagonals with elements

$$[\mathbf{C}_k]_{\ell,\ell} = \cos(\vartheta_{\ell,k}), \qquad [\mathbf{S}_k]_{\ell,\ell} = \sin(\vartheta_{\ell,k}). \tag{5.8}$$

Only the butterfly implementation has been presented because it provides the lowest computational complexity for both the baseband and the passband ELT-MCM systems. Nevertheless, with the detailed study described in Ch. 4 the efficient implementation of the passband ELT-MCM system by means of both poliphase filters and lattice structures can be easily derived.

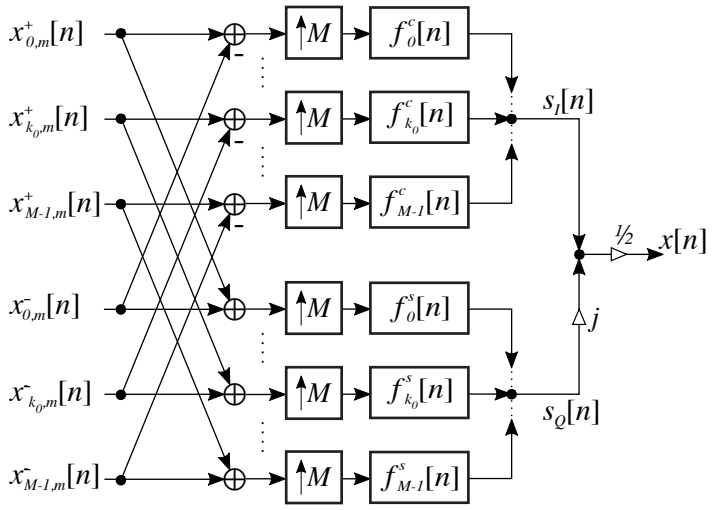

Fig. 5.2 General block diagram of the passband wavelet OFDM transmitter.

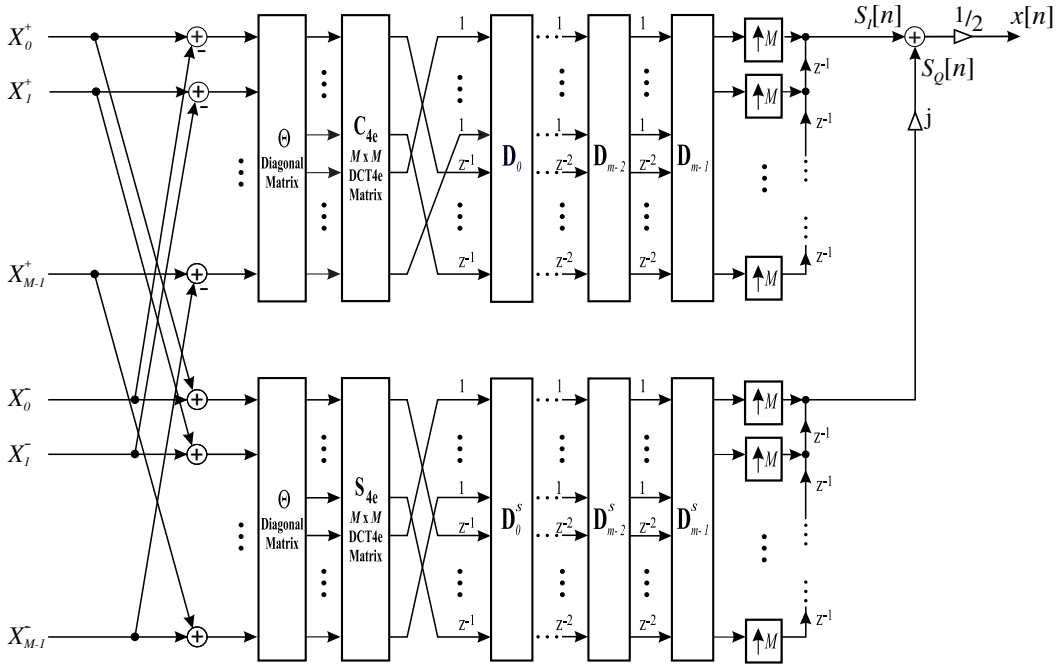

Fig. 5.3 Block diagram of the passband Wavelet OFDM transmitter implemented with butterfly structures.

5.1.2 Receiving Filter Bank

The previous transmitting bank leads to propose the following reception system:

$$h_k[n] = \sqrt{\frac{2}{M}} p[n] e^{j\cdot\left(\frac{\pi}{M}\left(k+\frac{1}{2}\right)\left(N-1-n+\frac{M+1}{2}\right)\right)} \cdot \cos\left(\theta_k\right). \tag{5.9}$$

In an equivalent way, we define

$$\begin{aligned} h_k^{\pm}[n] &= \pm h_k^c[n] - j \cdot h_k^s[n] \\ &= \pm f_k^c[N-1-n] - j \cdot f_k^s[N-1-n], \end{aligned} \tag{5.10}$$

where the k-th complex analysis filter can be implemented as the time reflection of the transmission bank

$$h_k^c[n] = \sqrt{\frac{2}{M}} \cdot p[n] \cdot \cos\left[\left(\frac{\pi}{M}\left(k+\frac{1}{2}\right)\left(N-1-n+\frac{M+1}{2}\right)\right)\right] \cdot \cos\left(\theta_k\right),$$

$$h_k^s[n] = \sqrt{\frac{2}{M}} \cdot p[n] \cdot \sin\left[\left(\frac{\pi}{M}\left(k+\frac{1}{2}\right)\left(N-1-n+\frac{M+1}{2}\right)\right)\right] \cdot \cos\left(\theta_k\right).$$

As far as the channel equalization is concerned, an ASCET can be used for ELT-based systems [38, 37, 126, 28]. Fig. 5.4 and 5.5 depict, respectively, the general block of the wavelet OFDM receiver that includes the easiest equalization technique (0-ASCET), and the receiver implemented by means of butterfly structures. With this equalizer, the transmission channel effects are compensated for by multiplying each output of the real and imaginary cosine/sine modulated receiving filter bank, respectively, by the constant numbers $c_k^{\pm}$ and $s_k^{\pm}$:

$$E_k(\omega)\big|_{\omega=(2k+1)\frac{2\pi}{4M}} = c_k^{+} - j s_k^{+} \tag{5.12a}$$

$$E_{M+k}(\omega)\big|_{\omega=(2(M+k)+1)\frac{2\pi}{4M}} = c_{M-1-k}^{-} - j s_{M-1-k}^{-} \tag{5.12b}$$

for $0 \leq k \leq M-1$. These constants $c_k^{\pm}$ and $s_k^{\pm}$ are the real and the imaginary part of E_k and E_{2M-1-k}, respectively, which can be calculated, under AWGN [37], as follows:

$$E_k\left(e^{j(2k+1)\frac{2\pi}{4M}}\right) = \frac{H_{ch}^{*}\left(e^{j(2k+1)\frac{2\pi}{4M}}\right)}{\left|H_{ch}\left(e^{j(2k+1)\frac{2\pi}{4M}}\right)\right|^2 + \frac{1}{SNR}}, \tag{5.13}$$

where H_{ch} is the channel frequency response and SNR is the signal-to-noise ratio. As as stated above, 0-ASCET could be not enough to compensate for the power line channel distortion and thus, the L-ASCET, $L > 0$, must be used. Following the development presented in Chapter 4.4.2, the coefficients of the 1-ASCET (3-tap FIR) filter, for the positives and negatives subbands, can be obtained as

$$c_{i,k}^{+} = \Re\{e_{i,k}\}, \tag{5.14a}$$

$$s_{i,k}^{+} = -\Im\{e_{i,k}\}, \tag{5.14b}$$

$$c_{i,M-1-k}^{-} = \Re\{e_{i,M+k}\}, \tag{5.14c}$$

$$s_{i,M-1-k}^{-} = -\Im\{e_{i,M+k}\}, \tag{5.14d}$$

where $0 \leq k \leq M-1$, $i = 0,1,2$, $\Re\{\cdot\}$ and $\Im\{\cdot\}$ stand for, respectively, the real and the imaginary parts,

$$e_{0,k} = \pm\frac{1}{2}\left(\frac{\eta_{0,k} - \eta_{2,k}}{2} - j\left(\eta_{1,k} - \frac{\eta_{0,k} + \eta_{2,k}}{2}\right)\right), \tag{5.15a}$$

$$e_{1,k} = \frac{\eta_{0,k} + \eta_{2,zk}}{2}, \tag{5.15b}$$

$$e_{2,k} = \pm\frac{1}{2}\left(\frac{\eta_{0,k} - \eta_{2,k}}{2} + j\left(\eta_{1,k} - \frac{\eta_{0,k} + \eta_{2,k}}{2}\right)\right), \tag{5.15c}$$

and

$$\eta_{i,k} = \frac{H_{ch}^{*}\left(e^{j\frac{\pi}{4M}(2k+i)}\right)}{\left|H_{ch}\left(e^{j\frac{\pi}{4M}(2k+i)}\right)\right|^{2} + \frac{1}{SNR}}. \tag{5.16}$$

If a higher order ASCET is required, then the same reasoning described in 4.4.2 can be used to obtain a 2-ASCET (5-tap) system.

5.1.3 Computational Complexity

The computational complexity of the proposed passband ELT-MCM receiver of Fig. 5.5, counted for length-M blocks, is here analyzed. This is derived from the best algorithm proposed in [26, 123, p. 209] with scaled coefficients in each butterfly structure, from the DCT4e implemented with the procedure presented in [129] and taking into account the results presented in Chapter 4 (see 4.5). From the foregoing it can be easily deduced that the computational complexity of this system is at least twice that the baseband ELT-MCM system. Specifically, assuming $\kappa = 2$, the multiplications of the whole receiver are contributed by the two CMFB blocks ($5M$), the two SMFB blocks ($5M$), the 0-ASCET equalizers ($4M$) and both DCT4e and DST4e, giving a total of $14M + 2 \cdot MUL_{best}$ MPIS. Likewise, the additions are contributed by the two CMFB ($5M$), the SMFB ($5M$), the 0-ASCET equalizers ($6M$) and the DCT4e and DST4e blocks, with a total of $16M + 4 \cdot ADD_{best}$ APIS. Considering one of the IEEE 1901 specifications ($M = 512$, $\kappa = 2$, and $N = 2048$), we have 18160 MPIS and 34360 APIS.

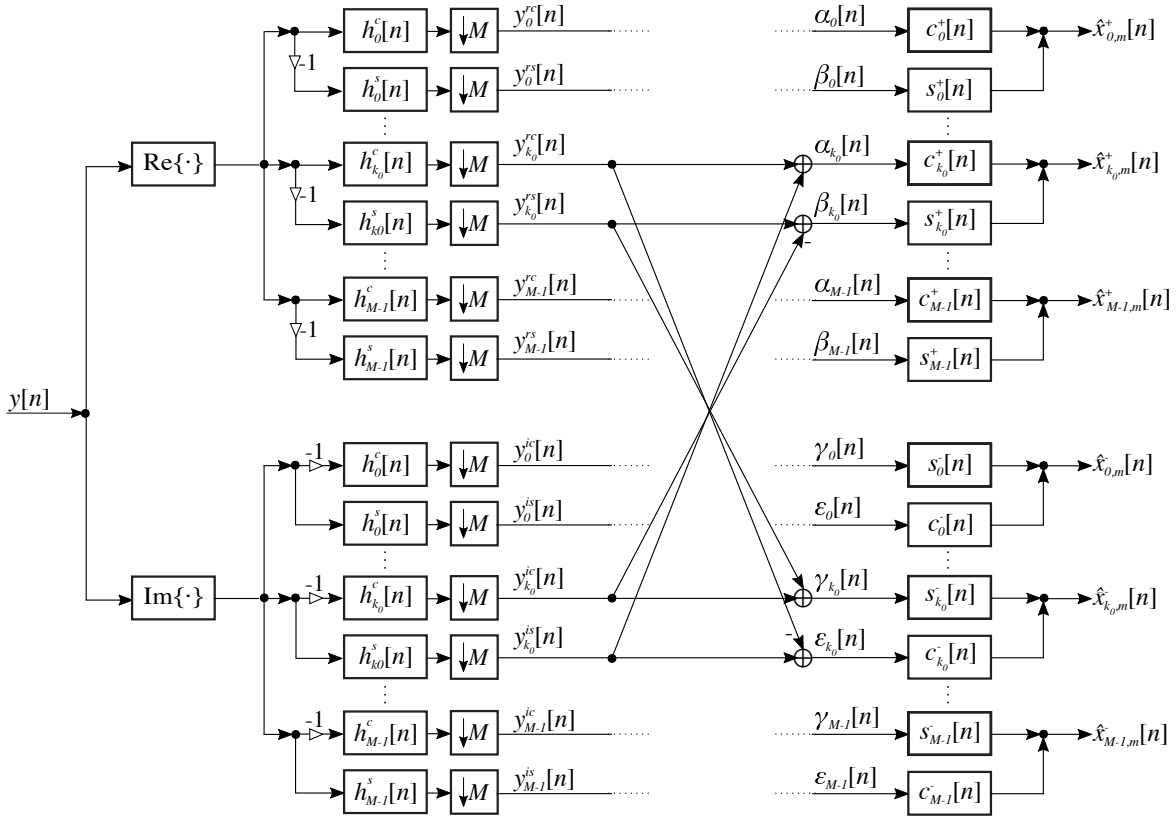

Fig. 5.4 Block diagram of the passband wavelet OFDM receiver with ASCET.

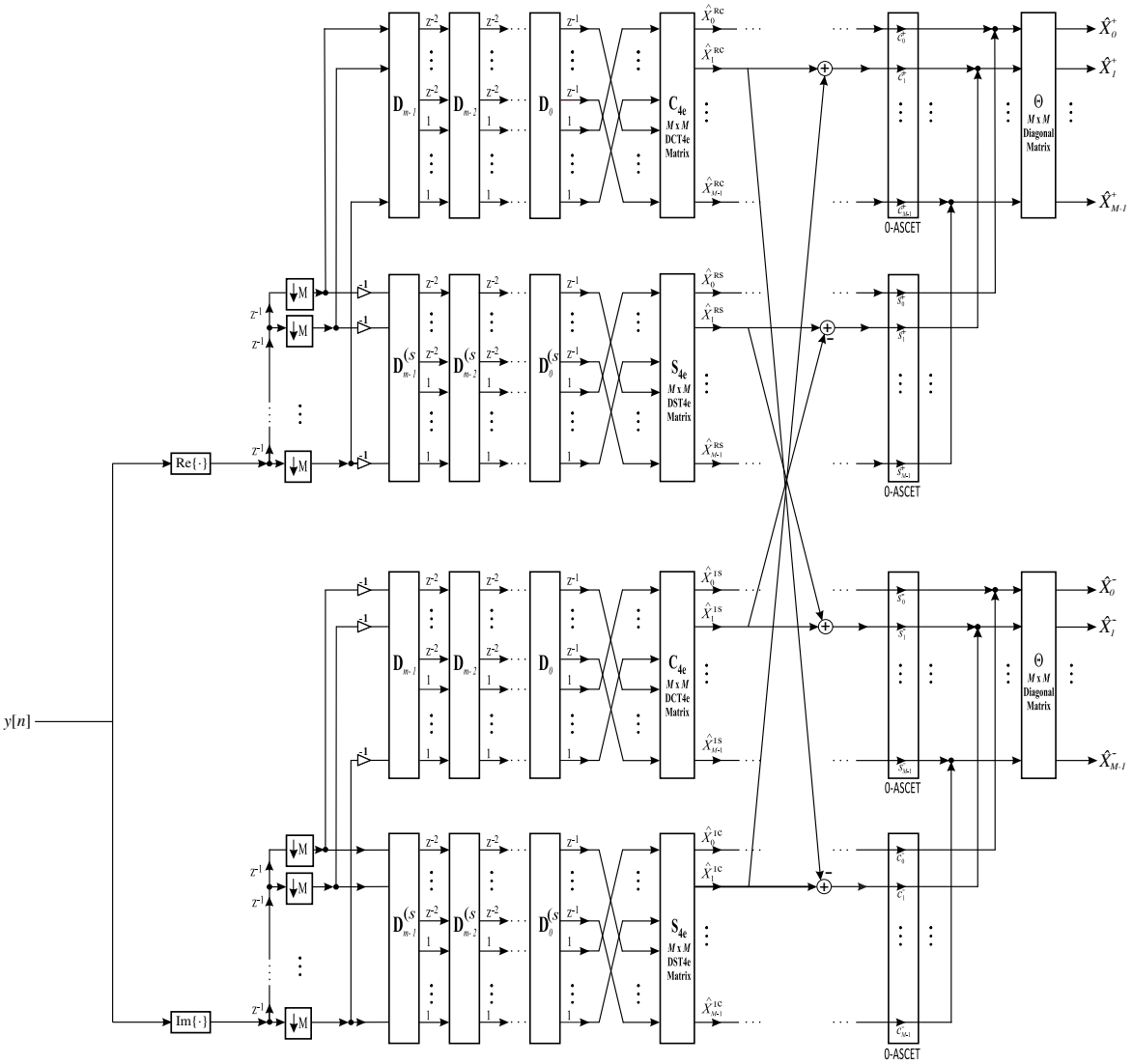

Fig. 5.5 Block diagram of the passband Wavelet OFDM receiver implemented with butterfly structures including a 0-ASCET.

5.2 Achievable data rate

This section derives the expressions to determinate the theoretical data rate of a bandpass ELT-MCM system. As in the baseband system case, this derivation is based on each transfer function that relates any input of the transmitter side to any output at the receiver side. In addition, a constellation of infinity granularity has been assumed which means that each subcarrier can transport a fractional and unlimited number of bits.

Let us consider the general block diagram of the bandpass ELT-MCM transceiver, depicted in Fig. 5.2. The discrete-time transmitted signal in the z-domain can be expressed as follows

$$X(z) = S^I(z) + j \cdot S^Q(z), \tag{5.17}$$

where

$$S^I(z) = \sum_{k \in \mathbb{K}_{on}} F_k^c(z) \left(X_k^+ \left(z^M \right) - X_k^- \left(z^M \right) \right), \tag{5.18a}$$

$$S^Q(z) = \sum_{k \in \mathbb{K}_{on}} F_k^s(z) \left(X_k^+ \left(z^M \right) + X_k^- \left(z^M \right) \right), \tag{5.18b}$$

and $F_k^c(z)$ and $F_k^s(z)$ are the system function of each filter given in (5.3a) and (5.3b), respectively. $X_k^+(z)$ ($X_k^-(z)$) is the symbol in the kth subcarrier of the positive (negative) subband, assumed to be zero-mean wide-sense stationary (WSS) process. In particular, the variance $\sigma_x^2(k)$ is assumed identical for all $X_k^{\pm}$ which are independent and identically distributed for every $k \in \mathbb{K}_{on}$. The different signals defined in (5.17) and (5.18) are plotted in the block diagram of Fig. 5.2, that represents the wavelet OFDM transmitter.

Let us consider a complex channel impulse response and complex channel noise in the z-domain, respectively expressed as $H_{ch}(z) = H_{ch}^I(z) + j \cdot H_{ch}^Q(z)$ and $R(z) = R^I(z) + j \cdot R^Q(z)$. The first block in the receiver side must introduce a delay of β samples to obtain proper system operation. Therefore, the receiver signal can be written as

$$\begin{aligned} Y(z) =& X(z) \cdot H_{ch}(z) \cdot z^{-\beta} + R(z) \cdot z^{-\beta} \\ =& \left[S^I(z) H_{ch}^I(z) - S^Q(z) H_{ch}^Q(z) + j \left(S^I(z) H_{ch}^Q(z) + S^Q(z) H_{ch}^I(z) \right) \right] \cdot z^{-\beta} + R(z) \cdot z^{-\beta}. \end{aligned} \tag{5.19}$$

First, the real part is analyzed. Thus, the ith output of the analysis CMFB in the absence of noise can be obtained as

$$\begin{aligned}
Y_i^{rc}(z) &= \frac{1}{M}\sum_{l\in\mathbb{K}_{on}} H_i^c\left(z^{\frac{1}{M}}W^l\right)\Re\left\{Y\left(z^{\frac{1}{M}}W^l\right)\right\} \\
&= \frac{1}{M}\sum_{l\in\mathbb{K}_{on}} H_i^c\left(z^{\frac{1}{M}}W^l\right)\left[S^I\left(z^{\frac{1}{M}}W^l\right)H_{ch}^I\left(z^{\frac{1}{M}}W^l\right) - S^Q\left(z^{\frac{1}{M}}W^l\right)H_{ch}^Q\left(z^{\frac{1}{M}}W^l\right)\right]\left(z^{\frac{1}{M}}W^l\right)^{-\beta} \\
&= \frac{1}{M}\sum_{l\in\mathbb{K}_{on}} H_i^c\left(z^{\frac{1}{M}}W^l\right)\left[\sum_{k\in\mathbb{K}_{on}} F_k^c\left(z^{\frac{1}{M}}W^l\right)\left(X_k^+(z) - X_k^-(z)\right)H_{ch}^I\left(z^{\frac{1}{M}}W^l\right)\right. \\
&\quad \left. - \sum_{k\in\mathbb{K}_{on}} F_k^s\left(z^{\frac{1}{M}}W^l\right)\left(X_k^+(z) + X_k^-(z)\right)H_{ch}^Q\left(z^{\frac{1}{M}}W^l\right)\right] z^{-\frac{\beta}{M}}W^{-l\beta},
\end{aligned} \tag{5.20}$$

where $H_k^c(z)$ is the z-transform of the filter given in (5.11a). Rearranging terms, the previous expressions can be rewritten as

$$\begin{aligned}
Y_i^{rc}(z) &= \frac{1}{M}\sum_{k\in\mathbb{K}_{on}} X_k^+(z)\sum_{l\in\mathbb{K}_{on}} H_i^c\left(z^{\frac{1}{M}}W^l\right)F_k^c\left(z^{\frac{1}{M}}W^l\right)H_{ch}^I\left(z^{\frac{1}{M}}W^l\right)z^{-\frac{\beta}{M}}W^{-l\beta} \\
&\quad - \frac{1}{M}\sum_{k\in\mathbb{K}_{on}} X_k^+(z)\sum_{l\in\mathbb{K}_{on}} H_i^c\left(z^{\frac{1}{M}}W^l\right)F_k^s\left(z^{\frac{1}{M}}W^l\right)H_{ch}^Q\left(z^{\frac{1}{M}}W^l\right)z^{-\frac{\beta}{M}}W^{-l\beta} \\
&\quad - \frac{1}{M}\sum_{k\in\mathbb{K}_{on}} X_k^-(z)\sum_{l\in\mathbb{K}_{on}} H_i^c\left(z^{\frac{1}{M}}W^l\right)F_k^c\left(z^{\frac{1}{M}}W^l\right)H_{ch}^I\left(z^{\frac{1}{M}}W^l\right)z^{-\frac{\beta}{M}}W^{-l\beta} \\
&\quad - \frac{1}{M}\sum_{k\in\mathbb{K}_{on}} X_k^-(z)\sum_{l\in\mathbb{K}_{on}} H_i^c\left(z^{\frac{1}{M}}W^l\right)F_k^s\left(z^{\frac{1}{M}}W^l\right)H_{ch}^Q\left(z^{\frac{1}{M}}W^l\right)z^{-\frac{\beta}{M}}W^{-l\beta}.
\end{aligned} \tag{5.21}$$

Thus, defining $T_{i,k}^{ccI}(z) = H_i^c(z)\cdot F_k^c(z)\cdot H_{ch}^I(z)$ and $T_{i,k}^{csQ}(z) = H_i^c(z)\cdot F_k^s(z)\cdot H_{ch}^Q(z)$, we get

$$\begin{aligned}
Y_i^{rc}(z) &= \frac{1}{M}\sum_{k\in\mathbb{K}_{on}} X_k^+(z)\sum_{l\in\mathbb{K}_{on}} T_{i,k}^{ccI}\left(z^{\frac{1}{M}}W^l\right)z^{-\frac{\beta}{M}}W^{-l\beta} - \frac{1}{M}\sum_{k\in\mathbb{K}_{on}} X_k^+(z)\sum_{l\in\mathbb{K}_{on}} T_{i,k}^{csQ}\left(z^{\frac{1}{M}}W^l\right)z^{-\frac{\beta}{M}}W^{-l\beta} \\
&\quad - \frac{1}{M}\sum_{k\in\mathbb{K}_{on}} X_k^-(z)\sum_{l\in\mathbb{K}_{on}} T_{i,k}^{ccI}\left(z^{\frac{1}{M}}W^l\right)z^{-\frac{\beta}{M}}W^{-l\beta} - \frac{1}{M}\sum_{k\in\mathbb{K}_{on}} X_k^-(z)\sum_{l\in\mathbb{K}_{on}} T_{i,k}^{csQ}\left(z^{\frac{1}{M}}W^l\right)z^{-\frac{\beta}{M}}W^{-l\beta} \\
&= \sum_{k\in\mathbb{K}_{on}} X_k^+(z)\left(U_{i,k}^{ccI}(z) - U_{i,k}^{csQ}(z)\right) + \sum_{k\in\mathbb{K}_{on}} X_k^-(z)\left(-U_{i,k}^{ccI}(z) - U_{i,k}^{csQ}(z)\right),
\end{aligned} \tag{5.22}$$

where the relation in the time-domain between $U(z)$ and $T(z)$ is given by $u_{i,k}^{ccI}[n] = t_{i,k}^{ccI}[nM-\beta]$ and $u_{i,k}^{csQ}[n] = t_{i,k}^{csQ}[nM-\beta]$. It is important to note that when the subchannel filters show both high selectivity and discrimination between subcarriers, the functions $t_{i,k}^{ccI}[nM-\beta]$ and $t_{i,k}^{csQ}[nM-\beta]$ are nearly zero for $k \neq \{i-1, i, i+1\}$.

Applying the same reasoning of the previous steps, the ith output of the real part of analysis SMFB, in the absence of noise, yields

$$\begin{aligned}
Y_i^{rs}(z) = &-\frac{1}{M}\sum_{k\in\mathbb{K}_{on}} X_k^+(z)\sum_{l\in\mathbb{K}_{on}} T_{i,k}^{scI}\left(z^{\frac{1}{M}}W^l\right)z^{-\frac{\beta}{M}}W^{-l\beta} + \frac{1}{M}\sum_{k\in\mathbb{K}_{on}} X_k^+(z)\sum_{l\in\mathbb{K}_{on}} T_{i,k}^{ssQ}\left(z^{\frac{1}{M}}W^l\right)z^{-\frac{\beta}{M}}W^{-l\beta}\\
&+\frac{1}{M}\sum_{k\in\mathbb{K}_{on}} X_k^-(z)\sum_{l\in\mathbb{K}_{on}} T_{i,k}^{scI}\left(z^{\frac{1}{M}}W^l\right)z^{-\frac{\beta}{M}}W^{-l\beta} + \frac{1}{M}\sum_{k\in\mathbb{K}_{on}} X_k^-(z)\sum_{l\in\mathbb{K}_{on}} T_{i,k}^{ssQ}\left(z^{\frac{1}{M}}W^l\right)z^{-\frac{\beta}{M}}W^{-l\beta}\\
= &\sum_{k\in\mathbb{K}_{on}} X_k^+(z)\left(-U_{i,k}^{scI}(z)+U_{i,k}^{ssQ}(z)\right)+\sum_{k\in\mathbb{K}_{on}} X_k^-(z)\left(U_{i,k}^{scI}(z)+U_{i,k}^{ssQ}(z)\right), \qquad (5.23)
\end{aligned}$$

where $H_k^s(z)$ is the z-transform of the filter given in (5.11a), and $T_{i,k}^{scI}(z) = H_i^s(z)\cdot F_k^c(z)\cdot H_{ch}^I(z)$, $T_{i,k}^{ssQ}(z) = H_i^s(z)\cdot F_k^s(z)\cdot H_{ch}^Q(z)$, $u_{i,k}^{scI}[n] = t_{i,k}^{scI}[nM-\beta]$ and $u_{i,k}^{ssQ}[n] = t_{i,k}^{ssQ}[nM-\beta]$.

Once the real part has been analyzed, the same study must be applied to the imaginary part. Therefore, the ith output of the analysis CMFB and SMFB, in the absence of noise, can be written as

$$\begin{aligned}
Y_i^{\imath c}(z) = &-\frac{1}{M}\sum_{k\in\mathbb{K}_{on}} X_k^+(z)\sum_{l\in\mathbb{K}_{on}} T_{i,k}^{ccQ}\left(z^{\frac{1}{M}}W^l\right)z^{-\frac{\beta}{M}}W^{-l\beta} - \frac{1}{M}\sum_{k\in\mathbb{K}_{on}} X_k^+(z)\sum_{l\in\mathbb{K}_{on}} T_{i,k}^{csI}\left(z^{\frac{1}{M}}W^l\right)z^{-\frac{\beta}{M}}W^{-l\beta}\\
&+\frac{1}{M}\sum_{k\in\mathbb{K}_{on}} X_k^-(z)\sum_{l\in\mathbb{K}_{on}} T_{i,k}^{ccQ}\left(z^{\frac{1}{M}}W^l\right)z^{-\frac{\beta}{M}}W^{-l\beta} - \frac{1}{M}\sum_{k\in\mathbb{K}_{on}} X_k^-(z)\sum_{l\in\mathbb{K}_{on}} T_{i,k}^{csI}\left(z^{\frac{1}{M}}W^l\right)z^{-\frac{\beta}{M}}W^{-l\beta}\\
= &\sum_{k\in\mathbb{K}_{on}} X_k^+(z)\left(-U_{i,k}^{ccQ}(z)-U_{i,k}^{csI}(z)\right)+\sum_{k\in\mathbb{K}_{on}} X_k^-(z)\left(U_{i,k}^{ccQ}(z)-U_{i,k}^{csI}(z)\right), \qquad (5.24)
\end{aligned}$$

where $T_{i,k}^{ccQ}(z) = H_i^c(z)\cdot F_k^c(z)\cdot H_{ch}^Q(z)$, $T_{i,k}^{csI}(z) = H_i^c(z)\cdot F_k^s(z)\cdot H_{ch}^I(z)$, $u_{i,k}^{ccQ}[n] = t_{i,k}^{ccQ}[nM-\beta]$ and $u_{i,k}^{csI}[n] = t_{i,k}^{csI}[nM-\beta]$. In addition, we have that

$$\begin{aligned}
Y_i^{\imath s}(z) = &\frac{1}{M}\sum_{k\in\mathbb{K}_{on}} X_k^+(z)\sum_{l\in\mathbb{K}_{on}} T_{i,k}^{scQ}\left(z^{\frac{1}{M}}W^l\right)z^{-\frac{\beta}{M}}W^{-l\beta} + \frac{1}{M}\sum_{k\in\mathbb{K}_{on}} X_k^+(z)\sum_{l\in\mathbb{K}_{on}} T_{i,k}^{ssI}\left(z^{\frac{1}{M}}W^l\right)z^{-\frac{\beta}{M}}W^{-l\beta}\\
&-\frac{1}{M}\sum_{k\in\mathbb{K}_{on}} X_k^-(z)\sum_{l\in\mathbb{K}_{on}} T_{i,k}^{scQ}\left(z^{\frac{1}{M}}W^l\right)z^{-\frac{\beta}{M}}W^{-l\beta} + \frac{1}{M}\sum_{k\in\mathbb{K}_{on}} X_k^-(z)\sum_{l\in\mathbb{K}_{on}} T_{i,k}^{ssI}\left(z^{\frac{1}{M}}W^l\right)z^{-\frac{\beta}{M}}W^{-l\beta}\\
= &\sum_{k\in\mathbb{K}_{on}} X_k^+(z)\left(U_{i,k}^{scQ}(z)+U_{i,k}^{ssI}(z)\right)+\sum_{k\in\mathbb{K}_{on}} X_k^-(z)\left(-U_{i,k}^{scQ}(z)+U_{i,k}^{ssI}(z)\right), \qquad (5.25)
\end{aligned}$$

where $T_{i,k}^{scQ}(z) = H_i^s(z) \cdot F_k^c(z) \cdot H_{ch}^Q(z)$, $T_{i,k}^{ssI}(z) = H_i^s(z) \cdot F_k^s(z) \cdot H_{ch}^I(z)$, $u_{i,k}^{scQ}[n] = t_{i,k}^{scQ}[nM-\beta]$ and $u_{i,k}^{ssI}[n] = t_{i,k}^{ssI}[nM-\beta]$. By adding (5.22) and (5.25), it is obtained that

$$\begin{aligned}
\alpha_i(z) =& Y_i^{rc}(z) + Y_i^{ts}(z) \\
=& \sum_{k\in\mathbb{K}_{on}} X_k^+(z)\left(U_{i,k}^{ccI}(z) - U_{i,k}^{csQ}(z) + U_{i,k}^{scQ}(z) + U_{i,k}^{ssI}(z)\right) \\
&+ \sum_{k\in\mathbb{K}_{on}} X_k^-(z)\left(-U_{i,k}^{ccI}(z) - U_{i,k}^{csQ}(z) - U_{i,k}^{scQ}(z) + U_{i,k}^{ssI}(z)\right) \\
=& \sum_{k\in\mathbb{K}_{on}} X_k^+(z)\alpha'_{i,k}(z) + \sum_{k\in\mathbb{K}_{on}} X_k^-(z)\alpha''_{i,k}(z).
\end{aligned} \tag{5.26}$$

In the same way, we get

$$\begin{aligned}
\beta_i(z) =& Y_i^{rs}(z) - Y_i^{tc}(z) \\
=& \sum_{k\in\mathbb{K}_{on}} X_k^+(z)\left(-U_{i,k}^{scI}(z) + U_{i,k}^{ssQ}(z) + U_{i,k}^{ccQ}(z) + U_{i,k}^{csI}(z)\right) \\
&+ \sum_{k\in\mathbb{K}_{on}} X_k^-(z)\left(U_{i,k}^{scI}(z) + U_{i,k}^{ssQ}(z) - U_{i,k}^{ccQ}(z) + U_{i,k}^{csI}(z)\right) \\
=& \sum_{k\in\mathbb{K}_{on}} X_k^+(z)\beta'_{i,k}(z) + \sum_{k\in\mathbb{K}_{on}} X_k^-(z)\beta''_{i,k}(z).
\end{aligned} \tag{5.27}$$

$$\begin{aligned}
\gamma_i(z) =& Y_i^{rs}(z) + Y_i^{tc}(z) \\
=& \sum_{k\in\mathbb{K}_{on}} X_k^+(z)\left(-U_{i,k}^{scI}(z) + U_{i,k}^{ssQ}(z) - U_{i,k}^{ccQ}(z) - U_{i,k}^{csI}(z)\right) \\
&+ \sum_{k\in\mathbb{K}_{on}} X_k^-(z)\left(U_{i,k}^{scI}(z) + U_{i,k}^{ssQ}(z) + U_{i,k}^{ccQ}(z) - U_{i,k}^{csI}(z)\right) \\
=& \sum_{k\in\mathbb{K}_{on}} X_k^+(z)\gamma'_{i,k}(z) + \sum_{k\in\mathbb{K}_{on}} X_k^-(z)\gamma''_{i,k}(z),
\end{aligned} \tag{5.28}$$

$$\begin{aligned}
\varepsilon_i(z) =& -Y_i^{rc}(z) + Y_i^{ts}(z) \\
=& \sum_{k\in\mathbb{K}_{on}} X_k^+(z)\left(-U_{i,k}^{ccI}(z) + U_{i,k}^{csQ}(z) + U_{i,k}^{scQ}(z) + U_{i,k}^{ssI}(z)\right) \\
&+ \sum_{k\in\mathbb{K}_{on}} X_k^-(z)\left(U_{i,k}^{ccI}(z) + U_{i,k}^{csQ}(z) - U_{i,k}^{scQ}(z) + U_{i,k}^{ssI}(z)\right) \\
=& \sum_{k\in\mathbb{K}_{on}} X_k^+(z)\varepsilon'_{i,k}(z) + \sum_{k\in\mathbb{K}_{on}} X_k^-(z)\varepsilon''_{i,k}(z).
\end{aligned} \tag{5.29}$$

Next, assuming that an L_A-ASCET is chosen as channel equalization technique, the ith demodulated symbol of the positive $(+)$ and negative $(-)$ subband can be written as

$$\begin{aligned}\hat{X}_i^+(z) &= \alpha_{i,k}(z)C_i^+(z) + \beta_{i,k}(z)S_i^+(z) \\ &= \sum_{k\in\mathbb{K}_{in}} X_k^+(z)\left(\alpha'_{i,k}(z)C_i^+(z) + \beta''_{i,k}(z)S_i^+(z)\right) + \sum_{k\in\mathbb{K}_{in}} X_k^-(z)\left(\alpha''_{i,k}(z)C_i^+(z) + \beta''_{i,k}(z)S_i^+(z)\right) \\ &= \sum_{k\in\mathbb{K}_{in}} X_k^+(z)\Upsilon'_{i,k}(z) + \sum_{k\in\mathbb{K}_{in}} X_k^-(z)\Upsilon''_{i,k}(z), \end{aligned} \tag{5.30}$$

and

$$\begin{aligned}\hat{X}_i^-(z) &= \gamma_{i,k}(z)S_i^-(z) + \varepsilon_{i,k}(z)C_i^-(z) \\ &= \sum_{k\in\mathbb{K}_{in}} X_k^+(z)\left(\gamma'_{i,k}(z)C_i^+(z) + \varepsilon''_{i,k}(z)S_i^+(z)\right) + \sum_{k\in\mathbb{K}_{in}} X_k^-(z)\left(\gamma''_{i,k}(z)C_i^+(z) + \varepsilon''_{i,k}(z)S_i^+(z)\right) \\ &= \sum_{k\in\mathbb{K}_{in}} X_k^+(z)\Psi'_{i,k}(z) + \sum_{k\in\mathbb{K}_{in}} X_k^-(z)\Psi''_{i,k}(z), \end{aligned} \tag{5.31}$$

where $C_i^{\pm}(z)$ and $S_i^{\pm}(z)$ are, respectively, the z-transform of

$$c_i^{\pm}[n] = \sum_{\mu=-L_A}^{L_A} c_{i,\mu}^{\pm} \cdot \delta[n-\mu], \tag{5.32a}$$

$$s_i^{\pm}[n] = \sum_{\mu=-L_A}^{L_A} s_{i,\mu}^{\pm} \cdot \delta[n-\mu], \tag{5.32b}$$

with $c_i[n]$ and $s_i[n]$ being the impulse response of the subcarrier filters that carry out the frequency domain equalization. Then, the reconstructed symbol can be calculated as follows

$$\hat{X}_i^+(z) = X_i^+(z)\Upsilon'_{i,i}(z) + X_i^-(z)\Upsilon''_{i,i}(z) + \sum_{\substack{k\in\mathbb{K}_{in}\\k\neq i}} X_k^+(z)\Upsilon'_{i,k}(z) + \sum_{\substack{k\in\mathbb{K}_{in}\\k\neq i}} X_k^-(z)\Upsilon''_{i,k}(z), \tag{5.33}$$

$$\hat{X}_i^-(z) = X_i^+(z)\Psi'_{i,i}(z) + X_i^-(z)\Psi''_{i,i}(z) + \sum_{\substack{k\in\mathbb{K}_{in}\\k\neq i}} X_k^+(z)\Psi'_{i,k}(z) + \sum_{\substack{k\in\mathbb{K}_{in}\\k\neq i}} X_k^-(z)\Psi''_{i,k}(z). \tag{5.34}$$

The above expressions in the time-domain yields

$$\begin{aligned}\hat{x}_i^+[n] =& \sum_{\ell}\left(v'_{i,i}[\ell]\cdot x_i^+[n-\ell]+v''_{i,i}[\ell]\cdot x_i^-[n-\ell]\right)+\sum_{\substack{k\in\mathbb{K}_{in}\\k\neq i}}\sum_{\ell}\left(v'_{i,k}[\ell]\cdot x_i^+[n-\ell]+v''_{i,k}[\ell]\cdot x_i^-[n-\ell]\right)\\ =& v'_{i,i}[0]\cdot x_i^+[n]+v''_{i,i}[0]\cdot x_i^-[n]+\underbrace{\sum_{\substack{\ell\\\ell\neq 0}}\left(v'_{i,i}[\ell]x_i^+[n-\ell]+v''_{i,i}[\ell]x_i^-[n-\ell]\right)}_{\text{ISI}}\\ &+\underbrace{\sum_{\substack{k\in\mathbb{K}_{in}\\k\neq i}}\sum_{\ell}\left(v'_{i,k}[\ell]\cdot x_i^+[n-\ell]+v''_{i,k}[\ell]\cdot x_i^-[n-\ell]\right)}_{\text{ICI}},\end{aligned}\tag{5.35}$$

$$\begin{aligned}\hat{x}_i^-[n] =& \sum_{\ell}\left(\psi'_{i,i}[\ell]\cdot x_i^+[n-\ell]+\psi''_{i,i}[\ell]\cdot x_i^-[n-\ell]\right)+\sum_{\substack{k\in\mathbb{K}_{in}\\k\neq i}}\sum_{\ell}\left(\psi'_{i,k}[\ell]\cdot x_i^+[n-\ell]+\psi''_{i,k}[\ell]\cdot x_i^-[n-\ell]\right)\\ =& \psi'_{i,i}[0]\cdot x_i^+[n]+\psi''_{i,i}[0]\cdot x_i^-[n]+\underbrace{\sum_{\substack{\ell\\\ell\neq 0}}\left(\psi'_{i,i}[\ell]x_i^+[n-\ell]+\psi''_{i,i}[\ell]x_i^-[n-\ell]\right)}_{\text{ISI}}\\ &+\underbrace{\sum_{\substack{k\in\mathbb{K}_{in}\\k\neq i}}\sum_{\ell}\left(\psi'_{i,k}[\ell]\cdot x_i^+[n-\ell]+\psi''_{i,k}[\ell]\cdot x_i^-[n-\ell]\right)}_{\text{ICI}},\end{aligned}\tag{5.36}$$

where ISI and ICI denote, respectively, the inter-symbol and the inter-carrier interference.

Finally, the power of the *i*th subcarrier signal can be calculated as

$$P_\gamma(i)^+ = \sigma_x^2\left(\left|v'_{i,i}[0]\right|^2+\left|v''_{i,i}[0]\right|^2\right),\tag{5.37}$$

$$P_\gamma(i)^- = \sigma_x^2\left(\left|\psi'_{i,i}[0]\right|^2+\left|\psi''_{i,i}[0]\right|^2\right).\tag{5.38}$$

Similarly, the power corresponding to the intersymbol and intercarrier interference of the *i*th subcarrier ($P_{ISI}(i)$ and $P_{ICI}(i)$) can be obtained as

$$\begin{aligned}P^+_{\text{INT}}(i) &= P^+_{\text{ISI}}(i)+P^+_{\text{ICI}}(i)\\ &= \sigma_x^2\left(\sum_{\substack{\ell\\\ell\neq 0}}\left(\left|v'_{i,i}[\ell]\right|^2+\left|v''_{i,i}[\ell]\right|^2\right)+\sum_{\substack{k\in\mathbb{K}_{in}\\k\neq i}}^{M-1}\sum_{\ell}\left(\left|v'_{i,k}[\ell]\right|^2+\left|v''_{i,k}[\ell]\right|^2\right)\right),\end{aligned}\tag{5.39}$$

$$P_{\mathrm{INT}}^{-}(i) = P_{\mathrm{ISI}}^{-}(i) + P_{\mathrm{ICI}}^{-}(i)$$
$$= \sigma_x^2 \left(\sum_{\substack{\ell \\ \ell \neq 0}} \left(\left| \psi'_{i,i}[\ell] \right|^2 + \left| \psi''_{i,i}[\ell] \right|^2 \right) + \sum_{\substack{k \in \mathbb{K}_{in} \\ k \neq i}}^{M-1} \sum_{\ell} \left(\left| \psi'_{i,k}[\ell] \right|^2 + \left| \psi''_{i,k}[\ell] \right|^2 \right) \right). \tag{5.40}$$

With regard to the noise at the ith output of the analysis CMFB/SMFB, related to the real and imaginary part, it can be obtained as

$$r_i^{rc}[n] = \sum_t h_i^c[t] \cdot r_I[nM - t - \beta], \tag{5.41}$$

$$r_i^{rs}[n] = \sum_t h_i^s[t] \cdot r_I[nM - t - \beta], \tag{5.42}$$

$$r_i^{ic}[n] = \sum_t h_i^c[t] \cdot r_Q[nM - t - \beta], \tag{5.43}$$

$$r_i^{is}[n] = \sum_t h_i^s[t] \cdot r_Q[nM - t - \beta]. \tag{5.44}$$

Therefore, the noise at the ith demodulated symbol of the positive subbands is

$$r_i^{+}[n] = \sum_{\mu=-L_A}^{L_A} c_{i,\mu} \left(r_i^{rc}[n-\mu] + r_i^{is}[n-\mu] \right) + s_{i,\mu} \left(r_i^{rs}[n-\mu] - r_i^{ic}[n-\mu] \right), \tag{5.45}$$

whereas that of the negative subbands is given by

$$r_i^{-}[n] = \sum_{\mu=-L_A}^{L_A} c_{i,\mu} \left(-r_i^{rc}[n-\mu] + r_i^{is}[n-\mu] \right) + s_{i,\mu} \left(r_i^{rs}[n-\mu] + r_i^{ic}[n-\mu] \right). \tag{5.46}$$

Therefore, the noise power yields

$$
\begin{aligned}
P_r^+(i) = & \sum_{\mu_1=-L_A}^{L_A}\sum_{\mu_2=-L_A}^{L_A}\left[\sum_{t_1}\sum_{t_2} R_r^{II}(t_1+\mu_1 M, t_2+\mu_2 M)\right. \\
& \left.\times\left(c_{i,\mu_1}^+ c_{i,\mu_2}^+ h_i^c[t_1]h_i^c[t_2] + s_{i,\mu_1}^+ s_{i,\mu_2}^+ h_i^s[t_1]h_i^s[t_2] + 2c_{i,\mu_1}^+ s_{i,\mu_2}^+ h_i^c[t_1]h_i^s[t_2]\right)\right] \\
& + 2\sum_{\mu_1=-L_A}^{L_A}\sum_{\mu_2=-L_A}^{L_A}\left[\sum_{t_1}\sum_{t_2} R_r^{IQ}(t_1+\mu_1 M, t_2+\mu_2 M)\right. \\
& \left.\times\left(c_{i,\mu_1}^+ c_{i,\mu_2}^+ h_i^c[t_1]h_i^s[t_2] - c_{i,\mu_1}^+ s_{i,\mu_2}^+ h_i^c[t_1]h_i^c[t_2] + s_{i,\mu_1}^+ c_{i,\mu_2}^+ h_i^s[t_1]h_i^s[t_2] - s_{i,\mu_1}^+ s_{i,\mu_2}^+ h_i^s[t_1]h_i^c[t_2]\right)\right] \\
& + \sum_{\mu_1=-L_A}^{L_A}\sum_{\mu_2=-L_A}^{L_A}\left[\sum_{t_1}\sum_{t_2} R_r^{QQ}(t_1+\mu_1 M, t_2+\mu_2 M)\right. \\
& \left.\times\left(c_{i,\mu_1}^+ c_{i,\mu_2}^+ h_i^s[t_1]h_i^s[t_2] + s_{i,\mu_1}^+ s_{i,\mu_2}^+ h_i^c[t_1]h_i^c[t_2] - 2c_{i,\mu_1}^+ s_{i,\mu_2}^+ h_i^s[t_1]h_i^c[t_2]\right)\right],
\end{aligned}
\tag{5.47}
$$

$$
\begin{aligned}
P_r^-(i) = & \sum_{\mu_1=-L_A}^{L_A}\sum_{\mu_2=-L_A}^{L_A}\left[\sum_{t_1}\sum_{t_2} R_r^{II}(t_1+\mu_1 M, t_2+\mu_2 M)\right. \\
& \left.\times\left(c_{i,\mu_1}^- c_{i,\mu_2}^- h_i^c[t_1]h_i^c[t_2] + s_{i,\mu_1}^- s_{i,\mu_2}^- h_i^s[t_1]h_i^s[t_2] - 2c_{i,\mu_1}^- s_{i,\mu_2}^- h_i^c[t_1]h_i^s[t_2]\right)\right] \\
& + 2\sum_{\mu_1=-L_A}^{L_A}\sum_{\mu_2=-L_A}^{L_A}\left[\sum_{t_1}\sum_{t_2} R_r^{IQ}(t_1+\mu_1 M, t_2+\mu_2 M)\right. \\
& \left.\times\left(-c_{i,\mu_1}^- c_{i,\mu_2}^- h_i^c[t_1]h_i^s[t_2] - c_{i,\mu_1}^- s_{i,\mu_2}^- h_i^c[t_1]h_i^c[t_2] + s_{i,\mu_1}^- c_{i,\mu_2}^- h_i^s[t_1]h_i^s[t_2] + s_{i,\mu_1}^- s_{i,\mu_2}^- h_i^s[t_1]h_i^c[t_2]\right)\right] \\
& + \sum_{\mu_1=-L_A}^{L_A}\sum_{\mu_2=-L_A}^{L_A}\left[\sum_{t_1}\sum_{t_2} R_r^{QQ}(t_1+\mu_1 M, t_2+\mu_2 M)\right. \\
& \left.\times\left(c_{i,\mu_1}^- c_{i,\mu_2}^- h_i^s[t_1]h_i^s[t_2] + s_{i,\mu_1}^- s_{i,\mu_2}^- h_i^c[t_1]h_i^c[t_2] + 2c_{i,\mu_1}^- s_{i,\mu_2}^- h_i^s[t_1]h_i^c[t_2]\right)\right],
\end{aligned}
\tag{5.48}
$$

where

$$
R_r^{II}(t_1+\mu_1 M, t_2+\mu_2 M) = E\left[r_I\left[(n-\mu_1)M - t_1 - \beta\right] r_I\left[(n-\mu_2)M - t_2 - \beta\right]\right], \tag{5.49}
$$

$$
R_r^{IQ}(t_1+\mu_1 M, t_2+\mu_2 M) = E\left[r_I\left[(n-\mu_1)M - t_1 - \beta\right] r_Q\left[(n-\mu_2)M - t_2 - \beta\right]\right], \tag{5.50}
$$

$$
R_r^{QQ}(t_1+\mu_1 M, t_2+\mu_2 M) = E\left[r_Q\left[(n-\mu_1)M - t_1 - \beta\right] r_Q\left[(n-\mu_2)M - t_2 - \beta\right]\right], \tag{5.51}
$$

with $R_r(t_1,t_2)$ and $E[\cdot]$ denoting the noise autocorrelation between times t_1 and t_2 and the expected value, respectively. Assuming that the PLC noise is a stationary stochastic processes, $R_r(t_1+\mu_1 M, t_2+\mu_2 M)$ can be rewritten as $R_r(\tau)$ being $\tau=(t_2-t_1)+M(\mu_2-\mu_1)$. Meanwhile, it is important to note that if the PLC noise is AWGN, (5.47) and (5.48) can be simplified as follows

$$P_r^+(k_0)=\sigma_r^2\left(\sum_{t=0}^{N+2L_A}\left|h_{k_0,\mu}^{cc+}[t]+h_{k_0,\mu}^{ss+}[t]\right|^2+\left|h_{k_0,\mu}^{cs+}[t]-h_{k_0,\mu}^{sc+}[t]\right|^2\right), \tag{5.52}$$

$$P_r^-(k_0)=\sigma_r^2\left(\sum_{t=0}^{N+2L_A}\left|h_{k_0,\mu}^{cc-}[t]-h_{k_0,\mu}^{ss-}[t]\right|^2+\left|h_{k_0,\mu}^{cs-}[t]+h_{k_0,\mu}^{sc-}[t]\right|^2\right), \tag{5.53}$$

where

$$h_{k_0,\mu}^{cc\pm}[n]=h_{k_0}^{c}[n]*c_k^{\pm}[n], \qquad h_{k_0,\mu}^{ss\pm}[n]=h_{k_0}^{s}[n]*s_k^{\pm}[n], \tag{5.54}$$

$$h_{k_0,\mu}^{cs\pm}[n]=h_{k_0}^{c}[n]*s_k^{\pm}[n], \qquad h_{k_0,\mu}^{sc\pm}[n]=h_{k_0}^{s}[n]*c_k^{\pm}[n]. \tag{5.55}$$

With this information, the SINR can be calculated as

$$\mathrm{SINR}^{\pm}(i)=\frac{P_{\gamma}^{\pm}(i)\,\sigma_x^2}{P_{ICI+ISI}^{\pm}(i)+P_r^{\pm}(i)}. \tag{5.56}$$

Finally, the wavelet OFDM achievable data rate can be obtained as

$$T_R^{\pm}=\sum_{m=0}^{M-1}\Delta_f\cdot C^{\pm}(i), \tag{5.57}$$

where $C^{\pm}(i)$ is the maximal data rate for the ith subcarrier, which can be calculated by means of the following expression:

$$C^{\pm}(i)=\log_2\left(1+\frac{\mathrm{SINR}^{\pm}(i)}{\chi}\right), \tag{5.58}$$

where χ has been fixed to 5.57 dB, leading to a target SER of 10^{-3}.

5.3 Simulation results

In this section, the performance of the bandpass ELT-MCM system is analyzed in terms of BER and data rate. The system is implemented with the following IEEE 1901 specifications, however, the maximum transmitted power has been fixed to -35 dBm/Hz. The number of subcarriers in positive and negative subbands is $M=512$, with only 360 active subcarriers (M_{ac}) in the range of $[1.8-50]$ MHz. Additionally, the prototype filter is selected with $\kappa=2$. The frequency spacing (Δ_f) equals 61.035 KHz. FEC system, based on the concatenated encoder with a coding rate of $1/2$ [10, 14.3], has been also used to calculate the BER. Meanwhile, a non-FEC system has been employed to obtain the

achievable data rate. Besides, the equalization process is carried out by 0-ASCET (1-tap), 1-ASCET (3-tap) or 2-ASCET (5-tap).

The in-home PLC channels are modeled following the Tonello's model. Particularly, a set of 100 realizations of the channel models: Class 9 (little signal attenuation), Class 5 (medium attenuation) and Class 1 (strong attenuation) have been employed. Furthermore, and as in previous simulations, it is assumed that the channel remains constant during each multicarrier symbol and that it is perfectly known at the receiver side.

For the simulations, the average Signal-to-Noise Ratio (SNR) is obtained from the receiver side as follows [15]:

$$\mathrm{SNR_{RX}} = 10\log_{10}\left(\frac{1}{M_{ac}}\sum_{k\in\mathbb{K}_{on}}\frac{|H_k|^2\sigma_x^2(k)}{\sigma_n^2(k)}\right), \tag{5.59}$$

where H_k is the frequency channel coefficient and $\sigma_n^2(k)$ denotes the noise level at the k-th subcarrier. Furthermore, the noise in the PLC system consists of colored background noise (BGN), periodic impulsive noise synchronous (PINS) and asynchronous (PINA) to mains frequency (PINs), asynchronous impulsive noise (AIN) and narrowband interference (NBI) [86]. For simplicity, PINS and PINA will be grouped and referred to as "periodic impulsive noises" (PINs). All of these noises have been modeled by the Lampe's model [105].

Fig. 5.6 depicts the BER obtained, under the above conditions for a BPSK (referred to as 2-PAM by the standard) modulation. As can be appreciated, the system achieves a very good performance even when PINs and AIN are added to BGN. Nevertheless, the system efficiency declines when NBI appears, even when the equalizer complexity is increased up to 5-tap (2-ASCET).

Fig. 5.7 shows the resulting data rate, considering a constellation of infinity granularity, and Table 5.1 summarizes the results obtained by each equalizer for SNR=20 dB, considering either BGN or all kind of noises. It can be noticed that even though the performance in terms of BER is quite similar, the data rate achieved for the system increases when the equalizer complexity also increases. For instance, the ELT-MCM data rate associated with 2-ASCET is 605% higher than 0-ASCET and 8% greater than 1-ASCET for Class 9 and BGN, SNR= 20 dB. Nonetheless, these results suggest that the difference in data rate will be negligible if a more complex equalizer (e.g. 3-ASCET or higher) is used, therefore, a 2-ASCET could be a good ending point.

Finally, Fig. 5.8 and 5.9 show the empirical cumulative distribution function (CDF) of the BER and empirical complementary cumulative distribution function (CCDF) of the achievable data rate, respectively. They provide a simple comparison between all of the scenarios that have been analyzed. It can be concluded that when the NBI is not taken into account, the BER is lower than $1\cdot10^{-3}$ at least the 68% (21%) of the time for the Class 9 (Class 5) PLC channel. Likewise, the 90th percentile of the CCDF is equal to 3.8 Mbps, 8.68 Mbps and 10 Mbps, respectively for 0-, 1- and 2-ASCET in the worst case. However, the BER is severely affected, despite the ECC system, and the data rate decreases around 35% when NBI disrupts the channel.

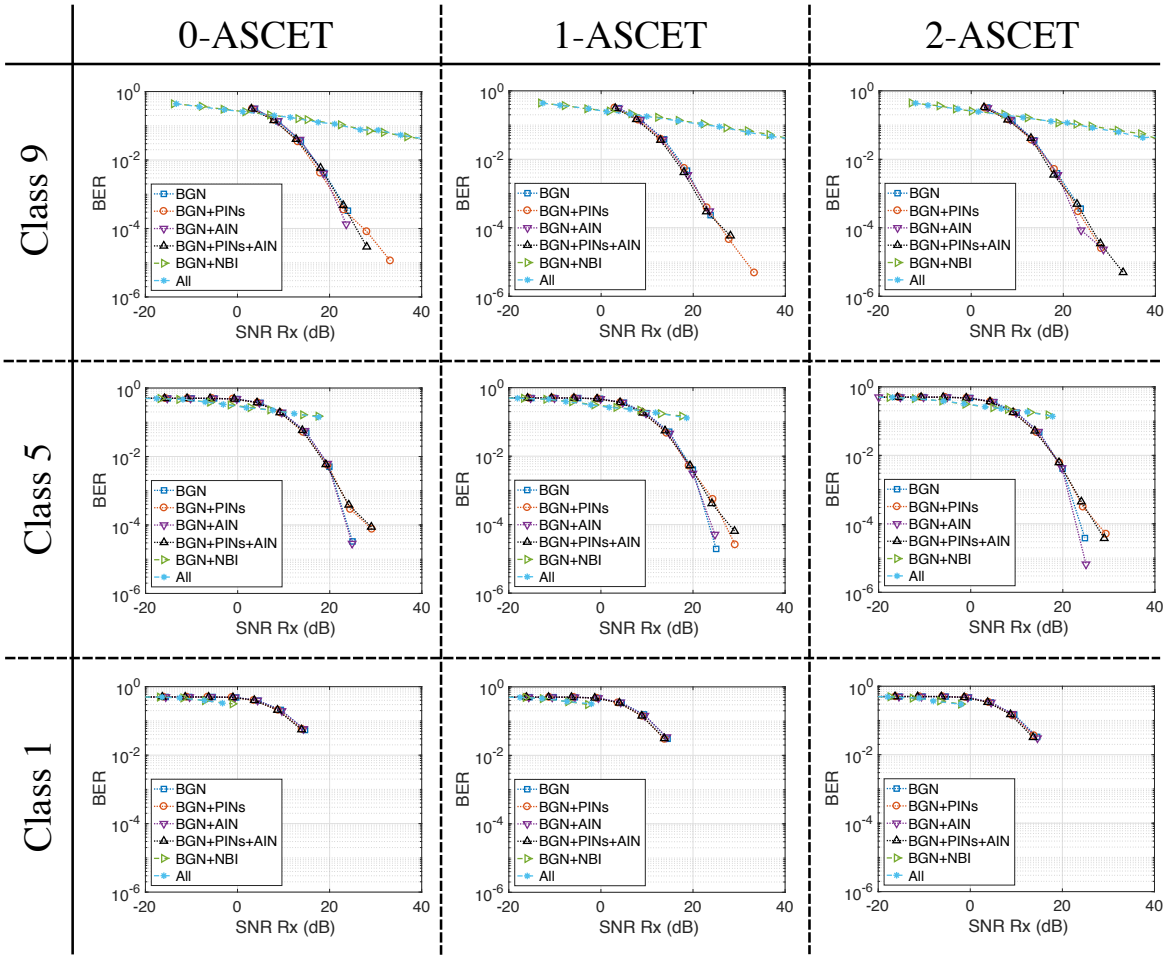

Fig. 5.6 BER for different in-home PLC channel, noises and equalizers.

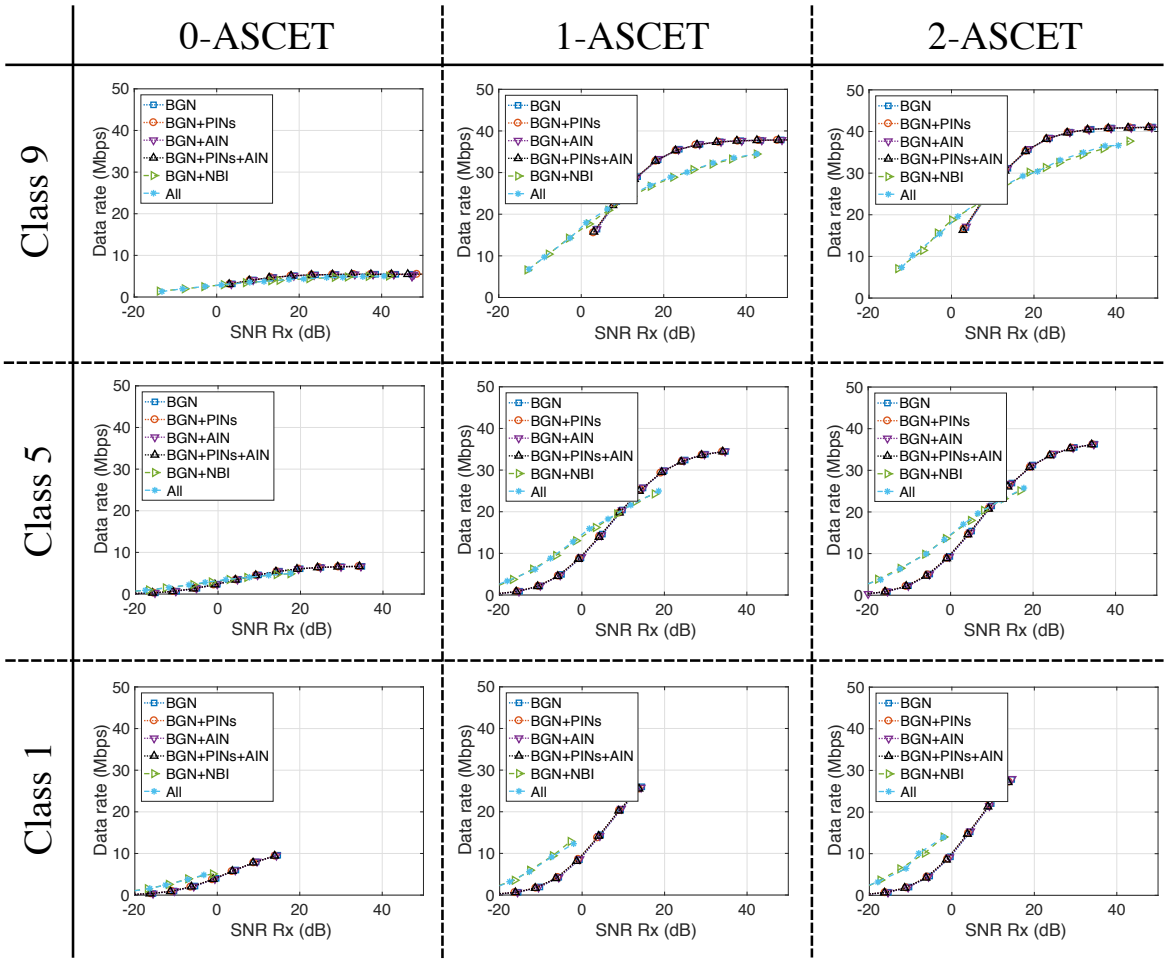

Fig. 5.7 Achievable data rate for different in-home PLC channel, noises and equalizers.

Table 5.1 Results of data Rate for Different Noises (SNR= 15 dB).

	0-ASCET	**1-ASCET**	**2-ASCET**
	Class 9		
Data rate with BGN (Mbps)	4.83	30.10	32.33
Data rate with all noises (Mbps)	4.02	26.08	28.11
	Class 5		
Data rate with BGN (Mbps)	5.50	25.88	27.03
Data rate with all noises (Mbps)	4.74	23.16	24.30
	Class 1		
Data rate with BGN (Mbps)	9.59	26	27.84
Data rate with all noises (Mbps)	−−	−−	−−

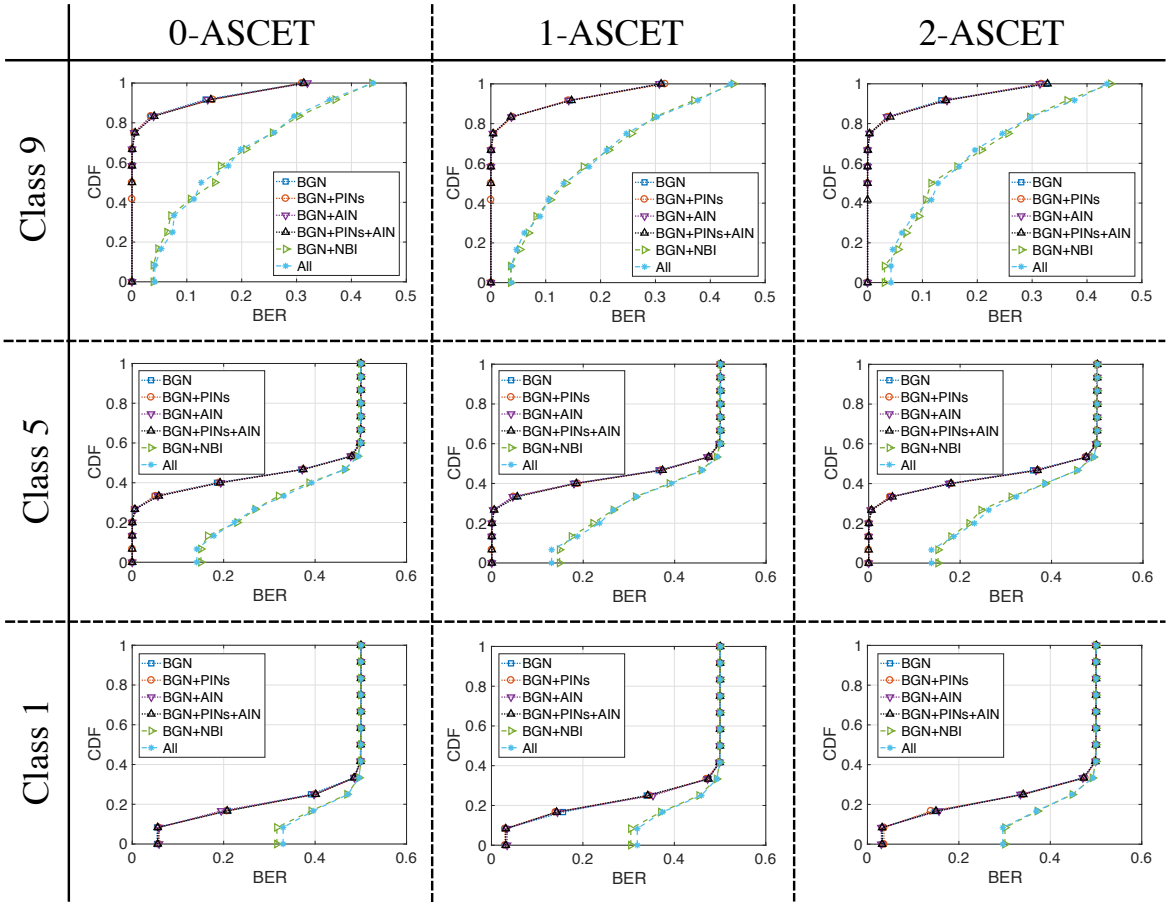

Fig. 5.8 Empirical CDF of BER for different PLC channel under different noise conditions.

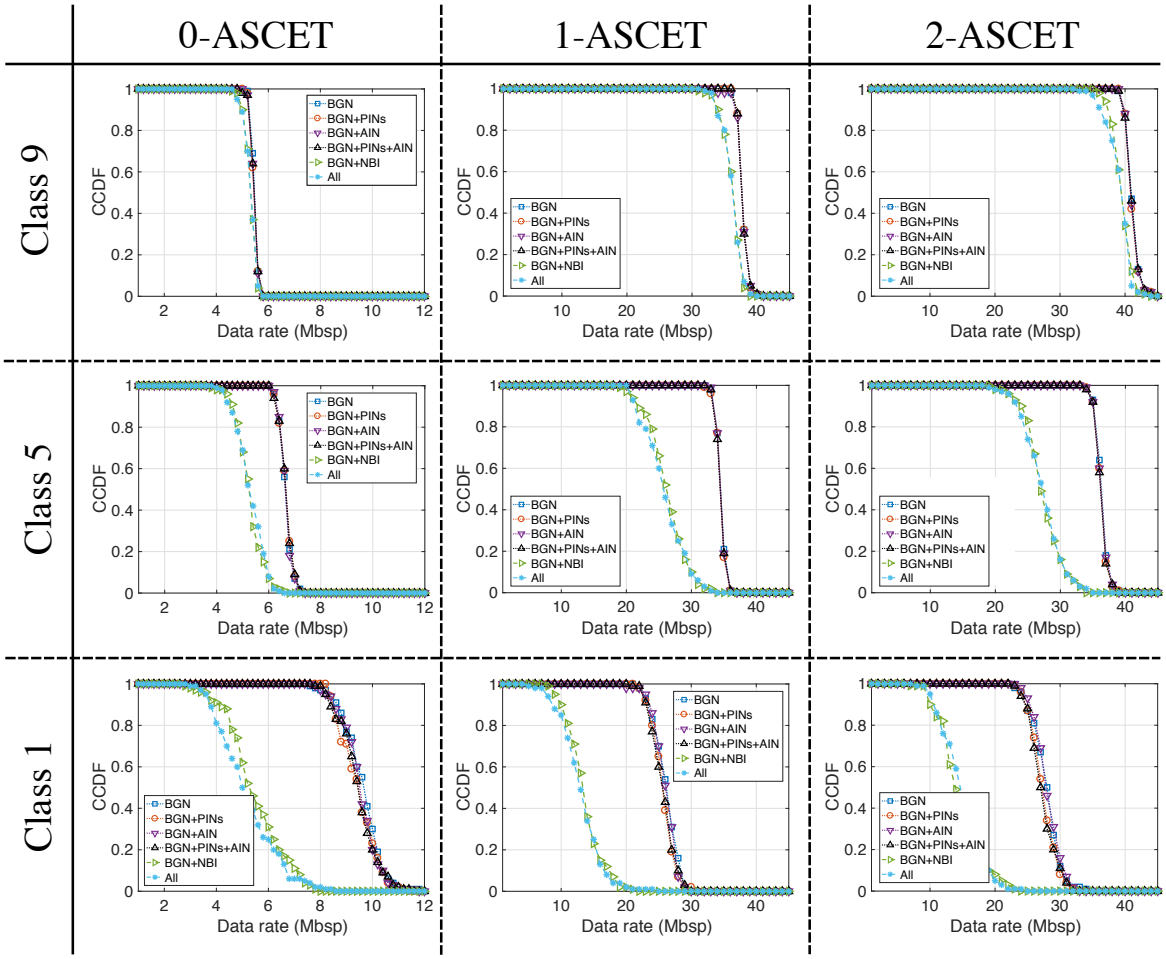

Fig. 5.9 Empirical coverage for different PLC channel under different noise conditions.

Since the maximum transmitted power was fixed to -35 dBm/Hz and the Class 1 attenuation is really high, the system can not reach a BER lower than 10^{-2}. Nonetheless, this issue can be solved increasing the transmitted power, not practical in real implementation, or applying noise reduction techniques.

CHAPTER 6

Conclusions and Further Research

The popularity of broadband communications over the electrical wiring for smart grid, IoT, in-vehicle applications and for outdoors and in-home data communications systems, has grown a great deal. Broadband PLC can be a good solution for the "last mile" problem since it provides communication to isolated places, and for the "last inch" problem since it implements indoor high-speed networks. In addition, it simplifies design and reduces development and maintenance costs, which are really attractive features for the automotive and aerospace industries. Because of the importance of the topic, this thesis is aimed at developing a communication system that achieves a high performance under different PLC conditions. To this end, an in-depth review of the main aspects of the wavelet OFDM physical layer for broadband PLC, defined by the IEEE P1901 working group, has been realized. In the rest of this chapter, we formulate the main conclusions of this thesis in section 6.1, highlight the main novel contributions in section 6.2, and give some suggestions for further research in section 6.3.

6.1 Conclusions

The analysis of the time-domain waveform signal defined by the standard demonstrates that this system is neither based on the wavelet transform nor the conventional definition of cosine modulated filter bank, but it is indeed a filter bank multicarrier system based on the extended lapped transform (ELT-MCM), in contrast to what is claimed in the rest of the scientific literature.

In reference to the prototype filter deployed by the standard, it has been derived the expression to obtain the coefficients of the recommended prototype filter with an overlapping factor $\kappa = 2$. It has been shown that it belongs to a family of windows proposed by Malvar that fulfills the perfect

reconstruction property. Specifically, it has been defined with a γ-factor (trade-off between the stopband attenuation and the transition band width) equals 0.3.

It has also proven that prototype filter with $\kappa = 3$ does not fulfill the perfect reconstruction property. It must be emphasized that the effects of γ-factor on the system performance has been analyzed in terms of bit-error-rate and data rate, concluding that, under the scenarios described in the thesis, the system performance improves as γ increases. Moreover, the performance obtained with the recommended prototype filter has been compared with other widely used window functions (e.g. Hanning, Hamming and Blackman), and it has been concluded that there are another options that can provide a better system performance.

Regarding the equalization process, the ASCET is one of the simplest frequency-domain equalizers for CMFB system. In general terms, it provides a good performance under different PLC conditions, i.e. in-home, in-car and in-aircraft PLC, provided that the equalizer order is higher than 0. Nevertheless, increasing the order of the equalizer directly leads to an increase of the computational complexity at the receiver. Therefore, a trade-off between these both concepts must be derived. Results indicate that the difference in system performance will be negligible if a 3-ASCET equalizer (or higher) is used, therefore, a 2-ASCET could be a good ending point.

With respect to the baseband wavelet OFDM system, it can be efficiently implemented by means of polyphase filters, lattice structures and butterfly structures. Nonetheless, the computational complexity analysis proves that the butterfly structures provides the lowest cost in terms of MPIS and APIS.

It has been proven that baseband wavelet OFDM communication scheme achieves an excellent performance in terms of BER and throughput, under both in-home PLC and in-vehicle PLC scenarios. Indeed, the simulation results have shown that wavelet OFDM outperforms windowed OFDM under hostile PLC channels, providing the former a more uniform data rate than the latter. This phenomenon has been explained analyzing the interference power of both multicarrier schemes.

A broadband bandpass system has also been developed, and the whole transceiver has been efficiently implemented by means of butterfly structures, using the same prototype filter that has been recommended for the baseband case. In order to preserve the spectral efficiency, it is necessary to include, at the transmitter, a synthesis side of a sine modulated filter bank for generation of the quadrature signal. Outcomes indicate that bandpass ELT-MCM system exhibits an excellent behaviour, in terms of both BER and data rate, assuming an ASCET equalizer and under different and realistic PLC scenarios.

Finally, as a final conclusion of this thesis, wavelet OFDM is a viable and attractive solution for in baseband and bandpass communications over the electrical wiring to the deployment and development of home area network, smart energy/grid, IoT and for transportation platforms applications.

6.2 Contributions

This thesis deals with the physical layer specifications provided by the standard IEEE 1901, proposing several contributions at different levels. From the results of the research activity developed within this work, the following original contributions can be listed:

- The understanding on the wavelet OFDM for baseband communications over the mains network is extended. Some key features, as the kind of modulation scheme proposed as transmitter, as well as the time-domain waveforms recommended as prototype filter to obtain the transmitter filters, have been clarified.
- An efficient implementation of the whole baseband wavelet OFDM system, based on the IEEE 1901 physical layer specification (by means of polyphase filters, lattice and butterfly structures) has been developed, and their computational complexities analyzed.
- A set of expressions to calculate the coefficients of these prototype filters has been presented. We have shown a nontrivial trade-off between the stopband attenuation and the transition bandwidth, which has an effect on the system performance.
- A family of frequency-domain equalizer has been proposed for the recommended system.
- To our knowledge, this is the first time that theoretical expression to obtain the different powers (signal, interferences and noise) for a filter bank based on the extended lapped transform have been derived. These expressions have been presented in a generalized and simplified way considering an L-ASCET equalizer and assuming either additive white Gaussian noise and non-AWGN noise.
- An in-depth study about the wavelet OFDM system performance under different kind of low voltage PLC channel (i.e., in-home, in-car and in-aircraft) and different type of PLC noises (e.g., colored background noise, periodic impulsive noise synchronous/asynchronous to the mains frequency, among others), has been carried out.
- A bandpass ELT-MCM system has been developed and tested under different PLC conditions.
- A performance comparison study in terms of data rate, between wavelet OFDM and windowed OFDM, has been carried out.

The results achieved in this research work have been presented at several international events and accepted for scientific publications. In particular, 3 papers have been published in relevant international journals, and during the realization of this thesis, 4 and 5 papers have been presented at international and national congresses, respectively. In addition, a whole transceiver has been patented (Spanish Patent No. ES2556148). A complete list of the papers related to the research work performed in this thesis can be seen in the appendix.

6.3 Future research lines

Despite the different results obtained from this research work, there are still several directions in which subsequent studies could progress. Some of the detected areas to be addressed more deeply in near future include:

- In all the simulations here reported, we assume that the channel remains constant during each multicarrier symbol, and perfect channel knowledge is also assumed in the receiver side. The first natural extension of the research regarding the wavelet OFDM system is the channel estimation. This issue, together with adaptive filtering techniques to perform the channel equalization, could provide a more realistic system performance.

- In this sense, another extension of this work is the analysis of the system performance under different equalization technique. ASCET provides a good performance, as long as the order is higher than zero, but it increases the computation complexity of the receiver. Therefore, it would be useful to define another equalization process that provides, at least, the same performance but decreasing the computational cost.

- This thesis focuses on communications over the electrical wiring. However, nowadays, ELT-based system, which is a filter bank multicarrier, can be an attractive alternative to OFDM as modulation technique for the fifth generation of the wireless network (5G). Besides, it can be also used for underwater communications or even for satellite communications. Some physical layer would change such as the frequency range, the frequency spacing, the number of active subcarriers, among others, but the strategy and the core of the system would remain the same.

- Likewise, the analysis realized in this thesis considers only in-home, in-car and in-aircraft conditions as well as broadband communications. Therefore, the study can be extended to other PLC scenarios such as high-voltage lines, medium-voltage lines, other transportation platforms (ships or spacecraft) and to narrowband communications.

- With the theoretical expression for the desired signal, inter-symbol and inter-carrier interference and noise power derived in this thesis, we open the door to the resource allocation issue. Thus, resource allocation technique, such as water-filling algorithm, can be applied to wavelet OFDM system increasing even further the system performance. Regarding this latter point, we suggest following the IEEE 1901.2 physical layer specifications.

- The really deep notches that the power line network presents in its frequency response can severely degrade the multicarrier system efficiency. Therefore, a single-carrier system could reach a better performance. In this respect, it is proposed to develop a new single-carrier system based on the ELT, and analyze its behaviour under different PLC scenarios.

APPENDIX A

List of publications

This section is a compilation of the various scientific publications produced as a result of this research work, apart from those other not directly related to this thesis.

A.1 Papers related to the research work realized in this PhD.

Patents

1. F. Cruz-Roldán, **F. A. Pinto-Benel**, M. Blanco-Velasco, F. J. Reynoso, A. Hernández, J. Ureña-Ureña (2016). Spanish Patent No. ES2556148. Madrid, Spain: Oficina Española de Patentes y Marcas.

International journals

1. P. Poudereux, A. Hernández, R. Mateos, **F. A. Pinto-Benel**, and F. Cruz-Roldán, "Design of a filter bank multi-carrier system for broadband power line communications," *Signal processing*, vol. 128, pp. 57-67, Nov 2016, DOI 10.1016/j.sigpro.2016.03.014, JCR 2016: 3.110.

2. F. Cruz-Roldán, **F. A. Pinto-Benel**, José D. Osés del Campo and M. Blanco-Velasco, "A Wavelet OFDM receiver for baseband power line communications," *Journal of the Franklin Institute*, vol. 357, Issue 7, pp. 1654-1671, May 2016, DOI 10.1016/j.jfranklin.2016.02.015, JCR 2016: 3.139.

3. **F. A. Pinto-Benel**, M. Blanco-Velasco, F. Cruz-Roldán, "Throughput Analysis of Wavelet OFDM in Broadband Power Line Communications," *IEEE Access*, vol. 6, pp. 16727-16736, Jan 2018, DOI 10.1109/ACCESS.2018.2796618, JCR 2016: 3.244.

4. **F. A. Pinto-Benel**, F. Cruz-Roldán, "A Bandpass Wavelet OFDM System for Power Line Communications," *Journal of the Franklin Institute*, (Under review).

International conferences

1. **F. A. Pinto-Benel**, F. J. Reynoso, F. Cruz-Roldán, "Aplicación de un sistema con banco de filtros multiportadora de banda ancha con igualador ASCET en presencia de un canal PLC," *IV Congreso Internacional de Computación y Telecomunicaciones (COMTEL)*, Lima (Peru), 2014.

2. **F. A. Pinto-Benel**, F. Cruz-Roldán, "2-ASCET for Broadband Multicarrier Transmission over In-home and In-vehicle Power Line Networks," *2015 IEEE 18th International Conference on Intelligent Transportation Systems (ITSC)*, Las Palmas (Spain).

3. **F. A. Pinto-Benel**, F. Cruz-Roldán, "Exploring the performance of prototype filters for broadband PLC," *2017 IEEE International Symposium on Power Line Communications and its Applications (ISPLC)*, Madrid (Spain).

4. **F. A. Pinto-Benel**, M. Blanco-Velasco, F. Cruz-Roldán, "Comparing the Wavelet OFDM and Windowed OFDM data rate for in-home PLC," *2018 IEEE International Symposium on Circuits and Systems (ISCAS)*, Florence (Italy).

National conferences

1. **F. A. Pinto-Benel**, F. J. Reynoso, José Sáez Landete, F. Cruz-Roldán, "Implementación de un sistema multiportadora con bancos de filtros para PLC de banda ancha," *XXIX Simposium Nacional de la Unión Científica Internacional de Radio (URSI)*, Valencia (Spain), 2014.

2. **F. A. Pinto-Benel**, M. Blanco-Velasco, F. Cruz-Roldán, "Desarrollo de un sistema en banda base Wavelet OFDM para PLC," *XXXI Simposium Nacional de la Unión Científica Internacional de Radio (URSI)*, Madrid (Spain), 2016.

3. **F. A. Pinto-Benel**, F. Cruz-Roldán, "Estudio de formas de onda para comunicaciones a través de la red eléctrica," *XXXII Simposium Nacional de la Unión Científica Internacional de Radio (URSI)*, Cartagena (Spain), 2017.

4. **F. A. Pinto-Benel**, M. Blanco-Velasco, F. Cruz-Roldán, "Estudio del rendimiento de las comunicaciones a través de la red eléctrica sobre plataformas con Wavelet OFDM," *V Congreso nacional de i+d en Defensa y Seguridad*, Toledo (Spain), 2017.

5. F. García Gangoso, **F. A. Pinto-Benel**, F. Cruz-Roldán, "Análisis comparativo de las tecnologías de capa física propuestas en el estándar IEEE P1901-2010", *XXXII Simposium Nacional de la Unión Científica Internacional de Radio (URSI)*, Granada (Spain), 2018.

A.2 Other results achieved during this PhD.

International conferences

1. F. Cruz-Roldán, **F. A. Pinto-Benel**, M. E. Domínguez-Jiménez, G Sansigre-Vidal, "Single-carrier frequency division multiple access with discrete cosine transform type-I," *2015 IEEE 13th International New Circuits and Systems Conference (NEWCAS)*, Grenoble (France), 2015.

National conferences

1. F. J. Reynoso, **F. A. Pinto-Benel**, M. Blanco-Velasco, F. Cruz-Roldán, "Estimación de canal con símbolos piloto para sistemas DCT-MCM en presencia de CFO," *XXIX Simposium Nacional de la Unión Científica Internacional de Radio (URSI)*, Valencia (Spain), 2014.

References

[1] V. Degardin, I. Junqua, M. Lienard, P. Degauque, and S. Bertuol, "Theoretical approach to the feasibility of power-line communication in aircrafts," *IEEE Transactions on Vehicular Technology*, vol. 62, pp. 1362 – 1366, March 2013.

[2] T. Zheng, M. Raugi, and M. Tucci, "Time-invariant characteristics of naval power-line channels," *IEEE Transactions on Power Delivery*, vol. 27, pp. 858–865, April 2012.

[3] S. Barmada, A. Gaggelli, A. Musolino, R. Rizzo, M. Raugi, and M. Tucci, "Design of a PLC system onboard trains: Selection and analysis of the PLC channel," in *IEEE International Symposium on Power Line Communications and Its Applications (ISPLC)*, (Pisa, Italy), pp. 13–17, 2008.

[4] V. Degardin, P. Laly, M. Lienard, and P. Degauque, "Investigation on power line communication in aircrafts," *IET Communications*, vol. 8, no. 10, pp. 1868–1874, 2014.

[5] P. T. W. Group, "Specification for powerline intelligent metering evolution," October 2014.

[6] "G3-PLC physical layer specification," 2009.

[7] I. S. Association, "IEEE Standard for Low-Frequency (less than 500 kHz) Narrowband Power Line Communications for Smart Grid Applications."

[8] "ITU-T G.9960. Unified high-speed wireline-based home networking transceivers - System architecture and physical layer specification," standard, July 2015.

[9] HomePlug AV White Paper. Available at http://www.homeplug.org/tech/whitepapers/HPAV-White-Paper_050818.pdf [Feb. 2017].

[10] IEEE Std 1901-2010, "IEEE standard for broadband over power line networks: Medium access control and physical layer specifications," December 2010.

[11] B. Farhang-Boroujeny, "Filter bank multicarrier modulation: A waveform candidate for 5G and beyond," *Advances in Electrical Engineering*, vol. 2014, 2014.

[12] P. Banelli, S. Buzzi, G. Colavolpe, A. Modenini, F. Rusek, and A. Ugolini, "Modulation formats and waveforms for 5G networks: Who will be the heir of OFDM?," *IEEE Signal Processing Magazine*, pp. 80–93, 2014.

[13] J. Cioffi, *Digital Communications, chap. 4: Multichannel Modulation.* https://web.stanford.edu/group/cioffi/doc/book/chap4.pdf.

[14] Y. G. Li and G. L. Stuber, *Orthogonal frequency division multiplexing for wireless communications*. Springer Science & Business Media, 2006.

[15] P. Achaichia, M. L. Bot, and P. Siohan, "OFDM/OQAM: A solution to efficiently increase the capacity of future PLC networks," *IEEE Transactions on Power Delivery*, vol. 26, pp. 2443–2455, Oct 2011.

[16] M. Bellanger and J. Daguet, "TDM-FDM transmultiplexer: Digital polyphase and FFT," *IEEE Transactions on Communications*, vol. 22, pp. 1199–1205, Sep 1974.

[17] M. Bellanger, "On computational complexity in digital transmultiplexer filters," *IEEE Transactions on Communications*, vol. 30, pp. 1461–1465, July 1982.

[18] B. Farhang-Boroujeny, "OFDM versus filter bank multicarrier," *IEEE Signal Processing Mag.*, vol. 28, pp. 92–112, May 2011.

[19] S. Premnath, D. Wasden, S. K. Kasera, N. Patwari, and B. Farhang-Boroujeny, "Beyond OFDM: Best-effort dynamic spectrum access using filterbank multicarrier," *IEEE/ACM Transactions on Networking*, vol. 21, pp. 869–882, June 2013.

[20] Y. P. Lin, S. M. Phoong, and P. P. Vaidyanathan, *Filter Bank Transceivers for OFDM and DMT systems*. Cambridge University Press, 2010.

[21] S. D. Sandberg and M. A. Tzannes, "Overlapped discrete multitone modulation for high speed copper wire communications," *IEEE Journal on Selected Areas in Communications*, vol. 13, pp. 1571–1585, December 1995.

[22] G. Cherubini, E. Eleftheriou, S. Ölçer, and J. M. Cioffi, "Filter bank modulation techniques for very high-speed digital subscriber lines," *IEEE Communications Magazine*, pp. 98–104, May 2000.

[23] A. Akansu and X. Lin, "A comparative performance evaluation of DMT (OFDM) and DWMT (DSBMT) based DSL communications systems for single and multitone interference," in *Proceedings of the 1998 IEEE International Conference on Acoustics, Speech and Signal Processing, 1998*, vol. 6, pp. 3269–3272, May 1998.

[24] G. Cherubini, E. Eleftheriou, and S. Ölçer, "Filtered multitone modulation for very high-speed digital subscriber lines," *IEEE Journal on Selected Areas in Communications*, pp. 1016–1028, June 2002.

[25] L. Lin and B. Farhang-Boroujeny, "Cosine-modulated multitone for very-high-speed digital subscriber lines," *Eurasip Journal on Applied Signal Processing*, vol. 2006, pp. Article ID 19329, 16 pages, 2006.

[26] H. Malvar, *Signal Processing with Lapped Transforms*. Norwood MA: Artech House, 1992.

[27] F. A. Pinto-Benel and F. Cruz-Roldán, "2-ASCET for broadband multicarrier transmission over in-home and in-vehicle power line networks," in *IEEE 18th International Conference on Intelligent Transportation Systems*, pp. 1351 – 1356, 2015.

[28] F. Cruz-Roldán, F. Pinto-Benel, J. Osés del Campo, and M. Blanco-Velasco, "A wavelet OFDM receiver for baseband power line communications," *Journal of the Franklin Institute*, vol. 353, pp. 1654–1671, May 2016.

[29] F. A. Pinto-Benel and F. Cruz-Roldán, "Exploring the performance of prototype filters for broadband PLC," in *IEEE International Symposium on Power Line Communications and its Applications (ISPLC), 2017*, 2017.

[30] F. A. Pinto-Benel, M. Blanco-Velasco, and F. Cruz-Roldán, "Throughput analysis for wavelet OFDM in broadband power line communications," *IEEE ACCESS*, vol. 6, pp. 16727–16736, 2018. Under review.

[31] H. Lin and P. Siohan, "Capacity analysis for indoor PLC using different multi-carrier modulation schemes," *IEEE Transactions on Power Delivery*, vol. 25, pp. 113–124, Jan 2010.

[32] H. Wang, X. Wang, L. Xu, and W. Du, "Hybrid PAPR reduction scheme for FBMC/OQAM systems based on multi data block PTS and TR methods," *IEEE Access*, vol. 4, pp. 4761–4768, 2016.

[33] A. Rezazadeh-Reyhani and B. Farhang-Boroujeny, "Capacity analysis of FBMC-OQAM systems," *IEEE Communications Letters*, vol. 21, no. 5, pp. 999–1002, 2017.

[34] P. P. Vaidyanathan, *Multirate Systems and Filter Banks*. Englewood Cliffs NJ: Prentice–Hall Englewood Cliffs, 1993.

[35] B. Farhang-Boroujeny and C. H. Yuen, "Cosine modulated and offset QAM filter bank multicarrier techniques: A continuous-time prospect," *EURASIP Journal on Advances in Signal Processing*, vol. 2010, p. 6, 2010.

[36] D. Umehara, H. Nishiyori, and Y. Morihiro, "Performance evaluation of CMFB transmultiplexer for broadband power line communications under narrowband interference," in *IEEE International Symposium on Power Line Communications and Its Applications (ISPLC)*, pp. 50–55, 2006.

[37] K. Izumi, D. Umehara, and S. Denno, "Performance evaluation of wavelet OFDM using ASCET," in *IEEE International Symposium on Power Line Communications and Its Applications (ISPLC)*, pp. 246–251, March 2007.

[38] J. Alhava and M. Renfors, "Adaptive sine-modulated/cosine-modulated filter bank equalizer for transmultiplexers," in *European Conference on Circuit Theory and Design, Espoo, Finland*, pp. 337–340, 2001.

[39] P. A. Brown, "Power line communications - past, present, and future," in *International Symposium on Power Line Communications and its Applications (ISPLC)*, pp. 1–8, 1999.

[40] K. Dostert, *Powerline Communications*. Prentice Hall PTR, 2001.

[41] A. Zanella, N. Bui, A. Castellani, L. Vangelista, and M. Zorzi, "Internet of things for smart cities," *IEEE Internet of Things Journal*, vol. 1, no. 1, pp. 22–32, February 2014.

[42] X. Li, R. Lu, X. Liang, X. Shen, J. Chen, and X. Lin, "Smart community: An internet of things application," *IEEE Communications Magazine*, vol. 49, no. 11, pp. 68–75, November 2011.

[43] Y. Qian, J. Yan, H. Guan, J. Li, X. Zhou, S. Guo, and D. N. K. Jayakody, "Design of hybrid wireless and power line sensor networks with dual-interface relay in IoT," *IEEE Internet of Things Journal (Early Access)*, 2018.

[44] Communication from the commission to the european parliament, the council, the european economic and social commitee and the commitee of the regions, "Smart grids: from innovation to deployment." Available at http://eur-lex.europa.eu/legal-content/EN/TXT/PDF/?uri=CELEX:52011DC0202&from=EN [Feb. 5, 2018].

[45] L. T. Berger, A. Schwager, and J. J. Escudero-Garzás, "Powerline communications for smart grid applications," *Journal of Electrical and Computer Engineering - Special issue on Power-Line Communications: Smart Grid, Transmission, and Propagation*, vol. 2013, January 2013.

[46] A. Majumber and J. J. Caffery, "Power line comunications: An overview," *IEEE Potentials Magazine*, vol. 23, no. 4, pp. 4–8, October 2004.

[47] S. Galli, A. Scaglione, and Z. Wang, "For the grid and through the grid: The role of power line communications in the smart grid," *Proceedings of the IEEE*, vol. 99, pp. 998–1027, June 2011.

[48] N. energy technology laboratory, "Broadband over power lines could accelerate the transmission smart grid," tech. rep., U. S. Departmet of Energy, 2010.

[49] J. F. Adami, P. M. Silveira, M. L. B. Martinez, R. C. Perez, and A. C. Dallbello, "New approach to improve high-voltagetransmission line reliability," *IEEE Transaction on Power Delivery*, vol. 24, no. 3, 2009.

[50] W. de Villiers, J. H. Cloete, L. M. Wedepohl, and A. Burger, "Real-time sag monitoring system for high-voltage overhead transmission lines based on power-line carrier signal behavior," *IEEE Transaction on Power Delivery*, vol. 23, no. 1, pp. 389–395, 2008.

[51] A. Cataliotti, A. Daidone, and G. Tinè, "Power line communication in medium voltage systems: Characterization of MV cables," *IEEE Transactions on Power Delivery*, vol. 23, pp. 1896–1902, March 2008.

[52] A. Kitamura, M. Okamoto, F. Yamamoto, K. Nakaji, H. Matsuda, and K. Hotta, "Islanding phenomenon elimination study at rokko test center," in *IEEE First World Conference on Photovoltaic Energy Conversion*, 1994.

[53] R. Benato and R. Caldon, "Application of PLC for the control and the protection of future distribution networks," in *IEEE International Symposium on Power Line Communications and Its Applications (ISPLC)*, 2007.

[54] M. E. Ropp, K. Aaker, J. Haigh, and N. Sabbah, "Using power line carrier communications to prevent islanding," in *IEEE Photovoltaic Specialists Conference*, pp. 1675–1678, 2000.

[55] P. Meier, M. Bittner, H. Widmer, J. L. Bermudez, A. Vukicevic, M. Rubinstein, and J. S. Miravalles, "Pathloss as a function of frequency, distance and network topology for various LV and MV European powerline networks," *The OPERA Consortium, Project Deliverable, EC/IST FP6 Project no. 507667 D5v0.9.*, 2005.

[56] E. P. R. I. (EPRI), "Report to NIST on the smart grid interoperability standards roadmap," 2009.

[57] J. Wolf, "Power line communication (PLC) in space - current status and outlook," in *Proceedings ESA Workshop on Aerospace EMC*, 2012.

[58] M. Antoniali, A. M. Tonello, M. Lenardon, and A. Qualizza, "Measurements and analysis of PLC channels in a cruise ship," in *IEEE International Symposium on Power Line Communications and Its Applications (ISPLC)*, (Udine, Italy), pp. 102 – 107, 2011.

[59] M. Antoniali, M. D. Piante, and A. M. Tonello, "PLC noise and channel characterization in a compact electrical car," in *IEEE 17th International Symposium on Power Line Communications and Its Applications (ISPLC)*, 2013.

[60] C. A. Winterhalter, J. Teverovsky, P. Wilson, J. Slade, W. Horowitz, E. Tierney, and V. Sharma, "Development of electronic textiles to support networks, communications, and medical applications in future u.s. military protective clothing systems," *IEEE Transactions on Information Technology in Biomedicine*, vol. 9, pp. 402–406, September 2005.

[61] C. Glaros, D. I. Fotiadis, A. Likas, and A. Stafylopatis, "A wearable intelligent system for monitoring health condition and rehabilitation of running athletes," pp. 276–279, 2014.

[62] T. C. Chou, N. F. Chiu, F. R. Liao, S. S. Lu, F. Ping, C. R. Yang, and C. W. Lin, "A multi parameters wearable telemetric system for cardio-pulmonary fitness of e-health," in *27th Annual International Conference of the Engineering in Medicine and Biology Society (IEEE-EMBS)*, pp. 3498–3501, 2005.

[63] T. Martin, E. Jovanov, and D. Raskovic, "Issues in wearable computing for medical monitoring applications: a case study of a wearable ECG monitoring device," in *The Fourth International Symposium on Wearable Computers*, pp. 43–48, October 2000.

[64] H. C. Ferreira, L. Lampe, J. Newburry, and T. G. Swart, *Power Line Communications: Theory and Applications for Narrowband and Broadband Communications over Power Lines*. John Wiley & Sons Ltd, 2010.

[65] D. E. Nordell, "Communication systems for distribution automation," in *IEEE/PES Transmission and Distribution Conference and Exposition*, 2008.

[66] S. T. Mak and D. L. Reed, "TWACS, a new viable two-way automatic communication system for distribution networks. Part I: Outbound communication," *IEEE Transactions on Power Apparatus and Systems*, vol. PAS-101, pp. 2941–2949, 1982.

[67] S. T. Mak and T. G. Moore, "TWACS, a new viable two-way automatic communication system for distribution networks. Part II: Inbound communication," *IEEE Transactions on Power Apparatus and Systems*, vol. PAS-103, pp. 2141–2147, 1984.

[68] International Organization for Standartization, "Information technology - control network protocol - part 3: power line channel specification."

[69] International Organization for Standartization, "Information technology - home electronic system (HES) architecture - part 3-5: media and media dependent layers - power line for network based control of HES Class 1."

[70] "Distribution automation using distribution line carrier systems - part 5-1: lower layer profiles - the spread frequency shift keying (S-FSK) profile."

[71] S. Galli, M. K. nad H. Latchman, S. Lee, and V. Oksman, *Industrial and international standards on PLC base networking technologies*, pp. 363–412. 2010.

[72] "ITU-T G.9901. Narrowband orthogonal frequency division multiplexing power line communication transceivers - Power spectral density specification," standard, Telecommunication sector of ITU, 6 2017. [Online, Feb 2018]. Avaible: https://www.itu.int/rec/T-REC-G.9901-201706-I/en.

[73] "ITU-T G.9902. Narrowband orthogonal frequency division multiplexing power line communication transceivers for ITU-T G.hnem networks," standard, Telecommunication sector of ITU, 10 2012. [Online, Feb 2018]. Avaible: https://www.itu.int/rec/T-REC-G.9902-201210-I.

[74] "ITU-T G.9903. Narrowband orthogonal frequency division multiplexing power line communication transceivers for G3-PLC networks," standard, Telecommunication sector of ITU, 8 2017. [Online, Feb 2018]. Avaible: https://www.itu.int/rec/T-REC-G.9903-201708-I/en.

[75] "ITU-T G.9904. Narrowband orthogonal frequency division multiplexing power line communication transceivers for PRIME networks," standard, Telecommunication sector of ITU, 10 2012. [Online, Feb 2018]. Avaible: https://www.itu.int/rec/T-REC-G.9904-201210-I/en.

[76] C. Cano, A. Pittolo, D. Malone, L. Lampe, A. M. Tonello, and A. G. Dabak, "State of the art in power line communications: From the applications to the medium," *IEEE Journal on Selected Areas in Communications*, vol. 34, pp. 1935–1952, July 2016.

[77] M. K. Lee, R. E. Newman, H. A. Latchman, S. Katar, and L.Yonge, "Homeplug 1.0 powerline communication LANs - protocol description and performance results," *International Journal of communications systems*, vol. 16, no. 5, pp. 447–473, 2003.

[78] H. A. Latchman, S. Katar, L. Yonge, and S. Gavette, *HomePlug AV and IEEE 1901*. 2013.

[79] L. Yonge, J. Abad, K. Afkhamie, L. Guerrieri, S. Katar, H. Lioe, P. Pagani, R. Riva, D. M. Schneider, and A. Schwager, "An overview of the HomePlug AV2 technology," *Journal of Electrical and Computer Engineering*, 2013.

[80] "HomePlug Green. HomePlug Green PHY Specification Release Version 1.1.1," standard, HomePlug Alliance, 2013. [Online, Feb 2018]. Avaible: https://www.homeplug.org/media/filer_public/74/40/7440ccd5-8c66-49ed-a2ce-5ef661932c27/homeplug_gp_specification_v111_final_public.pdf.

[81] "ITU-T G.9964. Unified high-speed wireline-based home networking transceivers - Power spectral density specification," standard, Telecommunication sector of ITU, 2011. [Online, Feb 2018]. Avaible: https://www.itu.int/rec/T-REC-G.9964-201112-I/en.

[82] S. A. Elghafar, S. M. Diab, B. M. Sallam, E. S. Hassan, M. Shokair, W. Al-Nauimy, M. I. Dessouky, E. M. El-Rabaie, S. A., and F. E. A. El-Samie, "Utilization of discrete transforms to conquer the problems of multi-tone systems," *Journal of the Franklin Institute*, vol. 351, no. 3, pp. 1778–1800, 2014.

[83] F. Cruz–Roldán, M. Domínguez-Jiménez, G. Sansigre–Vidal, J. Piñeiro–Ave, and M. Blanco–Velasco, "Single-carrier and multicarrier transceivers based on discrete cosine transform type-IV," *IEEE Transactions on Wireless Communications*, vol. 12, pp. 6454–6463, December 2013.

[84] A. Viholainen, *Modulated Filter Bank Design for Communication Signal Processing*. PhD thesis, Tampere University of Technology, 2004.

[85] H. S. Malvar, "Lapped transforms for efficient transform/subband coding," *IEEE Transactions on Acoustics Speech and Signal Processing*, vol. 38, no. 6, pp. 969 – 978, 1990.

[86] M. Zimmermann and K. Dostert, "Analysis and modeling of impulsive noise in broad-band powerline communications," *IEEE Transactions on Electromagnetic Compatibility*, vol. 44, pp. 249–258, Feb 2002.

[87] M. Zimmermann and K. Doster, "A multipath model for the powerline channel," *IEEE Transactions on Communications*, vol. 50, no. 4, pp. 553–559, April 2002.

[88] A. M. Tonello, "Wideband impulse modulation and receiver algorithms for multiuser power line communications," *EURASIP Journal on Advances in Signal Processing*, vol. 2007, 2007.

[89] M. Tlich, A. Z. F. Moulin, and F. Gauthier, "Indoor power-line communications channel characterization up to 100 MHz - Part I: One-parameter deterministic model," *IEEE Transactions on Power Delivery*, vol. 23, no. 3, pp. 1392–1401, July 2008.

[90] Seventh Framework Programme: Theme 3 ICT-213311 OMEGA, "Deliverable D3.2: PLC channel characterization and modelling," tech. rep., 2008. http://www.ict-omega.eu/.

[91] F. J. Cañete, J. A. Cortés, L. Díez, and J. T. Entrambasaguas, "A channel model proposal for indoor power line communications," *IEEE Communications Magazine*, vol. 49, pp. 166–174, December 2011.

[92] L. Guerrieri, P. Bisaglia, I. S. Stievano, and F. G. Canavero, "Statistical assessment of automotive plc multipath channel models," in *Proc. IEEE ISPLC*, (Glasgow, Scotland), pp. 45–51, 2014.

[93] L. Lampe, "Data base of in-vehicle power line channel measurements." Available at http://www.ece.ubc.ca/~lampe/VehiclePLC.html [Feb. 2015].

[94] M. Mohammadi, L. Lampe, M. Lok, S. Mirabbasi, M. Mirvakili, R. Rosales, and P. van Veen, "Measurement study and transmission for in-vehicle power line communication," in *Proc. IEEE ISPLC*, (Germany), pp. 73 – 78, 2009.

[95] A. B. Vallejo-Mora, J. J. Sánchez-Martínez, F. J. Cañete, J. A. Cortés, and L. Díez, "Characterization and evaluation of in-vehicle power line channels," in *IEEE Global Communication Conference, Exhibition and Industry forum (GLOBECOM)*, pp. 1–5, 2010.

[96] V. Degardin, M. Lienard, P. Degauque, I. Junqua, and S. Bertuol, "Power line communication in aircraft: Channel modelling and performance analysis," in *8th International Caribbean Conference on Devices, Circuts and Systems (ICCDCS)*, 2012.

[97] J. A. Cortés, L. Díez, F. J. Cañete, and J. J. Sánchez-Martínez, "Analysis of the indoor broadband power-line noise scenario," *IEEE Transactions on Electromagnetic Compatibility*, vol. 52, pp. 849–858, November 2010.

[98] G. Prasad, L. Lampe, and S. Shekhar, "In-band full duplex broadband power line communications," *IEEE Transactions on Communications*, vol. 64, no. 9, pp. 3915–3931, 2016.

[99] M. Tlich, A. Zeddam, F. Moulin, and F. Gauthier, "Indoor power-line communications channel characterization up to 100 MHz - Part II: time-frequency analysis," *IEEE Transactions on Power Delivery*, vol. 23, no. 3, pp. 1402–1409, July 2008.

[100] A. Tonello, "Brief tutorial on the statistical top-down PLC channel generator," 2010.

[101] A. Tonello, S. D'Alessandro, and L. Lampe, "Cyclic prefix design and allocation in bit-loaded OFDM over power line communication channels," *IEEE Transactions on Communications*, vol. 58, pp. 3265–3276, November 2010.

[102] F. J. Cañete, "User guide for PLC channel generator V.2." http://www.plc.uma.es/canales.htm [Feb 2018], 2011.

[103] H. Meng, Y. L. Guan, and S. Chen, "Modeling and analysis of noise effects on broadband power-line communications," *IEEE Transactions on Power Delivery*, vol. 20, no. 2, pp. 630–637, April 2005.

[104] D. Benyoucef, "A new statistical model of the noise power density spectrum for powerline communication," in *IEEE International Symposium on Power Line Communications and Its Applications (ISPLC)*, pp. 136–141, 2003.

[105] L. Lampe, "A cumulative power line noise generator." Available at http://www.ece.ubc.ca/~gauthamp/PLCnoise/ [Feb 2018].

[106] T. Esmailian, P. G. Gulak, and F. R. Kschischang, "A discrete multitone power line communications system," in *IEEE International Conference on Acoustics, Speech, and Signal Processing (ICASSP)*, pp. 2953–2956, 2000.

[107] R. Hormis, I. Berenguer, and X. Wang, "A simple baseband transmission scheme for power line channels," *IEEE Journal on Selected Area in Communications*, vol. 24, no. 7, pp. 1351–1363, 2006.

[108] M. Antoniali, M. Girotto, and A. M. Tonello, "In-car power line communications: Advanced transmission techniques," *International Journal of Automotive Technology*, vol. 144, no. 625-632, 2013.

[109] N. Bahrani and V. Gaudet, "Measurements and channel characterization for in-vehicle power line communications," in *18th IEEE International Symposium on Power Line Communications and Its Applications (ISPLC)*, 2014.

[110] A. Schiffer, "Statistical channel and noise modeling of vehicular DC-lines for data communication," in *2000 IEEE 51st Vehicular Technology Conference Proceedings*, 2000.

[111] V. Degardin, M. Lienard, P. Degauque, and P. Laly, "Performances of the HomePlug PHY layer in the context of in-vehicle powerline communications," in *IEEE International Symposium on Power Line Communications and Its Applications*, 2007.

[112] J. Granado, A. Torralba, and J. Chávez, "Using broadband power line communications in non-conventional applications," *IEEE Transactions on Consumer Electronics*, vol. 57, no. 3, pp. 1092–1098, 2011.

[113] J. A. Cortés, M. Cerdá, L. Díez, and F. J. Cañete, "Analysis of the periodic noise on in-vehicle broadband power line channels," in *IEEE International Symposium on Power Line Communications and Its Applications*, pp. 334–339, 2012.

[114] V. Degardin, M. Lienard, P. Degauque, E. Simon, and P. Laly, "Impulsive noise characterization of in-vehicle power line," *IEEE Transactions on Electromagnetic Compatibility*, vol. 50, no. 4, pp. 861–868, 2008.

[115] R. E. Crochiere and L. R. Rabiner, *Multirate Digital Signal Processing*. Prentice Hall, 1983.

[116] T. Nhan-Vo, K. Amis, T. Chonavel, and P. Siohan, "Achievable throughput optimization in OFDM systems in the presence of interference and its application to power line networks," *IEEE Transactions on Communications*, vol. 62, no. 5, pp. 1704–1715, 2014.

[117] L. L. B. Farhang-Boroujeny, "Cosine-modulated multitone for very-high-speed digital subscriber lines," in *EURASIP Journal on Applied Signal Processing*, pp. 1–16, 2006.

[118] H. S. Malvar, "Modulated QMF filter banks with perfect reconstruction," *Electronics Letters*, vol. 26, no. 13, pp. 906–907, 1990.

[119] R. D. Koilpillai and P. P. Vaidyanathan, "Cosine-modulated FIR filter banks satisfying perfect reconstruction," *IEEE Transactions on Signal Processing*, vol. 40, pp. 770–783, April 1992.

[120] S. A. Martucci, "Symmetric convolution and the discrete sine and cosine transforms," *IEEE Transactions on Signal Processing*, vol. 42, pp. 1038–1051, May 1994.

[121] V. Sánchez, P. García, A. M. Peinado, J. C. Segura, and A. J. Rubio, "Diagonalizing properties of the discrete cosine transform," *IEEE Transactions on Signal Processing*, vol. 43, pp. 2631–2641, November 1995.

[122] P. Vaidyanathan, "Passive cascaded-lattice structures for low-sensitivity FIR filter design, with applications to filter banks," *IEEE Transactions on Circuits and Systems*, vol. 33, pp. 1045–1064, Nov 1986.

[123] H. S. Malvar, "Extended lapped transforms: Properties, applications and fast algorithms," *IEEE Transactions on Signal Processing*, vol. 40, pp. 2703–2714, November 1992.

[124] A. Viholainen, J. Alhava, and M. Renfors, "Efficient implementation of complex modulated filter banks using cosine and sine modulated filter banks," *EURASIP Journal on Applied Signal Processing*, vol. 2006, pp. Article ID 58564, 10 pages, 2006.

[125] Y. Yang, T. Ihalainen, M. Rinne, and M. Renfors, "Frequency-domain equalization in single-carrier transmission: Filter bank approach," *EURASIP Journal on Applied Signal Processing*, vol. 2007, no. 1, pp. 135–135, 2007.

[126] T. Ihalainen, T. Hidalgo Stitz, M. Rinne, and M. Renfors, "Channel equalization in filter bank based multicarrier modulation for wireless communications," *EURASIP Journal on Advances in Signal Processing*, vol. 2007, 2007.

[127] V. Britanak, "The fast DCT-IV/DST-IV computation via the MDCT," *Signal Processing*, vol. 83, pp. 1803–1813, august 2003.

[128] G. Plonka and M. Tasche, "Fast and numerically stable algorithms for discrete cosine transforms," *Linear Algebra and its Applications*, vol. 394, pp. 309–345, january 2005.

[129] X. Shao and A. G. Johnson, "Type-IV DCT, DST, and MDCT algorithms with reduced numbers of arithmetic operations," *Signal Processing*, vol. 88, pp. 1313–1326, june 2008.

[130] T. Ihalainen, T. H. Stitz, and M. Renfors, "Efficient per-carrier channel equalizer for filter bank based multicarrier systems," in *Proc. Int. Symp. on Circuits and Systems*, (Kobe, Japan), pp. 3175 –3178, May 2005.